

Université du Québec
Institut National de la Recherche Scientifique
Centre Énergie Matériaux Télécommunications

**FIRST-PRINCIPLES INVESTIGATION OF MULTIFERROIC
 $\text{Bi}_2\text{FeCrO}_6$ EPITAXIAL THIN-FILMS**

Par
Liliana Braescu

Mémoire ou thèse présentée pour l'obtention du grade de
Philosophiae doctor (Ph.D.)
en sciences de l'énergie et des matériaux

Jury d'évaluation

Président du jury et examinateur interne	Federico Rosei INRS – Énergie, Matériaux et Télécommunications
Examinateur externe	Michel Côté Département de Physique Université de Montréal
Examinateur externe	Riad Nechache Département Génie Électrique École de Technologie Supérieure
Directeur de recherche	François Vidal INRS – Énergie, Matériaux et Télécommunications
Codirecteur de recherche	Alain Pignolet INRS – Énergie, Matériaux et Télécommunications

AKNOWLEDGEMENTS

I am grateful to my advisor Professor François Vidal and my co-supervisor Professor Alain Pignolet, for the mentorship that they have provided at the Institut National de la Recherche Scientifique, Centre Énergie, Matériaux et Télécommunications (INRS-EMT), for keeping questioning my results and for introducing me to the perovskites kingdom. They also taught me how to improve the story telling of my research at an outstanding and modern level, in a strong and effective manner, both as scientific papers and presentations. I thank them for allowing me to work on the exciting and challenging topic of multiferroics and multiferroic thin films. This work would also not have been possible without the support from the NSERC Alexander Graham Bell Canada Graduate Scholarships-Doctoral program, infrastructure for research provided by Compute Canada, INRS-EMT and Alfaisal University.

Furthermore, I also would like to thank Professor Federico Rosei for the opportunity created by him inviting me to give a research talk on crystal growth (extension of my first PhD project as an applied mathematician) that represented a turning point in my career, when I inquired about the possibility of starting a PhD project at INRS-EMT. I thank him for having introduced me to several research topics concerning the thin films experimental growth, and to have supervised me on the Alexander Graham Bell research proposal together with Professor François Vidal.

I also thank Professors Michel Côté, Matthias Ernzerhof and Alain Rochfort for sharing their knowledge on the modelling at the atomic scale and guiding my steps through various ab initio methods and density functional theory (DFT).

Likewise I would like to thank Marc Goffinet, Philippe Ghosez, and Michel Côté for discussions and feedback regarding the appropriate theoretical approaches to follow in the course of my PhD project, as well as for various helpful computational hints to obtain consistent results.

I thank the entire Materials Design team, especially to the René Windiks and Walter Wolf, for technical support within the MedeA environment and for numerous discussions

on the appropriate VASP computational schemes that helped to generate valuable data and predict the materials properties better and faster.

And not to be forgotten, I would like to thank my fellow research group members Ali, Catalin, Csaba, Julien, Luca, Mohamed and Thameur, for their availability to discuss our scientific results, and for their willingness to share their ideas & experience.

I am very grateful to my family and friends for their patience and support during my entire career, for their constant encouragements and trust in my knowledge that helped me to dream big and follow my passion for sciences.

Finally, I would like to thank the president of the jury Professor Federico Rosei for the extreme kindness and availability, along with the other members of the jury, Professor Michel Côté of Université de Montréal and Dr. Riad Néchache of École de Technologie Supérieure, for accepting to evaluate my thesis and for their valuable guidance.

ABSTRACT

$\text{Bi}_2\text{FeCrO}_6$ (BFCO) is a double-perovskite identified as a candidate with a unique potential to exhibit multiferroic behaviors, due to its good ferroelectric and magnetic properties that were predicted theoretically by ab-initio calculations several years ago, and then experimentally demonstrated on epitaxial thin films for the first time grown by Pulsed Laser Deposition (PLD) at INRS-EMT, and exceeding the theoretical prediction showing a multiferroic behaviour at room temperature.

In the present work, theoretical studies were performed for collinear and noncollinear spin structures to provide new insights into the subtle interplay among electron correlations, lattice distortions, oxygen-octahedron rotations/tiltings and spin-orbit coupling (SOC), as well as their effects on the multiferroic properties of BFCO. Using first-principles density functional theory (DFT), calculations within the *Vienna ab initio Simulation Package* (VASP) as integrated in the MedeA® computational environment, investigations were performed on the four possible configurations of BFCO: the ferrimagnetic phases with Fe^{3+} - high spin (FiMHS) & low spin (FiMLS), and the ferromagnetic phases for Fe^{3+} high spin (FMHS) & low spin (FMLS). For an appropriate computational scheme, fully optimized spin-polarized collinear and noncollinear calculations including SOC, were performed using the local-spin-density approximation with a *Hubbard-U* correction (LSDA+U), and the modern Perdew-Burke-Ernzerhof (PBE) generalized gradient approximations in two implementations: PBEsol+U which improves equilibrium properties of densely packed solids, and RevPBE+U which improves the chemisorption energetics of atoms and molecules on transition-metal surfaces.

In the case of collinear spin calculations (without SOC), the existence of the four stable states has been confirmed, with the order on the energy scale for all considered functionals, going as follows with increasing energy: FiMHS (I), FMHS (II), FiMLS (III), and FMLS (IV). FiMHS represents the ground state with a net magnetic ordering of $2 \mu_B/\text{f.u.}$, followed by FMHS with a net magnetic moment of $8 \mu_B/\text{f.u.}$. The small energy difference between FiMHS and FMHS phases (in the range 68.7 to 164 meV/f.u., depending on the chosen functional) allows to envision the possibility of using appropriate perturbations (such as strains, defects, etc.) in order to obtain the FMHS phase of BFCO as a material for industrial applications requiring higher magnetization. The Fe^{3+} low-spin states FiMLS, with a net magnetic moment of $2 \mu_B/\text{f.u.}$, also presents some interest because it corresponds to the experimental value, and it could possibly be obtained in strained films. In addition, for the first time, two spin channels for FMLS magnetic phase are reported, where metallic and semiconducting properties are combined in a single system at the microscopic level within the unit cell (half-metallic). Regarding ferroelectric properties of BFCO, calculated spontaneous polarizations are about 64.0 to $86.5 \mu\text{C}/\text{cm}^2$ for all considered functionals (i.e., in the range of the measured values for BFCO), and they appear to be along the [111] direction for all phases. A significant result of the present work is that it shows that the main contribution to polarization comes from the oxygen atoms and not from the Bi atoms with the lone electron pair as in the case of $(\text{BiFeO}_3)_2$, which is due to the asymmetry of the Fe-O and Cr-O bonds lengths, leading to larger displacements of the oxygen atoms in BFCO.

When SOC effects are included, the noncollinear magnetic vectors were initially aligned with the different spin quantization axes, and then they rotated during the optimization procedure until convergence to a minimum of energy, without any constraint on the symmetry (e.g., the \mathbf{k} -points mesh is not restricted anymore to a symmetry-irreducible set of the primitive cell). Calculations showed that the orbital magnetic moments for Cr^{3+} and Fe^{3+} -high spin (HS) are strongly quenched (i.e., orbital moments are very small, and hence the total magnetic moment

is due to the spin) for both FiMHS and FMHS states. The orbital moments of Fe-high spin and Cr participate to a small extent (about 1%-4%) to the total magnetic moment, while the spin moments of Fe-high spin and Cr contribute for about 74%-86%. This effect is opposite in the case of Fe^{3+} -low spin, where largely unquenched magnetic orbital moments were observed. Furthermore, magnetocrystalline anisotropy energy (MAE) shows that a saturation of the magnetization, with a magnetic moment of about $2 \mu_B/\text{f.u.}$ for FiMHS, is achieved along the easy axis, which is perpendicular to the polarization direction [111]. Our studies on MAE show that the physics becomes more complex for the states FiMLS, FMHS and FMLS, e.g., the easy axis for the LS cases is parallel to the polarization direction [111] within LSDA+U and RevPBE+U functionals, while the PBEsol+U functional gives an easy axis perpendicular to [111]. Finally, the effect of SOC on polarization consists in an additional contribution of about 0.3 to $4.6 \mu\text{C}/\text{cm}^2$ to the polarization (of about $80 \mu\text{C}/\text{cm}^2$) obtained within collinear calculations.

Keywords: density functional theory, collinear magnetic calculations, noncollinear calculations, spin-orbit coupling, magnetization, distortions, Born charges, spontaneous polarization, ferroelectricity, multiferroics

RÉSUMÉ

Le $\text{Bi}_2\text{FeCrO}_6$ (BFCO) est un double-perovskite identifié comme un candidat ayant un potentiel unique de manifester des comportements multiferroïques, en raison de ses bonnes propriétés ferroélectriques et magnétiques qui ont été prédites théoriquement par des calculs ab-initio il y a plusieurs années, puis démontrées expérimentalement sur des couches minces épitaxiées pour la première fois par la technique PLD (Pulse Laser Deposition) à l'INRS-EMT. Les mesures expérimentales ses sont avérées plus favorables que les prédictions théoriques et ont démontré un comportement multiferroïques à la température ambiante.

Dans ce travail, des études théoriques ont été réalisées pour obtenir de nouvelles informations sur l'interaction entre les corrélations électroniques, les distorsions du réseau cristallin, les rotations/inclinaisons des octaèdres d'oxygène et le couplage spin-orbite (SOC), ainsi que leurs effets sur les propriétés multiferroïques du BFCO. Au moyen de la théorie de la fonctionnelle de densité (DFT), qui découle des premiers principes, mise en œuvre au moyen du logiciel *Vienna ab initio Simulation Package* (VASP) intégré dans l'environnement de calcul MedeA®, les quatre configurations possibles du BFCO ont été étudiées: les phases ferrimagnétiques avec Fe^{3+} -haut spin (FiMHS) et -bas spin (FiMLS), et les phases ferromagnétiques pour Fe^{3+} -haut spin (FMHS) et -bas spin (FMLS). Pour un schéma de calcul approprié, des calculs en spins polarisés colinéairement et non colinéairement, incluant le SOC, ont été effectués en utilisant l'approximation de densité locale de spin avec une correction U de Hubbard (LSDA + U) et les approximations modernes de gradient généralisé de Perdew-Burke-Ernzerhof (PBE) dans deux implémentations: PBEsol+U qui améliore les propriétés d'équilibre des solides denses, et RevPBE+U qui améliore l'énergétique de chimisorption des atomes et des molécules sur les surfaces de métaux de transition.

Dans le cas des calculs colinéaires (sans SOC), l'existence des quatre états stables a été confirmée, avec un ordre sur l'échelle d'énergie, pour toutes les fonctionnelles considérées, allant comme suit: FiMHS (I), FMHS (II), FiMLS (III), et FMLS (IV). FiMHS représente l'état fondamental avec un ordre magnétique net de $2 \mu_B/\text{f.u.}$, suivi de FMHS avec un moment magnétique net de $8 \mu_B/\text{f.u.}$ La faible différence d'énergie entre les phases FiMHS et FMHS (entre 68.7 et 164 meV, selon la fonctionnelle choisie) permet d'envisager la possibilité d'utiliser des perturbations appropriées (telles que des déformations, des défauts, etc.) pour obtenir la phase FMHS du BFCO comme matériau pour des applications industrielles nécessitant une magnétisation plus élevée. L'état Fe^{3+} -bas spin, FiMLS, avec un moment magnétique net de $2 \mu_B/\text{f.u.}$, présente également un intérêt car il correspond à la valeur expérimentale, et il pourrait être obtenu dans des films contraints. En outre, pour la première fois, sont rapportés deux canaux de spin pour la phase magnétique FMLS, où les propriétés métalliques et semi-conductrices sont combinées dans un seul système au niveau microscopique au sein de la cellule unitaire (semi-métallique). Concernant les propriétés ferroélectriques du BFCO, les polarisations spontanées calculées sont entre 64.0 et $86.5 \mu\text{C}/\text{cm}^2$ considérant toutes les fonctionnelles considérées (c'est-à-dire dans la plage des valeurs mesurées pour BFCO), et elles sont dans la direction [111] pour toutes les phases. Un résultat significatif de ce travail est que la contribution principale à la polarisation provient des atomes d'oxygène et non des atomes de Bi avec une paire d'électrons libres comme dans le cas de BiFeO_3 , et à l'asymétrie des longueurs de liaisons Fe-O et Cr-O, conduisant à de plus grands déplacements des atomes d'oxygène dans le cas du BFCO .

Lorsque les effets du SOC sont inclus, les vecteurs magnétiques non colinéaires sont d'abord alignés selon différents axes de quantification du spin, puis ils tournent pendant la procédure d'optimisation jusqu'à converger vers un minimum d'énergie, sans contrainte de symétrie (par exemple, le maillage des points k n'est plus limité à un ensemble de symétries irréductibles de la cellule unitaire). Les calculs ont montré que les moments magnétiques orbitaux pour Cr³⁺ et Fe³⁺ -haut spin (HS) sont fortement atténués (les moments orbitaux sont très petits, et donc le moment magnétique total est dû au spin) pour les états FiMHS et FMHS. Les moments orbitaux de Fe -haut spin et Cr participent à un petit pourcentage (environ 1%-4%) au moment magnétique total, tandis que les moments de spin de Fe -haut spin et Cr contribuent pour environ 74%-86%. L'effet est opposé dans le cas de Fe³⁺ -bas spin où des moments orbitaux magnétiques largement non-atténués ont été observés. En outre, l'énergie d'anisotropie magnétocristalline (MAE) montre qu'une saturation de l'aimantation, avec un moment magnétique d'environ 2 μ_B /f.u. pour FiMHS, est réalisée le long de l'axe magnétique facile, qui est perpendiculaire à la direction de polarisation [111]. L'étude du MAE montre que la physique devient plus complexe pour les autres états FiMLS, FMHS et FMLS. Par exemple, l'axe magnétique facile pour les cas LS est parallèle à la direction de la polarisation [111] pour les fonctionnelles LSDA+U et RevPBE+U, alors que pour la fonctionnelle PBEsol+U, l'axe magnétique facile est perpendiculaire à [111]. Enfin, les effets du SOC sur la polarisation consistent en une augmentation de 0.3 à 4.6 $\mu\text{C}/\text{cm}^2$ de la polarisation (d'environ 80 $\mu\text{C}/\text{cm}^2$) obtenue par le calcul colinéaire.

Mots-clés: théorie fonctionnelle de la densité, calculs magnétiques colinéaires, calculs non colinéaires, couplage spin-orbite, magnétisme, distorsions, charges de Born, polarisation spontanée, ferroélectricité, multiferroïque.

SYNOPSIS

Les matériaux multiferroïques présentent au moins deux des propriétés ferroïques primaires dans la même phase. Les multiferroïques ont suscité un intérêt croissant, en partie à cause de la possibilité d'un couplage entre les propriétés magnétiques et électriques qui ouvre la voie au contrôle de la polarisation avec un champ magnétique ou de l'aimantation avec un champ électrique. Ce couplage magnétoélectrique (ME), présent dans les matériaux comportant des propriétés ferroélectriques et magnétiques, pourrait également exister dans les matériaux piézoélectriques/électrostrictifs et piézomagnétiques/magnétostRICTIFS, par l'intermédiaire des propriétés élastiques à leurs interfaces. De nombreuses applications des matériaux multiferroïques et magnétoélectriques ont été proposées, telles que les mémoires multi-états (Guterman & Fong, 2001) en l'absence de couplage entre matériaux ferroélectriques et ferromagnétiques (Spaldin & Fiebig, 2005; Spaldin et al., 2008), des capteurs magnétiques sensibles fonctionnant à la température de la pièce (Nan et al., 2008), des dispositifs micro-ondes accordables (Lou et al., 2008), et de nombreux dispositifs spintroniques potentiels (Bea 2008) pour des couplages ME forts. En particulier, le couplage ME offre des perspectives intéressantes pour la conception de mémoires ferroélectriques avec une lecture magnétique non destructive (le cycle de l'hystérésis ferroélectrique lors de chaque lecture de l'état de mémoire, produisant une fatigue et finalement la perte des données stockées, étant le principal défi des mémoires ferroélectriques), ainsi que pour les mémoires magnétiques à accès aléatoire (MRAM) comportant une procédure d'écriture électrique (MERAM) (Bibes & Barthelemy, 2008).

Les matériaux multiferroïques présentent au moins deux des propriétés ferroïques primaires dans la même phase. Les multiferroïques ont suscité un intérêt croissant, en partie à cause de la possibilité d'un couplage entre les propriétés magnétiques et électriques qui ouvre la voie au contrôle de la polarisation avec un champ magnétique ou de l'aimantation avec un champ électrique. Ce couplage magnétoélectrique (ME), présent dans les matériaux comportant des propriétés ferroélectriques et magnétiques, pourrait également exister dans les matériaux piézoélectriques/électrostrictifs et piézomagnétiques/magnétostRICTIFS, par l'intermédiaire des propriétés élastiques à leurs interfaces. De nombreuses applications des matériaux multiferroïques et magnétoélectriques ont été proposées, telles que les mémoires multi-états (Guterman & Fong, 2001) en l'absence de couplage entre matériaux ferroélectriques et

ferromagnétiques (Spaldin & Fiebig, 2005; Spaldin et al., 2008), des capteurs magnétiques sensibles fonctionnant à la température de la pièce (Nan et al., 2008), des dispositifs micro-ondes accordables (Lou et al., 2008), et de nombreux dispositifs spintroniques potentiels (Bea 2008) pour des couplages ME forts. En particulier, le couplage ME offre des perspectives intéressantes pour la conception de mémoires ferroélectriques avec une lecture magnétique non destructive (le cycle de l'hystérésis ferroélectrique lors de chaque lecture de l'état de mémoire, produisant une fatigue et finalement la perte des données stockées, étant le principal défi des mémoires ferroélectriques), ainsi que pour les mémoires magnétiques à accès aléatoire (MRAM) comportant une procédure d'écriture électrique (MERAM) (Bibes & Barthelemy, 2008).

Un exemple de matériau multiferroïque ayant le potentiel de révolutionner l'industrie électronique est la double perovskite $\text{Bi}_2\text{FeCrO}_6$ (BFCO), en raison de ses bonnes propriétés ferroélectriques et magnétiques à la température ambiante qui ont été théoriquement prédites par des calculs ab-initio (Baettig & Spaldin, 2005a; et al., 2005b, Ederer & Spaldin, 2005a, 2005b), et expérimentalement démontrées sur des couches minces épitaxiales (Nechache et al., 2012; 2009; 2006) pour la première fois par la technique de déposition par laser pulsé (PLD) à l'INRS-EMT.

Dans le BFCO (voir Figure S.1b-d), les calculs ab-initio utilisant la fonctionnelle de densité locale de spin (LSDA), avec et sans correction pour la répulsion de Coulomb U, ont mis en évidence que les propriétés multiferroïques du BFCO pourraient être supérieures à celles des matériaux multiferroïques connus, par exemple le BiFeO_3 (voir Figure S.1a), le BiCrO_3 et le PbTiO_3 (Baettig et Spaldin, 2005a, Baettig et al., 2005b). L'état fondamental calculé possède une symétrie rhomboédrique avec un groupe spatial $R3$, et des moments magnétiques orientés de façon opposée pour les ions Fe^{3+} et Cr^{3+} qui donnent un ordre magnétique net de $2 \mu_B/\text{f.u.}$ et une polarisation ferroélectrique de $79.6 \mu\text{C}/\text{cm}^2$.

A titre de comparaison, les couches minces de BiFeO_3 ont une faible aimantation $\sim 0.1 \mu_B/\text{f.u.}$ due à l'inclinaison des moments magnétiques orientés de Fe^{3+} , et une large gamme de polarisations ferroélectriques rapportées: $2.2 \mu\text{C}/\text{cm}^2$ (Palkar et al., 2002); $\sim 6 \mu\text{C}/\text{cm}^2$ (Wang et al., 2003, Teague et al., 1970) ou $84\text{-}87 \mu\text{C}/\text{cm}^2$ (Neaton et al., 2005) pour la phase rhomboédrique $R3c$; et $50\text{-}60 \mu\text{C}/\text{cm}^2$ (Wang et al., 2003) ou $143.5 \mu\text{C}/\text{cm}^2$ (Ricinschi et al., 2006) pour la phase tétragonale $P4mm$.

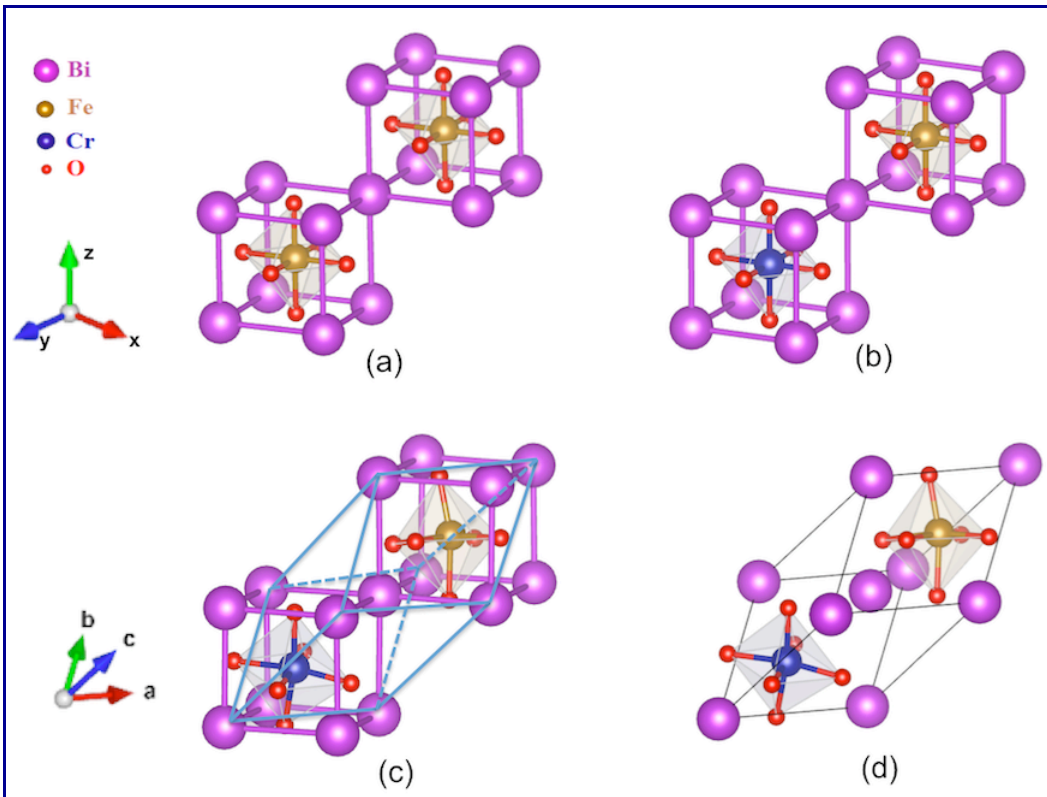


Figure S.1 La structure cubique idéale de la peroskite unique (BiFeO_3)₂ (a); Structure cubique idéale de la double péroksite $\text{Bi}_2\text{FeCrO}_6$ (b); La symétrie rhomboédrique $R3$ (c-d) du $\text{Bi}_2\text{FeCrO}_6$. Les visualisations sont réalisées avec VESTA (Momma & Izumi, 2011).

Les propriétés multiferroïques supérieures du BFCO ont également été confirmées théoriquement, au moyen de la fonctionnelle de gradient généralisé GGA+U, par Ju et Guo (Ju & Guo, 2008), et un effet magnétoélectrique optique non linéaire colossal dans le BFCO a également été révélé.

En raison du fort intérêt pour le BFCO en tant que matériau multifonctionnel potentiel pour de nombreuses applications attrayantes, ses propriétés ont été récemment réexaminées (Goffinet et al., 2012) en utilisant différents schémas théoriques: LSDA, différentes variantes de LSDA+U et la fonctionnelle hybride B1-WC (Bilc et al., 2008). Dans toutes les fonctionnelles utilisées, Goffinet et al. ont mis en évidence l'existence de quatre états stables différents: (i) les états ferrimagnétiques avec Fe^{3+} dans une configuration de haut spin (FiMHS) et une configuration de bas spin (FiMLS), ainsi que (ii) les états ferromagnétiques correspondants pour les configurations à haut spin (FMHS) et à bas spin (FMLS). Des études sur la stabilité relative de ces quatre états ont montré que toutes les fonctionnelles prédisent systématiquement que l'état

fondamental est FiMHS, et un croisement de spin entre FiMHS et FiMLS a été trouvé en contrainte compressive.

Les développements récents dans la croissance et la caractérisation des couches minces épitaxiales du BFCO (Nechache et al., 2012) ont montré que les films épitaxiaux étaient contraints épitaxialement et présentaient une variation des propriétés multiferroïques en épaisseur qui ont été attribuées à la dépendance en l'épaisseur de l'ordre cationique Fe/Cr, lui-même lié aux longueurs des liaisons et aux angles résultant des contraintes épitaxiales induites par les substrats de SrTiO_3 utilisés. D'autres études sont nécessaires pour comprendre les détails des mécanismes déterminant l'ordre cationique Fe/Cr et pour expliquer l'origine de l'épaisseur critique au-delà de laquelle les propriétés magnétiques diminuent fortement.

Dans cette thèse, des études théoriques ont été réalisées sur des structures de spin colinéaires et non-colinéaires afin de fournir de nouvelles informations sur les interactions subtiles entre les corrélations électroniques, les distorsions du réseau cristallin, les rotations des octaèdres d'oxygène et le couplage spin-orbite (SOC), ainsi que leurs effets sur les propriétés multiferroïques du BFCO. Au moyen de la théorie de la fonctionnelle de densité (DFT), mise en œuvre au moyen du logiciel VASP (*Vienna ab initio Simulation Package*) intégré dans l'environnement de calcul MedeA®, des études ont été effectuées sur les quatre configurations possibles du BFCO: soient les phases FiMHS, FiMLS, FMHS et FMLS. Des calculs en spins polarisés colinéairement et non colinéairement, entièrement optimisés, incluant le SOC ont été effectués en utilisant l'approximation de densité locale de spin avec une correction U de Hubbard (LSDA+U) et les approximations modernes de gradient généralisé de Perdew-Burke-Ernzerhof (PBE) dans deux implémentations distinctes: PBEsol+U qui améliore les propriétés d'équilibre des solides denses, et RevPBE+U qui améliore l'énergétique de chimisorption des atomes et des molécules sur les surfaces de métaux de transition.

Ce manuscrit est organisé de la manière suivante :

Chapitre 1: Introduction. Ce chapitre présente les matériaux multiferroïque ainsi que leurs applications possibles. Ensuite sont présentés un aperçu des travaux théoriques et expérimentaux passés, les problèmes ouverts, la motivation et le but de cette thèse.

Chapitre 2: Effet magnétoélectrique et multiferroïque. Dans ce chapitre, les notions d'effet magnétoélectrique et de couplage magnétoélectrique sont introduites, ainsi qu'un bref historique de l'intérêt suscité par le couplage magnétoélectrique, en mettant l'accent sur le

nombre de publications, selon Web of Science, de 1970 à ce jour. Ensuite, quelques classifications de multiferroïques sont présentées:

- (i) Fiebig a distingué quatre principaux types cristallographiques de multiferroïques (Fiebig, 2005): les composés à structure de perovskite, les composés à structure hexagonale, les composés de la famille des boracites et les composés BaMF_4 avec $\text{M} = \text{Mg}, \text{Mn}, \text{Fe}, \text{Co}, \text{Ni}, \text{Zn}$.
- (ii) Selon le mécanisme de la brisure de la symétrie d'inversion dans les ferroélectriques, la Réf. (Cheong & Mostovoy, 2007) classifie les multiferroïques comme: les ferroélectriques magnétoélectriques au sens propre, où la ferroélectricité est provoquée par des cations comportant une paire d'électrons libres, stéréochimiquement actifs, ou par une liaison covalente entre un métal de transition $3d^0$ et l'oxygène; et les autres ferroélectriques magnétoélectriques qui permettent des contraintes plus faibles sur la coexistence avec le magnétisme.
- (iii) Khomskii et ses collaborateurs (Brink & Khomskii, 2008; Khomskii, 2009) ont classé les multiferroïques comme: les multiferroïques de type I dans lesquels la ferroélectricité et le magnétisme ont des sources différentes et sont largement indépendants l'un de l'autre; et les multiferroïques de type II dans lesquels la ferroélectricité n'apparaît que dans l'état magnétiquement ordonné, c'est-à-dire que le magnétisme provoque une ferroélectricité, impliquant un fort couplage entre les paramètres des deux ordres.

Ensuite, dans ce chapitre, les pérovskites idéales et les doubles pérovskites sont introduites, ainsi que les diverses distorsions possibles et les inclinaisons/rotations des octaèdres d'oxygène. En outre, la compatibilité entre la pérovskite et la ferroélectricité est expliquée, afin de pouvoir reconnaître la présence de la ferroélectricité.

Chapitre 3: Contexte théorique. Le chapitre 3 apporte des détails sur les aspects méthodologiques des calculs de premier principe des structures électroniques, et sont brièvement présentés les systèmes fortement corrélés, la DFT pour les systèmes de spins polarisés, la fonctionnelle d'échange-corrélation pour les matériaux fortement corrélés, le magnétisme non colinéaire dans le cadre de la DFT relativiste, et le concept de couplage spin-orbite dans le contexte des pseudopotentiels. Ensuite, un résumé de la théorie de la polarisation est présenté, ainsi que des concepts et des techniques à utiliser pour calculer la polarisation dans les ferroélectriques.

Chapitre 4: Etude DFT du $\text{Bi}_2\text{FeCrO}_6$: calculs en spins polarisés colinéairement. Le chapitre 4 présente une discussion des propriétés structurales, électroniques, magnétiques et ferroélectriques de la symétrie rhomboédrique $R\bar{3}$ du BFCO pour les structures de spin

colinéaires correspondant: (i) aux phases ferrimagnétiques avec Fe³⁺-haut spin (FiMHS) et Fe³⁺-bas spin (FiMLS), et (ii) aux phases ferromagnétiques pour les configurations Fe³⁺-haut spin (FMHS) et -bas spin (FMLS).

Les calculs ont été réalisés à l'aide du formalisme PAW (Projected Augmented Plan-Wave) de la théorie de la fonctionnelle de densité, en traitant explicitement 15 électrons de valence pour Bi ($5d^{10}6s^26p^3$), 14 pour Fe ($3p^63d^64s^2$), 12 pour Cr ($3p^63d^54s^1$) et 6 pour l'oxygène ($2s^22p^4$), au moyen du logiciel VASP 5.3 (Kresse & Furthmüller 1996a, 1996b) intégré dans l'environnement de calcul MedeA® (MedeA 2017; 2015). Pour une meilleure description des électrons 3d de Fe et Cr, nous avons utilisé la fonctionnelle de densité locale de spin avec une correction de U de Hubbard (LSDA+U). Pour traiter l'échange et la corrélation dans ces systèmes fortement corrélés, nous avons considéré la formulation dite formulation limite entièrement localisée (Liechtenstein et al., 1995; Anisimov et al., 1997), avec les paramètres U = 3 eV pour la répulsion de Coulomb, et J = 0.8 eV pour l'interaction d'échange (Baettig et Spaldin, 2005a, Baettig et al., 2005b, Goffinet et al., 2012).

De plus, de nouvelles approximations de fonctionnelles ont été utilisées, à savoir les approximations de gradient généralisé de Perdew-Burke-Ernzerhof (PBE) (Perdew et al., 1996), soient la fonctionnelle PBE révisée pour les métaux de transition, RevPBE (Hammer et al., 1999), et la fonctionnelle PBE optimisée pour les solides, PBEsol (Perdew et al., 2008), incluant les corrections U de Hubbard correspondantes. Pour déterminer les paramètres de maille de la cellule unitaire de BFCO à utiliser en entrée, une relaxation a été effectuée à partir de la symétrie *Fm-3m* (groupe spatial #225), correspondant à la structure de sel gemme cubique idéale (voir Fig.S.2a). Chaque métal de transition a été entouré d'un octaèdre d'anions oxygène ayant toutes les longueurs de liaison Cr-O et Fe-O égales (voir Fig. S.2a, b).

La relaxation complète des positions des atomes a conduit à la même symétrie *Fm-3m* avec une constante de réseau $a_c = 5.30 \text{ \AA}$ et un volume $V_c = 105.4 \text{ \AA}^3$. Les angles du réseau étaient $\alpha_c = 60^\circ$, et les octaèdres FeO_6 et CrO_6 n'étaient pas déformés et/ou pivotés. Cette structure correspond en fait à un minimum local d'énergie qui n'est pas le plus bas et, par conséquent, certaines distorsions ont dû être induites manuellement dans la structure afin d'obtenir une convergence vers le minimum réel d'énergie. À noter que la symétrie *Fm-3m* ne permet pas la ferroélectricité.

Pour forcer la rupture de la symétrie *Fm-3m*, les octaèdres d'oxygène adjacents ont été tournés dans des directions opposées autour de l'axe [111] et déplacés par rapport aux cations central de Bi, dans des directions opposées le long de l'axe [111] (Côté, 2013).

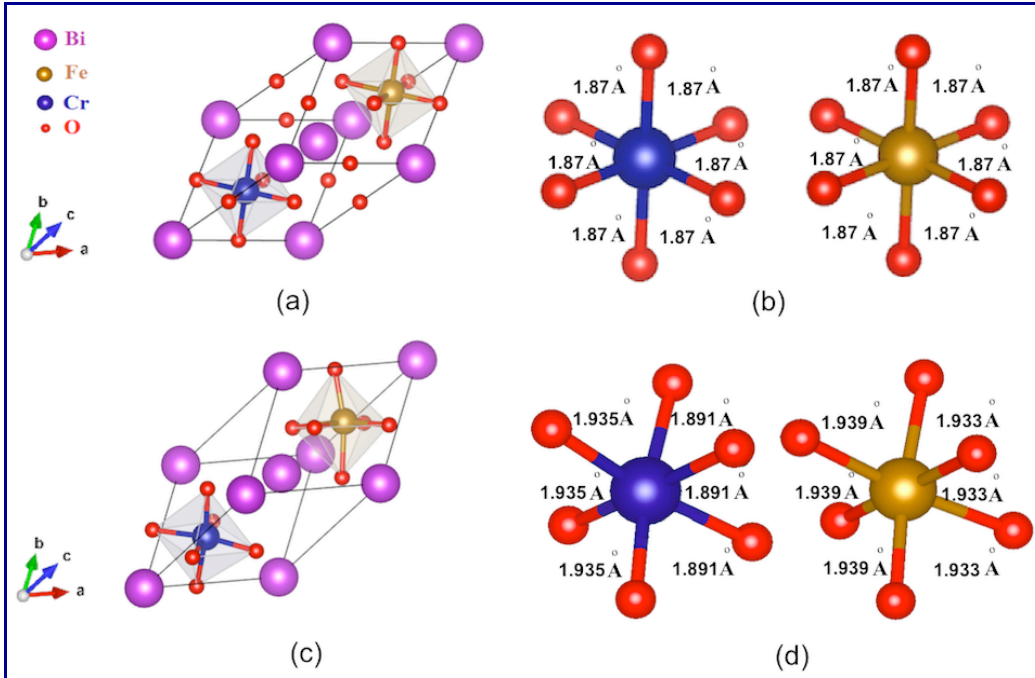


Figure S.2 La structure non magnétique *Fm-3m* optimisée correspondant à la structure de sel gemme cubique idéale du BFCO, comme le montre la figure 4.1b (a); Les longueurs calculées des liaisons Cr-O et Fe-O des octaèdres non déformés correspondant à la symétrie *Fm-3m* du BFCO (b); La structure rhomboédrique *R3* non magnétique optimisée du BFCO (c); Les longueurs des liaison Cr-O et Fe-O des octaèdres déformés correspondant à la symétrie *R3* du BFCO (d).

Après optimisation, l'énergie s'est abaissée et la structure rhomboédrique avec la symétrie *R3* (groupe spatial #146) a été obtenue (voir Fig. S.2b,c). Les octaèdres FeO_6 et CrO_6 ont été déformés, et les cages d'oxygène ont été tournées autour de la direction cartésienne [111]. En outre, dans le BFCO *R3* optimisé, les longueurs de liaison Cr-O et Fe-O se sont trouvées allongées par rapport à la structure cubique idéale (pour une meilleure comparaison, voir les longueurs des liaisons de la Fig. S.2b par rapport à la Fig. S.2d). Les calculs auto-cohérents en spins polarisés, comprenant les moments magnétiques du Fe - haut spin et bas spin, et du Cr, ont été effectués à partir de la structure rhomboédrique non magnétique de symétrie *R3* décrite ci-dessus.

Dans le cas du BFCO, les orbitales d du Fe^{3+} ($3d^5$) se divisent en deux ensembles : un ensemble triplement dégénéré d_{xy} , d_{xz} , d_{yz} (niveau t_{2g}), et un ensemble doublement dégénéré $d_{x^2-y^2}$, d_z^2 (niveau e_g) légèrement plus élevé en énergie, comme attendu pour une coordination octaédrique. Dépendamment de la différence d'énergie entre les niveaux t_{2g} et e_g , il peut en résulter une configuration électronique du Fe^{3+} -bas spin (LS) ($t_{2g\downarrow\uparrow}$) 5 ($e_{g\uparrow}$) 0 , ou une configuration électronique du Fe^{3+} -haut spin (HS) ($t_{2g\uparrow}$) 3 ($e_{g\uparrow}$) 2 . Les orbitales d du Cr^{3+} ($3d^3$) se divisent

également en niveaux t_{2g} et e_g , mais toujours avec un niveau e_g vide, c'est-à-dire avec la configuration $(t_{2g\uparrow})^3(e_{g\uparrow})^0$.

A noter que les longueurs des liaisons Cr-O et Fe-O montrées dans les cas non-magnétiques de la Fig. S.2, et le degré de rotation des octaèdres FeO_6 et CrO_6 , pourraient avoir un effet profond sur l'interaction entre les spins et le couplage de super-échange dans $\text{Fe}^{3+}\text{-O}^{2-}\text{-Cr}^{3+}$ (interaction des échanges entre les cations Fe et Cr avec les spins non appariés provenant des anions O situés entre les cations (Kanamori, 1960, 1959, Windiks, 2000)). Selon la dépendance angulaire de l'interaction de super-échange dans $\text{Fe}^{3+}\text{-O}^{2-}\text{-Cr}^{3+}$ étudiée en utilisant la spectroscopie Mössbauer dans des structures simples de type pérovskite (Gibb, 1984, Moskvin et al., 1975), le couplage de super-échange s'avère être antiferromagnétique lorsque les angles de liaison Fe-O-Cr sont inférieurs à 156° , tandis que le couplage ferromagnétique ne se produit que pour les angles de liaison Fe-O-Cr plus proches de 180° . Ainsi, il est intéressant de vérifier si un couplage ferromagnétique (aussi appelé ferrimagnétique dans ce travail) et/ou ferromagnétique existe également dans des plages similaires d'angles de liaisons Fe-O-Cr pour la symétrie rhomboédrique $R3$ du BFCO.

Ainsi, à partir de la structure rhomboédrique non magnétique avec symétrie $R3$ décrite ci-dessus, des calculs auto-cohérents en spins polarisés ont été effectués pour les quatre différentes phases magnétiques possibles: Fe^{3+} -haut spin ferrimagnétique, FiMHS, et ferromagnétique, FMHS, et les états Fe^{3+} -bas spin correspondants, FiMLS et FMLS, en imposant des moments magnétiques colinéaires initiaux à Fe^{3+} et Cr^{3+} . Les moments magnétiques locaux calculés, ainsi que les paramètres structuraux respectifs, sont résumés dans le Tableau S.1 pour les trois fonctionnelles LSDA+U, PBEsol+U et RevPBE+U.

Les structures optimisées pour les phases magnétiques FiMHS, FiMLS, FMHS et FMLS sont représentées sur la Fig. S.3, où le spin du Fe^{3+} est marqué par une flèche jaune parallèle ou antiparallèle au spin du Cr^{3+} marqué par une flèche verte. À noter que dans les calculs colinéaires, le SOC n'est pas inclus, et donc la direction des spins est arbitraire (cependant, les spins de Fe^{3+} et Cr^{3+} sont parallèles ou antiparallèles). Dans la Fig. S.3, les orientations des spins de Fe^{3+} et Cr^{3+} ont été choisies perpendiculairement à la direction [111], car on suppose généralement (hypothèse commune mais non prouvée) que le vecteur magnétique est perpendiculaires au vecteur de polarisation.

Tableau S.1 Résumé des propriétés structurelles et électroniques des phases FiMHS, FiMLS, FMHS et FMLS du BFCO, calculées à l'aide des fonctionnelles LSDA+U, PBEsol+U et RevPBE+U. Les paramètres des cellules unitaires rhomboédriques sont la longueur a_r et l'angle α_r ; V_r est le volume de la cellule unitaire; x_i , y_i et z_i représentent les positions de Wyckoff du groupe d'espace 146 (symétrie R3) dans symétrie rhomboédrique, c'est-à-dire $Bi_{1,2}(x, x, x)$, $Fe(x, x, x)$, $Cr(x, x, x)$ et $O_1(x_{01}, y_{01}, z_{01})$, $O_2(z_{01}, x_{01}, y_{01})$, $O_3(y_{01}, z_{01}, x_{01})$, $O_4(x_{02}, y_{02}, z_{02})$, $O_5(z_{02}, x_{02}, y_{02})$, $O_6(y_{02}, z_{02}, x_{02})$; μM_{Fe} et μM_{Cr} sont les moments magnétiques locaux de Fe et Cr; μM_{BFCO} est le moment magnétique total par cellule unitaire; ΔE est la différence d'énergie par rapport à l'état fondamental FiMHS.

Phase	LSDA+U				PBEsol+U				RevPBE+U			
	FiMHS	FiMLS	FMHS	FMLS	FiMHS	FiMLS	FMHS	FMLS	FiMHS	FiMLS	FMHS	FMLS
a_r in Å	5.48	5.36	5.49	5.37	5.42	5.35	5.43	5.33	5.61	5.55	5.61	5.62
α_r in °	60.04	60.80	60.04	60.76	60.74	61.02	60.74	61.08	59.72	59.98	59.75	59.73
V_r , Å ³	116.3	111.1	116.9	111.5	114.7	111.2	115.1	110.2	124.4	121.3	124.7	125.3
x_{Bi}	0.000	0.000	0.000	0.000	0.000	0.000	0.000	0.000	0.000	0.000	0.000	0.000
x_{Bi}	0.503	0.495	0.504	0.496	0.504	0.496	0.505	0.497	0.511	0.505	0.512	0.505
x_{Fe}	0.732	0.726	0.731	0.727	0.732	0.726	0.731	0.726	0.732	0.726	0.731	0.725
x_{Cr}	0.226	0.227	0.226	0.228	0.226	0.228	0.225	0.228	0.224	0.225	0.224	0.227
x_{O1}	0.544	0.545	0.545	0.546	0.545	0.546	0.546	0.547	0.544	0.546	0.545	0.547
y_{O1}	0.950	0.952	0.949	0.950	0.950	0.948	0.948	0.947	0.947	0.948	0.947	0.946
z_{O1}	0.398	0.410	0.400	0.410	0.397	0.411	0.399	0.410	0.393	0.402	0.396	0.403
x_{O2}	0.046	0.041	0.044	0.041	0.047	0.038	0.044	0.039	0.044	0.044	0.042	0.043
y_{O2}	0.905	0.904	0.905	0.905	0.905	0.904	0.905	0.905	0.903	0.900	0.903	0.900
z_{O2}	0.447	0.457	0.449	0.454	0.447	0.456	0.449	0.455	0.445	0.450	0.446	0.450
μM_{Fe} in μ_B	-3.98	-0.86	+4.03	+1.02	-4.06	-0.75	+4.09	+0.91	-4.10	-0.93	+4.12	+0.87
μM_{Cr} in μ_B	+2.54	+2.74	+2.86	+2.72	+2.63	+2.75	+2.91	+2.76	+2.71	+2.89	+2.96	+2.82
μM_{BFCO} in μ_B	-1.98	+1.90	+7.66	+3.82	-1.99	+1.88	+7.69	+3.84	-1.98	+1.91	+7.71	+3.84
ΔE in meV	0 I	372.6 III	164 II	749.9 IV	0 I	713.9 III	112.8 II	1204.8 IV	0 I	1020.5 III	68.7 II	1199.4 IV

Nos paramètres structuraux calculés sont cohérents avec ceux rapportés par Goffinet et al. (Goffinet et al., 2012) pour les fonctionnelles LSDA+U et B1-WC qu'ils ont considérées. En particulier, l'ordre des états magnétiques FiMHS (I), FMHS (II), FiMLS (III) et FMLS (IV) sur l'échelle énergétique est le même que le leur pour les trois fonctionnelles que nous avons considérées. On peut voir que les deux états Fe^{3+} de haut spin, FiMHS (I) et FMHS (II), ayant respectivement les moments magnétiques nets de 2 μ_B /f.u. et 8 μ_B /f.u., sont plus stables que les états de bas spin, et ont des volumes significativement plus élevés (à l'exception de FMLS pour RevPBE). La différence d'énergie entre FiMHS et FMHS est faible pour LSDA+U, et beaucoup plus faible pour PBEsol et RevPBE. Ceci ouvre la possibilité que le FMHS, qui a le moment magnétique élevé de 8 μ_B /f.u., puisse être stabilisé par une perturbation appropriée (par exemple par des déformations du réseau cristallin ou par un champ magnétique), ce qui pourrait représenter un développement technologique important.

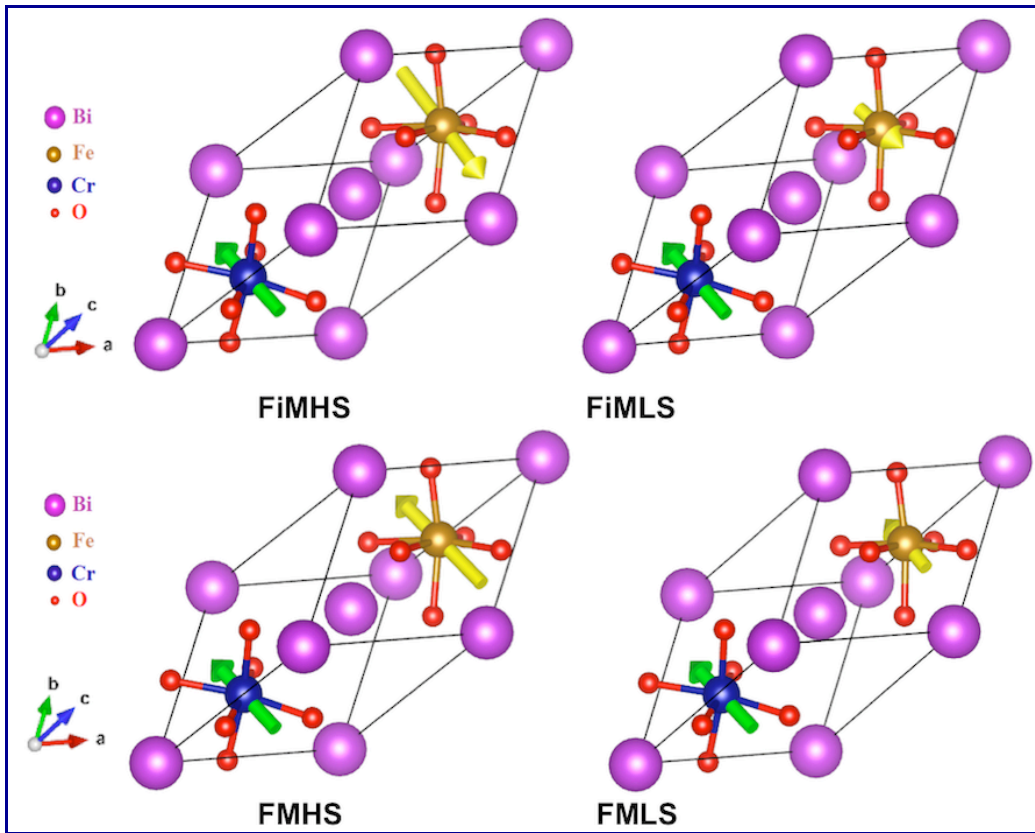


Figure S.3 Cellules unitaires rhomboédriques des structures de BFCO magnétiques colinéaires correspondant au Fe^{3+} ferrimagnétique haut spin (FiMHS) et bas spin (FiMLS), et au Fe^{3+} ferromagnétique haut spin (FMHS) et bas spin (FMLS). Le spin de Cr^{3+} est marqué par une flèche verte et le spin de Fe^{3+} est marqué par une flèche jaune parallèle ou antiparallèle à cette dernière, et perpendiculaire à la direction [111].

D'autre part, les deux états Fe^{3+} -bas spin, FiMLS (III) et FMLS (IV), ont un volume inférieur (à l'exception de FMLS pour RevPBE), qui pourrait être favorisé par des contraintes compressives. La différence d'énergie ΔE entre l'état fondamental FiMHS et les deux états LS est significativement plus grande que la différence d'énergie entre les deux états HS, ce qui indique des interactions plus faibles dans les phases LS. En ce qui concerne la fonctionnelle RevPBE utilisée pour vérifier nos résultats, on peut voir que les longueurs de réseau et les volumes des cellules sont supérieurs à ceux calculés au moyen de LSDA+U et PBEsol+U, et la différence d'énergie entre les états magnétiques FiMLS et FMLS est plus petite.

L'analyse des fonctions de localisation électronique (ELF) permet d'identifier les régions où les électrons sont localisés (Savin et al., 1997; Becke et al., 1990). Comme il n'y a pas de différences visibles entre les ELF calculées au moyen de LSDA+U, PBEsol+U et RevPBE+U, dans la suite, seules les ELF calculées au moyen de LSDA+U seront discutées. Les ELF

calculées pour le BFCO sont représentées sur la Fig. S.4, où la plage de tracé de contour a été réduite de [0; 1] à [0; 0,8] pour une meilleure visualisation.

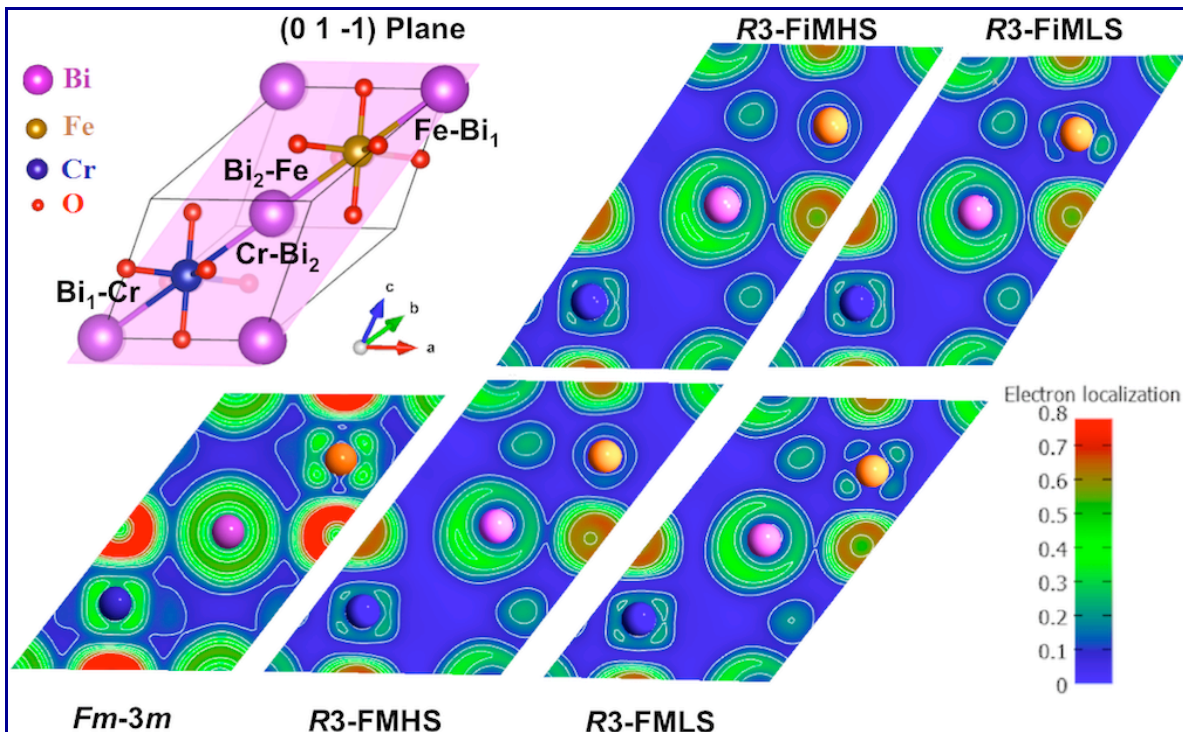


Figure S.4 Fonctions de localisation électronique (ELF) calculées pour la structure non magnétique hautement symétrique *Fm-3m* du BFCO (à gauche), et les structures optimisées rhomboédriques correspondant aux états magnétiques FiMHS, FiMLS, FMHS et FMLS. Le plan de coupe considéré ($0\ 1\ -1$), qui contient Bi, Fe, Cr et quatre atomes d'oxygène souligne les liens entre Bi₁, Cr, Bi₂ et Fe qui sont discutés dans cette thèse. Les visualisations ont été effectuées au moyen de Virtual NanoLab (Virtual NanoLab, 2016).

Les valeurs négligeables de l'ELF entre les atomes (bleu foncé) indiquent une liaison ionique dominante. En comparant les ELF calculées pour la structure *Fm-3m* hautement symétrique et les structures *R3* déformées, on peut voir que l'ELF prend des valeurs décroissantes sur les atomes en passant de la symétrie *Fm-3m* à *R3*, ce qui indique un fort transfert de charge dans les structures magnétiques optimisées. Ces résultats montrent un caractère mixte ionique-covalent des liaisons. De plus, une répulsion à courte distance entre des couches fermées adjacentes est observée pour la structure *Fm-3m* où les distorsions n'existent pas. En revanche, dans les cas des états magnétiques optimisés, des liaisons supplémentaires viennent stabiliser les distorsions qui sont à l'origine de la ferroélectricité.

Les paires 6s autour des atomes Bi, distribuées d'une manière quasi-sphérique dans la structure non magnétique *Fm-3m*, se déforment pour former des anneaux asymétriques (un comportement similaire a été rapporté (Seshadri & Hill, 2001) pour le BiFeO₃). Dans les

structures magnétiques, les ions Bi sont éloignés de leurs positions symétriques centrales le long de la direction [111] et les paires d'électrons libres se stabilisent en forme de lobe (géométrie en fer à cheval autour de Bi), entraînant des distorsions structurelles supplémentaires qui influenceront la ferroélectricité.

Pour appuyer ces observations, les densités d'états (DOS) et les structures de bandes ont été calculées pour la structure *Fm-3m* hautement symétrique, et pour les états rhomboédriques *R3* FiMHS, FiMLS, FMHS et FMLS en utilisant les fonctionnelles LSDA+U et PBE+U considérés. Par exemple, la Fig. S.5 compare les DOS partielles et totales du BFCO idéal hautement symétrique (paramagnétique) dans la phase FiMHS rhomboédrique déformée (ferrimagnétique) *R3*, et les structures de bande correspondantes, obtenues au moyen de la fonctionnelle LSDA+U.

Les images correspondant à la structure *Fm-3m* hautement symétrique idéale du BFCO montrent clairement le caractère métallique de la phase paramagnétique, car les bandes de valence et de conduction se chevauchent. Au contraire, la DOS et les bandes de la phase *R3* FiMHS du BFCO indiquent un caractère semi-conducteur, en accord avec les résultats rapportés dans les Réf. (Goffinet et al., 2012, Baettig et al., 2005b). Les orbitales proches du niveau de Fermi sont principalement Fe-3d et Cr-3d, qui ont des composantes significatives à la fois dans la bande de valence (VB) et dans la bande de conduction (CB).

En inspectant les DOS et les bandes en partant du bas vers le haut sur l'échelle d'énergie, un pic aigu entre -12 eV et -8 eV, correspondant à l'orbitale Bi-6s, est visible, et il est décalé vers le haut par rapport à la structure symétrique idéale en raison des distorsions structurelles (c'est-à-dire que l'énergie de Fermi a diminué). Dans la structure *R3* déformée, de nombreuses bandes évitent de se croiser dans la VB, montrant l'existence d'une hybridation qui ne se produit pas dans la structure symétrique.

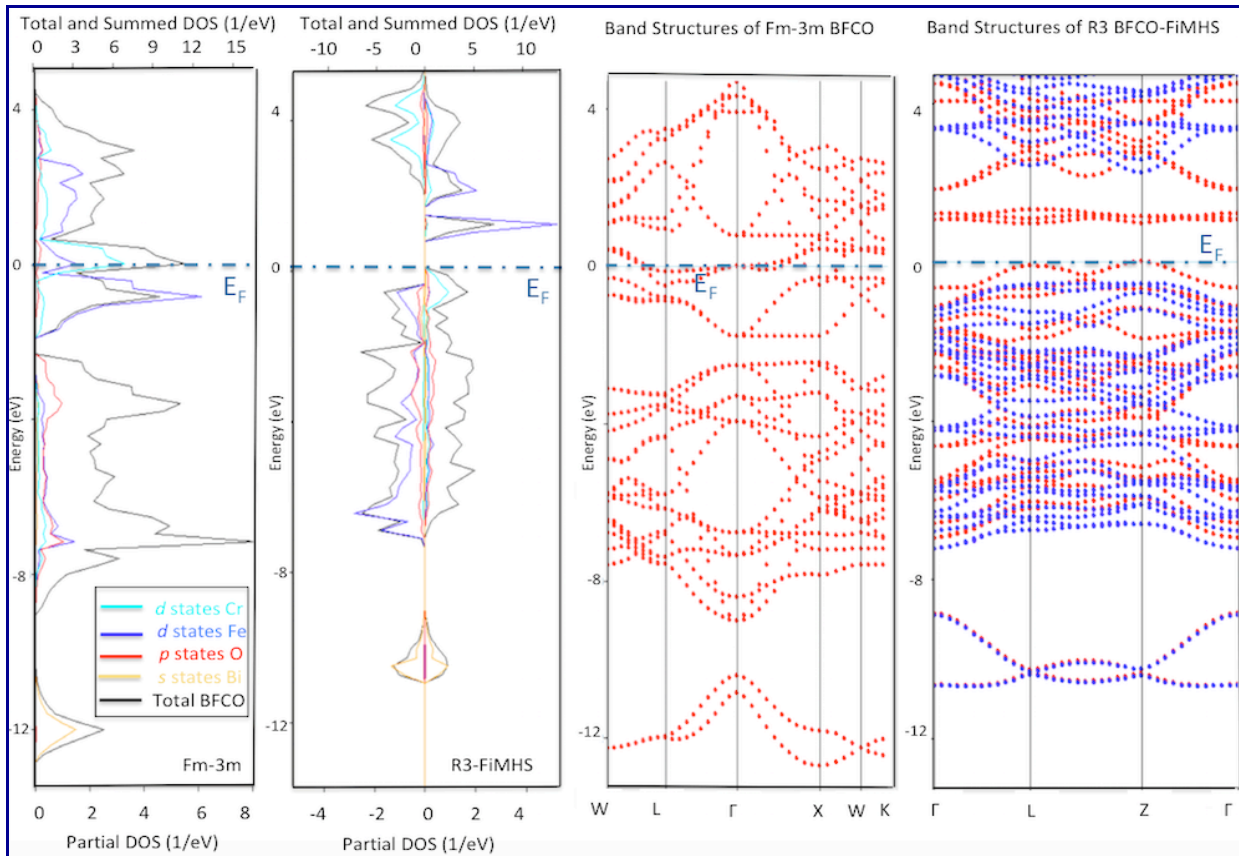


Figure S.5 Les DOS partielles et totales, et les structures de bande calculées au moyen de la fonctionnelle LSDA+U pour la structure BFCO hautement symétrique (*Fm-3m*) et pour l'état magnétique rhomboédrique *R3 FiMHS* du BFCO. À noter que l'axe inférieur, indiquant les DOS partielles, et l'axe supérieur, indiquant la DOS totale, ont des unités différentes.

Les valeurs des bandes interdites calculées au moyen des fonctionnelles LSDA+U et GGA+U sont présentées dans le Tableau S.2. Les calculs montrent que les valeurs des bandes interdites sont plus élevées pour PBEsol+U et RevPBE+U comparativement à LSDA+U, et que les valeurs obtenues au moyen de PBEsol+U sont plus proches de celles de LSDA+U. En outre, pour la première fois sont rapportés deux canaux de spin pour la phase magnétique FMLS, où les propriétés métalliques et semi-conductrices sont combinées dans un seul système au niveau microscopique au sein de la cellule unitaire.

Tableau S.2 Les bandes interdites calculées pour les phases magnétiques *R3 FiMHS*, *FiMLS*, *FMHS* et *FMLS* du BFCO au moyen des fonctionnelles LSDA+U, PBEsol+U et RevPBE+U.

Fonctionnel	Bandé interdite [eV] <i>FiMHS</i>	Bandé interdite [eV] <i>FiMLS</i>	Bandé interdite [eV] <i>FMHS</i>	Bandé interdite [eV] <i>FMLS</i>
LSDA+U	0.92	1.07	0.73	0.59 and 1.24
PBEsol+U	1.06	1.21	0.87	0.68 and 1.29
RevPBE+U	1.25	1.54	1.17	0.42 and 1.42

Selon la Réf. (Pickett & Eschrig, 2007), on peut parler de demi-métallicité quand un sous-système de spin est un métal et l'autre est un isolant ou semi-conducteur (bande interdite de valeur finie) ou un semi-métal (très faible bande interdite). C'est une propriété très intéressante pour la spintronique qui a longtemps recherché des matériaux ayant un comportement de demi-métallicité.

À noter que les valeurs des bandes interdites obtenues au moyen de LSDA+U sont généralement en accord avec celles indiquées dans la Réf. (Goffinet et al., 2012), à l'exception de l'état FMLS. Les divergences entre nos résultats et ceux de la Réf. (Goffinet et al., 2012) pour FMLS peuvent s'expliquer par le fait que le logiciel VASP fournit une décomposition de la densité d'états en termes des orbitales s, p, d, f pour chaque atome du système sans tenir compte de la symétrie du cristal, et donc les DOS partielles des atomes équivalents en termes de symétrie peuvent différer l'un de l'autre (ce qui se produit probablement pour FMLS). Les calculs rapportés dans ce travail ont été réalisés à l'aide de MedeA-VASP de Materials Design (MedeA 2017; 2015) qui effectue une étape supplémentaire au-delà de VASP, c'est-à-dire que MedeA-VASP symétrise les composants partiels des DOS et obtient les DOS partielles correctes s, p, d, f pour chaque site. Avant l'utilisation de MedeA, lorsque nous avons validé nos premiers résultats pour la fonctionnelle LSDA+U en utilisant VASP comme licence autonome, nous avons obtenu les mêmes valeurs de bandes interdites que Goffinet et al., y compris pour FMLS (avec une bande interdite de ~ 1 eV).

Nos investigations ont également révélé que les distorsions de Jahn-Teller et la rotation/inclinaison des octaèdres d'oxygène sont fortement couplées avec des arrangements de spin. Les longueurs de liaison calculées au moyen des fonctionnelles LSDA+U, PBEsol+U et RevPBE+U, entre les atomes Bi, Cr et Fe le long de la diagonale [111] (voir le panneau en haut à gauche de la Fig. S.4), ainsi que les longueurs de liaison correspondant à (x_{01}, y_{01}, z_{01}) et (x_{02}, y_{02}, z_{02}) , ont montré clairement les différences de longueurs de liaisons entre la structure paraélectrique *Fm-3m*, correspondant à la structure sel gemme cubique idéale, et les structures rhomboédriques distordues, comportant un décentrage des atomes de Fe et de Cr qui contribue à la ferroélectricité. L'atome Bi_2 à travers sa paire d'électrons libres et son déplacement vers Fe contribue au raccourcissement de la liaison $\text{Bi}_2\text{-Fe}$ et à l'allongement de la liaison Cr-Bi_2 . De plus, pour les phases magnétiques HS, les liaisons Fe-O et Fe-Bi sont plus longues que les liaisons similaires dans les phases LS (à l'exception de la phase FMLS calculée au moyen de

RevPBE+U). Des liaisons Cr-O plus longues ont été obtenues dans le cas FM par rapport au cas FiM.

Le couplage des distorsions Jahn-Teller avec les rotations des octaèdres est un autre facteur qui peut jouer un rôle important dans les propriétés ferroélectriques et magnétiques du matériau. Leurs interactions ne sont cependant pas bien comprises (Lufaso et Woodward, 2004). En plus de subir des distorsions, les octaèdres d'oxygène sont en outre inclinés/tournés afin de minimiser l'énergie de la structure.

Les inclinaisons des octaèdres sont mesurées par les angles de liaison Cr-O_{Cr,Fe}-Fe contenant l'atome O_{Cr,Fe}, appartenant aux deux octaèdres CrO₆ et FeO₆ adjacents, et peuvent être inclinés hors plan, comme esquissé sur la Fig. S.6b ou inclinés dans le plan comme sur la Fig. S.6c. Si ces angles sont égaux à 180°, les octaèdres ne sont pas inclinés (c'est le cas de la structure cubique idéale), et si ces angles sont différents de 180°, les octaèdres sont inclinés.

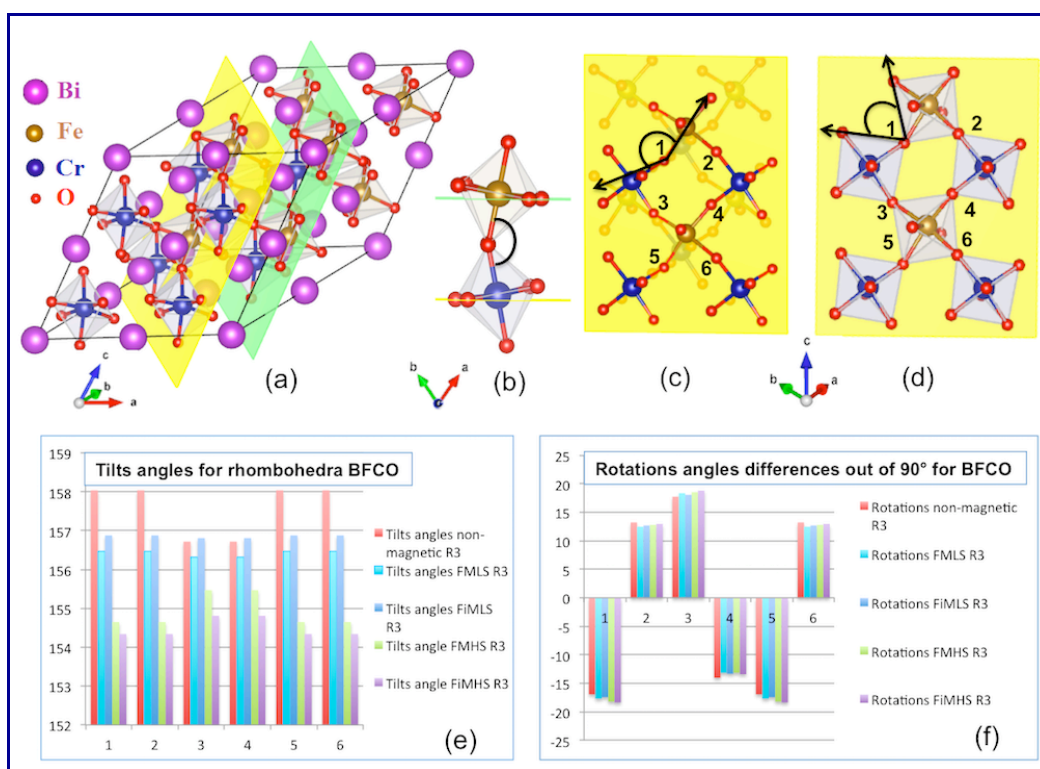


Figure S.6 Les octaèdres d'oxygène coupant les plans jaune et vert (110) du BFCO rhomboédrique périodique 2×2×2 pour la phase FiMHS (a); Esquisse de l'inclinaison hors plan (b); Angles calculés au moyen de LSDA+U, mesurant les inclinaisons dans le plan des angles de liaison Cr-O_{Cr,Fe}-Fe avec les O_{Cr,Fe}, notés 1, 2, 3, 4, 5, 6, appartenant aux octaèdres CrO₆ et FeO₆ adjacents (c); Angles calculés au moyen de LSDA+U, mesurant les rotations des oxygènes équatoriaux O_{Cr}-O_{Cr,Fe}-O_{Fe}, ayant les O_{Cr,Fe} aux coins 1, 2, 3, 4, 5 et 6 (d); Angles d'inclinaison calculés dans le plan indiqué en (c) pour toutes les structures R3 (e); Différences calculées par rapport à 90° pour les angles de rotation dans le plan des oxygènes équatoriaux O_{Cr}-O_{Cr,Fe}-O_{Fe} représentés en (d) pour toutes les structures R3 (f).

Les Figs. S.6c et S.6d montrent les atomes des octaèdres coupant le plan jaune (110) de la Fig. S.6a. Les angles d'inclinaison des liaisons Cr-O_{Cr,Fe}-Fe dans le plan, ayant les O_{Cr,Fe} marqués par 1, 2, 3, 4, 5, 6 sur la Fig. S.6c, sont illustrés sur l'histogramme sur la Fig. S.6e. Les barres les plus hautes (rouges) correspondant aux angles les plus élevés et donc aux octaèdres les moins inclinés, formant les angles les plus proches de 180°, sont obtenues pour le BFCO rhomboédrique non magnétique qui ne montre que les légères inclinaisons nécessaires pour produire la symétrie *R*3. Les octaèdres sont plus inclinés pour les phases magnétiques LS et davantage encore pour les phases HS.

Le couplage des distorsions de Jahn-Teller avec l'inclinaison et la rotation des octaèdres apporte diverses distorsions supportant la ferroélectricité. Pour prédire la polarisation spontanée dans les ferroélectriques, c'est-à-dire pour calculer la différence de polarisation ΔP entre deux états différents du même solide (structure de référence para-électrique centro-symétrique versus structure ferroélectrique), la première étape consiste à identifier la structure de référence paraélectrique (i.e., la structure cubique hautement symétrique), et de calculer le tenseur de la charge effective de Born pour chaque atome de cette structure *Fm-3m* du BFCO. La deuxième étape consiste à identifier les structures ferroélectriques (c'est-à-dire avec la symétrie *R*3), calculer le tenseur de charge effective de Born, et calculer les déplacements atomiques $\Delta u_{k,\alpha}$ des structures déformées par rapport à la structure de référence. Finalement, en utilisant la charge effective de Born moyenne proposée par Ghosez et ses collaborateurs (Ghosez et al., 1998), $Z_{k,\alpha\beta}^* = 0.68Z_{Cubic}^* + 0.32Z_{Ferro}^*$, on obtient les vecteurs de polarisation spontanée pour les fonctionnelles LSDA+U, PBEsol+U et RevPBE. Dans le cas de la fonctionnelle LSDA+U, le tableau S.3 présente les vecteurs de polarisation spontanée calculés ainsi que des estimations simples des polarisations ioniques en utilisant les charges nominales et de Bader.

Tableau S.3 Vecteurs de polarisation spontanée P_s dans les phases magnétiques FiMHS, FiMLS, FMHS et FMLS du BFCO calculés en utilisant les charges effectives de Born au moyen de la fonctionnelle LSDA+U, ainsi que des estimations simples de la polarisation ionique P_{ion}^N et P_{ion}^B en utilisant respectivement les charges nominales (formelles) et les charges de Bader calculées.

	$P_{ion}^N [\mu C/cm^2]$	$P_{ion}^B [\mu C/cm^2]$	$P_s [\mu C/cm^2]$	P_s / P_{ion}^N
FiMHS	$\ (31.4; 31.6; 31.6)\ =54.60$	$\ (19.3; 19.4; 19.4)\ =33.53$	$\ (40.0; 46.0; 47.2)\ =79.24$	1.451
FiMLS	$\ (34.3; 34.5; 34.5)\ =59.64$	$\ (21.3; 21.5; 21.5)\ =37.12$	$\ (46.3; 48.4; 49.8)\ =83.46$	1.399
FMHS	$\ (30.8; 30.9; 30.9)\ =53.46$	$\ (18.8; 18.9; 18.9)\ =32.67$	$\ (43.3; 45.3; 46.4)\ =77.97$	1.458
FMLS	$\ (35.5; 35.6; 35.6)\ =61.60$	$\ (22.8; 23.0; 23.0)\ =39.72$	$\ (47.5; 51.1; 51.2)\ =86.53$	1.405

Les polarisations spontanées pour les états magnétiques FiMLS, FMHS et FMLS sont données pour la première fois et révèlent une polarisation plus élevée pour les états magnétiques LS. La

phase FiMLS présente un intérêt particulier car elle possède un moment magnétique de même amplitude que la phase FiMHS, soit $\sim 2 \mu_B/\text{f.u.}$, qui correspond à la valeur expérimentale, et, dans le cas de films contraints, FiMLS pourrait devenir la phase la plus stable au lieu de FiMHS (Goffinet et al., 2012). En comparant les \mathbf{P}_s calculés au moyen d'estimations simples de la polarisation ionique en utilisant les charges nominales et de Bader, on peut voir que la polarisation spontanée calculée à partir des charges effectives de Born est plus grande avec un facteur de ~ 1.5 pour les états de haut spin et ~ 1.4 pour les états de bas spin. De plus, toutes les polarisations sont presque parallèles à [111], c'est-à-dire la direction des déplacements polaires entraînés par la paire d'électrons libres du Bi, comme on l'a vu précédemment dans l'ELF.

Pour comprendre la contribution des rotations des octaèdres d'oxygène à la polarisation spontanée, par rapport aux contributions de Bi, Fe et Cr, les mouvements atomiques ont été analysés. Comme le montre la Fig. S.7 (a), Bi₁ et Cr apportent des contributions antagonistes à la polarisation globale \mathbf{P}_s (le long de [111]) calculée au moyen des fonctionnelles LSDA+U, PBEsol+U et RevPBE+U pour toutes les phases magnétiques. Bi₂ (au centre de la cellule rhomboédrique) et Fe induisent des contributions qui appuient \mathbf{P}_s pour les états magnétiques HS, et des contributions antagonistes pour les états magnétiques LS lorsque les fonctionnelles LSDA+U et PBEsol+U sont utilisées.

Concernant les atomes d'oxygène, deux mouvements des octaèdres induisent un changement de la polarisation: un mouvement le long de l'axe [111] dû aux déplacements polaires, et un autre mouvement dans un plan orthogonal à [111] (flèches rouges dans le plan rose de la Fig. S.7) en raison de la rotation des deux octaèdres, respectivement dans le sens horaire et dans le sens antihoraire. La décomposition de ces mouvements est représentée sur la Fig. S.7b. Il est remarquable que les composantes de polarisation orthogonales à [111] des atomes d'oxygène autour de Fe et Cr, respectivement, s'annulent, et la polarisation totale est dominée par les composantes des atomes d'oxygène dans la direction [111]. Un résultat très significatif de notre calcul est que, dans le cas du Bi₂FeCrO₆ rhomboédrique, la principale contribution à la polarisation provient des atomes d'oxygène et non des atomes Bi avec la paire d'électrons libres, comme dans le cas de BiFeO₃ (Ravindran et al., 2006, Baettig & Spaldin, 2005b).

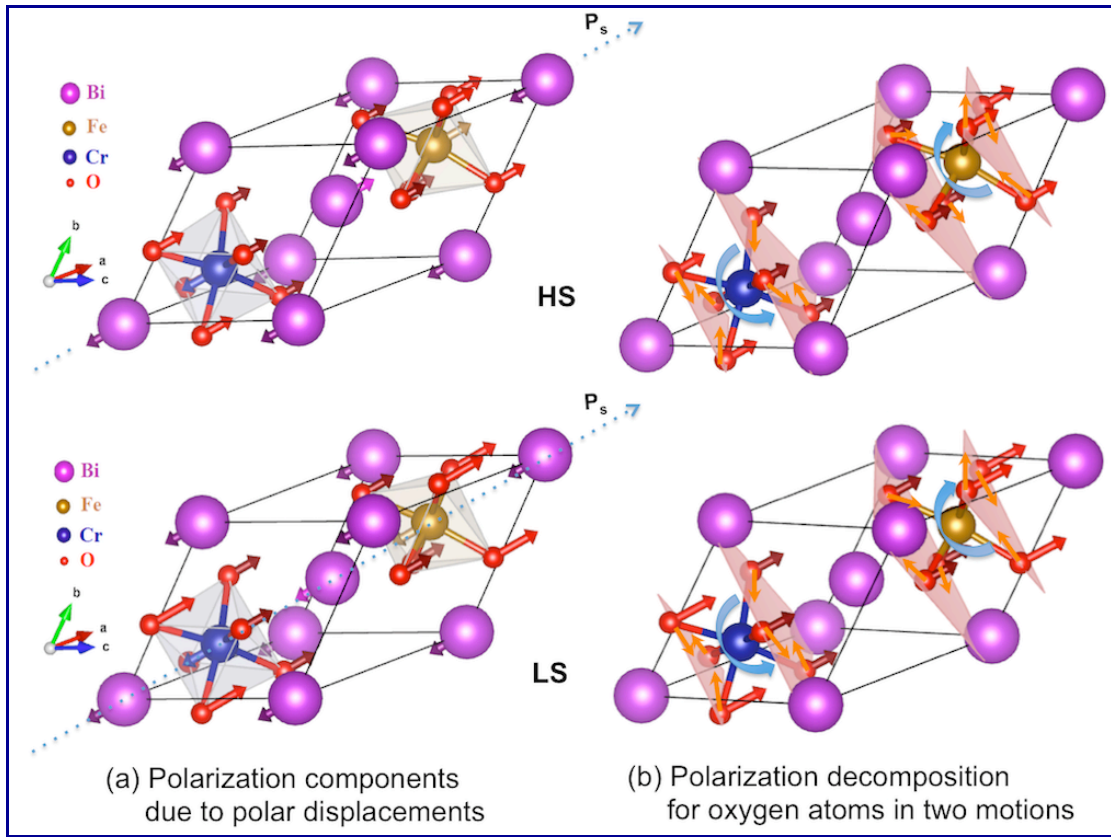


Figure S.7 Représentation schématique de la décomposition du vecteur de polarisation en deux mouvements associés aux déplacements polaires le long de l'axe [111] et aux rotations des octaèdres dans le sens horaire et antihoraire.

Chapitre 5: Etude DFT du $\text{Bi}_2\text{FeCrO}_6$: calculs en spins polarisés non colinéairement. Le chapitre 5 est consacré à une discussion étendue sur les structures de spins non-colinéaires lorsque le couplage spin-orbite (SOC) est inclus, ainsi que l'effet de ce dernier sur les propriétés multiferroïques du BFCO rhomboédrique. Les vecteurs magnétiques ont été initialement alignés selon différents axes de quantification du spin, puis ils ont tourné pendant la procédure d'optimisation jusqu'à la convergence vers le minimum d'énergie, sans contrainte sur la symétrie (le maillage des points k n'est plus limité à un ensemble de symétries irréductibles de la cellule primitive). Les calculs effectués au moyen des fonctionnelles LSDA+U, PBEsol+U et RevPBE+U en présence du SOC ont montré que les moments magnétiques orbitaux pour Cr^{3+} et Fe^{3+} -haut spin (HS) sont fortement atténués (les moments orbitaux sont très petits, et donc le moment magnétique total est dû au spin). Les moments orbitaux de Fe -HS et Cr participent à un petit pourcentage (environ 1% -4%) au moment magnétique total, tandis que les moments de spin du Fe³⁺ -haut spin et du Cr restent contribuer pour 74% -86%. L'effet est opposé dans le

cas de Fe^{3+} -bas spin où des moments orbitaux magnétiques importants ont été observés. En outre, l'énergie d'anisotropie magnétocristalline (MAE) montre qu'une saturation de l'aimantation, avec un moment magnétique d'environ $2 \mu_B/\text{f.u.}$ pour FiMHS, est réalisée le long de l'axe magnétique facile qui est perpendiculaire à la direction de polarisation [111]. Notre étude des MAE révèle que la physique devient plus complexe pour les autres états FiMLS, FMHS et FMLS. Par exemple, l'axe magnétique facile pour les cas LS est parallèle à la direction de polarisation [111] pour les fonctionnelles LSDA+U et RevPBE+U, alors que pour la fonctionnelle PBEsol+U, un axe magnétique facile est perpendiculaire à [111].

Pour mieux comprendre la structure électronique et l'effet du magnétisme non colinéaire dû au SOC sur le BFCO, les densités d'états (DOS) partielles et totales et les structures de bandes correspondantes ont été calculées. Des comparaisons entre les DOS et les structures de bandes obtenues des calculs colinéaires et non colinéaires avec le SOC ont été effectuées. À noter que, dans le cas de calculs en spins polarisés colinéairement, le spin de l'ion Cr définit l'état de spin up sur l'axe positif des courbes de DOS, et donc les états de spin down sont représentés sur l'axe négatif. Pour les calculs non colinéaires, où les notions de spin up et spin down n'ont plus de sens, puisque les spins électroniques peuvent s'orienter dans n'importe quelle direction de l'espace, toutes les DOS sont tracées sur l'axe positif. Dans ce résumé, un exemple comparant les DOS partielles et totales de la phase *R3* FiMHS obtenues de calculs colinéaires au moyen de LSDA+U, et celles obtenues de calculs non colinéaires, où le SOC est pris en compte, au moyen de LSDA+U, PBEsol+U et RevPBE+U, sont représentées sur la Fig. S.8. Comme il n'y a pas de différences majeures entre les DOS calculées pour différents axes de quantification de spin (à l'exception des très petites variations de la bande interdite que l'on peut voir dans le Tableau S.4), nous illustrons ici des DOS pour un seul axe de quantification de spin, soit $S=[111]$.

Les DOS montrent que le SOC mélange les composantes de spin up et de spin down des états de Bloch, et qu'une augmentation modérée de la bande interdite se produit pour FiMHS lorsque le SOC est inclus. En examinant la structure électronique détaillée près du niveau de Fermi E_F , une excitation orbitale large est observée au voisinage de E_F , car on s'attend normalement à avoir des excitations orbitales entre les bandes occupées et inoccupées en présence de SOC.

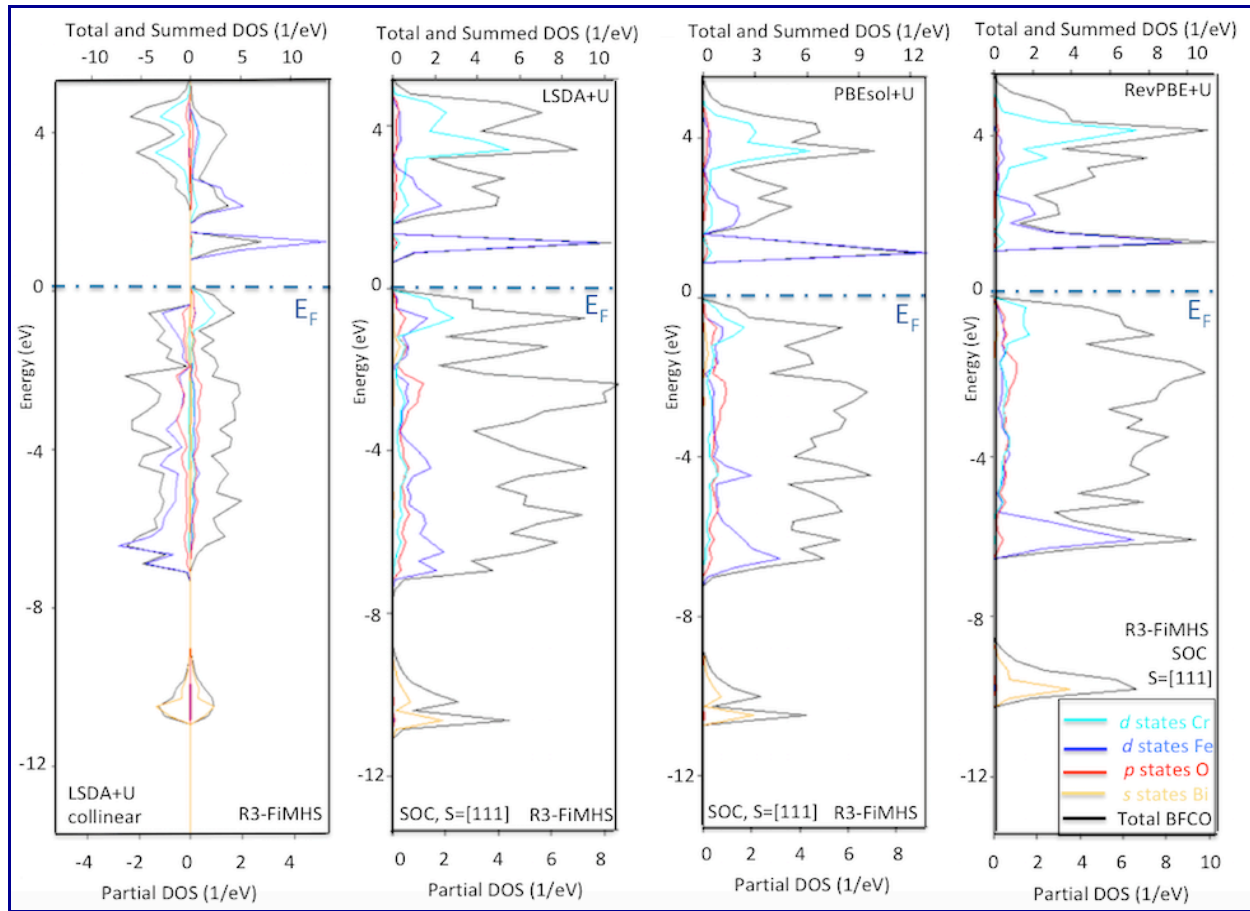


Figure S.8 DOS partielles et totales calculées pour l'état magnétique rhomboédrique *R3 FiMHS* du BFCO. La comparaison entre les DOS obtenues de calculs colinéaires au moyen de LSDA+U et celles obtenues de calculs non colinéaires prenant en compte le SOC en utilisant les fonctionnelles LSDA+U, PBEsol+U et RevPBE+U, où l'axe de quantification est $S = [111]$.

Tableau S.4 Les bandes interdites calculées pour les phases magnétiques *R3 FiLMS*, *FiLMS*, *FMHS* et *FMLS* du BFCO au moyen des fonctionnelles LSDA + U, PBEsol+U et RevPBE+U.

Functional	Bande interdite [eV] FiMHS	Bande interdite [eV] FiLMS	Bande interdite [eV] FMHS	Bande interdite [eV] FMLS
LSDA+U Calculs colinéaires	0.921	1.073	0.735	0.592 & 1.246 deux canaux de spin
LSDA+U non colinéaire SOC, $S=[111]$	0.968	0.974	0.610	0.976
LSDA+U non colinéaire SOC, $S=[-0.5\ 0.5\ 0]$	0.952	0.970	0.607	0.938
PBEsol+U Calculs colinéaires	1.058	1.210	0.873	0.686 & 1.299 deux canaux de spin
PBEsol+U non colinéaire SOC, $S=[111]$	1.220	0.993	0.969	1.025
PBEsol+U non colinéaire SOC, $S=[-0.5\ 0.5\ 0]$	1.113	1.165	0.842	0.550
RevPBE+U Calculs colinéaires	1.249	1.541	1.172	0.418 & 1.424 deux canaux de spin
RevPBE+U non colinéaire SOC, $S=[111]$	1.303	1.642	1.265	0.937
RevPBE+U non colinéaire SOC, $S=[-0.5\ 0.5\ 0]$	1.290	1.597	1.229	0.660

Les calculs montrent clairement les effets du SOC sur les bandes interdites: pour les états HS, les bandes interdites sont généralement plus grandes en présence de SOC, sauf pour quelques exceptions dans le cas du FMHS, tandis que pour les états FiMLS, les valeurs des bandes interdites sont plus faibles pour LSDA+U et RevPBE+U. Le cas du FMLS est analysé plus en détail car le SOC ne conserve pas la demi-métallicité (deux canaux de spin) observée dans les calculs colinéaires. Pickett et Eschrig ont effectué une étude sur l'effet du SOC sur la demi-métallicité (Pickett et Eschrig, 2007). Comme la théorie complètement relativiste (incluant le SOC) détruit en principe la demi-métallicité, la question est: « est-ce que cela fait des demi-métaux une demi-vérité? » Les auteurs ont montré que l'effet relativiste du SOC sur la demi-métallicité, est mineur pour les plus petits atomes magnétiques (nombre atomique $Z \sim 30$ ou moins). Cependant, bien que dans notre cas le nombre atomique pour Fe et Cr est dans cette gamme ($Z_{Cr} = 24$ et $Z_{Fe} = 26$) nous observons un effet évident.

En ce qui concerne l'effet du SOC sur les distorsions cristallines, le cas FiMHS montre que les distorsions trigonales de l'octaèdre sont conservées en présence de la brisure de la symétrie et du SOC. En comparant les longueurs des liaisons résultant des calculs colinéaires et non colinéaires, les longueurs des liaisons des triplets d'oxygène s'avèrent être allongées d'environ 1-4% par le SOC pour les fonctionnelles PBE+U, avec des pourcentages plus élevés pour les liaisons correspondant aux positions de Wyckoff de l'oxygène (x_{01}, y_{01}, z_{01}). Dans le cas du FiMLS, les distorsions trigonales des octaèdres sont préservées lorsque les fonctionnelles LSDA+U et PBEsol+U sont utilisées avec la brisure de la symétrie et le SOC, mais elles varient avec l'axe de quantification du spin. Lorsque la fonction RevPBE+U est utilisée, les effets de la brisure de la symétrie sont très visibles sur les longueurs des liaisons, car il n'y a plus de triplets. Dans le cas de FMHS et FMLS, des comportements similaires ont été observés, mais ce qui est nouveau dans le cas des états ferromagnétiques est le fait que le décentrage des ions Fe^{3+} et Cr^{3+} dans leurs octaèdres d'oxygène préserve les distorsions trigonales dans tous les états calculés au moyen de LSDA+U, PBEsol+U et RevPBE+U. L'effet de la brisure de la symétrie sur les états FM n'est pas aussi visible que pour les états FiM, et nous pensons que cela est dû au ferromagnétisme au lieu de l'anti-ferromagnétisme (ferrimagnétisme) pour les états FiM en raison des différences entre les angles Fe-O-Cr dans les deux cas.

Enfin, les effets du SOC sur la polarisation montrent une contribution additionnelle de 0.3 à 4.6 [$\mu C/cm^2$] par rapport à la polarisation obtenue dans les calculs colinéaires.

Chapitre 6: Conclusions et perspectives d'avenir. Au chapitre 6, des conclusions sont tirées et des perspectives futures sont suggérées. Les calculs colinéaires effectués au chapitre 4 (sans SOC) ont confirmé l'existence de quatre états fondamentaux ordonnés sur l'échelle énergétique comme : FiMHS (I), FMHS (II), FiMLS (III) et FMLS (IV), pour les 3 fonctionnelles LSDA+U, PBEsol+U et RevPBE+U. FiMHS représente l'état fondamental avec un ordre magnétique net de $2 \mu_B/f.u$, suivi de FMHS avec un moment magnétique net de $8 \mu_B/f.u$. La faible différence d'énergie entre les phases FiMHS et FMHS (de l'ordre de 68.7 à 164 meV, selon la fonctionnelle choisie) permet d'envisager la possibilité d'utiliser des perturbations appropriées (telles que les déformations, les défauts, etc.) pour obtenir la phase FMHS du BFCO comme matériau pour des applications industrielles nécessitant une magnétisation plus élevée. Les états du Fe^{3+} -bas spin, FiMLS, avec un moment magnétique net de $2 \mu_B/f.u$, présentent également un intérêt car ils correspondent à la valeur expérimentale, et ils pourraient être obtenus dans des films contraints. En outre, deux canaux de spin ont été trouvés pour la phase magnétique FMLS, où les propriétés métalliques et semi-conductrices sont combinées dans un seul système au niveau microscopique dans la cellule unitaire (semi-métallique).

Notre étude a également révélé que les distorsions de Jahn-Teller et les rotations/inclinaisons des octaèdres d'oxygène sont fortement couplées aux arrangements de spin, en raison des paires d'électrons libres des ions Bi^{3+} , et dans une moindre mesure par l'effet Jahn-Teller de premier ordre dans le Fe^{3+} -bas spin. Ces distorsions contribuent à la ferroélectricité du BFCO, comme le confirment les polarisations spontanées rapportées pour la première fois pour les quatre phases magnétiques. Leurs amplitudes calculées sont entre 64.0 et $86.5 \mu\text{C}/\text{cm}^2$ pour les fonctionnelles considérées (c'est-à-dire dans la gamme des valeurs mesurées pour BFCO), et elles sont dans la direction [111] pour toutes les phases. De plus, les charges effectives de Born des ions sont significativement plus grandes que les charges nominales, indiquant des échanges d'électrons importants entre les ions voisins. Un résultat significatif est que, pour toutes les phases, la contribution principale à la polarisation provient des atomes d'oxygène et non des atomes de Bi, avec leur paire d'électrons libres, comme dans le cas de BiFeO_3 (BFO), et cela est dû aux plus grands déplacements des atomes d'oxygène dans le cas de BFCO.

Le SOC a été pris en compte dans le chapitre 5, via des calculs non colinéaires, où les vecteurs magnétiques non colinéaires ont été initialement alignés le long de différents axes de quantification, puis ils ont pivoté pendant la procédure d'optimisation jusqu'à converger vers le minimum d'énergie, sans contrainte de symétrie. Les calculs ont montré que la brisure de la symétrie affecte les moments magnétiques orbitaux du Cr^{3+} et du Fe^{3+} -haut spin (HS) qui sont

petits, soient 0.049-0.056 μ_B par atome de Cr, et 0.018-0.029 μ_B par atome de Fe- HS (les moments orbitaux sont petit, et donc le moment magnétique total est dû au spin). Les résultats obtenus au moyen des fonctionnelles LSDA+U, PBEsol+U et RevPBE+U montrent que pour FiMHS et FMHS, les moments orbitaux de Fe et Cr participent à un faible pourcentage (environ 1% - 4%) du moment magnétique total, tandis que les moments de spin restent à environ 74% - 86%. L'effet est opposé dans le cas du Fe^{3+} -bas spin où des moments orbitaux magnétiques importants ont été observés. En outre, le calcul de l'énergie d'anisotropie magnétocristalline (MAE) a montré que la saturation de l'aimantation, avec un moment magnétique d'environ 2 $\mu_B/f.u.$ pour FiMHS, est réalisée le long de l'axe facile qui est perpendiculaire à la direction de polarisation [111]. Les vecteurs de moment magnétique et orbital sont inclinés parallèlement ou antiparallèles avec des axes de quantification de spin. Nos études sur le MAE révèlent que la physique est plus complexe pour FiMLS, FMHS et FMLS. Par exemple, l'axe facile des états LS est parallèle à la direction de polarisation [111] pour les fonctionnelles LSDA+U et RevPBE+U, tandis que le PBEsol+U montre un axe facile perpendiculaire à [111].

Les recherches ont également révélé l'effet du SOC sur les distorsions octaédriques: les distorsions trigonales sont préservées dans FiMHS même si la symétrie se brise, mais les longueurs des liaisons Fe-O et Cr-O changent. En comparant les calculs colinéaires et non colinéaires, nous avons trouvé que pour la phase FiMHS, les longueurs de liaison des triplets d'oxygène sont allongées d'environ 1-4% par le SOC pour les fonctionnelles PBE+U, avec des pourcentages plus élevés pour les liaisons correspondant aux positions de Wyckoff de l'oxygène (x_{01}, y_{01}, z_{01}). Dans le cas du FiMLS, les variations des longueurs de liaison Fe-O et Cr-O sont d'environ -0.2% à 1% pour LSDA+U et PBEsol+U, et de plus fortes variations d'environ -5% à 9% sont observées pour RevPBE+U de telle sorte que les longueurs de liaison des triplets ne sont plus conservées.

Les distorsions observées dans FiMLS sont les conséquences des moments orbitaux magnétiques non atténués pour Fe^{3+} -LS, la paire d'électrons libres de l'ion central Bi^{3+} , et d'autres phénomènes physiques non étudiés se combinant avec la brisure de la symétrie et le SOC. Des comportements similaires sont apparus pour FMHS et FMLS, à la différence que les distorsions trigonales sont conservées même dans le cas LS. Enfin, l'effet du SOC sur les polarisations spontanées est faible, de l'ordre de 0.3 à 4.6 $\mu C/cm^2$, les changements de longueur des liaisons étant contrebalancés par les changements des volumes.

Cette étude fournit de nouvelles perspectives pour contrôler les distorsions du réseau cristallin et ajuster les propriétés multiferroïques. Cependant, pour atteindre un objectif aussi ambitieux, des développements futurs sont nécessaires, et voici quelques perspectives:

- (i) En complément à l'étude des distorsions de Jahn-Teller, une nouvelle approche appelée effets de couplage vibronique JT pourrait être utilisée pour obtenir une meilleure compréhension de la physique présente dans une grande gamme spectrale (UV, rayons X, photoélectron), des transitions de phase structurales, de la ferroélectricité, de la magnétorésistance colossale, etc.
- (ii) Les calculs non colinéaires sont onéreux en temps, mais une continuation de ce travail consistant à considérer plus d'axes de quantification serait utile, de même que l'étude de la façon dont la réponse magnétique peut être augmentée en utilisant des contraintes épitaxiales.
- (iii) Des études détaillées sur la manière dont les propriétés BFCO sont affectées par les déformations épitaxiales seraient également très utiles pour comprendre les observations expérimentales sur le BFCO épitaxial développé sur différents substrats.
- (iv) Comme nos investigations ont montré que FMHS a le moment magnétique le plus élevé et qu'il est donc très intéressant pour les applications nécessitant une magnétisation plus élevée, on pourrait étudier comment on peut transiter entre ferrimagnétisme et ferromagnétisme, en se basant sur le fait que le FMHS est le deuxième sur l'échelle d'énergie après le Fmhs.
- (v) Une autre fonctionnelle populaire, à savoir la fonctionnelle hybride Heyd-Scuseria-Ernzerhof (HSE06) avec écrantage coulombien, qui contient une constante de mélange Hartree-Fock (25%), pourrait être utilisée pour améliorer les résultats obtenus au moyen des fonctionnelles PBE et révéler plus d'informations concernant les propriétés des multiferroïques.
- (vi) Des expériences récentes ont prouvé que l'ordre des cations Fe/Cr est facilité par les lacunes d'oxygène, et donc des études théoriques pourraient être faites pour examiner la dépendance des états de vacance/défaut sur la taille et la position des états excités, ainsi que la position attendue dans les systèmes réels avec les charges qui en résultent sur les vacances/défauts.
- (vii) Expérimentalement, il a été trouvé que le BFCO monophasé peut être obtenu dans une plage de pression-température très étroite. Pour comprendre la compétition entre les

différents états magnétiques en fonction de la pression et de la température, une combinaison entre les calculs DFT et de dynamique moléculaire (MC) pourrait apporter des informations importantes aux expérimentateurs, par exemple pour obtenir un diagramme de phase pression-température afin de s'assurer qu'une phase unique de BFCO soit obtenue expérimentalement avec la magnétisation la plus élevée (FMHS).

- (viii) Des études sur l'optimisation des supercellules dans différents arrangements des spins et des cations Fe et Cr permettraient d'étendre davantage les applications possibles du BFCO.

TABLE OF CONTENTS

CHAPTER 1. INTRODUCTION.....	1
CHAPTER 2. MAGNETOELECTRIC EFFECT AND MULTIFERROICS.....	7
2.1. Magnetoelectric effect and magnetoelectric coupling.....	7
2.2. Classification of magnetoelectric multiferroics.....	10
2.3. Simple and double perovskites: ideal structure, distortions, and octahedra rotations/tilting.....	13
2.3.1. The ideal perovskite structure.....	13
2.3.2. Tolerance factor.....	14
2.3.3. Octahedra distortions: Jahn-Teller effect.....	15
2.3.4. Octahedra tilting and rotations.....	18
CHAPTER 3. THEORETICAL BACKGROUND.....	23
3.1. Density Functional Theory.....	24
3.2. On-site Coulomb interaction.....	26
3.2.1. Strongly correlated systems.....	26
3.2.2. LDA and LDA+U.....	27
3.2.3. Appropriate computational scheme for Mott-Hubbard insulators.....	28
3.3. Relativistic Density Functional Theory.....	29
3.3.1. Noncollinear magnetism.....	30
3.3.2. Spin-orbit coupling in the pseudo-potential context.....	32
3.4. Polarization.....	33
3.4.1. The concept of Born effective charge.....	34
3.4.2. Polarization in ferroelectrics.....	36
CHAPTER 4. DFT STUDY OF Bi₂FeCrO₆: COLLINEAR SPIN POLARIZED CALCULATIONS	
4.1. Crystal structure of Bi ₂ FeCrO ₆	41
4.2. Computational details.....	43
4.3. Ground-state structures and magnetic orderings.....	45
4.4. Electronic properties	50
4.5. Distortions and octahedra tilting/rotations.....	56
4.6. Spontaneous polarization.....	61
CHAPTER 5. DFT STUDY OF Bi₂FeCrO₆: NONCOLLINEAR SPIN POLARIZED CALCULATIONS.....	71
5.1. Computational details.....	71
5.2. Ground-state structures and magnetic orderings.....	75

5.3. Electronic properties	82
5.4. Spin-orbit coupling effects on the magnetic structure distortions.....	86
5.5. Spin-orbit coupling effects on the spontaneous polarization.....	92
CHAPTER 6. CONCLUSIONS AND FUTURE PERSPECTIVES.....	95
CHAPTER 7. REFERENCES.....	99
APPENDIX I. The DOSs and band structures corresponding to the Bi, Fe, Cr and O atoms of the rhombohedral R3 BFCO, in the case of collinear spin polarized calculations within LSDA+U and PBEsol+U functionals.....	111

LIST OF TABLES

Table 4.1 Summary of the structural and electronic properties of the FiMHS, FiMLS, FMHS, and FMLS phases of BFCO as computed using the LSDA+U, PBEsol+U and RevPBE+U functionals. The rhombohedral unit cell parameters are length a_r and angle α_r ; V_r is the unit cell volume; x_i , y_i , and z_i represent the Wyckoff positions of the space group 146 (<i>R</i> 3 symmetry) in the rhombohedral setting, i.e. $Bi_{1,2}(x, x, x)$, $Fe(x, x, x)$, $Cr(x, x, x)$ and $O_1(x_{01}, y_{01}, z_{01})$, $O_2(z_{01}, x_{01}, y_{01})$, $O_3(y_{01}, z_{01}, x_{01})$, $O_4(x_{02}, y_{02}, z_{02})$, $O_5(z_{02}, x_{02}, y_{02})$, $O_6(y_{02}, z_{02}, x_{02})$; μM_{Fe} and μM_{Cr} are the local magnetic moments of Fe and Cr; μM_{BFCO} is the total magnetic moment per unit cell; Computed charges of Fe and Cr; ΔE is the energy difference between the corresponding phase and the FiMHS ground state.....	47
Table 4.2 The computed band-gaps of the R3 FiMHS, FiMLS, FMHS and FMLS magnetic phases of BFCO withing the LSDA+U, PBEsol+U and RevPBE+U functional.....	55
Table 4.3 The calculated bond lengths, within the LSDA+U, PBEsol+U and RevPBE+U functionals, between Bi_1 , Cr, Bi_2 and Fe (see top-left panel of Fig. 4.4) along the diagonal [111] direction.....	58
Table 4.4 The calculated Cr-O, Fe-O bond lengths within the LSDA+U, PBEsol+U and RevPBE+U functionals, corresponding to the oxygen positions (x_{01}, y_{01}, z_{01}) , (x_{02}, y_{02}, z_{02})	58
Table 4.5 Spontaneous polarization vectors P_s in the ferroelectric FiMHS, FiMLS, FMHS, and FMLS magnetic phases of BFCO calculated using Born effective charges within the LSDA+U functional, together with simple estimations of the ionic polarization P_{ion}^N using nominal (formal) charges and P_{ion}^B using computed Bader charges.....	62
Table 4.6 Spontaneous polarization vectors P_s in the ferroelectric FiMHS, FiMLS, FMHS, and FMLS magnetic phases of BFCO calculated using Born effective charges within the LSDA+U functional, compared with the corresponding vectors obtained within the PBEsol+U and RevPBE+U functionals.....	63
Table 4.7 Calculated Born effective charge tensors, within the LSDA+U functional, for each atom of the rhombohedral unit cell in the ferroelectric FiMHS, FiMLS, FMHS, FMLS phases of the double perovskite Bi_2FeCrO_6	64
Table 4.8 Spontaneous polarization vectors of Bi, Fe and Cr in the ferroelectric FiMHS, FiMLS, FMHS, and FMLS phases, and the polarization of all oxygen atoms O_1 - O_6 contribution to the BFCO spontaneous polarization P_s	65
Table 4.9 The calculated bonds lengths, within the LSDA+U functional, between Bi_1 , Fe_1 , Bi_2 and Fe_2 (see Fig. 4.10d) along the diagonal [111] direction, and the Fe-O bonds corresponding to the oxygen positions (x_{01}, y_{01}, z_{01}) and (x_{02}, y_{02}, z_{02}) of BFO, compared with similar bonds of BFCO (see Fig. 4.4 top-left panel).....	68
Table 4.10 Spontaneous polarization vectors of Bi, Fe, and all oxygen atoms O_1 - O_6 computed within the LSDA+U functional in the ferroelectric FiMHS phase of BFO compared with similar polarization values for BFCO.....	68
Table 5.1 Summary of the structural and electronic properties of the noncollinear SOC magnetic phases corresponding to the collinear FiMHS, FiMLS, FMHS, and FMLS phases of BFCO as computed using the LSDA+U functional starting from initial magnetic vectors parallel to spin quantizations $S=[111]$, $S=[-0.5\ 0.5\ 0]\perp[111]$. The rhombohedral unit cell lattice parameters are: lattice length a_r and angle α_r for collinear structure with R3 symmetry, and respectively lengths	

a_r , b_r , c_r and angles α_r , β_r , γ_r for when symmetry is turned off; V_r is the unit cell volume; x_i , y_i , and z_i represent the Wyckoff positions of the space group 146 (<i>R</i> 3 symmetry) in the rhombohedral setting, i.e. Bi _{1,2} (x, x, x), Fe(x, x, x), Cr(x, x, x) and O ₁ (x ₀₁ , y ₀₁ , z ₀₁), O ₂ (z ₀₁ , x ₀₁ , y ₀₁), O ₃ (y ₀₁ , z ₀₁ , x ₀₁), O ₄ (x ₀₂ , y ₀₂ , z ₀₂), O ₅ (z ₀₂ , x ₀₂ , y ₀₂), O ₆ (y ₀₂ , z ₀₂ , x ₀₂); μM_{Fe} and μM_{Cr} are the magnitudes of the local magnetic moments of Fe and Cr; μL_{Fe} and μL_{Cr} are the magnitudes of the orbital moments of Fe and Cr; μM_{BFCO} is the magnitude of the total magnetic moment per cell; ΔE is the energy difference between the corresponding collinear or noncollinear magnetic phases and the collinear FiMHS ground state.....	76
Table 5.2 As in Table 5.1 but for the PBEsol+U functional.....	77
Table 5.3 As in Table 5.1 but for the RevPBE+U functional.....	78
Table 5.4 The computed magneto-crystalline anisotropy energies for FiMHS state within the LSDA+U functional, corresponding to the spin quantization axes S ₁ =[111], S ₂ =[0.98 0.90 1.06], S ₃ =[0.97 0.84 1.09], S ₄ =[0.5, 1.0, 1.5], S ₅ =[0.70, 0.35, 1.06] and S ₆ = [-0.5, 0.5, 0] which make angles 0°, 9.4°, 14°, 22°, 45°, 90° with polarization axis [111]; as well as the computed magnitudes of the magnetic, μM , and orbital μL moments together with their corresponding vectors for Fe and Cr.....	80
Table 5.5 As in Table 5.4 but for the FiMLS state.....	81
Table 5.6 The computed easy and hard magnetization axes of R3 BFCO corresponding to the FiMHS, FiMLS, FMHS and FMLS states within LSDA+U, PBEsol+U and RevPBE+U functional approximations (SOC effect is included).....	81
Table 5.7 The computed band gaps of the R3 FiMHS, FiMLS, FMHS and FMLS magnetic phases of BFCO within the LSDA+U, PBEsol+U and RevPBE+U functional.....	85
Table 5.8a The calculated bond lengths between Bi ₁ , Cr, Bi ₂ and Fe (see top-left panel of Fig. 4.4, section 4.3) along the diagonal [111] of BFCO for FiMHS state. Comparison between values obtained using collinear calculations within the LSDA+U, PBEsol+U and RevPBE+U functionals, and noncollinear calculations with SOC effects and spin quantization axes S=[111] and S ⊥ [111].....	87
Table 5.8b The calculated Cr-O, Fe-O bond lengths corresponding to the oxygen positions (x ₀₁ , y ₀₁ , z ₀₁) and (x ₀₂ , y ₀₂ , z ₀₂) in the R3 BFCO for FiMHS state. Comparison between values obtained using collinear calculations within the LSDA+U, PBEsol+U and RevPBE+U functionals, and noncollinear calculations with SOC effects and spin quantization axes S=[111] and S ⊥ [111].....	88
Table 5.9a The calculated bond lengths between Bi ₁ , Cr, Bi ₂ and Fe (see top-left panel of Fig. 4.4, section 4.3) along the diagonal [111] of BFCO for FiMLS state. Comparison between values obtained using collinear calculations within the LSDA+U, PBEsol+U and RevPBE+U functionals, and noncollinear calculations with SOC effects and spin quantization axes S=[111] and S ⊥ [111].....	89
Table 5.9b The calculated Cr-O, Fe-O bond lengths corresponding to the oxygen positions (x ₀₁ , y ₀₁ , z ₀₁) and (x ₀₂ , y ₀₂ , z ₀₂) in the R3 BFCO for FiMLS state. Comparison between values obtained using collinear calculations within the LSDA+U, PBEsol+U and RevPBE+U functionals, and noncollinear calculations with SOC effects and spin quantization axes S=[111] and S ⊥ [111].....	89
Table 5.10a The calculated bond lengths between Bi ₁ , Cr, Bi ₂ and Fe (see top-left panel of Fig. 4.4, section 4.3) along the diagonal [111] of BFCO for FMHS state. Comparison between values obtained using collinear calculations within the LSDA+U, PBEsol+U and RevPBE+U functionals,	

and noncollinear calculations with SOC effects and spin quantization axes S=[111] and S \perp [111].....	90
Table 5.10b The calculated Cr-O, Fe-O bond lengths corresponding to the oxygen positions (x_{O1}, y_{O1}, z_{O1}) and (x_{O2}, y_{O2}, z_{O2}) in the R3 BFCO for FMHS state. Comparison between values obtained using collinear calculations within the LSDA+U, PBEsol+U and RevPBE+U functionals, and noncollinear calculations with SOC effects and spin quantization axes S=[111] and S \perp [111].....	91
Table 5.11a The calculated bond lengths between Bi ₁ , Cr, Bi ₂ and Fe (see top-left panel of Fig. 4.4, section 4.3) along the diagonal [111] of BFCO for FMLS state. Comparison between values obtained using collinear calculations within the LSDA+U, PBEsol+U and RevPBE+U functionals, and noncollinear calculations with SOC effects and spin quantization axes S=[111] and S \perp [111].....	91
Table 5.11b The calculated Cr-O, Fe-O bond lengths corresponding to the oxygen positions (x_{O1}, y_{O1}, z_{O1}) and (x_{O2}, y_{O2}, z_{O2}) in the R3 BFCO for FMLS state. Comparison between values obtained using collinear calculations within the LSDA+U, PBEsol+U and RevPBE+U functionals, and noncollinear calculations with SOC effects and spin quantization axes S=[111] and S \perp [111].....	92
Table 5.12 Spontaneous polarization vectors P_s in the ferroelectric FiMHS, FiMLS, FMHS, and FMLS phases of BFCO calculated using Born effective charges within the LSDA+U and PBEsol+U functionals, and the corresponding vectors due to SOC effect with spin quantization axis S=[111].....	93

LIST OF FIGURES

Figure 1.1 The relationship between multiferroic and magnetoelectric materials. Adapted from Ref. (Martin & Ramesh, 2012).....	1
Figure 1.2 The ideal cubic structure of $(\text{BiFeO}_3)_2$ single perovskite (a); Ideal cubic structure of $\text{Bi}_2\text{FeCrO}_6$ double perovskite (b); The rhombohedral $R\bar{3}$ symmetry (c-d) of $\text{Bi}_2\text{FeCrO}_6$. Visualizations are performed with VESTA (Momma & Izumi, 2011).....	3
Figure 2.1 Phase control of the multiferroics. <i>Ferromagnetism</i> implies the existence of a net magnetization M in absence of a magnetic field H . <i>Ferroelectricity</i> implies existence of net polarization P in absence of a electric field E . <i>Ferroelasticity</i> implies existence of a net deformation ε in absence of a mechanical stress σ . In a multiferroic material, at least two of the primary ferroic properties coexists in the same phase leading additional interactions. In a <i>magnetoelectric multiferroic</i> , a magnetic field H induces changes in the polarization P , or the electric field E induces changes in the magnetization M (green dashed arrows). Adapted from Ref. (Spaldin & Fiebig, 2005).....	8
Figure 2.2 Publications per year during the period 1970-2016 with “magnetoelectric” as a keyword according to the Web of Science. (Web of Science, 2017).....	10
Figure 2.3 The first identified perovskite structure CaTiO_3 : cubic perovskite unit cell visualized using VESTA (Momma & Izumi, 2011).....	10
Figure 2.4 The cubic AMX_3 perovskite structure: A cation in the corner of the cube (a); M cation together with the octahedra in the corner of the cube (b); M and M' cation ordering following the rock salt-structure in an ideal double perovskite (c). Adapted from Ref. (King & Woodward, 2010).....	14
Figure 2.5 Symmetry lowering distortions from the aristotype structure: Non-distorted BaTiO_3 compared with exaggeratedly distorted BaTiO_3 for which $t > 1$ (a); Counter-rotations of oxygen octahedra around [111] (blue curved arrows) in BiFeO_3 , coupled with polar displacements (blue dotted arrow) for which $t < 1$ (b).....	15
Figure 2.6 FOJT distorted perovskites: Side and top views of the orthorhombic LaMnO_3 in polyhedral representation where the MnO_6 octahedra are distorted and long (<i>l</i>), medium (<i>m</i>), short (<i>s</i>) Mn-O bonds shown (a) (Rivero et al., 2016); Top views of the KCuF_3 distorted octahedra where planes of octahedra are stacked (top) or unstacked (bottom) one directly above the other (b). Adapted from Refs. (Rivero et al., 2016; Carpenter & Woodward, 2009).....	16
Figure 2.7 SOJT in the rhombohedra $R\bar{3}c$ symmetry of BiFeO_3 : distorted BiFeO_3 seen as rock-salt structure (a); Distorted BiFeO_3 seen as rhombohedra $R\bar{3}c$ symmetry (blue full and dashed lines in (b) versus rock-salt structure (b, c); Calculated electron localized function of BiFeO_3 rhombohedra showing lone-pair for the central Bi^{3+} cation (d).....	17
Figure 2.8 Sketch of the tilts illustrated for the BFCO double perovskite. The reference planes are shown in yellow in (a)&(b). Absence of out-of-plane tilt: the $\text{Fe}-\text{O}_{\text{Fe},\text{Cr}}-\text{Cr}$ bond angle is equal to 180° (a); Presence of the out-of-plane tilt: the $\text{Fe}-\text{O}_{\text{Fe},\text{Cr}}-\text{Cr}$ bond angle differs from 180° (b); Out-of-plane tilts in a BFCO supercell where the $\text{Fe}-\text{O}_{\text{Fe},\text{Cr}}-\text{Cr}$ bond angles 1, 2, 3, 4 differ from 180° (c); In-plane tilts of the top layer from (c) with 1, 2, 3, 4 angles having same values as out-of-plane angles, due to lattice symmetry and cell periodicity (d); In-plane tilts of the bottom layer from (c) with the corresponding 1, 2, 3, 4 angles (e); Note that the $\text{Fe}-\text{O}_{\text{Fe},\text{Cr}}-\text{Cr}$ bond is bent in the opposite direction for the top and the bottom layers.....	18

Figure 2.9 Sketch of the octahedra rotations illustrated for the BFCO double perovskite: absence of oxygen-octahedra rotations defined by oxygen $O_{Fe}-O_{Fe,Cr}-O_{Cr}$ bond angle equal to 90° (a); Occurrence of oxygen-octahedra rotation when the oxygen $O_{Fe}-O_{Fe,Cr}-O_{Cr}$ bond angle differs from 90° (b); Various oxygen-octahedra rotations in a BFCO supercell when the oxygen $O_{Fe}-O_{Fe,Cr}-O_{Cr}$ bond angles differ from 90° (c).....	19
Figure 2.10 No octahedral tilt: $a^0a^0a^0$, i.e., cubic symmetry (a); Octahedral with opposite tilt around c axis: $a^0a^0c^-$ (b) (Garg, 2001). Adapted from Ref. (Rondinelli & Spaldin, 2011).....	20
Figure 2.11 Octahedra tilts versus phase transitions of the transition metal perovskites. Adapted from Ref. (Rondinelli & Spaldin, 2011).....	21
Figure 3.1 The $BaTiO_3$ perovskite structure: Paraelectric unit cell where all Ti-O bonds are equal (a); Ferroelectric unit cell: The Ti atom was shifted up as the Ti-O upper bond is shorter than Ti-O lower bond (b) vizualized using VESTA (Momma & Izumi, 2011).....	37
Figure 4.1 The ideal cubic rock-salt structure of $(BiFeO_3)_2$ (a); The ideal cubic rock-salt structure of Bi_2FeCrO_6 where one Fe atom from (a) was replaced by a Cr atom (b); The (111) plane projection of the BFCO ideal cubic structure shows perfect overlapping of the oxygen atoms belonging to the Cr and Fe octahedra (c); The rhombohedral $R3$ symmetry (d-e) of BFCO; The (111) plane projection of the $R3$ BFCO shows oxygen displacements as consequence of octahedra rotations in opposite directions and lattice distortions (f). Visualizations are performed using VESTA (Momma & Izumi, 2011).....	42
Figure 4.2 The non-magnetic $Fm\text{-}3m$ optimized structure corresponding to ideal cubic rock-salt structure of BFCO as seen in Figure 4.1b (a); The computed Cr-O and Fe-O bond lengths of the undistorted octahedra corresponding to the BFCO $Fm\text{-}3m$ symmetry (b); The non-magnetic optimized distorted rhombohedral $R3$ structure of BFCO (c); The Cr-O and Fe-O bond lengths of the distorted octahedra corresponding to the BFCO $R3$ symmetry (d).....	44
Figure 4.3 Rhombohedral unit cells of the collinear magnetic optimized BFCO structures corresponding to the ferrimagnetic Fe^{3+} -high spin (FiMHS), Fe^{3+} -low spin (FiMLS), ferromagnetic Fe^{3+} -high spin (FMHS), and Fe^{3+} -low spin (FMLS) states. The spin of Cr^{3+} is marked by a green arrow, and the spin of Fe^{3+} is marked by a yellow arrow parallel or in the opposite direction according to the chosen spin orientation (up/down perpendicular on [111] direction) and the computed spin size (high, low).....	48
Figure 4.4 Calculated electron localization functions (ELFs) for the BFCO highly symmetric $Fm\text{-}3m$ non-magnetic structure (left), and the rhombohedral optimized structures corresponding to the FiMHS, FiMLS, FMHS and FMLS magnetic states. The considered cutting plane (0 1 -1), which contains Bi, Fe, Cr and four oxygen atoms emphasizes the bonds between Bi_1 , Cr, Bi_2 and Fe which are discussed in this thesis. Visualizations have been performed using Virtual NanoLab (Virtual NanoLab, 2016).....	50
Figure 4.5 The computed partial and total DOS, and band structures within the LSDA+U functional for the BFCO highly symmetric structure ($Fm\text{-}3m$) as compared with the rhombobederal $R3$ FiMHS magnetic state of BFCO. Note that the bottom axis indicating partial DOS and the top axis indicating total DOS have different scales.....	52
Figure 4.6 The computed partial and total DOS and band structures within the LSDA+U functional for the FiMHS phase as compared with the FiMLS phase for the rhombobederal $R3$ BFCO.....	53
Figure 4.7 The computed partial and total DOS and band structures within the LSDA+U functional for the FMHS phase as compared with the FMLS phase for the rhombobederal $R3$ BFCO.....	54

Figure 4.8 The oxygen octahedra intersecting the (110) yellow and green planes of the periodic $2\times 2\times 2$ rhombohedral BFCO for the FiMHS phase (a); Sketch of the out-of-plane tilt (b); Computed angles within the LSDA+U functional, measuring in-plane tilts of the Cr-O _{Cr,Fe} -Fe bond with O _{Cr,Fe} angles between the adjacent CrO ₆ , FeO ₆ octahedra denoted by 1, 2, 3, 4, 5, 6 (c); Computed angles within the LSDA+U functional, measuring rotations from the equatorial oxygen O _{Cr} -O _{Cr,Fe} -O _{Fe} , having O _{Cr,Fe} at the corners 1, 2, 3, 4, 5 and 6 (d); Computed in-plane tilts angles shown in (c) for all R3 structures (e); Computed differences from 90° for the in-plane rotations angles of equatorial oxygen O _{Cr} -O _{Cr,Fe} -O _{Fe} shown in (d) for all R3 structures (f).....	60
Figure 4.9 Schematic view of polarization vector decomposition into two motions associated to the polar displacements along the [111] axis, and to the clockwise & counter clockwise octahedral rotations.....	66
Figure 4.10 The ideal cubic rock-salt structure of (BiFeO ₃) ₂ (a); The rhombohedral R3c symmetry of BiFeO ₃ (b); The computed optimized R3c magnetic structure of BiFeO ₃ within the LSDA+U functional (c); The Bi and Fe atoms emphasize the bonds between Bi ₁ , Fe, Bi ₂ and Fe (d).	67
Figure 5.1 The rhombohedral R3c symmetry of BiFeO ₃ versus the ideal cubic rock-salt structure of (BiFeO ₃) ₂ (a); The computed optimized R3c magnetic structure of BiFeO ₃ within LSDA+U functional (b-d). The ferromagnetic Fe ³⁺ -high spin state (FiMHS), without spin-orbit coupling (b); The ferromagnetic Fe ³⁺ -low spin state (FiMLS), without spin-orbit coupling (c); The ferrimagnetic Fe ³⁺ -high spin state (FiMHS) including spin-orbit coupling (d); The (111) plane projection of the optimized magnetic structure (d) emphasizing Bi, Fe atoms and the canted noncollinear magnetic moments (e). Visualizations are performed using VESTA (Momma & Izumi, 2011).....	73
Figure 5.2 The computed partial and total DOS for the rhombodederal R3 FiMHS magnetic state of BFCO. Comparison between DOSs obtained from collinear calculations within LSDA+U functional with those obtained from noncollinear calculations taking into account SOC effect within LSDA+U, PBEsol+U and RevPBE+U functionals where spin quantization axis is S=[111]. Note that the bottom axis indicating partial DOS and the top axis indicating total DOS have different units.....	83
Figure 5.3 As in Figure 5.2 but for the FMHS state.....	84
Figure 5.4 As in Figure 5.2 but for the FMLS state.....	86
Figure A1.1 The computed Bi density of states within the LSDA+U functional for the BFCO highly symmetric structure (Fm-3m) as compared with the corresponding Bi states of the rhombodederal BFCO (R3) for the FiMHS, FiMLS, FMHS and FMLS magnetic states.....	111
Figure A1.2 The computed Fe density of states within the LSDA+U functional for the BFCO highly symmetric structure (Fm-3m) as compared with the corresponding Fe states of the rhombodederal BFCO (R3) for the FiMHS, FiMLS, FMHS and FMLS magnetic states.....	112
Figure A1.3 The computed Cr density of states within the LSDA+U functional for the BFCO highly symmetric structure (Fm-3m) as compared with the corresponding Cr states of the rhombodederal BFCO (R3) for the FiMHS, FiMLS, FMHS and FMLS magnetic states.....	113
Figure A1.4 The computed O density of states within the LSDA+U functional for the BFCO highly symmetric structure (Fm-3m) as compared with the corresponding O states of the rhombodederal BFCO (R3) for the FiMHS, FiMLS, FMHS and FMLS magnetic states.....	114
Figure A1.5a DOSs of Bi for FiMHS, FiMLS from LSDA+U compared with PBEsol+U.....	115

Figure AI.5b DOSs of Bi for FMHS, FMLS from LSDA+U compared with PBEsol+U.....	116
Figure AI.6a DOSs of Fe for FiMHS, FiMLS from LSDA+U compared with PBEsol+U.....	117
Figure AI.6b DOSs of Fe for FMHS, FMLS from LSDA+U compared with PBEsol+U.....	118
Figure AI.7a DOSs of Cr for FiMHS, FiMLS from LSDA+U compared with PBEsol+U.....	119
Figure AI.7b DOSs of Cr for FMHS, FMLS from LSDA+U compared with PBEsol+U.....	120
Figure AI.8a DOSs of O for FiMHS, FiMLS from LSDA+U compared with PBEsol+U.....	121
Figure AI.8b DOSs of O for FMHS, FMLS from LSDA+U compared with PBEsol+U.....	122

LIST OF EQUATIONS

$$F = F(\mathbf{E}, \mathbf{H}, \sigma, T) \quad (2.1)$$

$$\begin{aligned} -F(\mathbf{E}, \mathbf{H}, \sigma; T) &= P_i^s E_i + M_i^s H_i + \varepsilon_{ij}^s \sigma_{ij} + \\ &+ \frac{1}{2} \varepsilon_0 \chi_{ij}^e E_i E_j + \frac{1}{2} \mu_0 \chi_{ij}^m H_i H_j + s_{ijkl} \sigma_{ij} \sigma_{kl} + \alpha_{ij} E_i H_j + d_{ijk} E_i \sigma_{jk} + q_{ijk} H_i \sigma_{jk} + \\ &+ \frac{1}{2} \beta_{ijk} E_i H_j H_k + \frac{1}{2} \gamma_{ijk} H_i E_j E_k + \frac{1}{6} \delta_{ijk} E_i E_j E_k + \frac{1}{6} \eta_{ijk} H_i H_j H_k + \dots \end{aligned} \quad (2.2)$$

$$P_k(\mathbf{H}; T) = -\left. \frac{\partial F}{\partial E_k} \right|_{E=0} = P_k^s + \alpha_{ki} H_i + \frac{1}{2} \beta_{kij} H_i H_j + d_{ijk} \sigma_{jk} + \dots \quad (2.3)$$

$$M_k(\mathbf{E}; T) = -\left. \frac{\partial F}{\partial H_k} \right|_{H=0} = M_k^s + \alpha_{ik} E_i + \frac{1}{2} \gamma_{kij} E_i E_j + q_{ijk} \sigma_{jk} + \dots \quad (2.4)$$

$$\alpha_{ij}^2 < \chi_{ii}^e \chi_{jj}^m \quad (2.5)$$

$$t = \frac{r_A + r_X}{\sqrt{2}(r_M + r_X)} \quad (2.6)$$

$$\hat{H}\Psi(\{\mathbf{R}\}, \{\mathbf{r}\}) = E\Psi(\{\mathbf{R}\}, \{\mathbf{r}\}) \quad (3.1)$$

$$\hat{H}_{el} = \hat{T}_e(\{\mathbf{r}\}) + \hat{U}_{en}(\{\mathbf{R}\}, \{\mathbf{r}\}) + \hat{V}_{ee}(\{\mathbf{r}\}) + \hat{V}_{nn} \quad (3.2)$$

$$\hat{H}_{KS}^\sigma(\mathbf{r}) = -\frac{1}{2} \nabla^2 + V_{KS}^\sigma(\mathbf{r}) \quad (3.3)$$

$$\hat{H}_{KS}^\sigma \psi_i^\sigma(\mathbf{r}) = \varepsilon_i^\sigma \psi_i^\sigma(\mathbf{r}) \Leftrightarrow \left(-\frac{1}{2} \nabla^2 + V_{ext}(\mathbf{r}) + \int \frac{\rho(\mathbf{r}')}{|\mathbf{r}' - \mathbf{r}|} d^3 \mathbf{r}' + V_{exc}^\sigma([\rho^\uparrow, \rho^\downarrow]; \mathbf{r}) \right) \psi_i^\sigma(\mathbf{r}) = \varepsilon_i^\sigma \psi_i^\sigma(\mathbf{r}) \quad (3.4)$$

$$\rho^\sigma(\mathbf{r}) = \sum_\sigma \rho(\mathbf{r}, \sigma) = \sum_\sigma \sum_{i=1}^{N_i^\sigma} \left| \psi_i^\sigma(\mathbf{r}) \right|^2 \Rightarrow \sum_{i=1}^{N_i^\sigma} f_i^\sigma \left| \psi_i^\sigma(\mathbf{r}) \right|^2, \quad (3.5)$$

$$E_{KS}^\sigma = \sum_\sigma \sum_i \left\langle \psi_i^\sigma \left| -\frac{1}{2} \nabla^2 \right| \psi_i^\sigma \right\rangle + \int V_{ext}(\mathbf{r}) \rho(\mathbf{r}) d^3 \mathbf{r} + E_H[\rho] + E_{xc}^\sigma[\rho^\uparrow, \rho^\downarrow] + E_{nn} \quad (3.6)$$

$$E_{xc}^{LDA}[\rho] = \int \rho(\mathbf{r}) \varepsilon_{XC}^{HEG}(\rho(\mathbf{r})) d^3 \mathbf{r} \quad (3.7)$$

$$E_{xc}^{LSDA} \left[\rho^{\uparrow}, \rho^{\downarrow} \right] = \int \rho(\mathbf{r}) \epsilon_{xc}(\rho^{\uparrow}(\mathbf{r}), \rho^{\downarrow}(\mathbf{r})) d^3\mathbf{r}. \quad (3.8)$$

$$E_{xc}^{GGA} \left[\rho^{\uparrow}, \rho^{\downarrow} \right] = \int \rho(\mathbf{r}) \epsilon_{xc}^{GGA}(\rho^{\uparrow}(\mathbf{r}), \rho^{\downarrow}(\mathbf{r}), |\nabla \rho^{\uparrow}|, |\nabla \rho^{\downarrow}|) d^3\mathbf{r}. \quad (3.9)$$

$$E^{LDA+U} = E^{LDA} - UN(N-1)/2 + U \sum_{i \neq j} n_i n_j / 2. \quad (3.10)$$

$$E^{LDA+U} \left[\rho^{\sigma}(\mathbf{r}), \{n^{\sigma}\} \right] = E^{LSDA} \left[\rho^{\sigma}(\mathbf{r}) \right] + E^{ee} \left[\{n^{\sigma}\} \right] - E^{dc} \left[\{n^{\sigma}\} \right] \quad (3.11)$$

$$E^{dc,FLL} = U \frac{1}{2} N(N-1) - J \sum_{\sigma} \frac{1}{2} N^{\sigma}(N^{\sigma}-1) = \frac{1}{2} UN(N-1) - \frac{1}{2} J \left[N^{\uparrow}(N^{\uparrow}-1) + N^{\downarrow}(N^{\downarrow}-1) \right] \quad (3.12)$$

$$\hat{H}^{DC} = c \mathbf{a} \cdot \hat{\mathbf{p}} + bmc^2 + \hat{U}_{en} + \hat{V}_{ee} + \hat{V}_{nn} \quad (3.13)$$

$$\hat{H}^{Pauli} = \frac{\hat{p}^2}{2} + V(r) - \frac{\hat{p}^4}{8c^2} + \frac{1}{2c^2} \frac{1}{r} \frac{\partial V}{\partial r} (\mathbf{S} \cdot \mathbf{L}) - \frac{1}{8c^2} \nabla^2 V \quad (3.14)$$

$$\hat{H}^{SOC} = \frac{1}{2c^2} \frac{1}{r} \frac{\partial V}{\partial r} (\mathbf{S} \cdot \mathbf{L}) \quad (3.15)$$

$$\begin{aligned} \rho^{\alpha\beta}(\mathbf{r}) &= \frac{1}{2} (\rho_{11} + \rho_{22}) I_2 + \frac{1}{2} (\rho_{11} - \rho_{22}) \sigma_3 + \frac{1}{2} (\rho_{12} + \rho_{21}) \sigma_1 + i \frac{1}{2} (\rho_{12} - \rho_{21}) \sigma_2 \\ &= \frac{1}{2} Tr \left[\rho^{\alpha\beta} \right] I_2 + \frac{1}{2} Tr \left[\rho^{\alpha\beta} \mathbf{s}^{\alpha\beta} \right] \cdot \mathbf{s}^{\alpha\beta}. \end{aligned} \quad (3.16)$$

$$\rho^{\alpha\beta}(\mathbf{r}) = \sum_{i=1}^{N_e^{\alpha\beta}} f_i \psi_i^{\alpha*}(\mathbf{r}) \psi_i^{\beta}(\mathbf{r}) \quad (3.17)$$

$$\hat{H}_{KS}^{\alpha\beta}(\mathbf{r}) = -\frac{1}{2} \nabla^2 + V_{KS}^{\alpha\beta}(\mathbf{r}). \quad (3.18)$$

$$E_{KS}^{\alpha\beta} = \sum_{\alpha} \sum_{i} \left\langle \psi_i^{\alpha} \left| -\frac{1}{2} \nabla^2 \right| \psi_i^{\alpha} \right\rangle + \int V_{ext}^{\alpha\beta}(\mathbf{r}) \sum_{\alpha\beta} \rho^{\alpha\beta}(\mathbf{r}) d^3\mathbf{r} + E_H \left[\rho_{Tr} + \rho_Z \right] + E_{xc}^{\alpha\beta} \left[\rho^{\alpha\beta} \right] \quad (3.19)$$

$$\mathbf{P} = \frac{1}{\Omega} \int_{\Omega} \mathbf{r} \rho(\mathbf{r}) d^3\mathbf{r} \quad (3.20)$$

$$\mathbf{P}(\mathbf{r}, t) = \int \mathbf{j}(\mathbf{r}, t) dt \quad (3.21)$$

$$\Delta \mathbf{P} = \int dt \frac{1}{\Omega} \int_{\Omega} \mathbf{j}(\mathbf{r}, t) d^3\mathbf{r} \quad (3.22)$$

$$\Delta \mathbf{P} = \int_0^1 \frac{d\mathbf{P}}{d\lambda} d\lambda \quad (3.23)$$

$$\mathbf{P}^{Formal} = \frac{e}{V} \sum_k Z_k^N \mathbf{u}_k \quad (3.24)$$

$$Z_{k,\alpha\beta}^* = \frac{V}{e} \frac{(\Delta P)_{k,\beta}}{\Delta u_{k,\alpha}} \quad (3.25)$$

$$\sum_k Z_{k,\alpha\beta}^* = 0 \quad (3.26)$$

$$P_{s,\beta} = (\Delta P)_\beta = \frac{e}{V} \sum_{k,\alpha} Z_{k,\alpha\beta}^* (\Delta u_{k,\alpha}) \quad (3.27)$$

$$Z_{k,\alpha\beta}^* = \frac{n_1 \cdot Z_{Paraelectric}^* + n_2 \cdot Z_{Ferroelectric}^*}{n_1 + n_2} \quad (3.28)$$

$$Z_k^* = \begin{pmatrix} Z_{xx}^* & Z_{xy}^* & Z_{xz}^* \\ Z_{yx}^* & Z_{yy}^* & Z_{yz}^* \\ Z_{zx}^* & Z_{zy}^* & Z_{zz}^* \end{pmatrix}. \quad (3.29)$$

$$P_s = (P_{s,x}, P_{s,y}, P_{s,z}) \quad (3.30)$$

$$P_{s,\varsigma} = \frac{e}{V} \sum_{k,\alpha} Z_{k,\alpha\varsigma}^* (\Delta u_{k,\alpha}) \quad (3.31)$$

LIST OF ABREVIATIONS

BFO	bismuth ferrite oxide BiFeO_3
BFCO	bismuth ferrite chromate oxide $\text{Bi}_2\text{FeCrO}_6$
CB	conduction band
DFT	density functional theory
DOS	density of states
FeRAM	ferroelectric random access memories
FiMHS	ferrimagnetic phase with Fe^{3+} in high spin configuration
FiMLS	ferrimagnetic phase with Fe^{3+} in low spin configuration
FMHS	ferromagnetic phase with Fe^{3+} in high spin configuration
FMLS	ferromagnetic phase with Fe^{3+} in low spin configuration
FOJT	first order Jahn-Teller distortion
GGA	gradient generalized approximation
HOMO	highest occupied molecular orbital
HS	high spin configuration
LAPW	linearized augmented plane wave
LDA	local density approximation
LDA+U	local density approximation with Hubbard-U correction
LS	low spin configuration
LSDA	local spin density approximation
LSDA+U	local spin density approximation with Hubbard-U correction
LUMO	lowest unoccupied molecular orbital
JT	Jahn-Teller distortion
MAE	magneto-crystalline anisotropy energy
ME	magnetoelectric effect

MRAM	magnetic random access memories
MERAM	magneto-electric random access memories
PAW	projector augmented plane wave
PBE	Perdew-Burke-Ernzerhof functional
PBEsol	optimized PBE method for solids
PBEsol+U	optimized PBE method for solids with Hubbard-U correction
PLD	pulsed laser deposition
R3	rhombohedral symmetry
RevPBE	revised PBE functional for transition metals
RevPBE+U	revised PBE functional for transitions metals with Hubbard-U correction
S	spin quantization axis (SAXIS in VASP manual)
SOC	spin orbit coupling
SOJT	second order Jahn-Teller distortion
VASP	Vienna Ab-initio Simulation Package for atomic scale materials modeling
VESTA	a 3D visualization software for structural models and volumetric data
VB	valence band

LIST OF VARIABLES AND CONSTANTS

a_c	lattice constant for ideal cubic structure
a_r	lattice constant for rhombohedral structure
α_c	lattice angle for ideal cubic structure
α_r	lattice angle for rhombohedral structure
$\Delta u_{k,\alpha}$	rigid displacement of the sublattice of the atom k in the direction α
E	energy (eigenvalue of the Schrödinger equation)
\mathbf{E}	electric field
E_F	Fermi energy
E_H	classical Coulomb interaction energy between electrons
E_{KS}	Kohn-Sham energy functional
E_{nn}	interaction energy between the nuclei
E_{XC}^σ	exchange-correlation energy corresponding to the nonrelativistic Schrödinger Eq.
$E_{XC}^{\alpha\beta}$	exchange-correlation energy corresponding to the relativistic Schrödinger Eq.
E_{xc}^{LSDA}	exchange-correlation energy in the local spin density approximation (LSDA)
ε	strain
ε_{xc}	energy per electron depending only upon densities in some neighbourhood
eZ_k^N	the nominal ionic charge of the ion k
\mathbf{H}	magnetic field
\hat{H}	nonrelativistic Hamiltonian
\hat{H}_{KS}^σ	Kohn-Sham Hamiltonian corresponding to the nonrelativistic Schrödinger Eq.

$\hat{H}_{KS}^{\alpha\beta}$	Kohn-Sham Hamiltonian corresponding to the relativistic Schrödinger Eq.
\hat{H}^{DC}	Dirac-Coulomb Hamiltonian
\hat{H}^{Pauli}	Pauli Hamiltonian
\hat{H}^{SOC}	spin orbit coupling Hamiltonian
L	the angular momentum operator
J	exchange parameter
M	magnetization
μL_{Cr}	the orbital moment of Cr
μL_{Fe}	the orbital moment of Fe
μM_{BFCO}	the local magnetic moment of BFCO unit cell
μM_{Cr}	the local magnetic moment of Cr
μM_{Fe}	the local magnetic moment of Fe
N_e	number of electrons interacting with one another
P	polarization
P^{Formal}	formal polarization (uses to nominal ionic charge of the ion)
P_s	spontaneous polarization
ΔP	difference in polarization between two different states of the same solid
\hat{p}	momentum operator
Ψ	wave function (eigenfunction of the Schrödinger equation)
Ψ^{DC}	wave function corresponding to the relativistic Hamiltonian
r_A	radius of A-site cation
r_M	radius of M-site cation
r_X	radius of X anion
$\{r\}$	set of all the electronic coordinates

$\{R\}$	set of all the nuclear coordinates
ρ^σ	density for collinear magnetism
$\rho^{\alpha\beta}$	density matrix for noncollinear magnetism
$\rho^\dagger(\mathbf{r}), \rho^\downarrow(\mathbf{r})$	electron spin for up and down z-components of the spin
\mathbf{s}	the spin operator
σ	stress tensor
σ	spin of the electron
σ_i	Pauli spin matrices
t	tolerance factor (Goldschmidt)
T	temperature
\hat{T}_e	nonrelativistic kinetic energy operator of the electrons
U	Coulomb repulsion parameter
\mathbf{u}_k	the position of the ion k
\hat{U}_{en}	potential energy operator due to the interaction of the electrons with the nuclei
V	volume of the unit cell
\hat{V}_{ee}	nonrelativistic electron-electron Coulomb repulsion
V_{ext}	external potential
V_{KS}^σ	Kohn-Sham effective local potential
\hat{V}_{nn}	energy associated with the nuclei interaction
\mathbf{Z}^*	Born effective charge tensor
$Z_{k,\alpha\beta}^*$	dynamical charge of an atom k (or Born effective charge)

CHAPTER 1

INTRODUCTION

The existence of a permanent magnetization in a magnet is well known and experienced by everybody, as is the fact that the direction of magnetization can be altered or switched by a magnetic field in *ferromagnetic* materials. This switching of the magnetization \mathbf{M} by a magnetic field \mathbf{H} has been used for a long time for data storage (e.g., on computer disk drives). The existence of a dielectric polarization induced by an electric field is also well known, as is the fact that such a polarization can be induced in piezoelectric materials by a uniaxial stress. Less known is the existence of a permanent dielectric polarization in pyroelectric materials, which can be altered and even reversed by an electric field in *ferroelectric* materials, in a way similar to what is done with magnetization in ferromagnetic materials. Ferroelectric materials in which the spontaneous electrical polarization \mathbf{P} can be switched by the application of an electric field \mathbf{E} are already used to design ferroelectric random access memories (FeRAM) (Eerenstein et al., 2006; Scott, 2007; Bea et al., 2008), and their piezoelectric properties are largely used in the sensors industry.

Multiferroics or multiferroic materials exhibit **both** ferroelectric and magnetic properties, hence the coexistence of the two ferroic orders (ferroelectric and ferromagnetic, extended in practice to antiferroelectric and antiferromagnetic). Multiferroics have drawn an increasing interest, in part because of the possibility of a coupling between magnetic and electric properties (Figure 1.1).

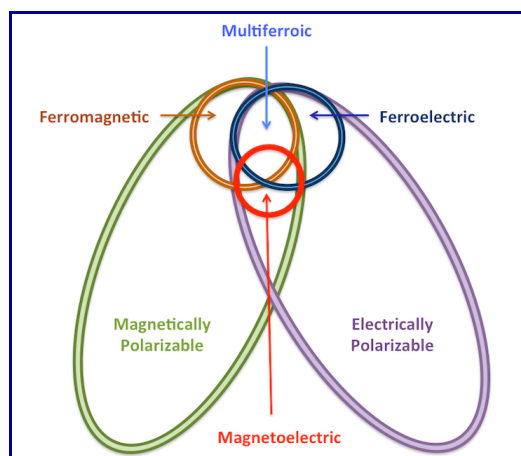


Figure 1.1 The relationship between multiferroic and magnetoelectric materials. Adapted from Ref. (Martin & Ramesh, 2012)

This magnetoelectric coupling between magnetism and ferroelectricity opens the way to control the polarization with a magnetic field or the magnetization with an electric field. This **magnetoelectric coupling**, present between ferroelectric and magnetic materials, could actually also exist between piezoelectric/electrostrictive and piezomagnetic/magnetostrictive materials, mediated by the elastic properties at their interfaces. Many applications of multiferroic and magnetoelectric materials have been proposed, from multi-state memories (Guterman & Fong, 2001) in the absence of coupling between ferroelectric and ferromagnetic materials (Spaldin & Fiebig, 2005 ; Spaldin et al., 2008) to sensitive room temperature magnetic sensors (Nan et al., 2008), tunable microwave devices (Lou et al., 2008) and many potential spintronic devices (Bea 2008) for strong magnetoelectric couplings. In particular, the magnetoelectric coupling offers interesting perspectives for the design of ferroelectric memories with a non-destructive magnetic reading (the cycling of the ferroelectric hysteresis during each reading of the memory state producing fatigue and eventually loss of the stored data being the main challenge of ferroelectric memories), as well as for magnetic random access memories (MRAM) with an electrical writing procedure (MERAM) (Bibes & Barthelemy, 2008).

However, single phase multiferroics are scarce (Ramesh & Spaldin, 2007) presumably due to the chemical and physical incompatibility between the conventional mechanism for cation off-centering present in many ferroelectrics (requiring formally empty *d* orbitals), and the formation of magnetic moment (usually resulting from partially filled *d* orbitals).

The double perovskite structure $\text{Bi}_2\text{MM}'\text{O}_6$, where the transition metal ions M and M' have partially filled e_g -orbitals, and empty e_g -orbitals, respectively, were identified as a potential candidates that may provide a unique opportunity to promote multiferroic behaviours, such as $\text{Bi}_2\text{FeCrO}_6$ (Baettig & Spaldin, 2005a; Baettig et al., 2005b; Ederer & Spaldin, 2005a, 2005b), $\text{Bi}_2\text{NiMnO}_6$ (Iliev et al., 2008), $\text{Bi}_2\text{FeMnO}_6$ (Miao et al., 2011).

For $\text{Bi}_2\text{FeCrO}_6$ (see Figure 1.2b-d), first principle calculations using local-spin-density approximation (LSDA) functional, with and without correction of the Coulomb repulsion U, have highlighted that the multiferroic properties of $\text{Bi}_2\text{FeCrO}_6$ (BFCO) could be superior to those of every known multiferroic materials, such as BiFeO_3 (see Figure 1.2a), BiCrO_3 , and PbTiO_3 (Baettig & Spaldin, 2005a; Baettig et al., 2005b). The calculated ground state has a rhombohedral symmetry and space group *R*3, with oppositely oriented magnetic moments of the Fe^{3+} and Cr^{3+} ions that gives a net magnetic ordering of $2\mu_B$ per formula unit, and a ferroelectric polarization of $79.6 \mu\text{C}/\text{cm}^2$. For comparison, BiFeO_3 thin films have weak

magnetization $\sim 0.1 \mu_B$ due to canting of the oppositely oriented magnetic moments of Fe^{3+} , and a wide range of reported ferroelectric polarizations: $2.2 \mu\text{C}/\text{cm}^2$ (Palkar et al., 2002); $\sim 6 \mu\text{C}/\text{cm}^2$ (Wang et al., 2003; Teague et al., 1970) or theoretical $84\text{-}87 \mu\text{C}/\text{cm}^2$ (Neaton et al., 2005) for rhombohedral $R3c$ phase; and $50\text{-}60 \mu\text{C}/\text{cm}^2$ (Wang et al., 2003) or giant polarization $143.5 \mu\text{C}/\text{cm}^2$ (Ricinschi et al., 2006) for tetragonal $P4mm$ phase.

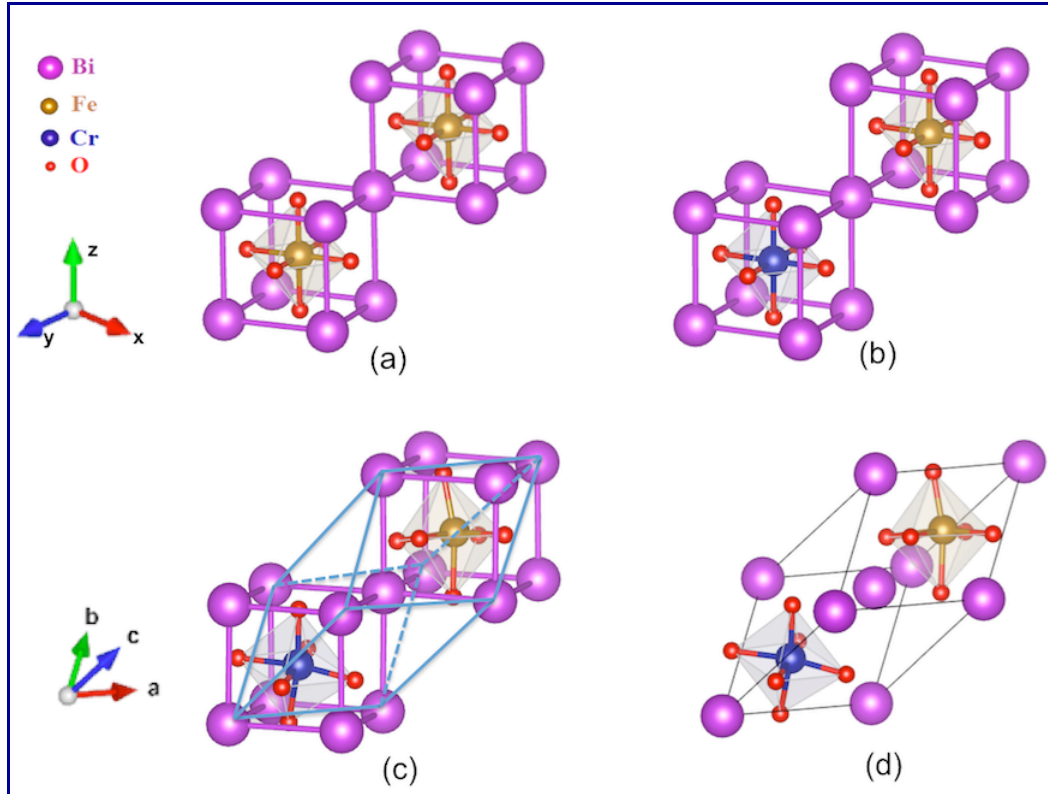


Figure 1.2 The ideal cubic structure of $(\text{BiFeO}_3)_2$ single perovskite (a); Ideal cubic structure of $\text{Bi}_2\text{FeCrO}_6$ double perovskite (b); The rhombohedral structure with $R3$ symmetry (c-d) of $\text{Bi}_2\text{FeCrO}_6$. Visualizations are performed with VESTA (Momma & Izumi, 2011).

The superior properties of BFCO were also confirmed theoretically using the generalized gradient approximation functional GGA+U by Ju and Guo (Ju & Guo, 2008), and a colossal nonlinear optical magnetoelectric effect in multiferroic BFCO was also revealed.

Due to the strong interest on BFCO as potential multifunctional material for many attractive applications, its properties were recently reinvestigated (Goffinet et al., 2012) using different theoretical schemes: LSDA, different LSDA+U variants, and the hybrid functional B1-WC (Bilc et al., 2008). Within all used functionals, the authors highlighted the existence of four different stable states: (i) the ferrimagnetic states with Fe^{3+} in a high spin configuration (FiMHS), and with

Fe^{3+} in a low spin configuration (FiMLS); and (ii) the corresponding ferromagnetic states for high spin (FMHS) and low spin (FMLS) configurations. Investigations on the relative stability of these four states showed that all functionals consistently predict the ground state to be FiMHS, and a spin crossover from the FiMHS to FiMLS was found under compressive pressure.

For some time, BFCO remained a novel multiferroic material with an estimated magnetic Curie temperature lower than 100K that was postulated theoretically, but didn't exist but as theoretical computations. Epitaxial thin films were successfully synthesized for the first time by Pulsed Laser Deposition (PLD) technique at INRS-EMT (Nechache et al., 2006). The BFCO thin films exhibited good ferroelectric, piezoelectric and magnetic properties at room temperature, therefore exceeding the prediction. However, single phase epitaxial multiferroic BFCO films were extremely challenging to get, and were obtained only for a very narrow window of deposition pressure (PO_2) and substrate temperature (T_s) (Nechache et al., 2009).

The recent developments in the growth and characterization of BFCO epitaxial thin films (Nechache et al., 2012) have shown that the epitaxial films were epitaxially constrained and exhibited a thickness variation of the multiferroic properties, which have been attributed to the thickness dependence of the Fe/Cr cationic order, itself related to bond distances and angles resulting from the epitaxial strains induced by the SrTiO_3 substrates used. Further studies are necessary to understand the details of the mechanisms leading to the Fe/Cr cation ordering as well as to explain the origin of the critical thickness after which the magnetic properties strongly decrease.

First-principles simulations can help acquiring some theoretical understanding by describing the properties of materials at the atomic-scale level through the fundamental laws of quantum mechanics and electromagnetism. Density functional theory (DFT) is nowadays the most widely used first-principles method, offering the opportunity to simulate various possible atomic configurations and obtain valuable information about the microscopic origin of the material properties.

For accurate calculations, some developments in first-principles-based methods, such as a fully noncollinear treatment of the spinor wave-functions and inclusion of the spin-orbit coupling (SOC), are essential for describing many of the interesting properties of multiferroic materials (Ederer & Spaldin, 2005a, 2005b). The merit of such an approach is demonstrated in the new and interesting results of the investigations presented in this thesis.

In this regard, the effect of the spin-orbit coupling on the BFCO properties is analyzed using noncollinear spin structures (Hobbs et al., 2000), which had not yet been done for this material. To provide new insights into the subtle interplay among electron correlation, lattice distortions, oxygen-octahedron rotations/tilting and SOC, as well as their effects on the multiferroic properties, comparative studies are performed for both collinear and noncollinear spin structures.

The thesis manuscript is organized as follows: After the present introduction (Chapter 1), we review in Chapter 2 the magnetoelectric effect and magnetoelectric coupling, the perovskite structure, the first and second order Jahn-Teller distortions, as well as the oxygen-octahedron tilting/rotations. Then, details of the methodological aspects of first-principles electronic structure calculations are presented in Chapter 3, in which we briefly present strong correlated systems, DFT for spin-polarized systems, exchange-correlation for strongly correlated materials, noncollinear magnetism and polarization. Chapter 4 presents a discussion of the structural, electronic, magnetic and ferroelectric properties of the rhombohedral *R*3 symmetry of BFCO for collinear spin structures corresponding to the: (i) ferrimagnetic phases with Fe³⁺- high spin (FiMHS), and Fe³⁺- low spin configurations (FiMLS); and (ii) ferromagnetic phases for Fe³⁺ high spin (FMHS) and low spin (FMLS) configurations. Chapter 5 is devoted to an extended discussion on the noncollinear spin structures when spin-orbit coupling (SOC) is included as well as their effects on the multiferroic properties of the rhombohedral BFCO. Finally, in Chapter 6 conclusions are drawn & future perspectives suggested.

CHAPTER 2

MAGNETOELECTRIC EFFECT AND MULTIFERROICS

2.1. Magnetoelectric effect and magnetoelectric coupling

The magnetoelectric effect (*ME*) is characterized by the appearance of an induced electric polarization \mathbf{P} under the application of a magnetic field \mathbf{H} (ME_H), or by the appearance of an induced magnetization \mathbf{M} under the application of an electric field \mathbf{E} (ME_E). The *ME* effect was first pointed out by Pierre Curie (Curie, 1894) and later by Landau and Lifshitz (Landau & Lifshitz, 1958), but higher order magnetoelectric effects (quadratic terms) were introduced by Schmid (Schmid, 1973; Schmid, 2008). The free energy

$$F = F(\mathbf{E}, \mathbf{H}, \sigma; T), \quad (2.1)$$

which is a function of the electric field \mathbf{E} , the magnetic field \mathbf{H} , the mechanical stress tensor σ and the temperature T , can be developed as a limited series as a function of E_i , H_i and σ_{ij}

$$\begin{aligned} -F(\mathbf{E}, \mathbf{H}, \sigma; T) = & P_i^s E_i + M_i^s H_i + \varepsilon_{ij}^s \sigma_{ij} + \\ & + \frac{1}{2} \varepsilon_0 \chi_{ij}^e E_i E_j + \frac{1}{2} \mu_0 \chi_{ij}^m H_i H_j + s_{ijkl} \sigma_{ij} \sigma_{kl} + \alpha_{ij} E_i H_j + d_{ijk} E_i \sigma_{jk} + q_{ijk} H_i \sigma_{jk} + \\ & + \frac{1}{2} \beta_{ijk} E_i H_j H_k + \frac{1}{2} \gamma_{ijk} H_i E_j E_k + \frac{1}{6} \delta_{ijk} E_i E_j E_k + \frac{1}{6} \eta_{ijk} H_i H_j H_k + \dots \end{aligned} \quad (2.2)$$

where Einstein summation convention was used (i.e., sum over repeated indices representing the Cartesian components).

The coefficients in the first line of (2.2) represent the 1st order invariants with P_i^s , M_i^s , ε_{ij}^s standing for spontaneous polarization, spontaneous magnetization, and spontaneous strain, respectively. In the second line of (2.2) the coefficients are the 2nd order invariants, where the first three terms represent the susceptibility terms: χ_{ij}^e , χ_{ij}^m are the electric and magnetic susceptibilities (ε_0 is electric permittivity and μ_0 is magnetic permeability in vacuum), and s_{ijkl} represents the elastic compliance, respectively. The last three 2nd order invariants are the coefficients of the linear magnetoelectric, piezoelectric, and piezomagnetic effects, respectively. The tensor α_{ij} corresponds to the induction of polarization by a magnetic field or of

magnetization by an electric field, which is designated as the *linear ME effect* (see Figure 2.1). In the third line of (2.2), the coefficients are the 3rd order invariants belonging to the tertiary ferroics, where β_{ijk} and γ_{ijk} are tensors corresponding to the *higher order ME effects* (Schmid, 2008; Fiebig, 2005), and δ_{ijk} and η_{ijk} are the non-linear electric and magnetic susceptibilities, respectively.

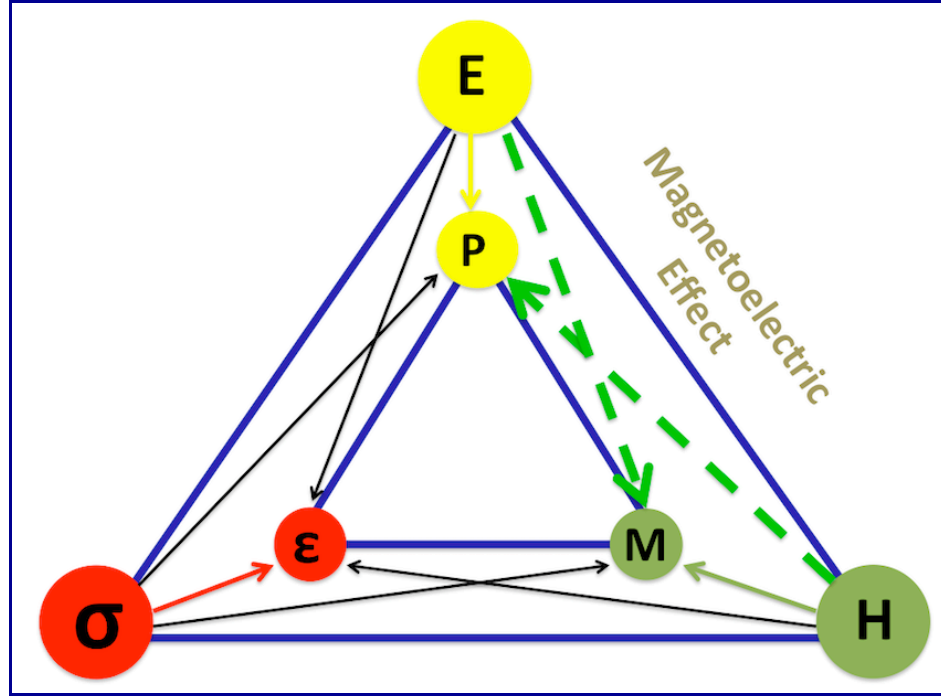


Figure 2.1 Couplings between ferroic properties in multiferroics. **Ferromagnetism** implies the existence of a net magnetization M in absence of a magnetic field H . **Ferroelectricity** implies existence of net polarization P in absence of an electric field E . **Ferroelasticity** implies existence of a net deformation ϵ in absence of a mechanical stress σ . In a multiferroic material, at least two of the primary ferroic properties coexist in the same phase leading additional interactions. In a **magnetoelectric multiferroic**, a magnetic field H induces changes in the polarization P , or the electric field E induces changes in the magnetization M (green dashed arrows). Adapted from Ref. (Spaldin & Fiebig, 2005).

The polarization and magnetization are obtained from (2.2) as follows:

$$P_k(\mathbf{H}; T) = -\left. \frac{\partial F}{\partial E_k} \right|_{E=0} = P_k^s + \alpha_{ki} H_i + \frac{1}{2} \beta_{kij} H_i H_j + d_{ijk} \sigma_{jk} + \dots \quad (2.3)$$

and

$$M_k(\mathbf{E}; T) = -\left. \frac{\partial F}{\partial H_k} \right|_{H=0} = M_k^s + \alpha_{ik} E_i + \frac{1}{2} \gamma_{kij} E_i E_j + q_{ijk} \sigma_{jk} + \dots \quad (2.4)$$

Because the ME response is limited by the relation (Fiebig, 2005)

$$\alpha_{ij}^2 < \chi_{ii}^e \chi_{jj}^m \quad (2.5)$$

the *ME* can be large only in ferroelectric and ferromagnetic materials. It could therefore be particularly large in magnetoelectric multiferroics exhibiting both large electric and magnetic susceptibilities: χ^e and χ^m . Consequently, ferroelectric-ferromagnetic materials, called in this thesis *multiferroics*¹, are prime candidates for displaying sizable *ME* effects.

Multiferroics were grown for the first time in 1958, when magnetically active $3d$ ions were used to substitute ions with a noble gas electron shell in ferroelectrically distorted lattices (Fiebig, 2005), while intense theoretical and experimental works have been reported around 1970s. Thereafter, the interest in magnetoelectrics evolved irregularly due to difficulty to develop useful applications, until a *first renaissance* in 1978 (see Figure 2.2), followed by a decline for almost two decades. The beginning of the new millennium brought revival of magnetoelectrics (*second renaissance*) with the evolution of magnetic read/write sensors and new technological requirements for hard disks with very densely packed information. *Magnetoelectrics* opened up new major research topics and trends, as well as wide prospects for practical applications of magnetic multiferroics in nanoelectronics, microwave electronics and optoelectronics. The extremely high interest in magnetoelectrics is proven by the dramatic increase of the number of publications mentioning “*magnetoelectric*,” as can be seen in Figure 2.2.

¹ We are using in this thesis the strict definition of multiferroics being ferromagnetic-ferroelectrics (which are very often also ferroelastic). A broader definition also includes antiferromagnetic-ferroelectrics, ferromagnetic-antiferroelectrics and antiferromagnetic-antiferroelectrics.

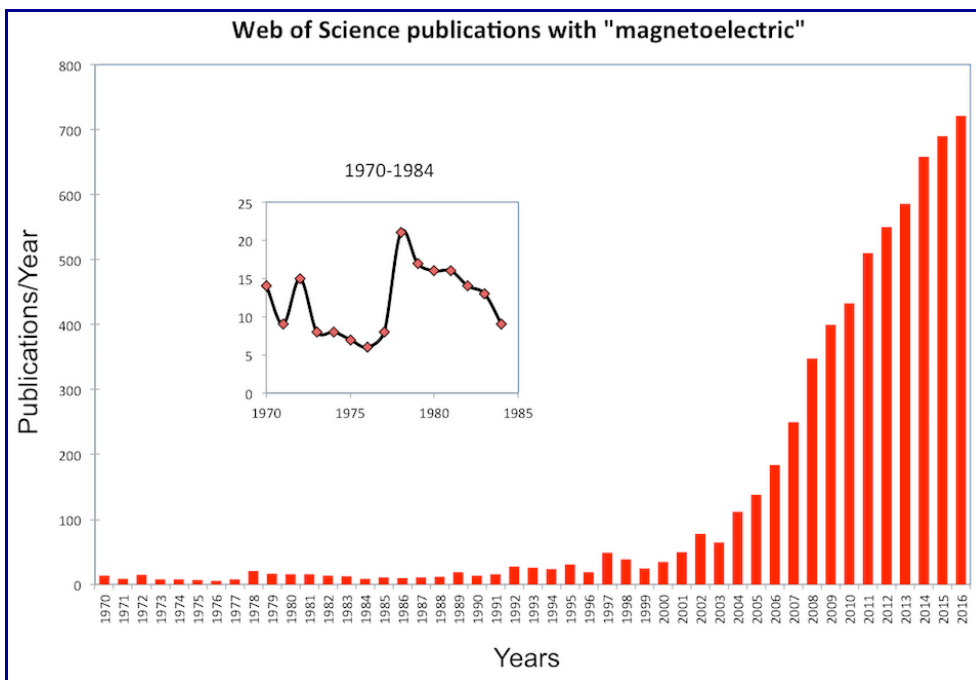


Figure 2.2 Publications per year during the period 1970-2016 with “magnetoelectric” as a keyword according to the Web of Science. (Web of Science, 2017)

While multiferroics have been the topic of many research papers (Fiebig, 2005), they still pose very interesting and rich fundamental physics problems. Creating novel materials and combinations of materials that exhibit good multiferroic and/or magnetoelectric properties at temperatures useful for applications (room temperature and above) is a very active field of research. In addition, multiferroics form a very diverse class of materials where there is no unique “*theory of multiferroics*”, and hence a classification of multiferroics is useful.

2.2 Classification of magnetoelectric multiferroics

According to the Chapter 1 (Figure 1.1), there is a small subgroup of all the magnetically and electrically polarizable materials that are either ferromagnetic or ferroelectric, and still fewer that are simultaneously ferromagnetic and ferroelectric (Martin & Ramesh, 2012). The ultimate goal for device functionality is to have - at room temperature - a single multiferroic phase with a strong coupling between the ferroelectric and ferromagnetic order parameters that enables a simple control of the magnetism via an applied electric field. One reason for the small number of multiferroics is that there are only 13 point groups that allow the presence of multiferroic behavior (Schmid, 1973; Schmid, 2008; Martin *et al.*, 2010). Moreover, the scarcity of magnetoelectric multiferroics also results from a chemical incompatibility between magnetism

and conventional ferroelectricity. This incompatibility is related to the fact that the most common mechanism for ferroelectricity in perovskite-structure oxides requires the presence in the octahedral oxygen cage of a transition metal cation having no electron on the *d*-orbital, i.e. a formal d^0 electron configuration, while magnetism occurs in transition metal oxides with cations having *d* electrons, with incompletely filled $3d$ shells (Ederer & Spaldin, 2005), but also in rare earths (or lanthanides) group $4f$, the platinum group $5d$, or actinides group $5f$. These conditions stimulated interest in designing and identifying new pathways for achieving multiferroic properties in materials, as well as investigating new mechanisms leading to magnetoelectric coupling.

In a first classification, in 2005, four major crystallographic types of multiferroics have been distinguished (Fiebig, 2005):

- *Compounds with perovskite or double perovskite structure* generally have a chemical formula AMX_3 or $A_2MM'X_6$, where M and M' are transition metals, and whose ferroelectric properties have already been the subject to numerous theoretical and experimental studies. The compound of this family that has been most extensively studied is BiFeO_3 , which is ferroelectric and weakly ferromagnetic (Ederer & Spaldin 2005; Baettig et al., 2005). More details about perovskites and double perovskites are presented in the next section, since the rest of the thesis will be dedicated to the first-principles study of the ground state structure and multiferroic properties of the $\text{Bi}_2\text{FeCrO}_6$ double perovskite.
- *Compounds with hexagonal structure*. When the cationic radius of A is sufficiently small in the compounds with general formula AMX_3 or $A_2MM'X_6$, they may crystallize in a hexagonal rather than a typical simple or double perovskite structure. For that reason, they are sometimes referred to as “hexagonal perovskites”. The largest group of hexagonal multiferroics is formed by the ferroelectric antiferromagnetic manganites $RMnO_3$ with R = Sc, Y, In, Ho, Er, Tm, Yb, and Lu.
- *Compounds from the boracites family* have the general formula $M_3B_7O_{13}X$ with M = Cr, Mn, Fe, Co, Cu, Ni as bivalent ion and X = Cl, Br, I. They are ferroelectric, ferroelastic and antiferromagnetic, and sometimes they are accompanied by a weak ferromagnetic moment.
- *BaMF₄ compounds* with M = Mg, Mn, Fe, Co, Ni, Zn have an orthorhombic structure and they are ferroelastic and ferroelectric, and display antiferromagnetic or weak

ferromagnetic ordering.

Another classification of the magnetoelectrics was made in 2007 according to the mechanism of inversion symmetry breaking in ferroelectrics (Cheong & Mostovoy, 2007):

- *Proper magnetoelectric ferroelectrics*, where ferroelectricity is caused by stereochemically active “lone-pair” cations (e.g., Bi^{3+} or Pb^{2+}): BiMnO_3 , BiFeO_3 , $\text{Pb}(\text{Fe}_{2/3}\text{W}_{1/3})\text{O}_3$; or when there exists covalent bonding between $3d^0$ transition metal (Ti) and oxygen, as in BaTiO_3 .
- *Improper magnetoelectric ferroelectrics* that put lower constraints on the coexistence with magnetism (the appearance of the polarization is not a primary effect but rather a secondary effect accompanying the appearance of some other order parameter). Cheong & Mostovoy distinguished three categories: (i) structural transition “geometric ferroelectrics” (K_2SeO_4 , Cs_2CdI_4 , hexagonal YMnO_3 where polarization is not a primary order parameter, but a phase transition is softening tilts of the trigonal bipyramids MnO_5 which leads to a shift of the equilibrium positions thus creating a ferroelectric distortion); (ii) charge ordering “electronic ferroelectrics” (LuFe_2O_4 where centers of Fe^{2+} and Fe^{3+} do not coincide in the unit cell, and hence ferroelectricity is induced by an electron density modulation); and (iii) magnetic ordering “magnetic ferroelectrics” (orthorhombic RMnO_3 , RMn_2O_5 , CoCr_2O_4).

Finally, an elegant classification of multiferroics is described by Khomskii and coworkers (Brink & Khomskii, 2008; Khomskii, 2009):

- *Type I multiferroics* are materials in which ferroelectricity and magnetism have different origins and appear largely independent of one another. Depending on the mechanism of ferroelectricity, several sub-classes of type-I multiferroics are considered: (i) multiferroic perovskites AMX_3 , where the stereochemical activity of an A-site cation with a lone pair (i.e., 6s electrons in Bi^{3+} or Pb^{2+}) is used to induce a structural distortion and ferroelectricity while the magnetism comes from the M-site cation; (ii) materials for which the multiferroic properties are geometrically driven effects, as in the case of YMnO_3 , where the ferroelectricity is caused by tilting of the MnO_5 blocks toward a stable state; (iii) charge-ordering-driven multiferroics, often observed in transition metal compounds, especially those formally containing transition metal ions with different valence, as in the case of TbMn_2O_5 and $\text{Ca}_3\text{CoMnO}_6$.
- *Type II multiferroics* are materials in which ferroelectricity occurs only in the magnetically

ordered state, i.e. ferroelectricity is induced by the structural distortions accompanying the magnetic properties, implying a strong coupling between the two order parameters. The prototypical examples are TbMnO_3 , $\text{Ni}_3\text{V}_2\text{O}_6$, and MnWO_4 , in which ferroelectricity appears in conjunction with a spiraling magnetic phase, whereby a spin rotation (along an axis) breaks the inversion symmetry and produces an electric polarization (Martin *et al.*, 2010).

2.3 Simple and double perovskites: ideal structure, distortions, and octahedra rotations/tilting

2.3.1 The ideal perovskite structure

Some of the best studied multiferroics possess the crystal structure of the perovskite, more precisely a double perovskite structure. This structure type is named after the mineral perovskite, CaTiO_3 , which was the first known compound with this crystal structure with a cubic symmetry belonging to the space group $Pm-3m$ (see Figure 2.3). Its mineral was first discovered in the Ural Mountains by Gustav Rose in 1839, and received the name «perovskite» in tribute to the Russian mineralogist Lev Aleksevich von Perovski (Souza & Muccillo, 2010). Currently, there are thousands of known compounds with this structure.

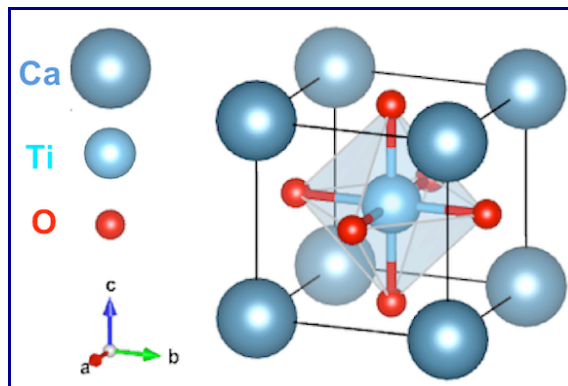


Figure 2.3 The first identified perovskite structure CaTiO_3 : cubic perovskite unit cell visualized using VESTA (Momma & Izumi, 2011).

The ideal perovskite has the chemical formula AMX_3 for simple perovskites, or $A_2MM'X_6$ for double perovskites. The cubic AMX_3 simple perovskite structure can be thought of as: (i) (see Figure 2.4a) a cubic network of large A -site cations (grey) with X anions (red) in the middle of the cube faces, and with the octahedrally coordinated smaller M -site cations (blue) located in the middle of the cube; or equivalently (ii) (see Figure 2.4b) a three-dimensional array of corner

sharing MX_6 octahedra (blue) with the 12-fold coordinated A-site cations (grey) occupying the cubo-octahedral cavity (King & Woodward, 2010) that is formed between any eight such MX_6 units.

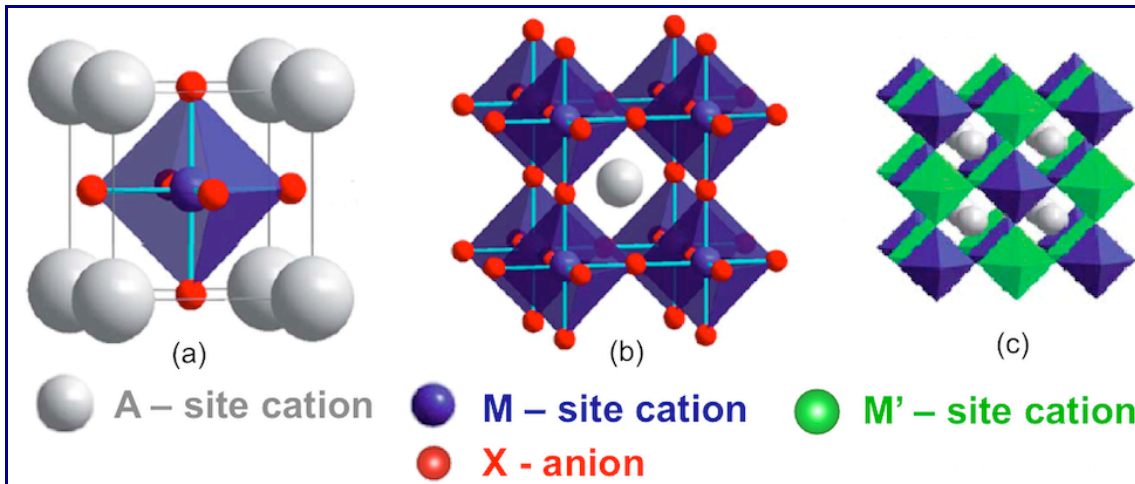


Figure 2.4 The cubic AMX_3 perovskite structure: A cation in the corner of the cube (a); M cation together with octahedra in the corner of the cube (b); M and M' cations ordering following the rock-salt structure in an ideal double perovskite (c). Adapted from Ref. (King & Woodward, 2010).

The doubled perovskites $A_2MM'X_6$ possesses a structure where the M and M' cations are ordered in such a way that the MX_6 and $M'X_6$ octahedra are alternatively arranged in the three space directions, following the well known NaCl rock-salt structure (Figure 2.4c).

Distortions from the aristotype (high-symmetry) structure can significantly impact the physical properties of perovskites: in particular, *structures lacking spatial inversion symmetry are compatible with the presence of ferroelectricity*.

2.3.2 Tolerance factor

If r_A is the radius of the A-site cation of AMX_3 , r_M the radius of the M-site cation, and r_X the radius of the anion, then a measure of the deviation from the ideal cubic perovskite structure, is the *tolerance factor* (Goldschmidt, 1926):

$$t = \frac{r_A + r_X}{\sqrt{2}(r_M + r_X)} . \quad (2.6)$$

Goldschmidt has shown that the ideal cubic perovskite structure occurs when $t \approx 1$. In general, when $t > 1$, the A-site cations are too large to fit in the cubo-octahedral cavities (or alternatively,

the M -site atom is really small and have space to move around within the X octahedra) and the structure develops a small polar distortion as illustrated by the tetragonal polar distortion of BaTiO_3 in Figure 2.5a (Ba is the large cation; the Ti cation displacement was artificially exaggerated for a better view). When $t < 1$, the M -site atom is too large for its octahedral cage, and the X anions move towards an “empty” space, resulting in a rotation of the corner-shared octahedra as illustrated by the case of the opposite rotations of the oxygen octahedra in the diagonally neighboring unit cells of the double perovskite BiFeO_3 in Figure 2.5b (Ederer & Spaldin, 2005).

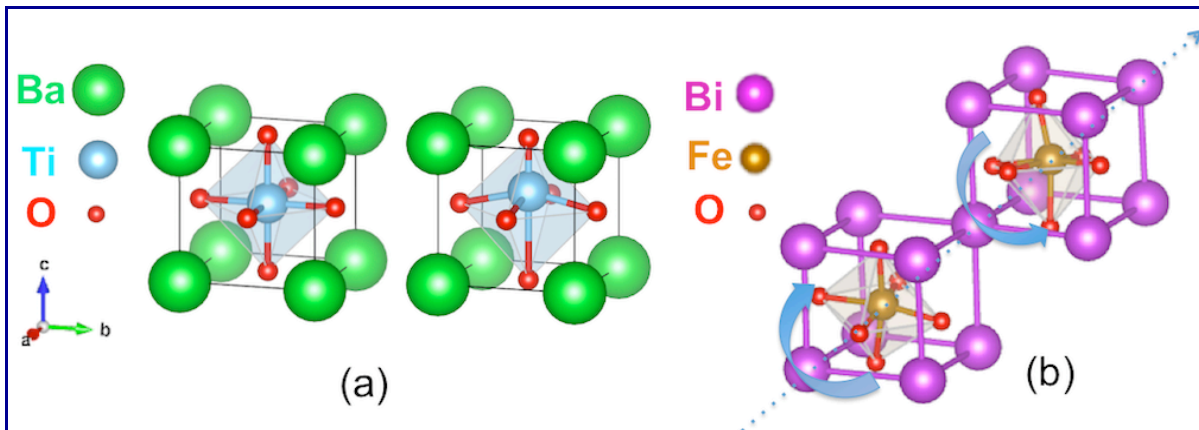


Figure 2.5 Symmetry lowering distortions from the aristotype structure: Non-distorted BaTiO_3 compared with exaggeratedly distorted BaTiO_3 for which $t > 1$ (a); Counter-rotations of oxygen octahedra around [111] (blue curved arrows) in BiFeO_3 , coupled with polar displacements (blue dotted arrow) for which $t < 1$ (b).

Since the tolerance factor depends on which values are taken for ionic radii, which are a matter of definition, it serves only as an estimate. For more rigorous investigations of the distortions that can arise in perovskites, electronic effects together with octahedra tilts and rotations should be studied using first-principle methods.

2.3.3 Octahedra distortions: Jahn-Teller effect

Distortions from the aristotype structure can be attributed to one of three mechanisms (Woodward, 1997): (i) cation displacements within the octahedra (e.g., BaTiO_3 in Figure 2.5a); (ii) distortions of the oxygen octahedra (e.g., LaMnO_3 in Figure 2.6a, KCuF_3 in Figure 2.6b); and (iii) tilting/rotations of the octahedra (e.g., KCuF_3 undergoes octahedra rotation as can be seen in Figure 2.6b, bottom, with unstacked octahedra corresponding to the $I4/mcm$ space-group symmetry; BiFeO_3 undergoes both rotations and tilting, Figure 2.5b).

This section is dedicated to the octahedra distortions explained by the *Jahn-Teller effect*, while tilts and rotations are discussed in the next section.

The Jahn-Teller effect implies the occurrence of a distortion of the ideal octahedral geometry, thus providing an energetic stabilization by removing the electronic degeneracy of the highest occupied molecular orbital (Kanamori, 1960). This is also called the first order Jahn–Teller distortion (FOJT).

For perovskites, a FOJT occurs when a cation has degenerate electronic states (King & Woodward, 2010). For an individual MX_6 octahedron, FOJT is associated with lifting the degeneracy of the d orbital electrons of the M -site cation, i.e. the $M-X$ bonds are contracted/elongated in such way as to remove the degeneracy and stabilize the structure by lowering the total energy. FOJT is most commonly observed when there is an odd number of electrons occupying the e_g orbitals of a transition metal in octahedral coordination: e.g., for LaMnO_3 , the transition metal Mn has $(t_{2g})^3(e_g)^1$ electron configuration and octahedra are distorted due to the distortions of Mn-O bonds (see Figure 2.6a); KCuF_3 has distorted Cu-F bonds due to $(t_{2g})^6(e_g)^3$ electron configuration of Cu (see Figure 2.6b).

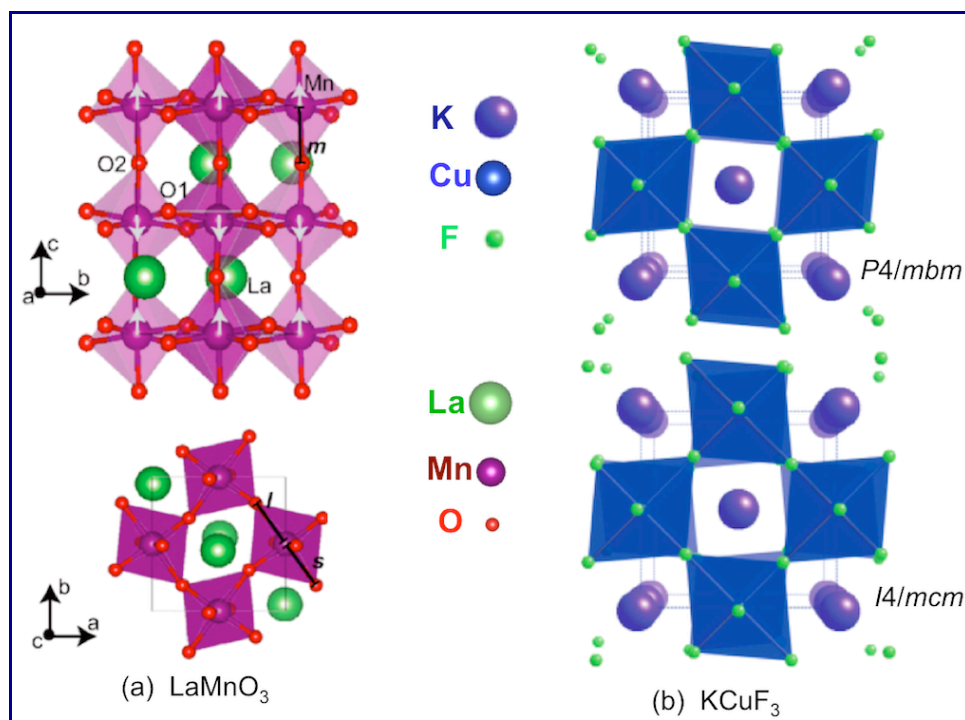


Figure 2.6 FOJT distorted perovskites: Side and top views of the orthorhombic LaMnO_3 in polyhedral representation, where the MnO_6 octahedra are distorted and long (l), medium (m), short (s) Mn-O bonds shown (a) (Rivero et al., 2016); Top views of the KCuF_3 distorted octahedra where planes of octahedra are stacked (top) or unstacked (bottom) one directly above the other (b). Adapted from Refs. (Rivero et al., 2016; Carpenter & Woodward, 2009).

A second order Jahn-Teller distortion (SOJT) can occur when there is a small energy gap between a filled HOMO (highest occupied molecular orbital) and the LUMO (lowest unoccupied molecular orbital); they are commonly observed for highly charged transition metals in octahedral coordination (King & Woodward, 2010). An example is BaTiO₃, shown in Figure 2.5a, where the transition metal Ti⁴⁺ has the $(t_{2g})^0(e_g)^0$ electron configuration. SOJT distortions can also occur when there are lone-pair cations on the A-site, which appears as a horseshoe-shaped electron localization function around the central Bi³⁺ of BiFeO₃ in Figure 2.7d.

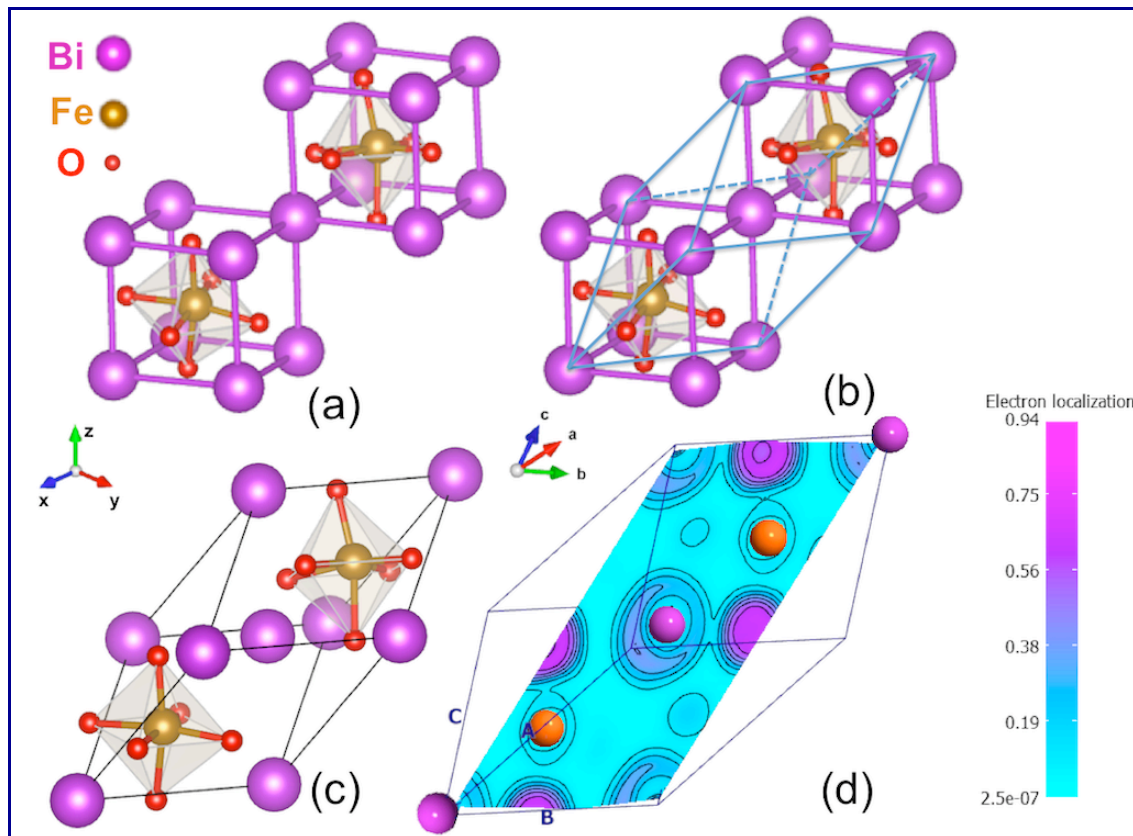


Figure 2.7 SOJT in the rhombohedral R3c symmetry of BiFeO₃: distorted BiFeO₃ seen as rock-salt distorted double perovskite structure (a); Distorted BiFeO₃ seen as rhombohedral unit cell with R3c symmetry (blue full and dashed lines in b) versus rock-salt structure (b, c); Calculated electron localized function of BiFeO₃ rhombohedra showing the characteristic horseshoe-shape electron density induced by the lone-pair for the central Bi³⁺ cation (d).

The 6s² electron orbitals of Bi³⁺ atoms, which are spherically symmetric for isolated ions, distort to form asymmetric rings of localization, which push away the Bi³⁺ neighboring atoms, thus driving structural distortions. This type of distortions were also reported in the case of BiMnO₃ (Seshadri & Hill, 2001), BiCrO₃ (Hill et al., 2002), BiFeO₃ (Neaton et al., 2005) and Bi₂FeCrO₆.

2.3.4 Octahedra tilts and rotations

Tilting of octahedra in perovskites can occur about one or more axes. In the following, for a better visualization of octahedra tilting, the $\text{Bi}_2\text{FeCrO}_6$ (BFCO) double perovskite is used as an example.

The octahedron *tilt* is defined by the $\text{Fe}-\text{O}_{\text{Fe,Cr}}-\text{Cr}$ bond angle containing the $\text{O}_{\text{Fe,Cr}}$ atom belonging to the two adjacent octahedra. We define “out-of-plane” tilts as those occurring between yellow planes (see Figure 2.8b), and “in-plane” tilts as those occurring within the layers of the yellow planes (see Figure 2.8d,e). In the general case, both out-of-plane tilts and in-plane tilts are present, as sketched in Figure 2.8c. The in-plane tilts of both the top and bottom layers of Fig. 2.8c are sketched in Figure 2.8d and 2.8e. If these angles are equal to 180° then octahedra are not tilted, as it can be seen in Figure 2.8a (this is the case of the ideal cubic structure). When these angles are different from 180° , then the octahedra are tilted.

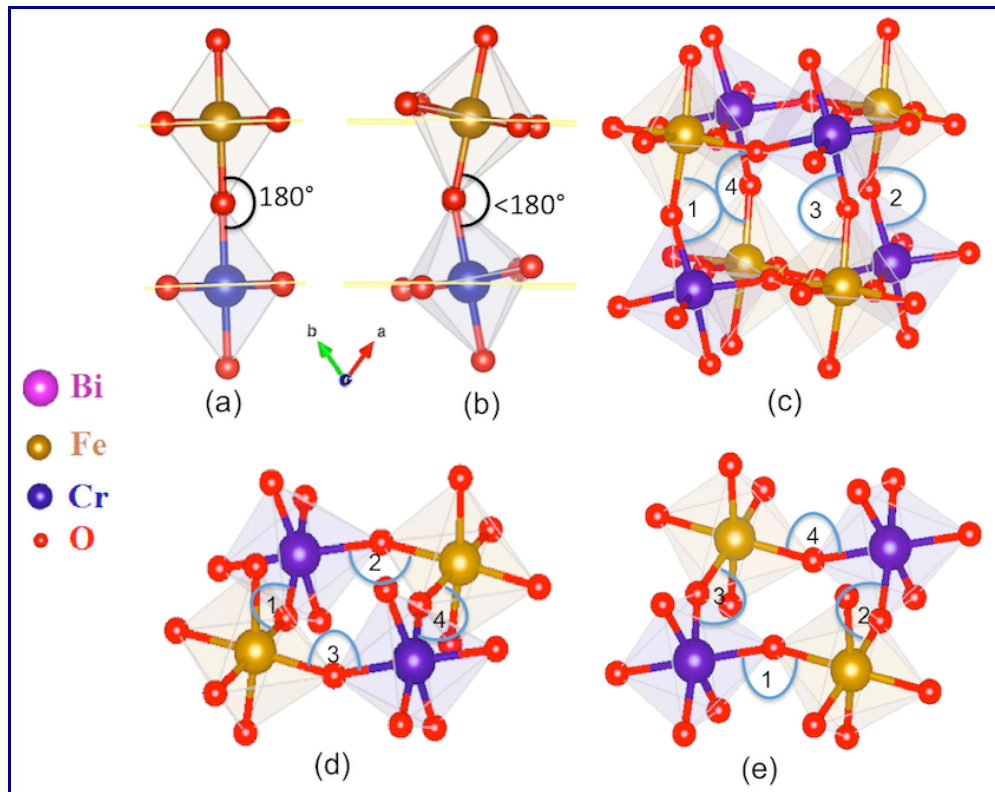


Figure 2.8 Sketch of the tilts illustrated for the BFCO double perovskite. The reference planes are shown in yellow in (a)&(b). Absence of out-of-plane tilt: the $\text{Fe}-\text{O}_{\text{Fe,Cr}}-\text{Cr}$ bond angle is equal to 180° (a); Presence of the out-of-plane tilt: the $\text{Fe}-\text{O}_{\text{Fe,Cr}}-\text{Cr}$ bond angle differs from 180° (b); Out-of-plane tilts in a BFCO supercell where the $\text{Fe}-\text{O}_{\text{Fe,Cr}}-\text{Cr}$ bond angles 1, 2, 3, 4 differ from 180° (c); In-plane tilts of the top layer from (c) with 1, 2, 3, 4 angles having same values as out-of-plane angles, due to lattice symmetry and cell periodicity (d); In-plane tilts of the bottom layer from (c) with the corresponding 1, 2, 3, 4 angles (e); Note that the $\text{Fe}-\text{O}_{\text{Fe,Cr}}-\text{Cr}$ bond is bent in the opposite direction for the top and the bottom layers.

Tilts can occur around all three axes, e.g., the out-of-plane tilt angle $\text{Fe}-\text{O}_{\text{Fe},\text{Cr}}-\text{Cr}$ presented in Figure 2.8b corresponds to the angle (1) from Figure 2.8c. Because of (i) the cubic symmetry (lattice parameters corresponding to the three crystal axes are equal $a=b=c$ and angles $\alpha=\beta=\gamma$) and (ii) the fact that the octahedra are all connected through their corners, the angle (1) also appears in the top and bottom layers as in-plane tilts, as shown in Figures 2.8c and d. The different values of the out-of plane tilt angles 1, 2, 3, 4 are therefore found in both the top- and bottom-layers as the values of in-plane tilts (shown in Fig. 2.8c-d) for the considered BFCO double perovskite.

The octahedron *rotation* is defined using the bond angles determined by the equatorial oxygen O_{Cr} and O_{Fe} (e.g., oxygen atoms in the yellow planes of Fig. 2.8a) and the $\text{O}_{\text{Cr},\text{Fe}}$ atom belonging to the two adjacent CrO_6 and FeO_6 octahedra between two equatorial planes, as it can be seen in the Figure 2.9. It should be noted that Figure 2.9a-c correspond to the Figure 2.8c seen from the top where the network of Bi atoms was included. If these angles are equal to 90° , as in the case of the ideal cubic structure (Fig. 2.9a), then the octahedra are not rotated. When the angles are larger/smaller than 90° then the octahedra are clockwise/counter-clockwise rotated, as it can be seen in the BFCO double perovskite structure of Fig. 2.9b-c.

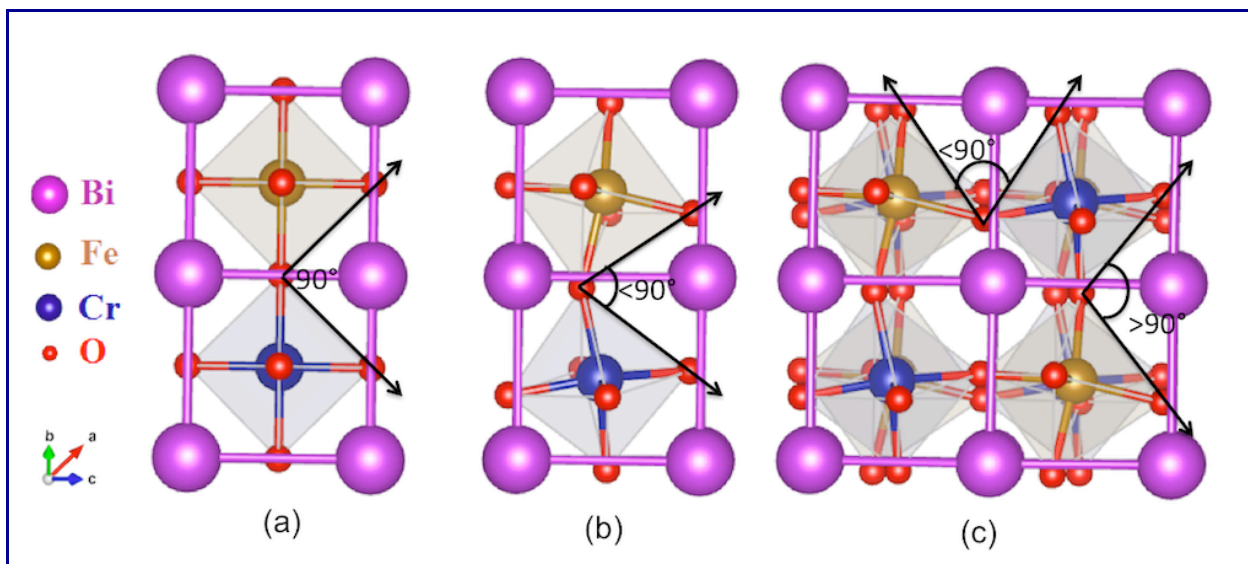


Figure 2.9 Sketch of the octahedra rotations illustrated for the BFCO double perovskite: absence of oxygen-octahedra rotations defined by oxygen $\text{O}_{\text{Fe}}-\text{O}_{\text{Fe},\text{Cr}}-\text{O}_{\text{Cr}}$ bond angle equal to 90° (a); Occurrence of oxygen-octahedra rotation when the oxygen $\text{O}_{\text{Fe}}-\text{O}_{\text{Fe},\text{Cr}}-\text{O}_{\text{Cr}}$ bond angle differs from 90° (b); Various oxygen-octahedra rotations in a BFCO supercell when the oxygen $\text{O}_{\text{Fe}}-\text{O}_{\text{Fe},\text{Cr}}-\text{O}_{\text{Cr}}$ bond angles differ from 90° (c).

Other examples of tilting/rotations can be seen in Figures 2.5 and 2.6. In Figure 2.5b octahedra present both tilts and clockwise/counter-clockwise rotations about [111] (in contrast to Figure 2.4 where there is no octahedra tilting or rotation). In Figure 2.6 are presented two cases: LaMnO₃ with both tilting and rotations, and KCuF₃ which does not undergo any octahedra tilting (only octahedra rotations are present).

A classification of the possible tilt systems in perovskites was introduced by Glazer (Glazer 1972) and was further refined by Woodward (Woodward, 1997). The magnitude of the tilts about the cubic crystallographic directions [100], [010] and [001] are denoted by a , b , and c , respectively. Tilts of equal magnitude are denoted by repeating the appropriate letter, and a superscript added to the letter indicates the tilting of adjacent octahedra along the corresponding axis: no tilt (0), tilts of two adjacent octahedra in phase (+), or in anti-phase (-).

Thus, using Glazer notation, octahedra without tilt, denoted by $a^0a^0a^0$, correspond to the starting perfect aristotype perovskite with cubic symmetry (Figure 2.10a); the tilted system $a^0a^0c^-$ indicates a tetragonal system, having no tilt along the [100] and [010] directions and opposite tilts of adjacent octahedra along the [001] direction (Figure 2.10b).

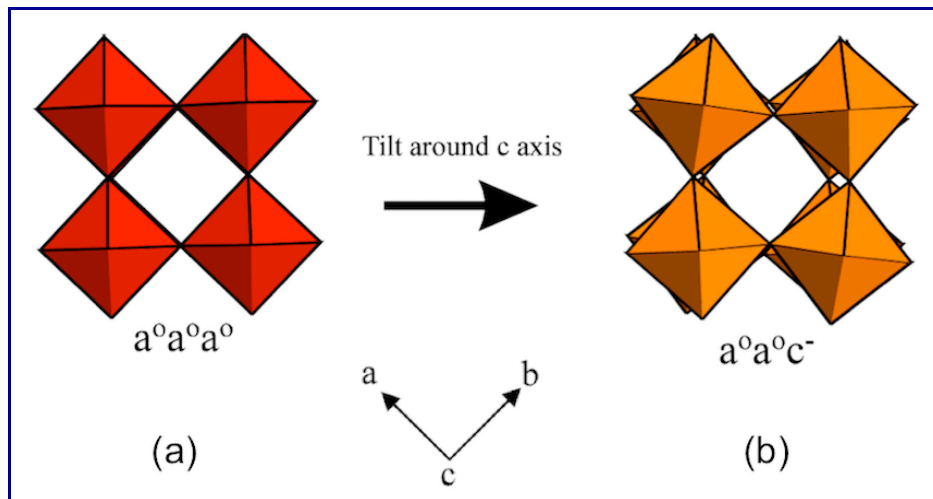


Figure 2.10 No octahedra tilt: $a^0a^0a^0$, i.e. ideal cubic symmetry (a); Octahedra with opposite tilts around c axis: $a^0a^0c^-$ (b). Adapted from Ref. (Garg, 2001).

In practice, Jahn-Teller distortions can be coupled with octahedra tilting and rotations. Carpenter and Woodward (Carpenter & Woodward, 2009) presented a group-theoretical treatment coupling 15 possible tilt systems with Jahn–Teller distortion schemes.

Understanding perovskite distortions is necessary because changes in temperature and pressure induce transformations that may change space group symmetry, and hence may

generate phase transitions as can be seen in Figure 2.11. Representative octahedral tilt patterns $a^0a^0c^+$ and $a^0a^0c^-$ with the in phase (c^+) and in anti-phase tilts (c^-) about the c -axis, respectively, transformed the cubic phase (i.e., no tilt $a^0a^0a^0$) into the tetragonal phase. The tilts $a^+a^+c^0$ and $a^-a^-c^0$ produce similar tilts of the octahedra in the ab -plane and hence transform cubic phase into the orthorhombic phase.

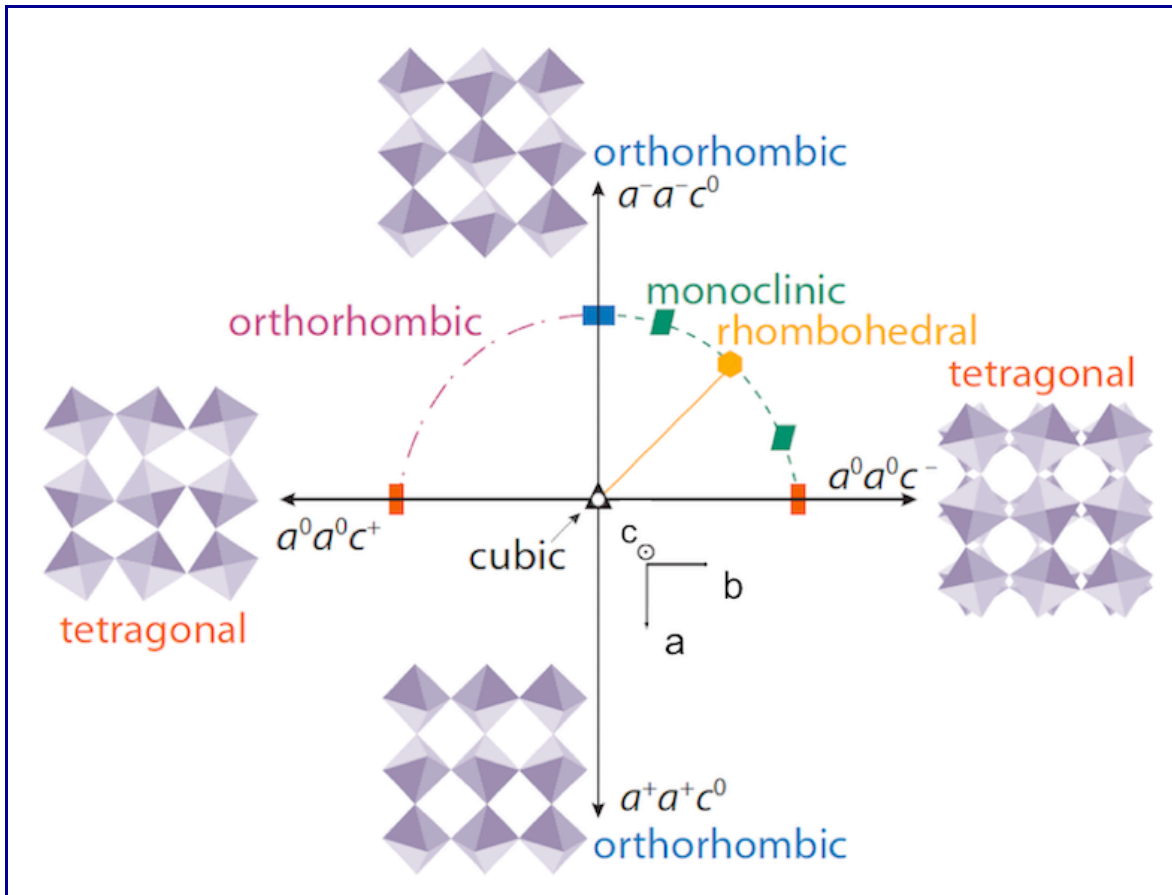


Figure 2.11 Phase transitions versus octahedra tilts for transition metal perovskites. Adapted from Ref. (Rondinelli & Spaldin, 2011).

CHAPTER 3

THEORETICAL BACKGROUND

By definition, a first principles study starts directly from the fundamental laws of physics, with minimal model assumptions or fitting parameters. In nonrelativistic quantum mechanics, the physics of a system of interacting particles at equilibrium is described by the time-independent Schrödinger equation:

$$\hat{H}\Psi(\{\mathbf{R}\},\{\mathbf{r}\})=E\Psi(\{\mathbf{R}\},\{\mathbf{r}\}) \quad (3.1)$$

where \hat{H} is the nonrelativistic Hamiltonian of the system, Ψ is the wave function for all the particles ("many-body" wave function) and E is the corresponding energy (eigenvalue); $\{\mathbf{R}\}$ represents the set of all the nuclear coordinates, and $\{\mathbf{r}\}$ represents the set of all the electronic coordinates.

In solid state physics, the starting point is the Hamiltonian for a system of interacting electrons and nuclei. Assuming that the nuclei are frozen (Born-Oppenheimer approximation), the electron Hamiltonian is expressed as (Szabo & Ostlund, 1996):

$$\hat{H}_{el}=\hat{T}_e(\{\mathbf{r}\})+\hat{U}_{en}(\{\mathbf{R}\},\{\mathbf{r}\})+\hat{V}_{ee}(\{\mathbf{r}\})+\hat{V}_{nn}, \quad (3.2)$$

where \hat{T}_e is the nonrelativistic kinetic energy operator of the electrons, \hat{V}_{ee} is the electron-electron Coulomb repulsion, \hat{U}_{en} is the potential energy operator due to the interaction of the electrons with the nuclei, and \hat{V}_{nn} (=constant) is the energy associated with the nuclei interaction (this term is conventionally included in the electron Hamiltonian). By using the Born-Oppenheimer approximation, describing the interacting electrons of N ions in a macroscopic solid ($N \approx 10^{23}$ in one cubic centimeter) is impossible in practice, hence other simplifications are required for estimating the electron-electron interactions.

3.1 Density Functional Theory

The Density Functional Theory (DFT) consists in replacing the many-body problem with an independent-particle problem (Hohenberg & Kohn, 1964; Kohn & Sham, 1965). The auxiliary Hamiltonian is chosen to have the usual kinetic energy operator and an effective *local* potential $V_{KS}^\sigma(\mathbf{r})$ acting on each electron of spin σ at point $\mathbf{r}=(x,y,z)$:

$$\hat{H}_{KS}^\sigma(\mathbf{r}) = -\frac{1}{2}\nabla^2 + V_{KS}^\sigma(\mathbf{r}). \quad (3.3)$$

The problem is reduced to determining the ground-state total energy $E[\rho]$ and electron spin densities $\rho^\uparrow(\mathbf{r}), \rho^\downarrow(\mathbf{r})$ for up and down z-components of the spin, respectively (where $\rho(\mathbf{r}) = \rho^\uparrow(\mathbf{r}) + \rho^\downarrow(\mathbf{r})$), for a collection of N_e electrons interacting with one another, within the external potential $V_{ext}(\mathbf{r})$. These are found by the self-consistent solution of the auxiliary one-electron Schrödinger equation (Perdew & Kurth, 2003) :

$$\hat{H}_{KS}^\sigma \psi_i^\sigma(\mathbf{r}) = \varepsilon_i^\sigma \psi_i^\sigma(\mathbf{r}) \Leftrightarrow \left(-\frac{1}{2}\nabla^2 + V_{ext}(\mathbf{r}) + \int \frac{\rho(\mathbf{r}')}{|\mathbf{r}'-\mathbf{r}|} d^3\mathbf{r}' + V_{exc}^\sigma([\rho^\uparrow, \rho^\downarrow]; \mathbf{r}) \right) \psi_i^\sigma(\mathbf{r}) = \varepsilon_i^\sigma \psi_i^\sigma(\mathbf{r}), \quad (3.4)$$

$$\rho^\sigma(\mathbf{r}) = \sum_\sigma \rho(\mathbf{r}, \sigma) = \sum_\sigma \sum_{i=1}^{N_e^\sigma} \left| \psi_i^\sigma(\mathbf{r}) \right|^2 \Rightarrow \sum_{i=1}^{N_e^\sigma} f_i^\sigma \left| \psi_i^\sigma(\mathbf{r}) \right|^2, \quad (3.5)$$

where $\int \frac{\rho(\mathbf{r}')}{|\mathbf{r}'-\mathbf{r}|} d^3\mathbf{r}'$ is the Hartree potential (atomic units are used, $\hbar=m=e^2=1$); $V_{exc}^\sigma([\rho^\uparrow, \rho^\downarrow]; \mathbf{r})$

represents the exchange-correlation potential, which includes all the many particle interactions. The density of the auxiliary system $\rho^\sigma(\mathbf{r})$, Eq. (3.5), is given by a sum of the square of the orbital functions ψ_i^σ for each spin $\sigma=\uparrow$ or \downarrow (f_i represents the occupation number, namely the number of electrons in the orbital ψ_i^σ). Using the variational principle for non-interacting electrons, the solution of the Kohn-Sham (K-S) self-consistent system of equations (3.4)-(3.5) is equivalent to minimizing the K-S energy functional E_{KS} , under constraints of orthonormalization for occupied orbitals (Martin, 2004):

$$E_{KS}^\sigma = \sum_\sigma \sum_i \left\langle \psi_i^\sigma \left| -\frac{1}{2}\nabla^2 \right| \psi_i^\sigma \right\rangle + \int V_{ext}(\mathbf{r}) \rho(\mathbf{r}) d^3\mathbf{r} + E_H[\rho] + E_{xc}^\sigma[\rho^\uparrow, \rho^\downarrow] + E_{nn}. \quad (3.6)$$

In this expression, E_{nn} is the interaction energy between the nuclei; $\sum_\sigma \sum_{i=1}^{N_e^\sigma} \left\langle \psi_i^\sigma \left| -\frac{1}{2}\nabla^2 \right| \psi_i^\sigma \right\rangle$ is the independent-particle kinetic-energy given explicitly as a functional of spin-dependent orbitals

functions; $E_H[\rho] = \frac{1}{2} \int \frac{\rho(\mathbf{r})\rho(\mathbf{r}')}{|\mathbf{r}-\mathbf{r}'|} d^3\mathbf{r} d^3\mathbf{r}'$ represents the classical Coulomb interaction energy between electrons; $E_{xc}^\sigma[\rho^\uparrow, \rho^\downarrow] = \int \rho(\mathbf{r})\varepsilon_{xc}[\rho^\uparrow(\mathbf{r}), \rho^\downarrow(\mathbf{r})] d^3\mathbf{r}$ is the exchange-correlation energy, where $\varepsilon_{xc}(\rho^\uparrow(\mathbf{r}), \rho^\downarrow(\mathbf{r}))$ is an energy per electron at point \mathbf{r} that depends only upon densities in some neighbourhood of \mathbf{r} .

The exchange-correlation energy functional E_{xc}^σ is not known, and hence it must be approximated. There are various known approximations, but the simplest approximation is the ***local density approximation (LDA)*** that is based on the following assumptions:

- (i) the local exchange-correlation energy per particle only depends on the local density $\rho(\mathbf{r})$ (not on its derivatives, in contrast to the GGA discussed below); and
- (ii) it is equal to the local exchange-correlation energy per particle of an *homogeneous electron gas (HEG) of same density*, i.e., $\varepsilon_{xc}^{LDA}(\mathbf{r}; \rho) = \varepsilon_{xc}^{HEG}(\rho(\mathbf{r}))$.

It follows that the exchange-correlation energy functional for LDA is (Martin, 2004):

$$E_{xc}^{LDA}[\rho] = \int \rho(\mathbf{r}) \varepsilon_{xc}^{HEG}(\rho(\mathbf{r})) d^3\mathbf{r}. \quad (3.7)$$

For the magnetic spin-polarized systems (i.e., spatial orbitals are different for up and down spins), the corresponding exchange-correlation energy is the ***local spin density approximation (LSDA)***

$$E_{xc}^{LSDA}[\rho^\uparrow, \rho^\downarrow] = \int \rho(\mathbf{r}) \varepsilon_{xc}(\rho^\uparrow(\mathbf{r}), \rho^\downarrow(\mathbf{r})) d^3\mathbf{r}. \quad (3.8)$$

The success of the LSDA has led to the development of various ***generalized-gradient approximations (GGAs)*** which are generally more accurate than LSDA, but computationally more expensive. The exchange-correlation energy functional for GGA in the case of spin polarized systems is (Martin, 2004):

$$E_{xc}^{GGA}[\rho^\uparrow, \rho^\downarrow] = \int \rho(\mathbf{r}) \varepsilon_{xc}^{GGA}(\rho^\uparrow(\mathbf{r}), \rho^\downarrow(\mathbf{r}), |\nabla \rho^\uparrow|, |\nabla \rho^\downarrow|) d^3\mathbf{r}. \quad (3.9)$$

However LDA or GGA do not correctly describe strongly correlated systems (i.e., Mott-insulators that include transition-metal or rare earth metal ions with *partially filled d or f shells*) which tend to delocalize electrons. This is the case of BFCO discussed in this thesis because Fe^{3+} and Cr^{3+}

have partially filled $3d$ bands. For such systems, one has to use the so-called LDA+U (or GGA+U) approach, which adds the missing screened on-site Coulomb interaction to the theory.

3.2 On-site Coulomb interaction

3.2.1 Strongly correlated systems

The first important step toward taking into account electron-electron correlations for explaining the insulating state was made by Mott (Mott, 1956) and Hubbard (Hubbard, 1964) through the electron interaction energy parameter, U . They considered a lattice model with a single electronic orbital on each site. Without electron-electron interactions, a single band would be formed from the overlap of the atomic orbitals in this system, where the band becomes full when two electrons, one with spin-up and the other with spin-down, occupy each site. However, two electrons sitting on the same site would feel a large Coulomb repulsion, and will split the band in two: (i) *the lower band* formed from electrons that occupied an empty site; and (ii) *the upper band* formed from electrons that occupied a site already taken by another electron. These bands of width W are also called the *lower* and *upper Hubbard* bands, and their center is separated by the Coulomb energy U . Note that lower and upper Hubbard bands are seen only at half filling.

Generally speaking, the on-site Coulomb interaction U , for an open $3d$ ($4d$) shell, is the repulsion energy of two electrons occupying the same $3d$ ($4d$) orbital, and can be defined as the energy cost to place two electrons on the same site. Considering two d^n ions (where n is the number of electrons in the d orbital), the removal and addition of an electron would produce a d^{n+1} and a d^{n-1} configuration, respectively. Under a strong on-site electron correlation, $U > W$, the lower and upper Hubbard bands will not overlap and the material will be insulating (Imada et al., 1998). Zaanen and coworkers (Zaanen & Sawatzky, 1985) have extended these ideas by introducing a *charge-transfer energy* Δ , which occurs when the energies of some anion orbital (e.g. the $2p$ orbital of oxygen in oxides) are higher than the lower Hubbard band (the occupied valence band of metal ions), Δ being the energy difference between the center of the lower Hubbard band and the energy of the center of the anion orbital. In the Zaanen-Sawatsky-Allen classification scheme for transition metal compounds, there are two types of insulating ground state, the *charge-transfer insulator* for which $U > \Delta > W$ and the original *Mott-Hubbard insulator* for which $\Delta > U > W$.

3.2.2 LDA and LDA+U

LDA cannot be successful for *Mott-Hubbard insulators* since the potential used in K-S Hamiltonian of the one-electron method LDA is *the same for both occupied and unoccupied states*.

A way to correct the failure of the LDA approximation is to *take explicitly into account the interaction between d (or f) electrons through a Hubbard-like term* in the Hamiltonian. More precisely, electrons should be separated into two systems (Anisimov & Izyumov, 2010; Anisimov et al., 1997):

- (i) *localized d or f electrons* for which Coulomb *d-d* interaction are taken into account by a term $U \sum_{i \neq j} n_i n_j / 2$ (n_i are *d*-orbital occupancies) as in a mean-field (Hartree-Fock) approximation;
- (ii) *delocalized s, p electrons* which can be described by using an orbital-independent one-electron potential (LDA).

Thus, assuming that the Coulomb energy of *d-d* interactions as a function of the total number of *d* electrons $N = \sum n_i$ given by the LDA is a good approximation with $U \sum_{i \neq j} n_i n_j / 2$ representing

the energy corresponding to the Hubbard-like term, then the mean-field energy approximation of the correlated system is $E = UN(N-1)/2$, where U is the Coulomb repulsion parameter. To avoid double counting, i.e. to cancel the local electron-electron interaction already included in LDA functional, this expression is subtracted from the energy functional, and hence it results

$$E^{LDA+U} = E^{LDA} + U \sum_{i \neq j} n_i n_j / 2 - UN(N-1)/2 . \quad (3.10)$$

The orbital eigenvalue can be obtained by taking the derivative of the total energy with respect to the occupation number of that orbital, $\epsilon_i^{LDA+U} = \frac{\partial E^{LDA+U}}{\partial n_i} = \epsilon_i^{LDA} + U \left(\frac{1}{2} - n_i \right)$, and hence the *orbital-dependent potential* (a variation on the charge density of a particular i^{th} orbital $n_i(\mathbf{r})$ is taken into account) becomes $V_i^{LDA+U}(\mathbf{r}) = \frac{\partial E^{LDA+U}}{\partial n_i(\mathbf{r})} = V^{LDA}(\mathbf{r}) + U \left(\frac{1}{2} - n_i \right)$.

From this formulation of the LDA+U orbital-dependent potential, it can be seen that the LDA orbital energy is shifted by $-U/2$ for occupied orbitals ($n_i=1$) and by $+U/2$ for unoccupied orbitals ($n_i=0$). This proves that the LDA+U orbital-dependent potential gives upper and lower Hubbard

bands with the energy separation between them equal to the Coulomb parameter U . Hence LDA+ U is able to reproduce qualitatively the correct physics for Mott-Hubbard insulators.

3.2.3 Appropriate computational scheme for Mott-Hubbard insulators

For constructing a computational scheme, we need to define in a more general way an orbital basis set (“atomic spheres”) that provides an efficient representation of the highly inhomogeneous wavefunctions, and to properly take into account the direct and exchange Coulomb interactions inside a partially filled d (or f) atomic shell. One of the most important basis set used is that of the linearized augmented plane wave method (LAPW) in which space is partitioned in two regions: a spherical one around each atom, in which the wavefunction is expanded onto a local basis in order to describe its great variations, and an interstitial region in which another basis is chosen (plane waves for instance) and connected to the first local basis. Blöchl introduced a more general approach, the ***projector-augmented-wave method (PAW)*** (Blöchl, 1994), as an extension of both augmented-wave and pseudopotential methods. The PAW method has been implemented in several DFT codes (VASP, ABINIT, etc.). The LDA+ U method was implemented using both LAPW (Shick et al., 1999) and PAW (Amadon et al., 2008) basis sets. The main element of the LDA+ U implementation is the density matrix $\{n^\sigma\}$ (Anisimov et al., 1997), which is used to define the generalized LDA+ U functional as follows:

$$E^{LDA+U}[\rho^\sigma(\mathbf{r}), \{n^\sigma\}] = E^{LSDA}[\rho^\sigma(\mathbf{r})] + E^{ee}[\{n^\sigma\}] - E^{dc}[\{n^\sigma\}]. \quad (3.11)$$

In this expression, $\rho^\sigma(\mathbf{r})$ is the charge density for spin- σ electrons and $E^{LSDA}[\rho^\sigma(\mathbf{r})]$ is the standard LSDA (local spin-density approximation) functional. As in Eq. (3.10), the contributions to energy are the LSDA energy for a given density, the electron-electron interaction term E^{ee} from the Hubbard term (Amadon et al., 2008), and the double counting term $-E^{dc}$.

The implementations of the double counting term introduced to cancel the local electron-electron interaction already described in L(S)DA, can be done by different schemes. Most used is the Liechtenstein approach (Liechtenstein et al., 1995), also called the *fully localized limit (FLL)* formula, where E^{dc} corresponds to the value of E^{ee} in a reference system in which the occupation matrix is diagonal:

$$E^{dc,FLL} = U \frac{1}{2} N(N-1) - J \sum_{\sigma} \frac{1}{2} N^\sigma (N^\sigma - 1) = \frac{1}{2} UN(N-1) - \frac{1}{2} J [N^\uparrow (N^\uparrow - 1) + N^\downarrow (N^\downarrow - 1)], \quad (3.12)$$

where $N^\sigma = \text{Tr} \left(n_{mm}^\sigma \right)$, $N = N^\uparrow + N^\downarrow$, U is the *Coulomb parameter* defined as the energy needed to put two electrons on the same atomic site, and J is the *exchange parameter* defined as the exchange interaction among electrons on neighbouring sites.

3.3 Relativistic Density Functional Theory

Nonrelativistic quantum mechanics described by the Schrödinger equation (3.1) is very successful for problems in which the electron velocity is small compared with the speed of light. However, the nonrelativistic Schrödinger equation cannot describe correctly spin-orbit coupling, which is a relativistic effect. Relativistic effects also play an important role in thin films and surfaces, as Néel explained (Néel, 1954) in his model of the magnetocrystalline surface anisotropy described by pair-interaction of spins.

For a proper treatment of relativistic effects, the Hamiltonian \hat{H} from the equation (3.1) is replaced by its relativistic counterpart (Autschbach & Ziegler, 2002). All problems of the non-relativistic many-electron theory are present in the relativistic formulation and similar techniques are used for finding approximate solutions. Relativistic many-electron atomic and molecular computations rely on the use of the four-component “no-pair” Dirac-Coulomb Hamiltonian or some approximations obtained from it

$$\hat{H}^{DC} = c\mathbf{a} \cdot \hat{\mathbf{p}} + bmc^2 + \hat{U}_{en} + \hat{V}_{ee} + \hat{V}_{nn} \quad (3.13)$$

where $\hat{\mathbf{p}}$ is the momentum operator, and the (4×4) matrices \mathbf{a} and b are written in terms of the Pauli matrices

$$a_i = \begin{bmatrix} 0 & \sigma_i \\ \sigma_i & 0 \end{bmatrix}, \quad b = \begin{bmatrix} I_2 & 0 \\ 0 & -I_2 \end{bmatrix},$$

where σ_i represents the 2×2 Pauli spin matrices $\sigma_1 = \begin{bmatrix} 0 & 1 \\ 1 & 0 \end{bmatrix}$, $\sigma_2 = \begin{bmatrix} 0 & -i \\ i & 0 \end{bmatrix}$, $\sigma_3 = \begin{bmatrix} 1 & 0 \\ 0 & -1 \end{bmatrix}$, and $I_2 = \begin{bmatrix} 1 & 0 \\ 0 & 1 \end{bmatrix}$ is the identity 2×2 matrix.

The main difference between the relativistic Hamiltonian (3.13) and the nonrelativistic one (3.2) consists in the kinetic energy operator for an electron. The relativistic Hamiltonian takes into

account: the relativistic increase of the electron mass due to high velocities, the electron rest mass energy, the electron spin, and also the spin-orbit coupling, which is thus a relativistic effect. Note that the wave function has to be a four-component vector for which each component is a complex function of space $\Psi^{DC} = \begin{pmatrix} \varphi \\ \chi \end{pmatrix}$ where φ and χ are the so-called *upper* and *lower* components of the four-component orbital Ψ^{DC} , each of them made up of two components. Because φ and χ are not independent from each other, it is not possible to obtain a relativistic two-component equation for φ or χ alone. For many electrons systems, different approximate two-component Hamiltonians are considered in which the uncoupling of the two components is only achieved to a certain order in c^2 (small velocities of the valence electrons $v^2 / c^2 \ll 1$). A simple approach is the *Pauli Hamiltonian* in which spin and spin-orbit effects appear explicitly (atomic units are used, $\hbar=m=e^2=1$)

$$\hat{H}^{Pauli} = \frac{\hat{p}^2}{2} + V(r) - \frac{\hat{p}^4}{8c^2} + \frac{1}{2c^2} \frac{1}{r} \frac{\partial V}{\partial r} (\mathbf{S} \cdot \mathbf{L}) - \frac{1}{8c^2} \nabla^2 V . \quad (3.14)$$

In this expression, the first term and the second term, with $V = \hat{U}_{en} + \hat{V}_{ee} + \hat{V}_{nn}$, correspond to the nonrelativistic Schrödinger equation; the third term is the relativistic correction to the kinetic energy (or mass); the fourth term corresponds to spin-orbit coupling (called SOC Hamiltonian)

$$\hat{H}^{SOC} = \frac{1}{2c^2} \frac{1}{r} \frac{\partial V}{\partial r} (\mathbf{S} \cdot \mathbf{L}) \quad (3.15)$$

where \mathbf{L} is the angular momentum operator and \mathbf{S} is the spin operator; and the last term of Eq. (3.14) is the Darwin correction. The spin-spin interactions between electrons, and between electrons and the nucleus are generally neglected.

3.3.1 Noncollinear Magnetism

Magnetic spin-polarized DFT calculations do not impose any constraints on the direction of the atomic magnetic moments. As discussed in the previous section, in the usual *ab initio* calculations of a spin polarized system, there are two densities, $\rho^\uparrow(\mathbf{r})$ and $\rho^\downarrow(\mathbf{r})$, for spin up and spin down, respectively (i.e., *collinear* magnetic configuration, where the neighbouring magnetic moments are aligned parallel or antiparallel). This is not the most general case because the quantization spin axis can vary in space, as the spin structures reveal generally an arbitrary

alignment of the neighbouring magnetic moments (Martin, 2004). In the *noncollinear spin* case, following the von Barth and Hedin (Barth & Hedin, 1972) local-spin density theory allowing non-collinear spin arrangements within a generalization of the K-S theory, the density at every point is expressed in terms of a 2x2 matrix. The previous density formula (3.5) for collinear

magnetism $\rho^\sigma(\mathbf{r}) = \sum_{i=1}^{N_e^\sigma} f_i^\sigma |\psi_i^\sigma(\mathbf{r})|^2$ (where $\sigma = \uparrow$ or \downarrow is the z-component of spin) becomes equivalent to the 2x2 total density matrix (Hobbs *et al.*, 2000)

$$\rho^{\alpha\beta}(\mathbf{r}) = \begin{bmatrix} \rho_{11} & \rho_{12} \\ \rho_{21} & \rho_{22} \end{bmatrix}$$

that can be written in terms of Pauli matrices $\mathbf{s}^{\alpha\beta} = [\sigma_1 \ \sigma_2 \ \sigma_3]$ as follows

$$\begin{aligned} \rho^{\alpha\beta}(\mathbf{r}) &= \frac{1}{2}(\rho_{11} + \rho_{22})I_2 + \frac{1}{2}(\rho_{11} - \rho_{22})\sigma_3 + \frac{1}{2}(\rho_{12} + \rho_{21})\sigma_1 + i\frac{1}{2}(\rho_{12} - \rho_{21})\sigma_2 \\ &= \frac{1}{2}\text{Tr}[\rho^{\alpha\beta}]I_2 + \frac{1}{2}\text{Tr}[\rho^{\alpha\beta}\mathbf{s}^{\alpha\beta}]\cdot\mathbf{s}^{\alpha\beta}. \end{aligned} \quad (3.16)$$

Note that $\text{Tr}[\rho^{\alpha\beta}]$ denoted in the following as ρ_{Tr} , is the usual electron density. The components of the density matrix, given in term of solutions of the K-S equation, are written as

$$\rho^{\alpha\beta}(\mathbf{r}) = \sum_{i=1}^{N_e^\alpha} f_i \psi_i^\alpha(\mathbf{r}) \psi_i^\beta(\mathbf{r}) \quad (3.17)$$

and then the K-S Hamiltonian is the 2x2 matrix

$$\hat{H}_{KS}^{\alpha\beta}(\mathbf{r}) = -\frac{1}{2}\nabla^2 + V_{KS}^{\alpha\beta}(\mathbf{r}). \quad (3.18)$$

Thus, the K-S energy density functional (3.6), holding for collinear spins, becomes in the non-collinear case (Hobbs *et al.*, 2000)

$$E_{KS}^{\alpha\beta} = \sum_\alpha \sum_i \left\langle \psi_i^\alpha \left| -\frac{1}{2}\nabla^2 \right| \psi_i^\alpha \right\rangle + \int V_{ext}^{\alpha\beta}(\mathbf{r}) \sum_{\alpha\beta} \rho^{\alpha\beta}(\mathbf{r}) d^3\mathbf{r} + E_H[\rho_{Tr} + \rho_Z] + E_{xc}^{\alpha\beta}[\rho^{\alpha\beta}] \quad (3.19)$$

where $E_H[\rho_{Tr} + \rho_Z]$ is the electrostatic energy associated with the electronic charge density ρ_{Tr} and the point charge densities of the nuclei ρ_Z , and is defined by

$$E_H[\rho_{Tr} + \rho_Z] = \frac{1}{2} \iint \frac{[\rho_{Tr} + \rho_Z](\mathbf{r}) [\rho_{Tr} + \rho_Z](\mathbf{r}')}{|\mathbf{r} - \mathbf{r}'|} d^3\mathbf{r} d^3\mathbf{r}',$$

while $E_{xc}^{\alpha\beta}[\rho^{\alpha\beta}]$ is the electronic exchange-correlation energy, defined by

$$E_{xc}^{\alpha\beta}[\rho^{\alpha\beta}] = \int \rho_{Tr}(\mathbf{r}) \varepsilon_{xc}^{\alpha\beta}[\rho^{\alpha\beta}(\mathbf{r})] d^3\mathbf{r}.$$

It is notable that, the exchange-correlation energy is non-diagonal in $\alpha\beta$, and the real difficulty is coming from the functional $\varepsilon_{xc}^{\alpha\beta}$. In the local spin density approximation LSDA, the functional $\varepsilon_{xc}^{\alpha\beta}$ is obtained by finding the *local axis of spin quantization* (Martin, 2004), i.e., noncollinear magnetic vectors are initially aligned to a spin quantization axis, and then they are allowed to rotate from the initial orientation until the correct groundstate is obtained (Kresse & Lebacq, 2017).

There are various implementations of noncollinear magnetism in an electronic structure code, e.g., using augmented spherical-wave (Kübler et al., 1988), or using projector augmented-wave (PAW) method (Hobbs et al., 2000), as implemented in the *Vienna ab initio Simulation Package* (VASP).

In a noncollinear magnetic calculation the computational effort to diagonalize the Hamiltonian increases with almost the third power of the number of basis functions in comparison with collinear calculations. In addition, reduction of the symmetry of the system due to non-collinearity increases irreducible wedge of the Brillouin zone and hence noncollinear magnetic calculations are highly time-consuming.

3.3.2 Spin-orbit coupling in the pseudopotential context

In order to decrease the computational burden, the difficulties associated with (i) the description of the tightly bounded core states, and (ii) rapid oscillations of the valence bands orbitals inside the core region should be avoided. The first problem is solved within the frozen-core approximation, as the valence electrons responsible for the physical properties of the system are outside the core region, and the core electrons do not directly participate to the chemical bonding. The second problem is solved by the pseudopotential approximation that basically consists in a mathematical transformation in which the ionic potential screened by the core electrons is replaced by a fictitious potential such that the valence wavefunctions remain

unchanged beyond a given spatial cutoff distance and are replaced by smoothly varying pseudo-functions inside the core region. For an adequately chosen cutoff distance, it is expected that such a potential provides similarity between the real and pseudo-problem, whatever the modifications of the ionic environment within which the frozen core approximation remains valid. Nowadays, pseudopotential approach is a well-controlled approximation and the potentials are generated from first principles calculations.

To solve the K-S equations (see Eqs. (3.4)-(3.5) and their variants for spin and spin-orbit coupling) for elements with strongly localized orbitals (e.g., 3d transition metals and rare-earth elements), the resulting pseudopotentials require a large plane-wave basis set which makes calculations inefficient. To avoid this problem, a modern framework of the total energy functional by the projector augmented wave (PAW) approach (Blöchl, 1994; Kresse & Joubert, 1999), is most common. This framework, which is implemented in the VASP code (Hobbs *et al.*, 2000), consists in using pseudopotential operators while keeping the full core wavefunctions. The details regarding rearrangements of PAW functional, modified Hamiltonian operator, and several critical tests can be found in Ref. (Kresse & Joubert, 1999). As the PAW method within VASP is widely used, it was proven that the PAW method can handle the most difficult cases including problems involving strong magnetic moments or large electronegativity differences.

In order to treat spin-orbit coupling (SOC) in the PAW formalism, several approximations are made, and spin-orbit interaction is added to the all-electron part of the PAW Hamiltonian (variational treatment). Spin-orbit coupling has been implemented in VASP by Kresse and Lebac (Kresse & Lebacq, VASP Manual).

3.4 Polarization

Electric polarization is one of the basic quantities in physics, essential to the theory of dielectrics, effective charges in lattice dynamics, ferroelectricity, piezoelectricity etc.

In bulk solids, polarization \mathbf{P} could be considered as an intrinsic property in macroscopic systems. The electric polarization in a finite crystal is defined as an electric dipole moment per volume of the crystal. Considering the crystal neutral as a whole, i.e., $\mathbf{P}(\mathbf{r})=0$ outside the body, polarization can be expressed (Martin, 2004) as

$$\mathbf{P} = \frac{1}{\Omega} \int_{\Omega} \mathbf{r} \rho(\mathbf{r}) d^3 \mathbf{r} \quad (3.20)$$

where Ω represents the volume of the crystal, and $\rho(\mathbf{r})$ the charge density. However, this approach is flawed, because the result of (3.20) depends on the shape and location of the unit cell, and hence a different approach has to be used.

The modern theory of polarization (Resta *et al.*, 1993; Resta, 1994) overcomes this problem by replacing the definition (3.20) with a different form, i.e., using the macroscopic polarization current $\mathbf{j}(\mathbf{r}, t)$

$$\mathbf{P}(\mathbf{r}, t) = \int \mathbf{j}(\mathbf{r}, t) dt, \quad (3.21)$$

where the static changes in the polarization can be calculated from the *adiabatic* evolution of the system.

Thus a change in polarization $\Delta\mathbf{P}$ can be determined strictly from the polarization current that flows (charge flow) through the bulk (Resta & Vanderbilt, 2007)

$$\Delta\mathbf{P} = \int dt \frac{1}{\Omega} \int_{\Omega} \mathbf{j}(\mathbf{r}, t) d^3\mathbf{r}. \quad (3.22)$$

This equation is the basis of the modern theory of the polarization. The basic quantity of interest is the difference $\Delta\mathbf{P}$ in polarization between two different states of the same solid, i.e. a centrosymmetric non-polar reference structure and the structure of interest that possess a spontaneous polarization.

A new approach for calculating the polarization consists in varying adiabatically a parameter of the Hamiltonian, λ , during the transition from the centrosymmetric unpolarized reference structure ($\lambda=0$) to the final spontaneously polarized structure ($\lambda=1$)

$$\Delta\mathbf{P} = \int_0^1 \frac{d\mathbf{P}}{d\lambda} d\lambda, \quad (3.23)$$

The key feature exploited here is that $d\mathbf{P}/d\lambda$ is a well-defined bulk vector property (Resta & Vanderbilt, 2007).

3.4.1. The concept of Born effective charge

For calculating the polarization, it is essential to know the ion effective charges, which are involved in the polarization current $\mathbf{j}(\mathbf{r}, t)$ of Eq. (3.22). In addition, ion effective charges can be

measured accurately, providing a valuable test for the theory (Martin, 2004). Before seeing how effective charges are computed and then used for evaluating spontaneous polarization, it is important to distinguish between the concepts of *static* and *dynamical* charges.

The *static* charge is an intuitive concept based on partitioning the ground-state electronic density into contributions attributed to different atoms. The *static* charge is a well-defined quantity for an isolated atom, and is expected to be close to the so-called *nominal* charge in a purely ionic material, e.g., +2 for Ba, +3 for Bi, -2 for O, etc. A definition for *static* charge in the case of molecules and solids is difficult, as the partition of the electronic distribution can only be done unambiguously when a clear boundary can be drawn between ions, which is not possible in practice, especially when there is covalent bonding (Ghosez *et al.*, 1998). Hence, the *static* charge is an ill-defined quantity that depends on the artificially chosen convention to affect a given electron to a particular ion. The *nominal* charges are indeed used as a first approximation of the polarization, called *formal polarization* and written as (Vanderbilt *et al.*, 1993; Resta & Vanderbilt, 2007)

$$\mathbf{P}^{Formal} = \frac{e}{V} \sum_k Z_k^N \mathbf{u}_k, \quad (3.24)$$

where \mathbf{u}_k stands for the position of the ion k , eZ_k^N is the nominal ionic charge of the ion k , and V is the volume of the cell.

The *dynamical* charge (or effective charge) was introduced in solid state physics by Born, and it is directly related to the change of polarization created by atomic displacements. For periodic solids, the Born effective charge of an atom k is a tensor, conventionally defined as the coefficient of proportionality at the linear order with respect to the macroscopic polarization change $\Delta\mathbf{P}$ per unit cell created in direction β and a rigid displacement $\Delta u_{k,\alpha}$ of the sublattice of the atom k in the direction α (Ghosez *et al.*, 1998)

$$Z_{k,\alpha\beta}^* = \frac{V}{e} \frac{(\Delta P)_{k,\beta}}{\Delta u_{k,\alpha}}. \quad (3.25)$$

This is a dynamical concept in the sense that it concerns the response to an atomic displacement. Within an extreme rigid-ion model the Born charge coincides with the static charge of the model ion, i.e., the nominal value (Resta & Vanderbilt, 2007).

From its definition, the Born effective charge tensors, \mathbf{Z}^* , measure the macroscopic polarization induced by a unit cell displacement in a null external electric field (Pick *et al.*, 1970). Notice that, in low-symmetry situations, $Z_{k,\alpha\beta}^*$ is not symmetric in its Cartesian indices. Since any rigid translation of the whole solid does not include macroscopic polarization, the Born effective charge tensors satisfy the acoustic sum rule (translational invariance)

$$\sum_k Z_{k,\alpha\beta}^* = 0. \quad (3.26)$$

There are various techniques to evaluate Born charge tensors. Advances in *ab initio* techniques enable to predict accurate Born effective charges using perturbation theory or finite differences of polarization. The most powerful tool is the linear response method (Baroni *et al.*, 1987) that is implemented in the pseudopotential scheme using a plane-wave basis set. In this thesis, Born effective charges are calculated from linear response calculations using a variational formulation (Gonze *et al.*, 1992) of the density functional perturbation theory, as implemented in VASP within the MedeA environment (MedeA 2017; 2015). Because the effective-charge tensors are almost constant along the path connecting the paraelectric (i.e., centrosymmetric reference structure) and the ferroelectric phases (Resta *et al.*, 1993), the spontaneous (total) polarization is expressed in terms of the internal-strain displacement as

$$P_{s,\beta} = (\Delta P)_\beta = \frac{e}{V} \sum_{k,\alpha} Z_{k,\alpha\beta}^* (\Delta u_{k,\alpha}), \quad (3.27)$$

i.e., the polarization is obtained by summing over the effective charges contributions multiplied by the sublattice displacements. The effective charges $Z_{k,\alpha\beta}^*$ contained in (3.27) are computed as an average between Born effective charges corresponding to the paraelectric (reference) and ferroelectric structures. Ghosez *et al.* (Ghosez *et al.*, 1998) proposed the following general averaging expression

$$Z_{k,\alpha\beta}^* = \frac{n_1 \cdot Z_{\text{Paraelectric}}^* + n_2 \cdot Z_{\text{Ferroelectric}}^*}{n_1 + n_2}, \quad (3.28)$$

where $n_1=0.68$ and $n_2=0.32$.

3.4.2 Polarization in ferroelectrics

Spontaneous polarization can occurs in any crystal that lacks a center of inversion (in

piezoelectric, it appears when stressed). Ferroelectric materials display a broken-symmetry, as illustrated in Figure 3.1b for BaTiO_3 , a perovskite whose ferroelectric properties have been investigated experimentally long time ago (Axe, 1967). However, the subject remained neglected for more than two decades, until the first *ab initio* calculations were reported (Vanderbilt et al., 1993; Resta et al., 1993; Ghosez et al., 1995; Ghosez et al., 1996).

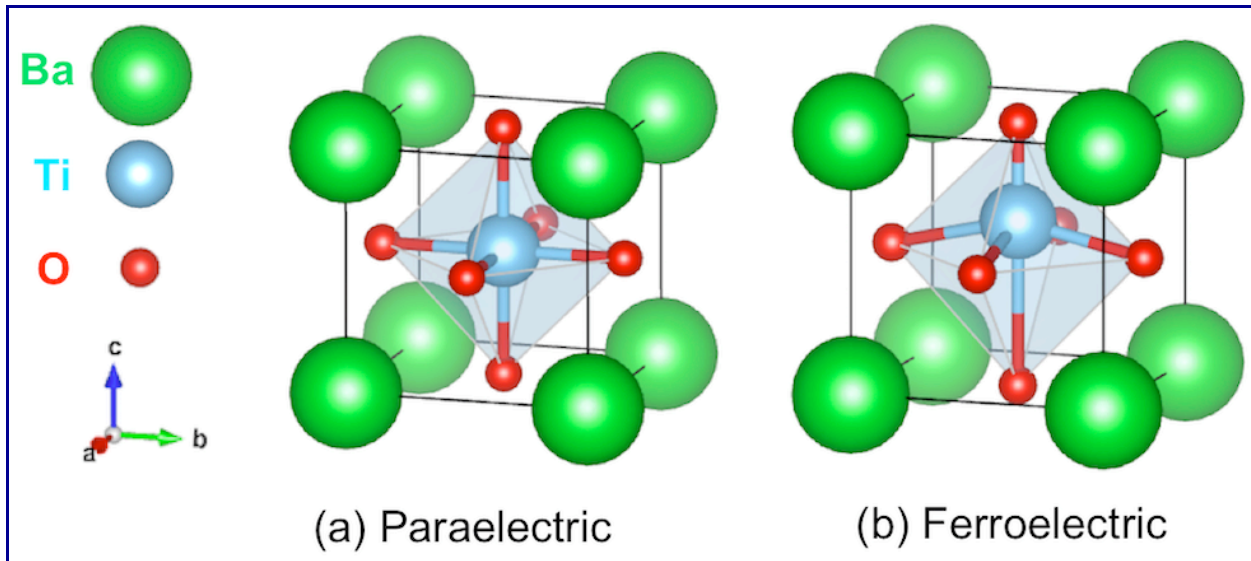


Figure 3.1 The BaTiO_3 perovskite structure: Paraelectric unit cell where all Ti-O bonds are equal in length (a); Ferroelectric unit cell: The Ti ion was shifted up as the Ti-O upper bond is shorter than Ti-O lower bond (b). Vizualized using VESTA (Momma & Izumi, 2011).

For most ferroelectric AMX_3 perovskites (i.e., $X=\text{O}$), the nominal charges are either 1, 2, or 3 for the A cation, either 5, 4, or 3 for the M cation, and -2 for oxygen. Modern calculations have demonstrated that calculated Born charges have larger values than the nominal charges (Resta & Vanderbilt, 2007). In addition, the *ab initio* calculations demonstrated that strong discrepancies between the nominal charges and the Born charges are due to the phenomenon of ferroelectricity.

To predict spontaneous polarization in ferroelectrics, i.e., to compute the difference $\Delta\mathbf{P}$ in the polarization between two different states of the same solid (centrosymmetric paraelectric reference structure versus ferroelectric structure), the first step is to identify the paraelectric reference structure (for ABX_3 perovskites, it is a cubic structure, see Figure 3.1a). Using *ab initio* methods, a structure optimization (i.e., minimizing the energy functional) is performed, and then the tensors of the Born charges can be computed for each atom of the paraelectric structure

$$Z_k^* = \begin{pmatrix} Z_{xx}^* & Z_{xy}^* & Z_{xz}^* \\ Z_{yx}^* & Z_{yy}^* & Z_{yz}^* \\ Z_{zx}^* & Z_{zy}^* & Z_{zz}^* \end{pmatrix}. \quad (3.29)$$

The second step consists in identifying the ferroelectric structure and atom displacements (compared with reference structure, e.g., Figure 3.1b compared with Figure 3.1a). It is notable that, in most cases, the ferroelectric structure can belong to a space group of symmetry that is different from the space group of the paraelectric structure; in this case, some additional calculations are necessary in order to bring the paraelectric structure to the same space group as the optimized ferroelectric structure, e.g., to displace atoms of the paraelectric structure within the unit cell while keeping its lattice parameters (Ghosez *et al.*, 1998). This allows to compute correctly the displacements $\Delta u_{k,\alpha}$ of the sublattice of atom k in direction α .

After the ferroelectric structure is optimized, a self-consistent calculation is performed and the tensors of the Born charges are computed for each atom of the structure. Then, the average between Born effective charges corresponding to the paraelectric and ferroelectric structures is computed using formula (3.28). These are the Born effective charges to be inserted in the spontaneous polarization formula (3.27). The volume V of the cell from (3.27) is a delicate choice, as generally, the paraelectric and ferroelectric structures have different volumes. In the following we will use the volume of the ferroelectric structure as this represents the ground-state of the compound.

Finally, from Eq. (3.28), one obtains the total polarization vector

$$P_s = (P_{s,x}, P_{s,y}, P_{s,z}), \quad (3.30)$$

where

$$P_{s,\zeta} = \frac{e}{V} \sum_{k,\alpha} Z_{k,\alpha\zeta}^* (\Delta u_{k,\alpha}), \quad (3.31)$$

where ζ stands for x, y, z .

The contribution of each ion k to the total polarization can be computed by isolating each term of the sum over k .

This procedure allows to identify the contribution of each ion to the *total spontaneous polarization of the ferroelectric structure*.

In addition, by comparing the Born effective charges of the paraelectric structure with the effective charges of the ferroelectric phase, the ionic and covalent character of the bonds can be revealed (Posternak *et al.*, 1994; Ghosez *et al.*, 1995). Furthermore, Born effective charges allow to visualize the mechanism of polarization as electronic currents produced by dynamical charges of orbital hybridizations (Posternak *et al.*, 1994; Ghosez *et al.*, 1998), and it helps to clarify the origin of the giant dipole-dipole interaction producing the ferroelectric instability (Ghosez *et al.*, 1996).

CHAPTER 4

DFT STUDY OF $\text{Bi}_2\text{FeCrO}_6$: COLLINEAR SPIN POLARIZED CALCULATIONS

4.1. Crystal structure of $\text{Bi}_2\text{FeCrO}_6$

Due to the high interest for designing new perovskite-structure that are ferroelectric, and with a large macroscopic magnetization, where coupling between magnetism and ferroelectricity allows to control the polarization with a magnetic field (or the magnetization with an electric field), exploration of multiferroic materials working at room temperature has focused on the BiFeO_3 (BFO) thin films (Wang et al., 2003; Ederer et al., 2005; Neaton et al., 2005) due to its large spontaneous polarization although its magnetic moment is weak ($0.1\text{-}1 \mu_B/\text{f.u.}$). The dependence of the latter upon lattice parameters and film thickness opened various strategies to improve the magnetic properties of BFO. Taking a lead from Ueda-Tabata-Kawai experimental investigations (Ueda et al., 1998), where ordered $\text{LaFeO}_3\text{-LaCrO}_3$ layers, deposited on a SrTiO_3 substrate along the [111] direction, showed a strong magnetic order, Baettig & Spaldin proposed ordered $\text{BiFeO}_3\text{-BiCrO}_3$ layers along the [111] direction by replacing one atom of Fe out of two with Cr in the $(\text{BiFeO}_3)_2$ compound, as can be seen in Figure 4.1a,b,c. (Baettig & Spaldin, 2005a; Baettig et al., 2005b). These authors performed DFT calculations for different structural symmetries of the new compound $\text{Bi}_2\text{FeCrO}_6$ (BFCO) belonging to the $Pm\bar{3}m$, $Cmca$, $P4/mnc$, $R3m$ and $R3$ space groups for two magnetic configurations: ferromagnetic and ferrimagnetic ordering for Fe^{3+} -high spin (hereafter called FMHS and FiMHS, respectively). They found that the FiMHS state, with $R3$ rhombohedral symmetry (space group 146) has the lowest-energy, with alternating rotations of the oxygen octahedra about the [111] direction, combined with relative displacements of all ions along [111], as can be seen in Figure 4.1d,e,f. They calculated that oppositely oriented magnetic moments of the Fe^{3+} and Cr^{3+} ions give a net magnetic moment of $2 \mu_B/\text{f.u.}$, and a ferroelectric polarization of $79.6 \mu\text{C}/\text{cm}^2$.

Due to high interest in BFCO as a multifunctional material for potential applications, in part due to the fact that thin films of BFCO have been experimentally realized (Nechache et al., 2015; 2012; 2011; 2009; 2006), and that BFCO is therefore not a theoretically postulated material

anymore, its structural, electronic and magnetic properties were reinvestigated recently by Goffinet et al. (Goffinet et al., 2012) using different DFT functionals: LSDA, different LSDA+U variants, and the hybrid functional B1-WC (Bilc et al., 2008).

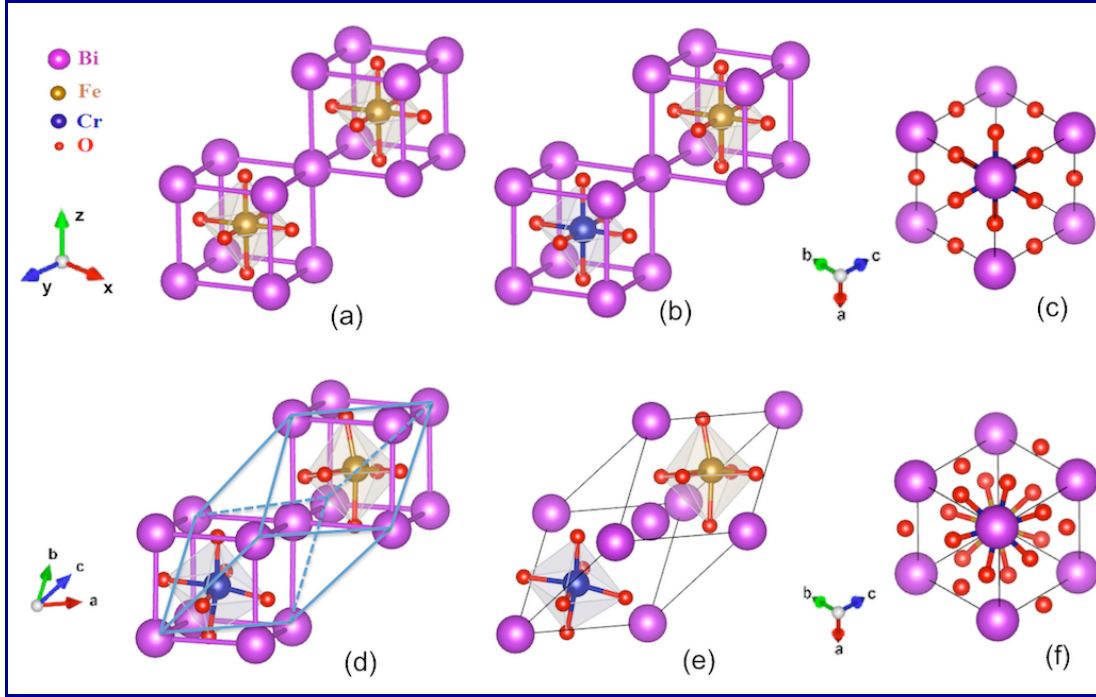


Figure 4.1 The ideal cubic rock-salt structure of $(\text{BiFeO}_3)_2$ (a); The ideal cubic rock-salt structure of $\text{Bi}_2\text{FeCrO}_6$ where one Fe atom from (a) was replaced by a Cr atom (b); The (111) plane projection of the BFCO ideal cubic structure shows perfect overlapping of the oxygen atoms belonging to the Cr and Fe octahedra (c); The rhombohedral $R\bar{3}$ symmetry (d-e) of BFCO; The (111) plane projection of the $R\bar{3}$ BFCO shows oxygen displacements as consequence of octahedra rotations in opposite directions and lattice distortions (f). Visualizations are performed using VESTA (Momma & Izumi, 2011).

These authors highlighted the existence of four different stable phases: (i) the ferrimagnetic phases with Fe^{3+} in a high spin configuration (FiMHS), and with Fe^{3+} in a low spin configuration (FiMLS); and (ii) the corresponding ferromagnetic phases for high spin (FMHS) and low spin (FMLS) configurations. Investigation on the relative stability of these four phases showed that all functionals consistently predicted FiMHS as the ground state, and a spin crossover from the FiMHS to FiMLS was found under compressive strain. Also, Goffinet and co-authors (Goffinet et al., 2012) noticed that their results are not directly comparable with those presented previously by Baettig, Ederer and Spaldin (Baettig & Spaldin, 2005a; Baettig et al., 2005b) because they did not refer to the same structures: in order to isolate structural and electronic effects, Baettig et al., used the structure obtained from LSDA with $U=0$ and computed the density of states (DOS) using different values of the Coulomb parameter U , while Goffinet et al., performed full

relaxation for each case.

In addition to these theoretical investigations, recent developments in the growth and characterization of BFCO epitaxial thin films (Nechache et al., 2012) have shown a thickness variation of the multiferroic properties, as Ueda-Tabata-Kawai found earlier for ordered LaFeO₃-LaCrO₃ layers along the [111] direction (Ueda et al., 1998), as well as ordered Fe and Cr with predominant +2 and +4 valence states in presence of oxygen vacancies, promoted by the low oxygen partial pressure and low growth rate used during the PLD growth (Nechache et al., 2015). Further studies are necessary to understand the mechanism leading to the Fe/Cr cation ordering as well as to explain the origin of the critical thickness, both having a strong effect on the magnetic properties.

4.2. Computational details

All calculations presented in this thesis were performed using the projector augmented plane-wave (PAW) formalism (Blöchl 1994; Kresse & Joubert, 1999) of density functional theory, by explicitly treating 15 valence electrons for Bi ($5d^{10}6s^26p^3$), 14 valence electrons for Fe ($3p^63d^64s^2$), 12 valence electrons for Cr ($3p^63d^54s^1$), and 6 valence electrons for oxygen ($2s^22p^4$), within the *Vienna ab initio Simulation Package* (VASP 5.3; 5.4) (Kresse & Furthmüller 1996a; 1996b) as integrated in the MedeA® computational environment (MedeA 2017; 2015).

For a better description of the Fe and Cr 3d electrons, the local-spin-density approximation with a *Hubbard-U* correction (LSDA+U) was used. For treating exchange and correlation, the so-called fully localized limit formulation (Liechtenstein et al., 1995; Anisimov et al., 1997) was considered, with parameters $U=3$ eV for the Coulomb repulsion, and $J=0.8$ eV for the exchange interaction, respectively, previously used in literature (Baettig & Spaldin, 2005a; Baettig et al., 2005b; Goffinet et al., 2012).

In addition, because the BFCO compound contains two different transition metals, Fe and Cr, the choice of the lowest order approximation, the LSDA+U formulation and its parameters, could be questionable (Goffinet et al., 2012). To circumvent this difficulty and to obtain conclusive theoretical results, other density functional approximations were used, namely the generalized gradient approximations with Perdew-Burke-Ernzerhof (PBE) functionals (Perdew et al., 1996): the revised PBE for transitions metals, RevPBE (Hammer et al., 1999); and the optimized PBE method for solids, PBEsol (Perdew et al., 2008), with the corresponding *Hubbard-U* correction. According to the Table 1 of Ref. (Perdew et al., 2008), tests of several functionals for 18 solids

(5 ionic solids, 4 transition metals, 4 simple metals and 5 semiconductors) show the smallest errors for the PBEsol functional.

The Kohn-Sham equations were solved self-consistently in their spin-polarized form (i.e., up and down spins have different spatial orbitals) employing an iterative matrix diagonalization and the spin interpolation of Vosko-Wilk-Nusair (Vosko et al., 1980) that is compatible with both LDA and PBE functionals. Wave functions represented in a plane-wave basis were truncated at 500 eV and electronic self-consistence cycles were converged down to the high precision 10^{-8} eV, necessary to achieve well-converged results at the meV scale. The integration over the first Brillouin zone is performed using symmetry-adapted Monkhorst–Pack grids (Monkhorst & Pack, 1976) of $8 \times 8 \times 8$ \mathbf{k} -points that generated 90 irreducible \mathbf{k} -points. For the density of states (DOS) and Born effective charges calculations, the Monkhorst-Pack grid was increased to $15 \times 15 \times 15$. Note that, \mathbf{k} -mesh was forced to be centered on the gamma point.

To determine the lattice parameters of the BFCO cell used as input, relaxations have been performed starting from the *Fm-3m* symmetry (space group #225) corresponding to the ideal cubic rock-salt structure (see Fig.4.2a). Each transition metal has been surrounded by an octahedron of oxygen anions having all Cr-O and Fe-O bond lengths equal (see Fig. 4.2a,b).

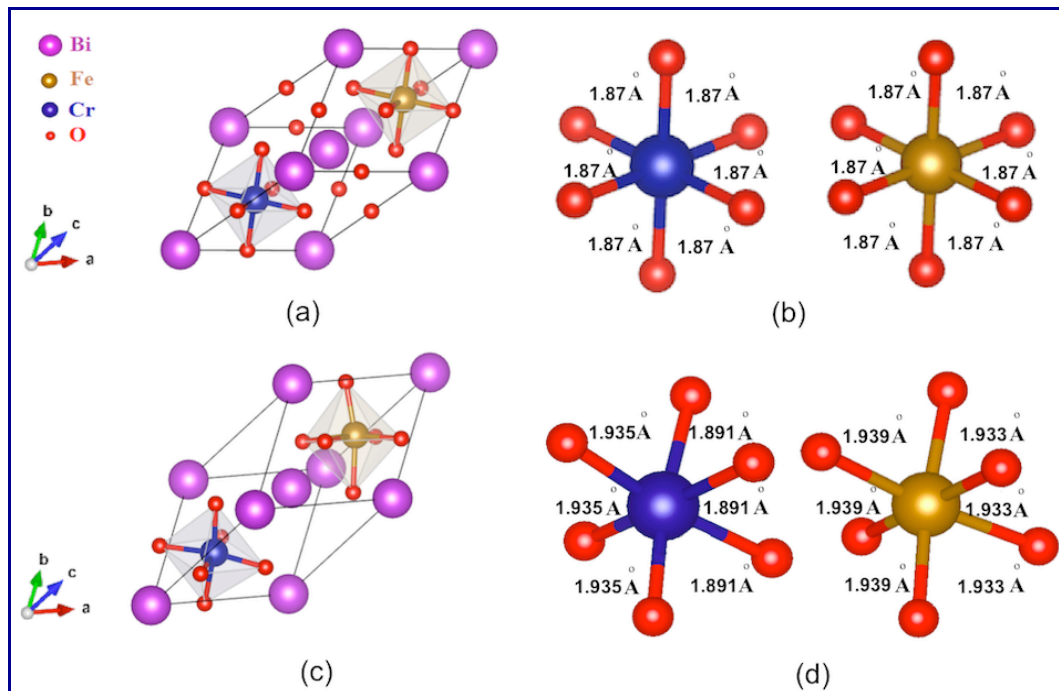


Figure 4.2 The non-magnetic *Fm-3m* optimized structure corresponding to the ideal cubic rock-salt structure of BFCO as seen in Figure 4.1b (a); The computed Cr-O and Fe-O bond lengths of the undistorted octahedra corresponding to the BFCO *Fm-3m* symmetry (b); The non-magnetic optimized distorted rhombohedral *R3* structure of BFCO (c); The Cr-O and Fe-O bond lengths of the distorted octahedra corresponding to the BFCO *R3* symmetry (d).

The full relaxation of atom positions has led to the same *Fm-3m* symmetry with a lattice constant $a_c = 5.30 \text{ \AA}$, and a volume $V_c = 105.4 \text{ \AA}^3$. The lattice angles were $\alpha_c = 60^\circ$, and the FeO_6 and CrO_6 octahedra were not distorted or/and rotated. This structure corresponds to a local minimum which is not the lowest one, and hence some distortions are manually added to the structure in order to achieve convergence to the true minimum. Moreover the *Fm-3m* symmetry does not allow ferroelectricity. Therefore, to force symmetry breaking, the adjacent oxygen octahedra were rotated in opposite directions about the [111] axis, and displaced relative to the central Bi cations, in opposite directions along the [111] axis (Côté, 2013). After optimization, the energy was lowered and a rhombohedral structure with *R3* symmetry (space group #146) was obtained (see Fig. 4.2c) with a lattice constant $a_r = 5.29 \text{ \AA}$, angles $\alpha_r = 61.2^\circ$ and volume $V_r = 107.7 \text{ \AA}^3$. The FeO_6 and CrO_6 octahedra were distorted, and the oxygen cages were rotated about the [111] Cartesian direction. Also, in optimized *R3* BFCO, the Cr-O and Fe-O bond lengths were elongated with respect to the ideal cubic structure (for a better comparison, see the bond lengths from Fig. 4.2b versus Fig 4.2d).

The above optimized *Fm-3m* and *R3* structures were obtained using non spin-polarized (i.e., non-magnetic) calculations. Further, self-consistent spin-polarized calculations, including the magnetic moments of Fe -high spin and -low spin, and Cr states, are performed, starting from the non spin-polarized calculation of the rhombohedral structure with *R3* symmetry.

4.3. Ground-state structures and magnetic orderings

Before pursuing into spin-polarized magnetic calculations, some considerations referring to the Fe and Cr formal valences are emphasized. In the previous theoretical investigations on the epitaxial BFCO thin films, highlighted in the Section 4.1, authors assumed formal valences +3, +3 for Fe and Cr. On the other hand, the bulk phase diagram relative to the formal valences and ionic radii of the transition metals reported by Ohtomo and coworkers for $\text{La}_2\text{FeCrO}_6$ (Ohtomo et al., 2013), showed that ordering of the transition ions facilitates synthesis of a bulk form when there is a large difference in the formal valences (i.e., +2 and +4 valence states in the case of Fe and Cr). In addition, XPS measurements in the epitaxial ordered BFCO thin films (Nechache et al., 2015) revealed the presence of predominantly Fe^{2+} and Cr^{4+} valence states, which have been attributed to the presence of oxygen vacancies.

The question is: *what are the appropriate valence states for Fe and Cr to be used in our DFT calculations?* For this aim, the charge densities depletion around Fe and Cr were computed together with relaxations of the BFCO using the methodology described in the Section 4.2 (oxygen vacancies are not included as they do not represent the subject of this thesis). Although it was found that the charges of the Fe and Cr ions are not +3, they are in the ratio ~1:1, which supports the hypothesis of the formal valence states of Fe^{3+} and Cr^{3+} , and not the hypothesis of the Fe^{2+} and Cr^{4+} valence states that would imply the ratio 1:2.

The charge states of Fe and Cr have obvious consequences on the electron configurations in d orbitals and on the magnetic moments. In the case of BFCO, the d orbitals of $\text{Fe}^{3+}(3d^5)$ are splitting into two sets, a triply degenerate set d_{xy} , d_{xz} , d_{yz} (t_{2g} level), and a doubly degenerate set d_x^2 , d_z^2 (e_g level) slightly higher in energy, as expected for an octahedral coordination. Depending on the energy difference between t_{2g} and e_g levels, it may result a Fe^{3+} -low spin (LS) electron configuration $(t_{2g\uparrow\downarrow})^5(e_{g\uparrow})^0$, or a Fe^{3+} -high spin (HS) electron configuration $(t_{2g\uparrow\downarrow})^3(e_{g\uparrow})^2$. The d orbitals of $\text{Cr}^{3+}(3d^3)$ also split into t_{2g} and e_g levels, but always with an empty e_g level, i.e. with occupation $(t_{2g\uparrow})^3(e_{g\uparrow})^0$. Therefore the magnetic moments of Fe^{3+} -HS, Fe^{3+} -LS and Cr^{3+} are expected to be ~ 5, 1 and 3 μ_B , respectively.

In this section, self-consistent spin-polarized calculations are performed for four different possible magnetic phases: Fe^{3+} high-spin ferrimagnetic FiMHS & ferromagnetic FMHS states, and the corresponding Fe^{3+} low-spin states FiMLS & FMLS. The computed local magnetic moments, together with respective structural parameters are summarized in Table 4.1 for all three functionals LSDA+U, PBEsol+U and RevPBE+U. The optimized structures for the FiMHS, FiMLS, FMHS and FMLS magnetic phases are depicted in Figure 4.3, where the spin of Fe^{3+} is marked by a yellow arrow parallel or antiparallel to the spin of Cr^{3+} marked by a green arrow. Note that in the collinear calculations, spin-orbit coupling is not included, and hence the spin direction is arbitrary (however, the spins for Fe^{3+} and Cr^{3+} are either parallel or antiparallel). In Figure 4.3, the spin orientations for Fe^{3+} and Cr^{3+} were chosen up/down perpendicular to the [111] direction, because it is usually assumed (a common but unproven assumption) that magnetic vectors like to be perpendicular to the polarization vector (spontaneous polarization was computed in the Section 4.6 and found to be parallel to the [111] direction).

Table 4.1 Summary of the structural and electronic properties of the FiMHS, FiMLS, FMHS, and FMLS phases of BFCO, as computed using the LSDA+U, PBEsol+U and RevPBE+U functionals. The rhombohedral unit cell parameters are length a_r and angle α_r ; V_r is the unit cell volume; x_i , y_i , and z_i represent the Wyckoff positions of the space group 146 (*R*3 symmetry) in the rhombohedral setting, i.e., $Bi_{1,2}(x, x, x)$, $Fe(x, x, x)$, $Cr(x, x, x)$ and $O_1(x_{01}, y_{01}, z_{01})$, $O_2(z_{01}, x_{01}, y_{01})$, $O_3(y_{01}, z_{01}, x_{01})$, $O_4(x_{02}, y_{02}, z_{02})$, $O_5(z_{02}, x_{02}, y_{02})$, $O_6(y_{02}, z_{02}, x_{02})$; μM_{Fe} and μM_{Cr} are the local magnetic moments of Fe and Cr; μM_{BFCO} is the total magnetic moment per unit cell; Computed charges of Fe and Cr; ΔE is the energy difference between the corresponding phase and the FiMHS ground state.

	LSDA+U				PBEsol+U				RevPBE+U			
Phase	FiMHS	FiMLS	FMHS	FMLS	FiMHS	FiMLS	FMHS	FMLS	FiMHS	FiMLS	FMHS	FMLS
a_r in Å	5.48	5.36	5.49	5.37	5.42	5.35	5.43	5.33	5.61	5.55	5.61	5.62
α_r in °	60.04	60.80	60.04	60.76	60.74	61.02	60.74	61.08	59.72	59.98	59.75	59.73
V_r , Å ³	116.3	111.1	116.9	111.5	114.7	111.2	115.1	110.2	124.4	121.3	124.7	125.3
X_{Bi}	0.000	0.000	0.000	0.000	0.000	0.000	0.000	0.000	0.000	0.000	0.000	0.000
X_{Bi}	0.503	0.495	0.504	0.496	0.504	0.496	0.505	0.497	0.511	0.505	0.512	0.505
X_{Fe}	0.732	0.726	0.731	0.727	0.732	0.726	0.731	0.726	0.732	0.726	0.731	0.725
X_{Cr}	0.226	0.227	0.226	0.228	0.226	0.228	0.225	0.228	0.224	0.225	0.224	0.227
X_{O1}	0.544	0.545	0.545	0.546	0.545	0.546	0.546	0.547	0.544	0.546	0.545	0.547
y_{O1}	0.950	0.952	0.949	0.950	0.950	0.948	0.948	0.947	0.947	0.948	0.947	0.946
Z_{O1}	0.398	0.410	0.400	0.410	0.397	0.411	0.399	0.410	0.393	0.402	0.396	0.403
X_{O2}	0.046	0.041	0.044	0.041	0.047	0.038	0.044	0.039	0.044	0.044	0.042	0.043
y_{O2}	0.905	0.904	0.905	0.905	0.905	0.904	0.905	0.905	0.903	0.900	0.903	0.900
Z_{O2}	0.447	0.457	0.449	0.454	0.447	0.456	0.449	0.455	0.445	0.450	0.446	0.450
μM_{Fe} in μ_B	-3.98 -3.98*	-0.86 -0.86*	+4.03 +4.03*	+1.02 +1.02*	-4.06 -4.06*	-0.75 -0.75*	+4.09 +4.09*	+0.91 +0.91*	-4.10 -4.11*	-0.93 -0.93*	+4.12 +4.13*	+0.87 +0.88*
μM_{Cr} in μ_B	+2.54 +2.51*	+2.74 +2.68*	+2.86 +2.80*	+2.72 +2.67*	+2.63 +2.60*	+2.75 +2.71*	+2.91 +2.85*	+2.76 +2.72*	+2.71 +2.70*	+2.89 +2.86*	+2.96 +2.92*	+2.82 +2.79*
μM_{BFCO} in μ_B	-1.98 -2.00*	+1.90 +2.00*	+7.66 +8.00*	+3.82 +4.00*	-1.99 -2.00*	+1.88 +2.00*	+7.69 +8.00*	+3.84 +4.00*	-1.98 -2.00*	+1.91 +2.00*	+7.71 +8.00*	+3.84 +4.00*
Charge Fe in e	+2.01	+1.74	+2.02	+1.64	+2.02	+1.78	+2.03	+1.70	+2.13	+1.94	+2.13	+2.01
Charge Cr in e	+2.01	+2.00	+2.01	+2.01	+2.01	+2.02	+2.01	+2.02	+2.02	+2.12	+2.13	+2.14
ΔE in meV	0 I	372.6 III	164 II	749.9 IV	0 I	713.9 III	112.8 II	1204.8 IV	0 I	1020.5 III	68.7 II	1199.4 IV

* The local magnetic moments computed by using Bader charge analysis.

Our first-principles structural parameters are consistent with those reported by Goffinet *et al.* (Goffinet *et al.*, 2012) for the LSDA+U and B1-WC functionals that they considered. In particular, the order of the magnetic states FiMHS (I), FMHS (II), FiMLS (III), and FMLS (IV) on the energy scale is preserved for our three considered functionals. In addition, for calculating the local magnetic moments, we performed Bader charge analysis (indicated by *) which, through integration of the electronic charge density (spin-up, spin-down charges) within Bader volumes, provides a better approximation than the usual spherical volumes from the plane-wave (PAW) set calculations (Tang *et al.*, 2009; Sanville *et al.*, 2007; Henkelman *et al.*, 2006). One observes that the computed charge of the Fe and Cr ions are in the ratio ~1:1 for all four magnetic states, all three functionals, and for both methods of computing the ionic charge.

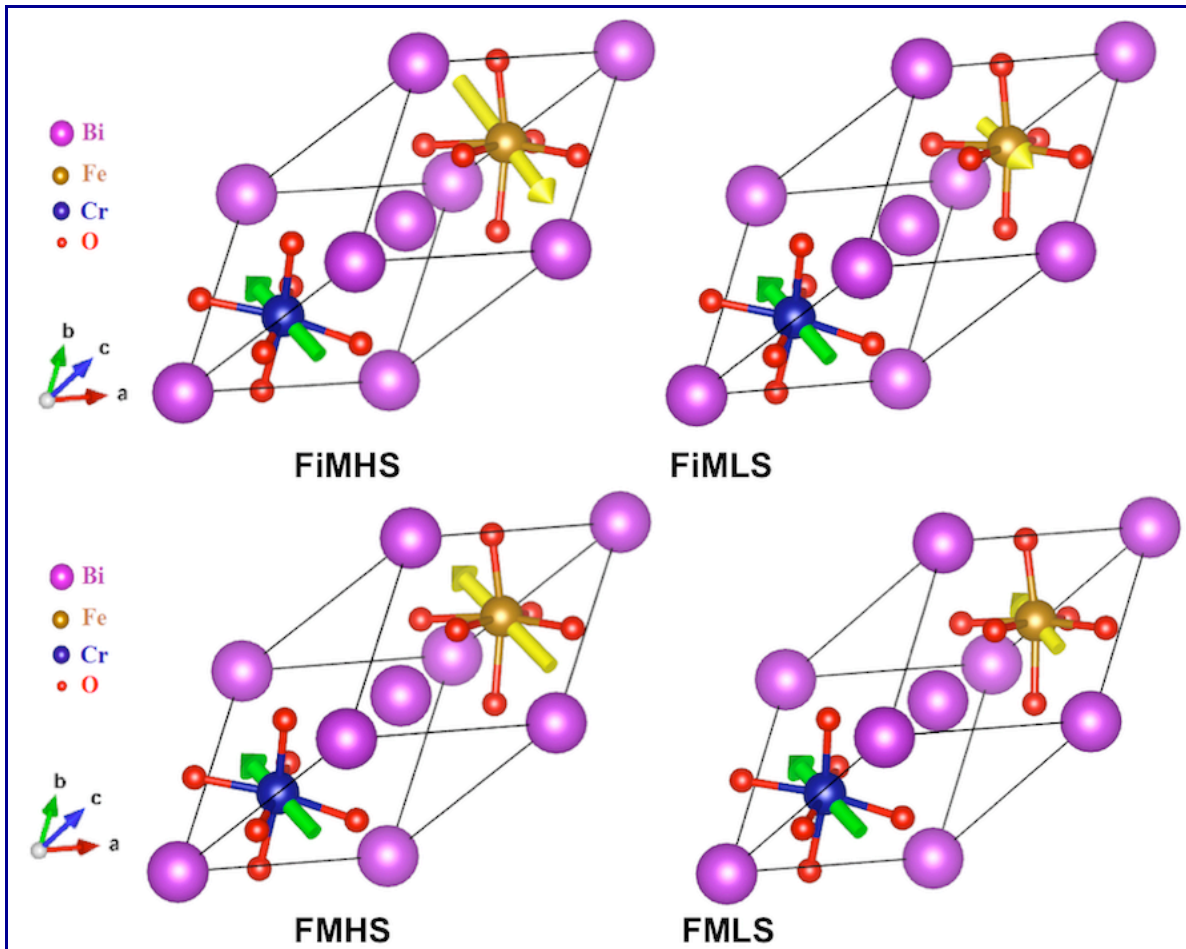


Figure 4.3 Rhombohedral unit cells of the collinear magnetic optimized BFCO structures corresponding to the ferrimagnetic Fe^{3+} -high spin (FiMHS), Fe^{3+} -low spin (FiMLS), ferromagnetic Fe^{3+} -high spin (FMHS), and Fe^{3+} -low spin (FMLS) states. The spin of Cr^{3+} is marked by a green arrow, and the spin of Fe^{3+} is marked by a yellow arrow parallel or antiparallel to the chosen spin orientation (up/down perpendicular on [111] direction) and the computed spin size (high, low).

It can be seen from Table 4.1 that both Fe^{3+} high-spin states, FiMHS (I) and FMHS (II), with net magnetic moments of $2 \mu_B/\text{f.u.}$ and $8 \mu_B/\text{f.u.}$, respectively, are more stable than the low spin states, and have significantly higher volumes (with the exception of FMLS for RevPBE). The energy difference between FiMHS and FMHS is small for LSDA+U, and much smaller for PBEsol & RevPBE functionals. This opens the possibility that FMHS, which has the high magnetic moment of $8 \mu_B/\text{f.u.}$, could be stabilized by an appropriate perturbation (e.g. lattice strains or magnetic field), and hence it could represent a significant development for many applications requiring higher magnetization.

On the other hand, both Fe^{3+} low-spin states, FiMLS (III) and FMLS (IV) have a lower volume (with the exception of FMLS for RevPBE), that could be favoured by compressive strains (due to

the negative lattice mismatch between film and substrate for instance). The energy difference ΔE between the ground state and the two LS states is significantly larger than the energy difference between the two HS states, which indicates weaker interactions in the LS phases. Regarding the RevPBE functional used to cross-check our results, it can be seen that lattice lengths and cell volumes are over the ranges computed using LSDA+U and PBEsol+U, and the energy difference between FiMLS and FMLS magnetic states is smaller, even though the order of the magnetic states is still preserved, in agreement with previous results (Goffinet et al., 2012).

More insights regarding electron localization can be found from the electron localization function (ELF) analysis which identifies regions where electrons are localized (Savin et al., 1997; Becke et al., 1990). As there are no visible differences of the contour plots between the ELFs of LSDA+U, PBEsol and RevPBE, in the following the computed ELF will be discussed only for LSDA+U.

The ELF is a probability measure and it is represented, for each atom, as a contour plot with values between 0 and 1. The calculated ELF for BFCO are depicted in Fig. 4.4, where the contour plot range was reduced from [0; 1] to [0; 0.8] for a better visualization.

The negligibly small values of the ELF between atoms (dark blue) indicate dominant ionic bonding. Comparing the computed ELF distributions of the highly symmetric *Fm-3m* structure with the distorted *R3* structures, it can be seen that the ELF shows decreasing values on the atoms when passing from the *Fm-3m* to the *R3* symmetry, indicating a strong charge-transfer interaction in the optimized magnetic structures. These results show a mixed ionic-covalent character of the bonds. In addition, a short-range repulsion between adjacent closed shells is observed for the highly symmetric structure where distortions do not exist. In contrast, in the case of optimized magnetic states, additional bonding act to stabilize the distortions necessary for ferroelectricity to exist.

The approximately spherically distributed 6s *lone pairs* around Bi atoms in the highly symmetric non-magnetic structure distort to form asymmetric green rings of localization (a similar behaviour was reported (Seshadri & Hill, 2001) for BiFeO_3). Bi ions are shifted away from their central symmetric positions along the [111] direction and lone pairs stabilize into lobe shape (horseshoe geometry around Bi in the case of magnetic states), driving additional structural distortions that will influence ferroelectricity.

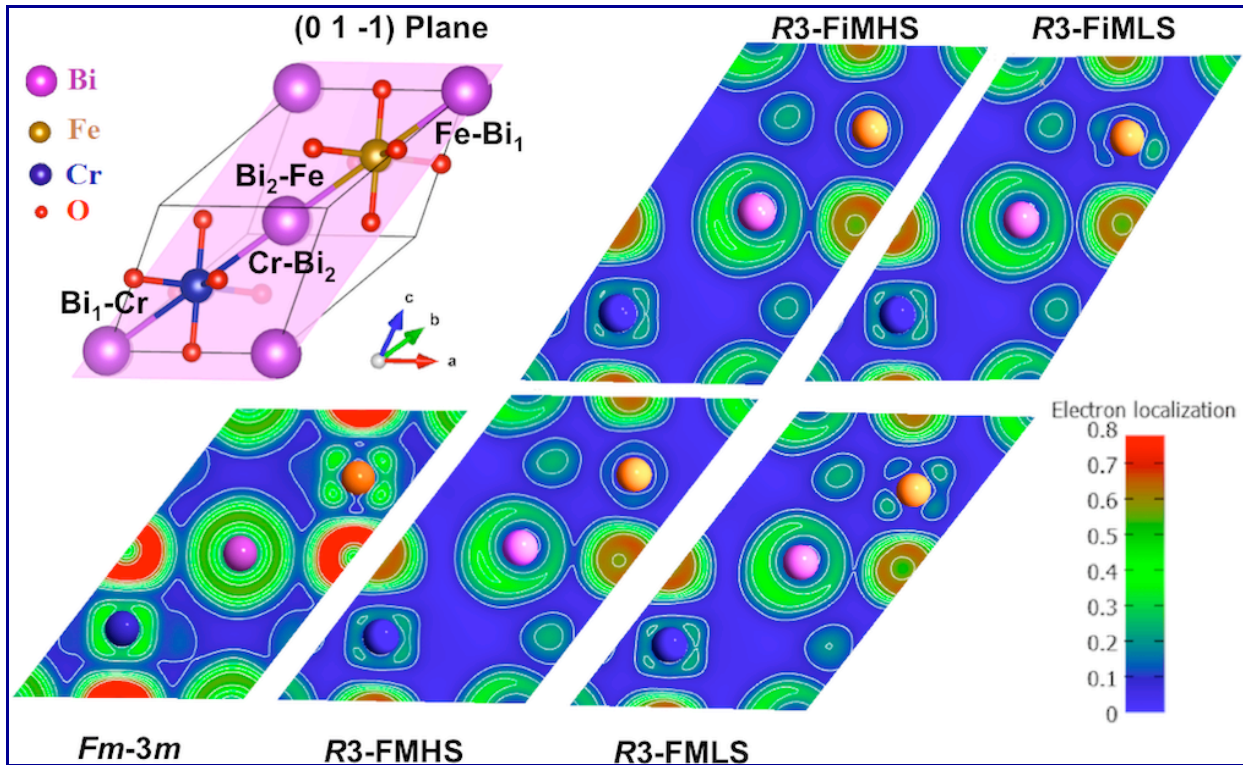


Figure 4.4 Calculated electron localization functions (ELFs) for the BFCO highly symmetric *Fm-3m* non-magnetic structure (left), and the rhombohedral optimized structures corresponding to the FiMHS, FiMLS, FMHS and FMLS magnetic states. The considered cutting plane (0 1 -1), which contains Bi, Fe, Cr and four oxygen atoms emphasizes the bonds between Bi₁, Cr, Bi₂ and Fe which are discussed in this thesis. Visualizations have been performed using Virtual NanoLab (Virtual NanoLab, 2016).

To find more insights supporting these findings, the density of states (DOS) band structures were calculated for the highly symmetric *Fm-3m* structure, and for the rhombohedral *R3* FiMHS, FiMLS, FMHS, and FMLS magnetic states using the considered LSDA+U and PBE+U functionals.

4.4. Electronic properties

To gain more insights into the electronic structure and bonding behaviour for BFCO, the electronic structure of the highly symmetric *Fm-3m* (called paramagnetic) phase, without including magnetic effects, is calculated first. Although this phase is experimentally inaccessible, it provides useful reference for understanding the spin-polarized structures and distortions within the rhombohedral *R3* BFCO that enhance ferroelectricity.

The partial and total density of states (DOS), and the corresponding band structures were calculated for fully optimized crystal structures of BFCO. Since the outer shell electron configurations for Bi ($5d^{10}6s^26p^3$), Fe ($3p^63d^64s^2$), Cr ($3p^63d^54s^1$), and O ($2s^22p^4$) are treated explicitly within the projector augmented plane-waves (PAW) formalism, their corresponding s, p and d states could be plotted and analyzed in detail. In *R3* spin-polarized calculations, the spin-up of the Cr ion defines the *spin-up states* depicted on the positive axis of the DOS plots (the same convention was used in Table 4.1).

The electronic bands are drawn along the standard pathways within irreducible edge of the Brillouin zone of the *Fm-3m* and *R3* lattices, where $\Gamma(0,0,0)$ is the center point, and Fermi energy E_F is set to zero (note that the computed E_F for *R3* magnetic states are lower than those for *Fm-3m*, i.e., the bands are translated up, compared with symmetric non-magnetic state, when E_F is set to zero). When the magnetic effects are included, bands are marked with red for spin-up electrons, and with blue for spin-down electrons.

Figure 4.5 compares the partial and total DOS of the ideal highly symmetric (paramagnetic) BFCO with the rhombohedral *R3* distorted (ferrimagnetic) FiMHS phase, and the corresponding band structures within the LSDA+U functional.

The pictures corresponding to the ideal highly symmetric *Fm-3m* structure of BFCO clearly show the metallic character of the paramagnetic phase, as the valence and conduction bands are overlapping. On the contrary, the DOS and bands of the *R3* FiMHS phase of BFCO indicate a semiconductor character, in agreement with the results reported in Refs. (Goffinet et al., 2012; Baettig et al., 2005b). The orbitals close to the Fermi level are mainly Fe-3d and Cr-3d, which have significant components into both the valence band (VB) and the conduction band (CB).

By inspecting the DOSs and bands starting from the bottom to the top of the energy scale, a sharp peak between -12 eV and -8 eV, corresponding to the Bi-6s orbital, is visible, and it is shifted up from the ideal symmetric structure due to structural distortions (i.e. the Fermi energy decreased). In the distorted *R3* structure, many bands avoid crossing in VB, showing the existence of hybridization (this does not take place in the case of the symmetric structure).

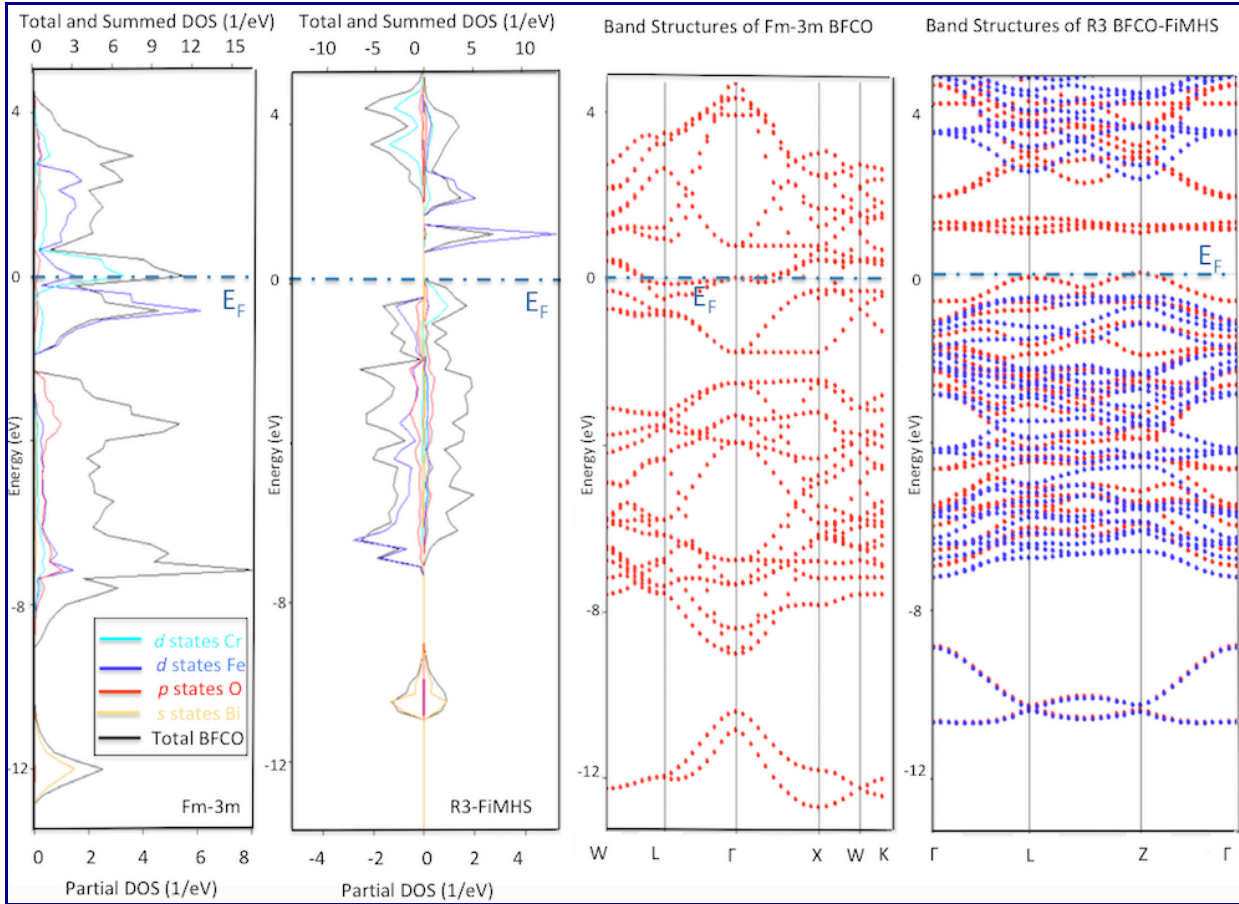


Figure 4.5 The computed partial and total DOS, and band structures within the LSDA+U functional for the BFCO highly symmetric structure (*Fm-3m*) compared with the rhombohedral *R3* FiMHS magnetic state of BFCO. Note that the bottom axis indicating partial DOS and the top axis indicating total DOS have different scales.

Figures 4.6 and 4.7 compare the DOSs and band structures between the ferrimagnetic phases FiMHS and FiMLS of the rhombohedral *R3* BFCO, and the ferromagnetic phases FMHS and FMLS, respectively, within the LSDA+U functional. Figure 4.6 shows small difference between the band gaps (i.e., 0.92 and 1.07 eV according to the computed values from Table 4.2), it also shows that the states of Cr-3d do not change considerably in the VB (see red bands), but the states of Fe-3d do change from HS to LS. It can be seen that many bands (blue) are crossing in the LS case indicating a decreased in the level of hybridization.

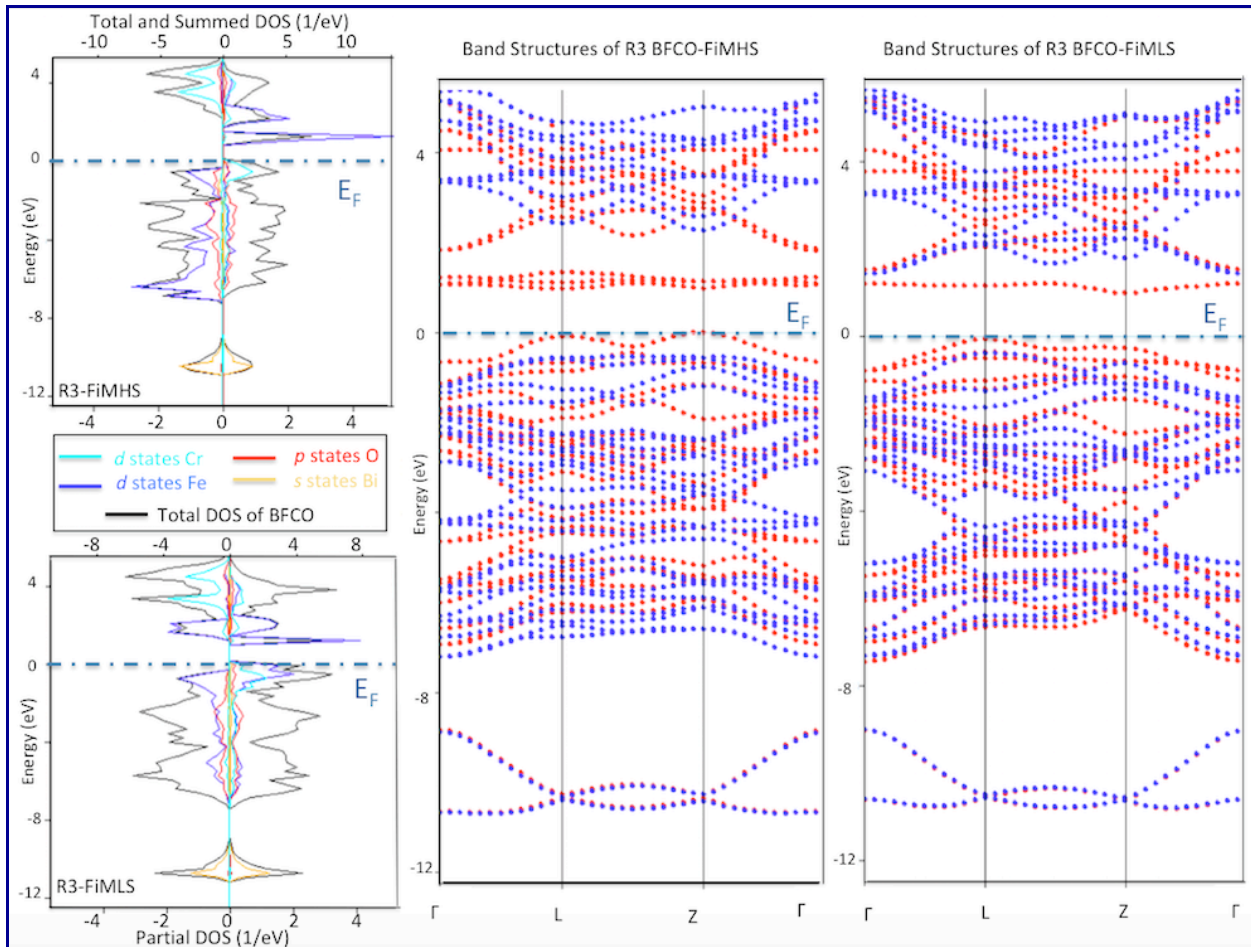


Figure 4.6 The computed partial and total DOS and band structures within the LSDA+U functional for the FiMHS phase compared with the FMLS phase for the rhombohedral R3 BFCO.

Figure 4.7, corresponding to the ferromagnetic (FM) phase, shows smaller values of the band gaps with Cr-3d valence band near the Fermi level for the FMHS, and Fe-3d valence band near the Fermi level for the FMLS, respectively.

To get more details, it is worth investigating s, p and d orbitals for each type of ion (Bi, Fe, Cr and O) within the LSDA+U functional. These orbitals are depicted in the Figures A1.1-A1.4 in Appendix I.

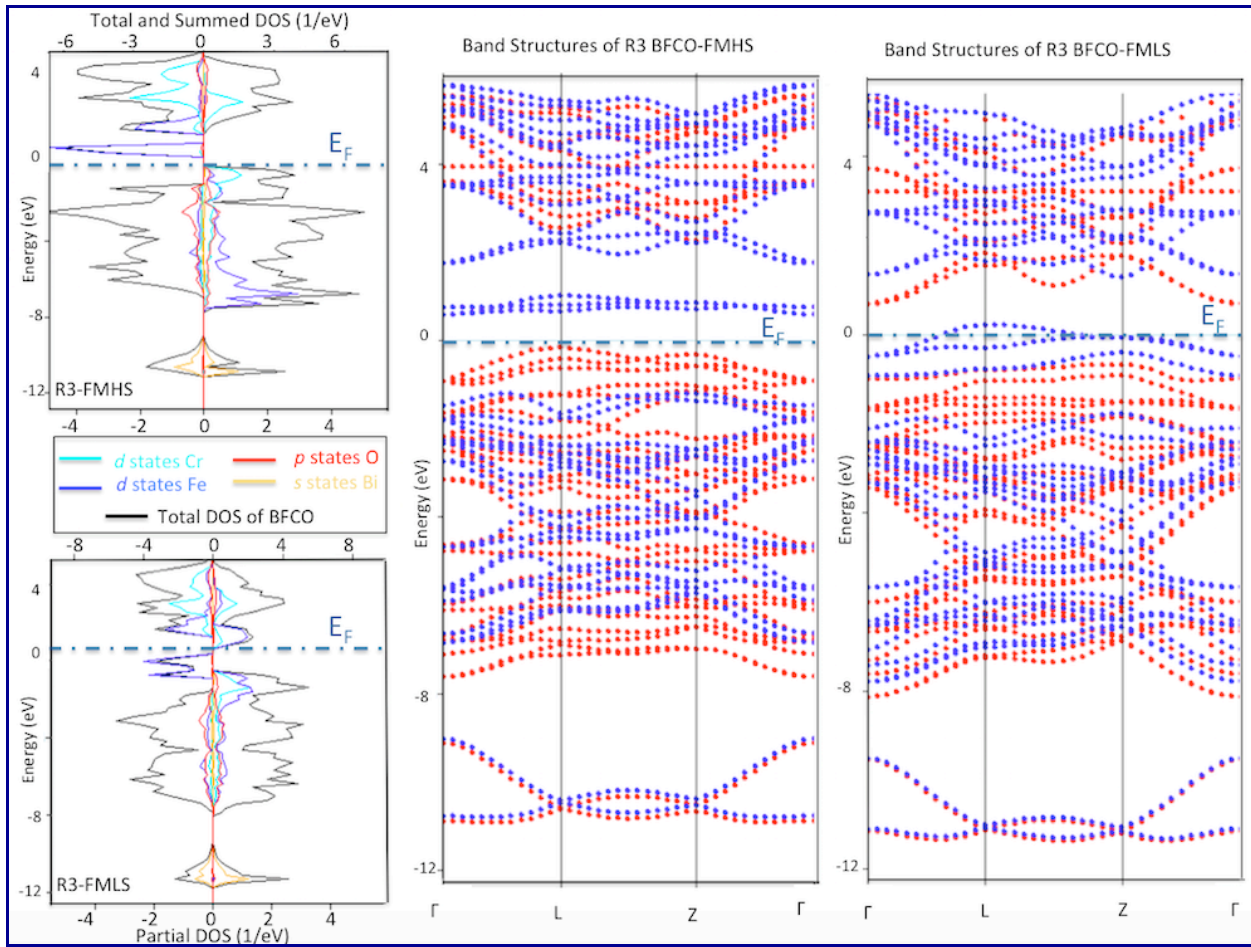


Figure 4.7 The computed partial and total DOS and band structures within the LSDA+U functional for the FMHS phase compared with the FMLS phase for the rhombohedral *R*3 BFCO.

In addition to the information found previously for the Bi-6s orbitals in the VB, Figure AI.1 shows the contribution of the Bi-6p orbitals to the CB. In the case of Fe (see Figure AI.2) comparing the contribution of the *s*, *p* and *d* states between the symmetric and the *R*3 FiMHS, FiMLS, FMHS and FMLS magnetic phases, it can be seen that the Fe-3p orbitals are present in the paramagnetic phase only. The bands for Fe-3d states are wider in the *R*3 cases, showing orbitals overlapping. In the case of Cr (see Figure AI.3), it can be seen that the contribution of the Cr-4s orbital is highest in the conduction band for the LS magnetic phases, in addition to the orbital overlapping from the VB. Finally, Figure AI.4 of the Appendix I, proves that the main contribution of the oxygen atoms is due to their p-orbitals from the VB that hybridize with both Fe-3d and Cr-3d orbitals.

To examine the band-gap opening for the ferro- and ferrimagnetic phases, features near the Fermi level E_F are examined more in detail for all atomic species. Figure AI.4 shows that the

contribution of the oxygen atoms is almost negligible in the vicinity of the Fermi level, but the dominant effect is coming from Fe-3d and Cr-3d orbitals. Actually, the gap is opened because the Fe-3d peak from the VB due to distortions is pushed up to the positive side of E_F in the CB.

To understand how the PBEsol+U and RevPBE+U functionals influence the electronic properties, the DOSs of all magnetic states were computed and compared with the LSDA+U. As PBEsol presumably produces results with the smallest errors (Perdew et al., 2008), the partial and total DOSs for PBEsol+U compared with LSDA+U functional are depicted in the Figures AI.5a,b-AI.8a,b for Bi, Fe, Cr and O. It can be seen that, within the PBEsol functional, the main contribution is brought by the Fe-3d peaks from the upper vicinity of E_F that are pushed a little bit upper to the higher energies, thus increasing slightly the band-gap values for all the FiMHS, FiMLS, FMHS and FMLS phases. Note that, as shown in Figures AI.7a,b, the Cr-4s orbital from the conduction band for the LSDA+U functional does not have any contribution. Instead, the contribution of the Cr-3d orbitals have been increased in the conduction band for FiMHS phase. Bi and O orbitals for PBEsol+U almost have the same contributions as in the case of LSDA+U. Very small variations can be seen for Bi-6s orbitals for PBEsol+U, and O-2p orbitals from the valence band have stronger hybridization in the case of FiMHS phase.

The computed band gap values for LSDA+U and GGA+U functionals are presented in the Table 4.2.

Table 4.2 The computed band gaps of the R3 FiMHS, FiMLS, FMHS and FMLS magnetic phases of BFCO within the LSDA+U, PBEsol+U and RevPBE+U functional.

Functional	Band gap [eV] FiMHS	Band gap [eV] FiMLS	Band gap [eV] FMHS	Band gap [eV] FMLS
LSDA+U	0.92	1.07	0.73	0.59 & 1.24 two spin channels
PBEsol+U	1.06	1.21	0.87	0.68 & 1.29 two spin channels
RevPBE+U	1.25	1.54	1.17	0.42 & 1.42 two spin channels
System	Semiconductor Ferrimagnet	Semiconductor Ferrimagnet	Semiconductor Ferromagnet	Half-metallic Ferromagnet

Calculations show increased band gaps for the PBEsol+U and RevPBE+U, while PBEsol+U shows closer values with those obtained using the LSDA+U functional. In addition, for the first time are reported two spin channels for FMLS magnetic phase are reported, where metallic and semiconducting properties are combined in a single system at the microscopic level within the unit cell. According to Ref. (Pickett & Eschrig, 2007), we can speak about half-metallicity when one spin subsystem (i.e., spin up or down) is a metal and the other is an insulator or

semiconductor (i.e., gapped) or a semi-metal (zero-gapped). This is a very interesting property for spintronics which has long sought materials candidates with half-metallicity behaviour. Note that LSDA+U band gap values are generally in agreement with those reported by Ref. (Goffinet et al., 2012), with the exception of the FMLS state. The discrepancies between our results and those of Ref. (Goffinet et al., 2012) for FMLS, can be explained by the fact that the VASP software provides a decomposition of density of states in terms of s, p, d, f orbitals for each atom of the system disregarding the crystal symmetry, and hence the partial DOS of actually equivalent atoms in terms of symmetry may differ from each other (wide difference for FMLS). The calculations reported in this work were done using MedeA-VASP from Materials Design (Materials Design 2017; 2011) which provides improvements and goes a step beyond VASP, i.e. it symmetrizes the partial DOS components and hence MedeA obtains the correct partial DOS (s, p, d, f) for each site. Before the use of MedeA-VASP, when we validated our first results for the LSDA+U functional using VASP license as a standalone software, we obtained the same band gaps as Goffinet and co-authors, including in the case of the FMLS magnetic state (with a band gap of ~1 eV).

4.5. Distortions and octahedra tilting/rotations

It was shown previously (Section 4.2) that the FeO_6 and CrO_6 octahedra were not distorted or rotated within the $Fm\text{-}3m$ symmetry corresponding to the ideal cubic rock-salt structure of BFCO (see Figure 4.2a), while the oxygen octahedra were rotated about the [111] direction and distorted in the case of the rhombohedral $R\bar{3}$ structure (see Figure 4.2c). In addition, the Fe-O and Cr-O bonds were elongated in the [111] direction and the O-Fe-O and O-Cr-O bond angles deviated substantially from the ideal cubic double perovskite structure (Figure 4.2b,d).

It is notable that perovskites containing Jahn-Teller ions (see Section 2.3.3) on the octahedral sites have been reported to exhibit interesting physical properties, such as spin ordering and cooperative Jahn-Teller (JT) distortions (Lufaso & Woodward, 2004). As it was already mentioned in this chapter, the d orbitals of $\text{Fe}^{3+}(3d^5)$ are splitting into two sets, a triply degenerate set d_{xy} , d_{xz} , d_{yz} (t_{2g} level), and a doubly degenerate set $d_x^2 - y^2$, d_z^2 (e_g level) slightly higher in energy, as expected from an octahedral coordination.

Since the $(t_{2g\downarrow\downarrow})^5(e_{g\uparrow})^0$ has t_{2g} shell unevenly occupied, Fe^{3+} -low spin undergoes a first-order Jahn-Teller (FOJT) distortion (King & Woodward, 2010), while Fe^{3+} -high spin and Cr^{3+} are first-order Jahn-Teller inactive since the e_g and t_{2g} shells are evenly filled (King & Woodward, 2010 ;

Lufaso & Woodward, 2004). The off-centering of Fe^{3+} -high spin and Cr^{3+} ions within their oxygen octahedra consequently cannot be driven by a FOJT distortion, but it might be driven by a second-order Jahn–Teller (SOJT) distortion (King & Woodward, 2010), which may require a formally empty d -electron configuration and/or an active lone-pair cation (the lone pair effect is so-called “JT combined with Pseudo Jahn-Teller distortion” (Bersuker, 2006; 2001)). This is the case of BiFeO_3 (Neaton et al., 2005), BiCrO_3 (Hill et al., 2002), and BiMnO_3 (Seshadri & Hill, 2001), where the lone pair on the Bi^{3+} ion is a well-established source of off-center distortion leading to ferroelectricity. More precisely, the $6s^2$ electron orbital of Bi^{3+} does not remain spherical and mixes with the p states of oxygen ions to form a spatially localized lobe (horseshoe-shaped ELF around the Bi atom, as seen in Fig. 4.4 for the $R3$ BFCO structures, which results in pushing away the Bi^{3+} neighbouring atoms.

For BFCO, Figures 4.2b and 4.2d, where the Cr-O and Fe-O bonds are depicted, show that the equal bonds of the ideal cubic structure are trigonal elongated, following the three-fold symmetry of $R3$, after full relaxation of the rhombohedral structure. Three bonds, corresponding to the first group of oxygen atoms with Wyckoff positions (x_{01}, y_{01}, z_{01}) , (z_{01}, x_{01}, y_{01}) , (y_{01}, z_{01}, x_{01}) , given in Table 4.1, are equally elongated along the [111] direction, on one side of the Fe^{3+} or Cr^{3+} cations. The other three bonds corresponding to the oxygen atoms with Wyckoff positions (x_{02}, y_{02}, z_{02}) , (z_{02}, x_{02}, y_{02}) , (y_{02}, z_{02}, x_{02}) , are also equally elongated on the other side of the Fe^{3+} or Cr^{3+} cations (by a different amount) showing clearly a trigonal distortion of the octahedra (Bersuker, 2006). Note that the most frequent distortions of the MO_6 octahedra are elongations of the two axial M-O bonds, and contractions of the other four in-plane M-O bonds. To understand the origin of the trigonal elongations present in $R3$ BFCO (on both sides of the Fe/Cr cations), a different approach called JT vibronic coupling effects (Bersuker, 2006) should be used, i.e., a tool referring to phonon modes which is applicable to any system with more than two atoms. Although, vibroning coupling effects are important in a whole range of spectroscopy techniques (UV, X-ray, photoelectron), structural phase transitions, ferroelectricity, colossal magneto-resistance, etc., calculations of the phonons are outside the scope of this thesis.

The computed bond lengths, within the LSDA+U, PBEsol+U and RevPBE+U functionals, between the Bi, Cr and Fe atoms along the [111] diagonal (see the top-left panel of Fig. 4.4), as well as the bond lengths, corresponding to (x_{01}, y_{01}, z_{01}) and (x_{02}, y_{02}, z_{02}) , are presented in Tables 4.3 and 4.4 for all considered structures, namely the ideal cubic rock-salt structure, non-magnetic optimized rhombohedra, as well as FiMHS, FiMLS, FMHS, and FMLS magnetic

phases. Here Bi_1 and Bi_2 are the Bi atoms at the lower left corner and at the center of the rhombohedron, respectively.

Table 4.3 The calculated bond lengths, within the LSDA+U, PBEsol+U and RevPBE+U functionals, between Bi_1 , Cr, Bi_2 and Fe (see top-left panel of Fig. 4.4) along the diagonal [111] direction.

BFCO symmetry	$\text{Bi}_1\text{-Cr}$ [\AA]	$\text{Cr}\text{-Bi}_2$ [\AA]	$\text{Bi}_2\text{-Fe}$ [\AA]	$\text{Fe}\text{-Bi}_1$ [\AA]	Diagonal $\text{Bi}_1\text{-Cr}\text{-Bi}_2\text{-Fe}\text{-Bi}_1$	Cell Volume [\AA^3]
Ideal cubic $Fm\text{-}3m$	3.31	3.31	3.31	3.31	13.24	105.4
Non-magnetic $R3$	3.01	3.37	3.00	3.41	12.79	107.7
FiMHS LSDA+U	3.02	3.72	3.06	3.60	13.40	116.3
FiMHS PBEsol+U	3.03	3.60	3.06	3.50	13.19	114.7
FiMHS RevPBE+U	3.07	3.86	3.11	3.73	13.77	124.4
FiMLS LSDA+U	2.97	3.49	3.01	3.57	13.04	111.1
FiMLS PBEsol+U	3.04	3.46	3.03	3.47	13.00	111.2
FiMLS RevPBE+U	3.06	3.74	3.06	3.74	13.60	121.3
FMHS LSDA+U	3.03	3.73	3.05	3.61	13.42	116.9
FMHS PBEsol+U	3.04	3.60	3.06	3.51	13.21	115.1
FMHS RevPBE+U	3.07	3.87	3.10	3.73	13.77	124.7
FMLS LSDA+U	3.02	3.50	3.03	3.50	13.05	111.5
FMLS PBEsol+U	3.05	3.44	3.02	3.45	12.96	110.2
FMLS RevPBE+U	3.07	3.84	3.05	3.85	13.81	125.3

Table 4.4 The calculated Cr-O, Fe-O bond lengths within the LSDA+U, PBEsol+U and RevPBE+U functionals, corresponding to the oxygen positions (x_{01}, y_{01}, z_{01}) and (x_{02}, y_{02}, z_{02}).

BFCO symmetry	Cr-O [\AA] for (x_{02}, y_{02}, z_{02})	Cr-O [\AA] for (x_{01}, y_{01}, z_{01})	Fe-O [\AA] for (x_{01}, y_{01}, z_{01})	Fe-O [\AA] for (x_{02}, y_{02}, z_{02})
Ideal cubic $Fm\text{-}3m$	1.870	1.870	1.870	1.870
Non-magnetic $R3$	1.935	1.891	1.939	1.933
FiMHS LSDA+U	1.979	1.949	2.072	1.943
FiMHS PBEsol+U	1.972	1.948	2.046	1.946
FiMHS RevPBE+U	2.037	1.966	2.125	1.982
FiMLS LSDA+U	1.982	1.953	1.931	1.922
FiMLS PBEsol+U	1.978	1.955	1.937	1.926
FiMLS RevPBE+U	2.039	2.001	2.018	1.982
FMHS LSDA+U	1.988	1.966	2.055	1.940
FMHS PBEsol+U	1.979	1.961	2.032	1.934
FMHS RevPBE+U	2.040	2.011	2.109	1.980
FMLS LSDA+U	1.989	1.950	1.944	1.920
FMLS PBEsol+U	1.986	1.954	1.920	1.912
FMLS RevPBE+U	2.072	2.024	2.037	2.003

Calculations within the LSDA+U, PBEsol+U and RevPBE+U functionals show clearly the bond length differences between the paraelectric $Fm\text{-}3m$, corresponding to the ideal cubic rock-salt structure, and the distorted rhombohedra structures, together with off-centering of Fe and Cr atoms, contributing to the ferroelectricity. The Bi_2 atom, through its lone pair and displacement toward Fe, contributes to the shortening of the $\text{Bi}_2\text{-Fe}$ bond and elongation of the Cr-Bi_2 bond. Also, for the HS magnetic phases, the Fe-O and Fe-Bi bonds are larger than similar bonds in the LS phases (with one exception for the FMLS phase computed within RevPBE+U). Comparing FiM with FM states, larger bonds were obtained for Cr-O in FM cases.

Coupling Jahn-Teller distortions with octahedra rotations is another factor that can play important role in material's ferroelectric and magnetic properties. Their interactions are however not well understood (Lufaso & Woodward, 2004). Beside undergoing distortions, the oxygen octahedra are additionally tilted/rotated in order to minimize the energy of the structure.

The octahedron *tilts* are measured by the $\text{Cr-O}_{\text{Cr},\text{Fe}}\text{-Fe}$ bond angles containing the $\text{O}_{\text{Cr},\text{Fe}}$ atom belonging to the two adjacent CrO_6 and FeO_6 octahedra, and can be out-of-plane tilts, as sketched in Fig. 4.8b (see also Fig. 2.8b,c), or in-plane tilts as in Fig. 4.8c (see also Fig. 2.8d,e). If these angles are equal to 180° (see Fig. 2.8a), then the octahedra are not tilted (this is the case of the ideal cubic structure). When these angles are different from 180° , then the octahedra are tilted.

The tilting angles values (defined as to be smaller than 180° , and hence the octahedra are more tilted when the angles are smaller) were computed for all optimized rhombohedral structures considered in this work: non-magnetic and FiMHS, FiMLS, FMHS, FMLS magnetic phases. For a better visualization of tilts and rotations, the rhombohedra structure of the FiMHS phase is plotted as a $2\times 2\times 2$ supercell in Fig. 4.8a (however, note that the work presented here is not about supercell optimization). Due to the continuity of the corner-shared octahedra network, the rhombohedral symmetry and (super)cell periodicity, the out-of-plane tilts (Fig. 4.8b; pay attention to the orientation of the vectors **a**, **b** and **c**) are equal to the corresponding in-plane tilts (Fig. 4.8c).

Figures 4.8c and 4.8d show the atoms of the octahedra intersecting the (110) yellow and green planes of Fig. 4.8a. The in-plane titling angles computed from the $\text{Cr-O}_{\text{Cr},\text{Fe}}\text{-Fe}$ bonds, having $\text{O}_{\text{Cr},\text{Fe}}$ marked by 1, 2, 3, 4, 5, 6 in Fig. 4.8c, are plotted using bars chart in Fig. 4.8e. The highest bars (red), corresponding to the highest angles and thus to the less tilted octahedra, having angles closest to 180° , are obtained for non-magnetic rhombohedral BFCO that shows

only the slight tilts needed to produce the $R\bar{3}$ symmetry. The octahedra show higher tilting for LS magnetic phases, and even higher for HS phases.

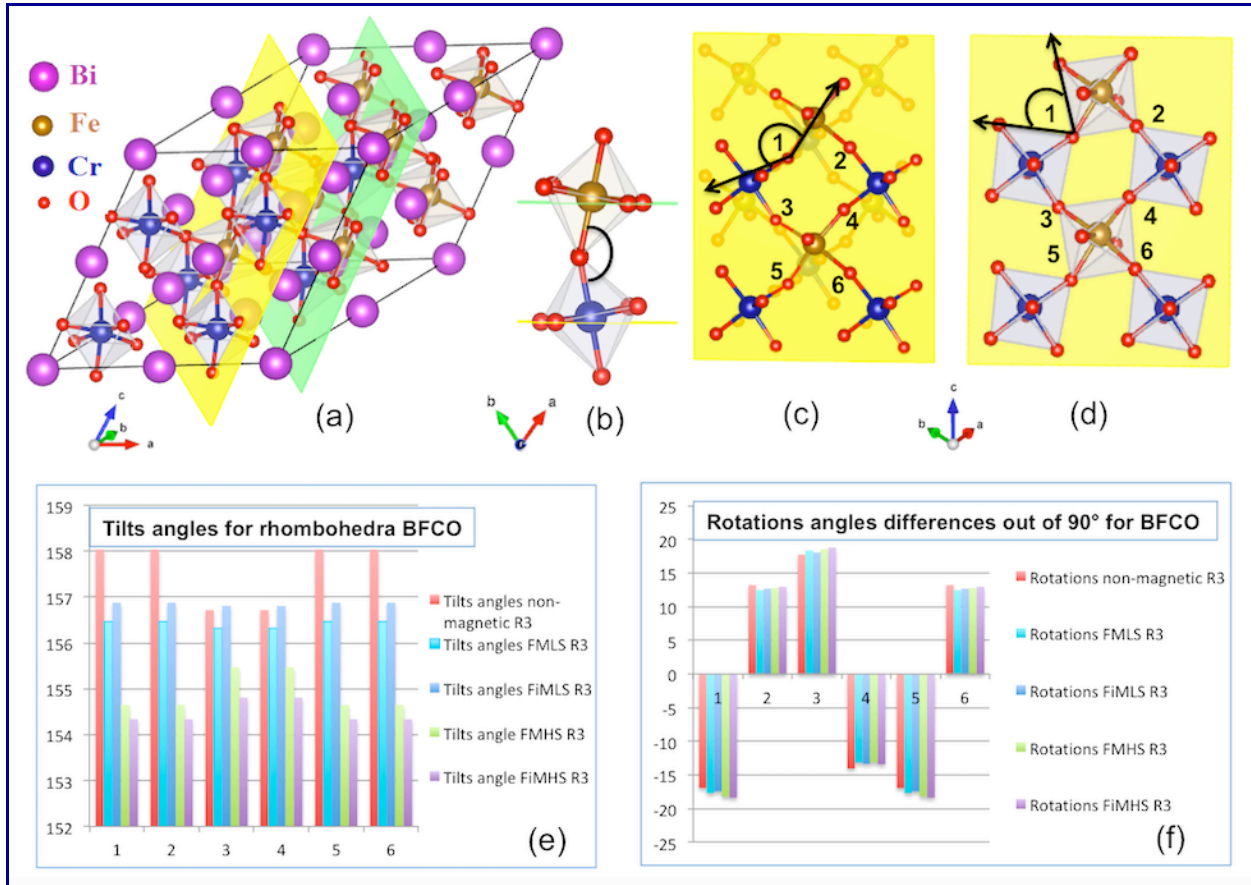


Figure 4.8 The oxygen octahedra intersecting the (110) yellow and green planes of the periodic $2\times 2\times 2$ rhombohedral BFCO for the FiMHS phase (a); Sketch of the out-of-plane tilt (b); Computed angles within the LSDA+U functional, measuring in-plane tilts of the $\text{Cr}-\text{O}_{\text{Cr},\text{Fe}}-\text{Fe}$ bond with $\text{O}_{\text{Cr},\text{Fe}}$ angles between the adjacent CrO_6 , FeO_6 octahedra denoted by 1, 2, 3, 4, 5, 6 (c); Computed angles within the LSDA+U functional, measuring rotations from the equatorial oxygen $\text{O}_{\text{Cr}}-\text{O}_{\text{Cr},\text{Fe}}-\text{O}_{\text{Fe}}$, having $\text{O}_{\text{Cr},\text{Fe}}$ at the corners 1, 2, 3, 4, 5 and 6 (d); Computed in-plane tilts angles shown in (c) for all R3 structures (e); Computed differences from 90° for the in-plane rotations angles of equatorial oxygen $\text{O}_{\text{Cr}}-\text{O}_{\text{Cr},\text{Fe}}-\text{O}_{\text{Fe}}$ shown in (f).

The Fe-O-Cr bond angles have a profound effect on the interaction between spins and $\text{Fe}^{3+}-\text{O}^{2-}-\text{Cr}^{3+}$ superexchange coupling called Kanamori-Goodenough rule (i.e., exchange interaction between Fe and Cr cations with unpaired spins arising through the O anions situated between the cations (Kanamori, 1960; 1959; Goodenough, 1955; Windiks, 2000)). According to the angular dependence of the super-exchange interaction $\text{Fe}^{3+}-\text{O}^{2-}-\text{Cr}^{3+}$ investigated using Mössbauer spectroscopy in systems with simple perovskite-like structures (Gibb, 1984; Moskvin et al., 1975), superexchange coupling was found to be antiferromagnetic for Fe-O-Cr bond angles

smaller than 156° , while ferromagnetic coupling occurred only for Fe-O-Cr bond angles closer to 180° . It can be seen in Figure 4.8e that the tilting angles range is between 154° and 157° . Comparing our computed angles with the measured Fe-O-Cr bond angles reported in Ref. (Moskvin et al. 1975), we observe that bond angles close to 180° for ferromagnetic coupling are not obtained in our case; this could be due to differences in the symmetry of the structures considered in both works. However, for antiferromagnetic coupling we are in the reported range, between 142° and 156° . In addition, for FMHS and FiMHS coupling we see the same trend as in Ref. (Moskvin et al. 1975), i.e., Fe-O-Cr bond angles for FM are larger than the corresponding angles from the FiM phase. It is worth mentioning that another possible source of discrepancies could be that our calculations were performed for temperature $T=0$ K, while in the Moskvin experiments investigations were made at a higher temperature (note that, there is a phase transition above Curie temperature when structure becomes tetragonal).

The octahedron *rotation* is given by the equatorial oxygen $O_{Cr}-O_{Cr,Fe}-O_{Fe}$ (in the yellow plane of Fig. 4.8a; see also Figure 2.9b,c) bond angles containing the $O_{Cr,Fe}$ atom belonging to the two adjacent CrO_6 and FeO_6 octahedra (Fig. 4.8d). If these angles are equal to 90° , as in the case of the ideal cubic structure, then the octahedra are not rotated (see Figure 2.9a). When the angles are larger/smaller than 90° , then the octahedra are clockwise/counter-clockwise rotated, as it can be seen in the rhombohedral BFCO structure of Fig. 4.8d. The in-plane rotation angles, as computed from the equatorial oxygen $O_{Cr}-O_{Cr,Fe}-O_{Fe}$ bonds having $O_{Cr,Fe}$ at the corners 1, 2, 3, 4, 5, 6 as shown in Fig. 4.8d, are depicted using bars chart in Fig. 4.8f. These angles are in fact deviations of the equatorial oxygen $O_{Cr}-O_{Cr,Fe}-O_{Fe}$ bond angles from 90° , i.e., negative bars are for acute angles and positive bars are for obtuse angles. The general trend shows larger rotations for HS phases.

Coupling the Jahn-Teller distortions with octahedra tilting and rotations bring various distortions supporting ferroelectricity. For a better understanding of the distortion-generated effects, the contributions of each atom to the spontaneous polarization are investigated in the following section.

4.6. Spontaneous polarization

As it was described in the Section 3.4, to predict spontaneous polarization in ferroelectrics, i.e., to compute the difference ΔP in the polarization between two different states of the same solid (centrosymmetric paraelectric reference structure versus ferroelectric structure), the first step is

to identify the paraelectric reference structure (i.e., the highly symmetric cubic structure shown in Figs. 4.1b and 4.2a), and to compute the tensors of the Born charges for each atom of the *Fm-3m* BFCO structure. Then, the second step consists in identifying the ferroelectric structures (i.e., distorted rhombohedral structures with *R3* symmetry corresponding to the FiMHS, FiMLS, FMHS and FMLS magnetic phases, shown in Figure 4.3), compute the tensors of the Born charges, and calculate the atom displacements $\Delta u_{k,\alpha}$ of the distorted structures versus the reference structure.

The effective charges have been calculated within the LSDA+U, PBEsol+U and RevPBE+U functionals for transformations starting from the non-magnetic BFCO ideal cubic (paraelectric) structure to the four rhombohedral (ferroelectric) structures with *R3* symmetry corresponding to the FiMHS, FiMLS, FMHS, and FMLS magnetic phases (see Fig. 4.3). Note that, for calculating the effective charges for the paraelectric highly symmetric structure, the atoms of the cubic structure were slightly displaced to their theoretical optimized position in rhombohedral symmetry, while keeping the *Fm-3m* optimized lattice parameters (Ghosez *et al.*, 1998); this step is necessary because the reference and ferroelectric structures must have the same symmetry to allow computing spontaneous polarization.

Then, using the mean charge proposed by Ghosez and coworkers (Ghosez *et al.*, 1998) $Z_{k,\alpha\beta}^* = 0.68Z_{Cubic}^* + 0.32Z_{Ferro}^*$ (see Eq. (3.28) from the Section 3.4.1), we obtained the spontaneous polarization vectors.

In the case of the LSDA+U functional, Table 4.5 presents the computed spontaneous polarization vectors along with simple estimations of the ionic polarizations using nominal and Bader charges.

Table 4.5 Spontaneous polarization vectors P_s in the ferroelectric FiMHS, FiMLS, FMHS, and FMLS magnetic phases of BFCO calculated using Born effective charges within the LSDA+U functional, together with simple estimations of the ionic polarization P_{ion}^N using nominal (formal) charges and P_{ion}^B using computed Bader charges.

	P_{ion}^N [$\mu\text{C}/\text{cm}^2$]	P_{ion}^B [$\mu\text{C}/\text{cm}^2$]	P_s [$\mu\text{C}/\text{cm}^2$]	P_s / P_{ion}^N
FiMHS	$\ (31.4; 31.6; 31.6)\ =54.60$	$\ (19.3; 19.4; 19.4)\ =33.53$	$\ (40.0; 46.0; 47.2)\ =79.24$	1.451
FiMLS	$\ (34.3; 34.5; 34.5)\ =59.64$	$\ (21.3; 21.5; 21.5)\ =37.12$	$\ (46.3; 48.4; 49.8)\ =83.46$	1.399
FMHS	$\ (30.8; 30.9; 30.9)\ =53.46$	$\ (18.8; 18.9; 18.9)\ =32.67$	$\ (43.3; 45.3; 46.4)\ =77.97$	1.458
FMLS	$\ (35.5; 35.6; 35.6)\ =61.60$	$\ (22.8; 23.0; 23.0)\ =39.72$	$\ (47.5; 51.1; 51.2)\ =86.53$	1.405

The calculated spontaneous polarization of the ground state FiMHS magnetic phase is in the range of the experimental data reported for different BFCO thin film thicknesses (see Fig. 10 of

Ref. (Nechache et al, 2012)), and consistent with the theoretical ferroelectric polarization of $79.6 \mu\text{C}/\text{cm}^2$ computed for the FiMHS, using the Berry phase formalism, reported in Refs. (Baettig & Spaldin, 2005a; Baettig et al., 2005b).

Spontaneous polarizations for the FiMLS, FMHS, and FMLS magnetic states are reported for the first time and reveal a higher polarization for low spin magnetic states. The FiMLS phase presents a special interest as it has a magnetic moment of the same magnitude as the FiMHS phase, namely $\sim 2 \mu_B/\text{f.u.}$ (which corresponds to the experimental value) and, in the case of strained films, the FiMLS (instead of FiMHS) could be the most stable phase (Goffinet et al., 2012). Comparing P_s with simple estimations of the ionic polarization using nominal and Bader charges, it can be seen that the spontaneous polarization calculated from Born effective charges is consistently larger with a factor of ~ 1.5 for high spin states and ~ 1.4 for low spin states. In addition, all polarizations are almost parallel to [111], i.e. the direction of the polar displacements driven by the Bi lone pair, as it was seen previously in the calculated ELF (Fig. 4.4).

Comparison between the spontaneous polarization vectors computed within the LSDA+U, PBEsol+U, and RevPBE+U functionals, are presented in Table 4.6.

Table 4.6 Spontaneous polarization vectors P_s in the ferroelectric FiMHS, FiMLS, FMHS, and FMLS magnetic phases of BFCO calculated using Born effective charges within the LSDA+U functional, compared with the corresponding vectors obtained within the PBEsol+U and RevPBE+U functionals.

	$P_s [\mu\text{C}/\text{cm}^2]$ LSDA+U functional	$P_s [\mu\text{C}/\text{cm}^2]$ PBEsol+U functional	$P_s [\mu\text{C}/\text{cm}^2]$ RevPBE+U functional
FiMHS	$\ (40.0; 46.0; 47.2)\ =79.24$	$\ (44.4; 46.3; 47.7)\ =79.92$	$\ (37.5; 39.3; 40.1)\ =67.49$
FiMLS	$\ (46.3; 48.4; 49.8)\ =83.46$	$\ (46.0; 47.5; 49.3)\ =82.24$	$\ (37.8; 39.5; 40.5)\ =68.06$
FMHS	$\ (43.3; 45.3; 46.4)\ =77.97$	$\ (43.9; 45.9; 47.3)\ =79.27$	$\ (35.6; 37.3; 38.0)\ =64.05$
FMLS	$\ (47.5; 51.1; 51.2)\ =86.53$	$\ (46.1; 48.1; 51.1)\ =83.97$	$\ (35.8; 37.5; 38.2)\ =64.33$

Calculations show that spontaneous polarizations within the PBEsol+U functional are consistent with the corresponding values obtained within LSDA+U, while spontaneous polarizations computed within RevPBE+U show more discrepancies due to higher cell distortions, and hence higher volumes of the cell, which are inversely proportional to the spontaneous polarizations (see relation (3.27) from the section 3.4). In addition, polarizations are almost parallel to the [111] direction for all considered functionals.

For a more detailed understanding of how each individual atom contributes to the spontaneous polarization P_s , the Born effective charge tensor computed within the LSDA+U functional for each atom of the rhombohedral unit cell are presented in Table 4.7.

Table 4.7 Calculated Born effective charge tensors, within the LSDA+U functional, for each atom of the rhombohedral unit cell in the ferroelectric FiMHS, FiMLS, FMHS, FMLS phases of the double perovskite $\text{Bi}_2\text{FeCrO}_6$.

	FiMHS	FiMLS	FMHS	FMLS
$Z_{\text{Bi}_1}^*$	$\begin{pmatrix} 5.19 & -0.21 & 0.00 \\ 0.21 & 5.19 & 0.00 \\ 0.00 & 0.00 & 4.41 \end{pmatrix}$	$\begin{pmatrix} 5.30 & -0.14 & 0.00 \\ 0.14 & 5.30 & 0.00 \\ 0.00 & 0.00 & 4.62 \end{pmatrix}$	$\begin{pmatrix} 5.17 & -0.25 & 0.00 \\ 0.25 & 5.17 & 0.00 \\ 0.00 & 0.00 & 4.39 \end{pmatrix}$	$\begin{pmatrix} 5.15 & -0.27 & 0.00 \\ 0.27 & 5.15 & 0.00 \\ 0.00 & 0.00 & 4.39 \end{pmatrix}$
$Z_{\text{Bi}_2}^*$	$\begin{pmatrix} 4.96 & 0.14 & 0.00 \\ -0.14 & 4.96 & 0.00 \\ 0.00 & 0.00 & 4.43 \end{pmatrix}$	$\begin{pmatrix} 5.16 & 0.14 & 0.00 \\ -0.14 & 5.16 & 0.00 \\ 0.00 & 0.00 & 4.67 \end{pmatrix}$	$\begin{pmatrix} 4.94 & 0.17 & 0.00 \\ -0.17 & 4.94 & 0.00 \\ 0.00 & 0.00 & 4.47 \end{pmatrix}$	$\begin{pmatrix} 5.02 & 0.05 & 0.00 \\ -0.05 & 5.00 & 0.00 \\ 0.00 & 0.00 & 4.94 \end{pmatrix}$
Z_{Fe}^*	$\begin{pmatrix} 4.74 & 0.22 & 0.00 \\ -0.22 & 4.74 & 0.00 \\ 0.00 & 0.00 & 4.16 \end{pmatrix}$	$\begin{pmatrix} 2.96 & -0.14 & 0.00 \\ 0.14 & 3.38 & 0.00 \\ 0.00 & 0.00 & 3.13 \end{pmatrix}$	$\begin{pmatrix} 4.38 & 0.29 & 0.00 \\ -0.29 & 4.38 & 0.00 \\ 0.00 & 0.00 & 3.92 \end{pmatrix}$	$\begin{pmatrix} 1.94 & 0.02 & 0.00 \\ -0.03 & 1.96 & 0.00 \\ 0.00 & 0.00 & 2.46 \end{pmatrix}$
Z_{Cr}^*	$\begin{pmatrix} 3.26 & -0.19 & 0.00 \\ 0.19 & 3.26 & 0.00 \\ 0.00 & 0.00 & 2.86 \end{pmatrix}$	$\begin{pmatrix} 3.38 & 0.15 & 0.00 \\ -0.15 & 3.38 & 0.00 \\ 0.00 & 0.00 & 3.25 \end{pmatrix}$	$\begin{pmatrix} 3.70 & 0.19 & 0.00 \\ -0.19 & 3.70 & 0.00 \\ 0.00 & 0.00 & 3.35 \end{pmatrix}$	$\begin{pmatrix} 3.95 & 0.37 & 0.00 \\ -0.36 & 3.95 & 0.00 \\ 0.00 & 0.00 & 3.37 \end{pmatrix}$
$Z_{\text{O}_1}^*$	$\begin{pmatrix} -2.76 & -0.34 & 0.50 \\ -0.09 & -3.19 & -0.27 \\ 0.61 & -0.26 & -2.66 \end{pmatrix}$	$\begin{pmatrix} -2.63 & -0.24 & 0.44 \\ -0.05 & -2.93 & -0.07 \\ 0.49 & -0.33 & -2.52 \end{pmatrix}$	$\begin{pmatrix} -2.78 & -0.38 & 0.48 \\ -0.04 & -3.14 & -0.22 \\ 0.66 & -0.38 & -2.70 \end{pmatrix}$	$\begin{pmatrix} -2.65 & -0.65 & 0.41 \\ 0.17 & -2.56 & -0.07 \\ 0.84 & -0.28 & -2.44 \end{pmatrix}$
$Z_{\text{O}_2}^*$	$\begin{pmatrix} -3.27 & -0.19 & -0.20 \\ 0.04 & -2.68 & 0.57 \\ -0.07 & 0.66 & -2.66 \end{pmatrix}$	$\begin{pmatrix} -2.98 & -0.15 & -0.16 \\ 0.04 & -2.57 & 0.42 \\ 0.03 & 0.59 & -2.52 \end{pmatrix}$	$\begin{pmatrix} -3.23 & -0.22 & -0.05 \\ 0.12 & -2.68 & 0.53 \\ 0.00 & 0.76 & -2.70 \end{pmatrix}$	$\begin{pmatrix} -2.78 & -0.25 & -0.16 \\ 0.57 & -2.44 & 0.39 \\ -0.18 & 0.87 & -2.44 \end{pmatrix}$
$Z_{\text{O}_3}^*$	$\begin{pmatrix} -2.89 & 0.17 & -0.49 \\ 0.41 & -3.06 & -0.30 \\ -0.53 & -0.39 & -2.66 \end{pmatrix}$	$\begin{pmatrix} -2.73 & 0.11 & -0.28 \\ 0.29 & -2.83 & -0.35 \\ -0.53 & -0.27 & -2.52 \end{pmatrix}$	$\begin{pmatrix} -2.86 & 0.08 & -0.43 \\ 0.43 & -3.05 & -0.31 \\ -0.66 & -0.38 & -2.70 \end{pmatrix}$	$\begin{pmatrix} -2.37 & -0.35 & -0.24 \\ 0.48 & -2.83 & -0.37 \\ -0.66 & -0.59 & -2.44 \end{pmatrix}$
$Z_{\text{O}_4}^*$	$\begin{pmatrix} -3.32 & -0.20 & 0.44 \\ -0.46 & -2.84 & -0.38 \\ 0.77 & -0.37 & -2.63 \end{pmatrix}$	$\begin{pmatrix} -2.91 & -0.34 & 0.35 \\ -0.52 & -2.78 & -0.26 \\ 0.61 & -0.25 & -2.71 \end{pmatrix}$	$\begin{pmatrix} -3.27 & -0.37 & 0.61 \\ -0.45 & -2.94 & -0.32 \\ 0.64 & -0.31 & -2.67 \end{pmatrix}$	$\begin{pmatrix} -3.19 & -0.44 & 0.64 \\ -0.99 & -2.79 & 0.05 \\ 0.77 & 0.11 & -2.57 \end{pmatrix}$
$Z_{\text{O}_5}^*$	$\begin{pmatrix} -3.25 & 0.50 & 0.11 \\ 0.24 & -2.91 & 0.58 \\ -0.07 & 0.85 & -2.63 \end{pmatrix}$	$\begin{pmatrix} -3.19 & 0.36 & 0.05 \\ 0.18 & -2.51 & 0.43 \\ -0.09 & 0.65 & -2.71 \end{pmatrix}$	$\begin{pmatrix} -3.38 & 0.38 & -0.03 \\ 0.31 & -2.83 & 0.68 \\ -0.05 & 0.71 & -2.67 \end{pmatrix}$	$\begin{pmatrix} -3.49 & 0.81 & -0.37 \\ 0.24 & -2.46 & 0.52 \\ -0.48 & 0.61 & -2.57 \end{pmatrix}$
$Z_{\text{O}_6}^*$	$\begin{pmatrix} -2.67 & 0.09 & -0.55 \\ -0.16 & -3.48 & -0.19 \\ -0.71 & -0.48 & -2.63 \end{pmatrix}$	$\begin{pmatrix} -2.44 & 0.25 & -0.40 \\ 0.07 & -3.26 & -0.17 \\ -0.52 & -0.41 & -2.71 \end{pmatrix}$	$\begin{pmatrix} -2.66 & 0.09 & -0.57 \\ -0.02 & -3.55 & -0.37 \\ -0.59 & -0.40 & -2.67 \end{pmatrix}$	$\begin{pmatrix} -2.27 & 0.46 & -0.26 \\ -0.08 & -3.67 & -0.56 \\ -0.28 & -0.72 & -2.57 \end{pmatrix}$

Table 4.7 shows that the diagonal components Z_{xx} , Z_{yy} , Z_{zz} of the Born effective charges of BFCO ions are significantly higher than the nominal ionic static charge values (+3 for Bi, Fe and Cr, and -2 for O). Similar anomalous Born charge amplitudes were already reported theoretically for different ABO_3 compounds (Roy et al., 2010; Ravindran et al., 2006; Ghosez et al., 1998). In this work, the large Born effective charges are attributed to the fact that Bi, Fe and Cr donate electrons while O accepts electrons, indicating hybridization, but also displacements of the

neighbouring ions, revealing a large dynamical contribution due to the atom displacements superimposed to the static charge given by the nominal charge. Moreover, the tensors relative to the Bi, Fe, and Cr are almost diagonal, while tensors relative to the oxygen atoms are off-diagonal. An anisotropy in the diagonal components Z_{xx} , Z_{yy} , Z_{zz} for all Born charge tensors can also be seen, confirming covalent bonding between O 2p and Fe 3d and Cr 3d orbitals (the same behaviour was reported for BiFeO₃ according to Ref. (Ravindran et al., 2006)).

Comparing the Born effective charge magnitudes of the same ions within the FiMHS, FiMLS, FMHS and FMLS phases, the calculated Bi effective charges for the FiM states are slightly higher than the corresponding charges for the FM states, showing a higher hybridization interaction between the Bi and neighbouring O atoms in the FiM phases. Analyzing in depth the changes in the charge magnitudes compared with nominal values, it can be seen that differences for Bi are between 46% and 76% relative to the nominal value, with higher amplitude for the FiM states; differences for Fe are in the range of 30%-58% for the HS states, and from -35% to 12% for the LS states; Cr has a different behaviour, with differences of -5% to 32%, with higher amplitude for the FM states. These differences can be attributed to the different strength of the covalent character of the Fe-O and Cr-O bonds.

To understand the contribution of the octahedral rotations to spontaneous polarization relative to the contributions of Bi, Fe, and Cr, the atomic motion decomposition is analyzed. Spontaneous polarization for Bi, Fe, and Cr are given in Table 4.8 for the LSDA+U, PBEsol+U and RevPBE+U functionals.

Table 4.8 Spontaneous polarization vectors of Bi, Fe and Cr in the ferroelectric FiMHS, FiMLS, FMHS, and FMLS phases, and the polarization of all oxygen atoms O₁-O₆ contribution to the BFCO spontaneous polarization \mathbf{P}_s .

	$\mathbf{P}_{s,\text{Bi}1} [\mu\text{C}/\text{cm}^2]$	$\mathbf{P}_{s,\text{Bi}2} [\mu\text{C}/\text{cm}^2]$	$\mathbf{P}_{s,\text{Fe}} [\mu\text{C}/\text{cm}^2]$	$\mathbf{P}_{s,\text{Cr}} [\mu\text{C}/\text{cm}^2]$	$\mathbf{P}_{s,\text{O}1-\text{O}6} [\mu\text{C}/\text{cm}^2]$
FiMHS LSDA+U	(-4.7; -4.7; -4.8)	(6.9; 7.0; 6.6)	(1.0; 1.2; 1.1)	(-4.5; -4.6; -4.6)	(45.3; 47.1; 48.9)
FiMHS PBEsol+U	(-7.8; -7.8; -8.1)	(2.7; 2.7; 2.6)	(0.5; 0.5; 0.5)	(-5.7; -5.9; -5.9)	(54.6; 56.8; 58.5)
FiMHS RevPBE+U	(-3.6; -3.6; -3.6)	(12.6; 12.7; 12.1)	(1.8; 1.9; 1.9)	(-2.1; -2.2; -2.2)	(28.8; 30.2; 31.8)
FiMLS LSDA+U	(-5.1; -5.1; -5.2)	(-2.1; -2.1; -2.0)	(-0.1; -0.1; -0.1)	(-6.8; -7.1; -7.2)	(60.4; 62.8; 64.3)
FiMLS PBEsol+U	(-5.2; -5.2; -5.3)	(-2.5; -2.5; -2.4)	(-0.1; -0.1; -0.1)	(-7.1; -7.4; -7.4)	(60.6; 63.1; 64.8)
FiMLS RevPBE+U	(-4.2; -4.2; -4.3)	(8.9; 9.0; 8.5)	(0.8; 0.9; 0.9)	(-3.0; -3.3; -3.1)	(35.2; 36.9; 38.6)
FMHS LSDA+U	(-4.9; -4.9; -5.0)	(7.5; 7.6; 7.2)	(0.9; 1.1; 1.0)	(-4.7; -4.9; -4.9)	(44.5; 46.4; 48.1)
FMHS PBEsol+U	(-5.3; -5.3; -5.4)	(2.8; 2.8; 2.6)	(0.4; 0.5; 0.5)	(-5.8; -6.1; -6.1)	(51.7; 54.0; 55.7)
FMHS RevPBE+U	(-3.7; -3.7; -3.8)	(12.7; 12.8; 12.1)	(1.6; 1.8; 1.7)	(-2.3; -2.4; -2.4)	(27.3; 31.8; 30.4)
FMLS LSDA+U	(-5.1; -5.1; -5.2)	(-2.3; -2.3; -2.3)	(-0.03; -0.1; -0.1)	(-6.7; -6.9; -7.0)	(61.6; 65.5; 65.8)
FMLS PBEsol+U	(-5.3; -5.3; -5.4)	(-3.2; -3.2; -3.1)	(-0.1; -0.1; -0.1)	(-7.2; -7.4; -7.5)	(61.9; 64.1; 67.2)
FMLS RevPBE+U	(-2.8; -2.8; -2.9)	(12.6; 12.6; 12.1)	(1.6; 1.7; 1.7)	(-1.5; -1.5; -1.5)	(25.8; 27.3; 28.6)

As shown in Fig. 4.9(a), Bi₁ and Cr bring antagonist contributions to the overall polarization \mathbf{P}_s (along [111]) computed within the LSDA+U, PBEsol+U and RevPBE+U functionals for all magnetic phases. Bi₂ (center of the rhombohedra cell) and Fe induce supportive contributions to \mathbf{P}_s for the HS magnetic states, and antagonist contributions for the LS magnetic states when the LSDA+U and PBEsol+U functionals are used. In the case of RevPBE+U functional, Bi₂ and Fe bring supportive contributions to \mathbf{P}_s for all HS and LS magnetic states. It is clear from Table 4.8 that the oxygen atoms have the highest contribution to the total polarization; for the RevPBE+U functional, the components of the oxygen polarization vectors are smaller than the corresponding values obtained for LSDA+U and PBEsol+U, but they are still higher than the Bi, Fe and Cr polarization vectors. Moreover, the total polarization of the LS states is higher than that for HS states (see Tables 4.5, 4.6); this could be caused by the additional weak-FOJT distortions induced in LS states compared with HS states where only SOJT distortions are present.

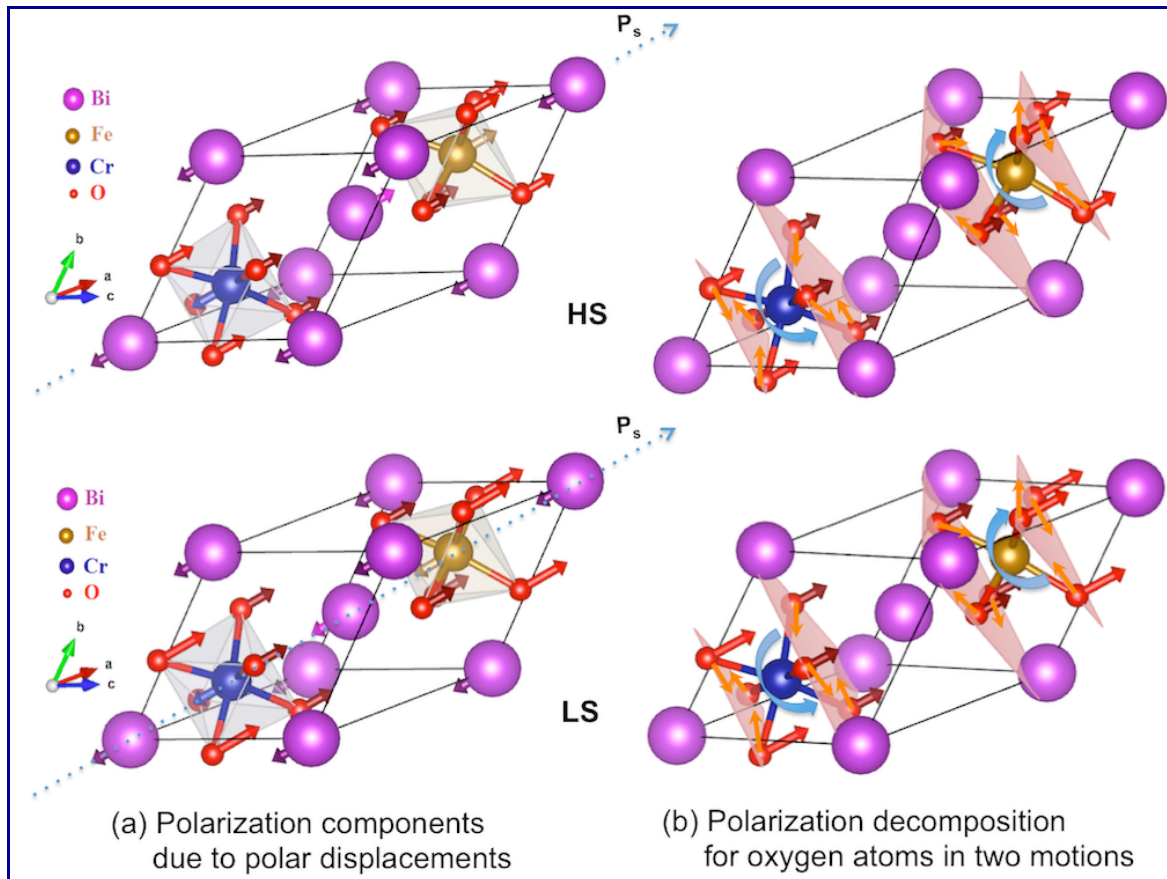


Figure 4.9 Schematic view of polarization vector decomposition into two motions associated to the polar displacements along the [111] axis, and to the clockwise & counter clockwise octahedral rotations.

For the O atoms, two motions of the oxygen octahedron induce change in the polarization: one motion along the [111] axis due to polar displacements, and another motion in a plane orthogonal to [111] (red arrows in the red plane in Fig. 4.9) due to clockwise and counter clockwise octahedron rotation. Decomposition of these motions is depicted in Fig. 4.9b. It is notable that the polarization components orthogonal to [111] of oxygen atoms around Fe and Cr, respectively, are cancelling each other, and hence the total polarization is dominated by the supportive components of the polarization along the [111] direction.

A very significant result of our calculation is that, in the case of rhombohedral $\text{Bi}_2\text{FeCrO}_6$, the main contribution to polarization comes from the oxygen atoms and not from the Bi atoms with the lone electron pair as in the case of BiFeO_3 (Ravindran et al., 2006; Baettig & Spaldin, 2005b). In order to further validate our calculations, we performed similar calculations using Born effective charges for the BiFeO_3 rhombohedral structure (*R*3c symmetry) with G-type antiferromagnetic ordering (Figure 4.10).

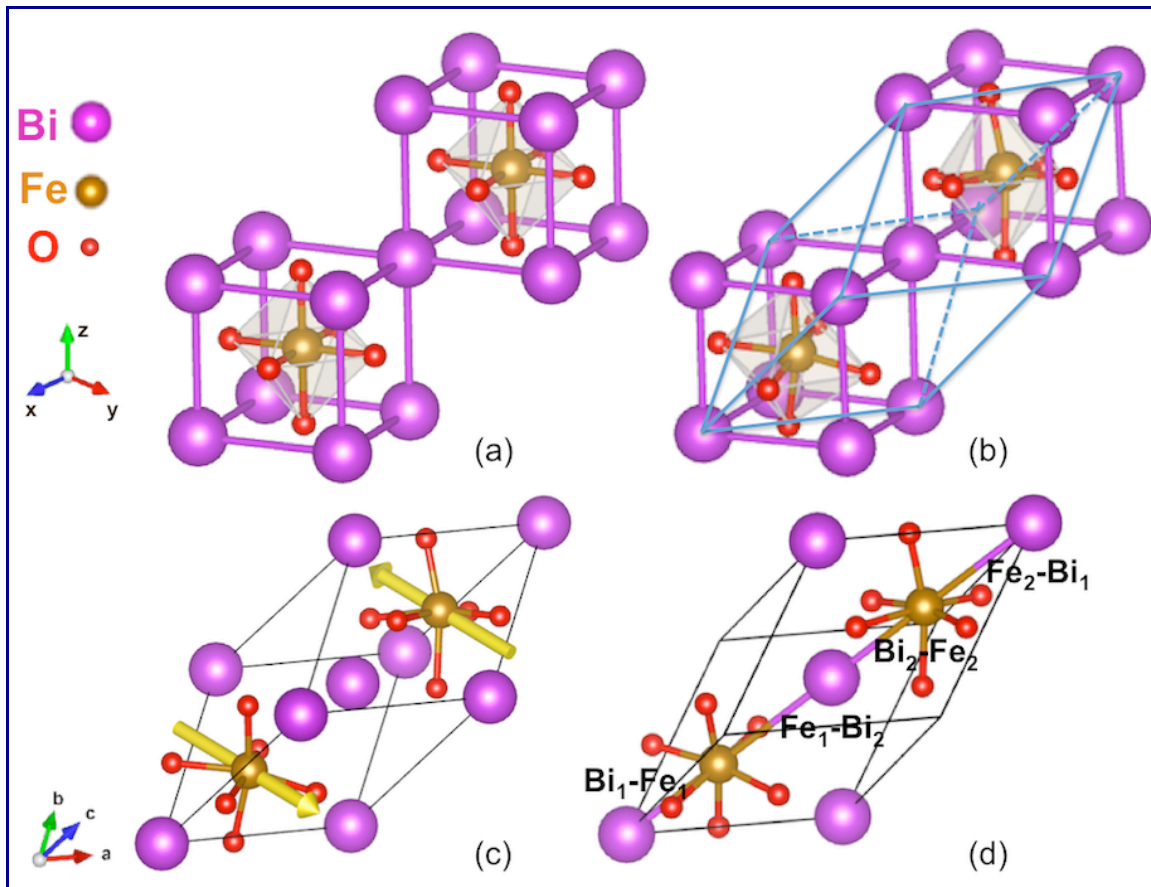


Figure 4.10 The ideal cubic rock-salt structure of $(\text{BiFeO}_3)_2$ (a); The rhombohedral *R*3c symmetry of BiFeO_3 (b); The computed optimized *R*3c magnetic structure of BiFeO_3 within the LSDA+U functional (c); The Bi and Fe atoms emphasize the bonds between Bi_1 , Fe, Bi_2 and Fe (d).

Our results faithfully reproduced the findings reported by other research groups (Ravindran et al., 2006; Baettig & Spaldin, 2005b), where Bi lone pairs drive distortions that have a dominant effect on the total spontaneous polarization. In addition, there are no major differences between the computed Born effective charges for BFO and BFCO ions, which indicates that ionic displacements make the difference between their spontaneous polarizations. By comparing distortions of the FiMHS phases of BFO and BFCO, it was found that the $\text{Bi}_1\text{-Fe}_1$ & $\text{Bi}_2\text{-Fe}_2$ bond lengths along the [111] diagonal, and $\text{Fe}_1\text{-Bi}_2$ & $\text{Fe}_2\text{-Bi}_1$ (see Fig. 4.10d), respectively, are equal for BFO, while the Cr atom brings asymmetry in the Bi-Fe and Bi-Cr bond lengths for BFCO (see Table 4.9). Similar behaviour can be seen for Fe-O and Cr-O bonds of BFO compared with BFCO, where the bond lengths of $\text{Fe}_1\text{-O}$ & $\text{Fe}_2\text{-O}$ corresponding to the oxygen Wyckoff positions (x_{02}, y_{02}, z_{02}) are equal (same for the oxygen (x_{01}, y_{01}, z_{01})), while Cr atom introduces asymmetries for BFCO, i.e., bond lengths of Cr-O & Fe-O corresponding to the oxygen Wyckoff positions (x_{02}, y_{02}, z_{02}) are not equal (same for the oxygen (x_{01}, y_{01}, z_{01})).

Table 4.9 The calculated bonds lengths, within the LSDA+U functional, between Bi_1 , Fe_1 , Bi_2 and Fe_2 (see Fig. 4.10d) along the diagonal [111] direction, and the Fe-O bonds corresponding to the oxygen positions (x_{01}, y_{01}, z_{01}) and (x_{02}, y_{02}, z_{02}) of BFO, compared with similar bonds of BFCO (see Fig. 4.4 top-left panel).

BFO R3c symmetry	$\text{Bi}_1\text{-Fe}_1$ [Å]	$\text{Fe}_1\text{-Bi}_2$ [Å]	$\text{Fe}_1\text{-O}$ [Å] (x_{02}, y_{02}, z_{02})	$\text{Fe}_1\text{-O}$ [Å] (x_{01}, y_{01}, z_{01})	$\text{Bi}_2\text{-Fe}_2$ [Å]	$\text{Fe}_2\text{-Bi}_1$ [Å]	$\text{Fe}_2\text{-O}$ [Å] (x_{02}, y_{02}, z_{02})	$\text{Fe}_2\text{-O}$ [Å] (x_{01}, y_{01}, z_{01})
Non-magnetic R3c	2.99	3.37	1.922	1.906	2.99	3.37	1.922	1.906
FiMHS LSDA+U	3.07	3.67	2.068	1.933	3.07	3.67	2.068	1.933
BFCO R3 symmetry	$\text{Bi}_1\text{-Cr}$ [Å]	$\text{Cr}\text{-Bi}_2$ [Å]	$\text{Cr}\text{-O}$ [Å] (x_{02}, y_{02}, z_{02})	$\text{Cr}\text{-O}$ [Å] (x_{01}, y_{01}, z_{01})	$\text{Bi}_2\text{-Fe}$ [Å]	$\text{Fe}\text{-Bi}_1$ [Å]	$\text{Fe}\text{-O}$ [Å] (x_{02}, y_{02}, z_{02})	$\text{Fe}\text{-O}$ [Å] (x_{01}, y_{01}, z_{01})
Non-magnetic R3	3.01	3.37	1.935	1.891	3.00	3.41	1.939	1.933
FiMHS LSDA+U	3.02	3.72	1.979	1.949	3.06	3.60	2.072	1.943

In addition, Table 4.10 shows that displacements of the Bi atoms bring a supportive contribution to the total polarization \mathbf{P}_s (along the [111] direction) for BFO, while for BFCO the displacements of Bi are mainly in the opposite direction (see Bi arrows in Fig. 4.9) so they bring an antagonist contribution to the BFCO polarization.

Table 4.10 Spontaneous polarization vectors of Bi, Fe, and all oxygen atoms $\text{O}_1\text{-O}_6$ computed within the LSDA+U functional in the ferroelectric FiMHS phase of BFO compared with similar polarization values for BFCO.

BFO	$\mathbf{P}_{s,\text{Bi}1}$ [$\mu\text{C}/\text{cm}^2$]	$\mathbf{P}_{s,\text{Bi}2}$ [$\mu\text{C}/\text{cm}^2$]	$\mathbf{P}_{s,\text{Fe}1}$ [$\mu\text{C}/\text{cm}^2$]	$\mathbf{P}_{s,\text{Fe}2}$ [$\mu\text{C}/\text{cm}^2$]	$\mathbf{P}_{s,\text{O}1\text{-O}6}$ [$\mu\text{C}/\text{cm}^2$]
FiMHS BFO R3c	(10.8; 10.8; 10.8)	(3.3; 3.3; 3.3)	(2.3; 2.3; 2.3)	(10.1; 10.1; 10.1)	(-2.5; 1.2; 2.7)
BFCO	$\mathbf{P}_{s,\text{Bi}1}$ [$\mu\text{C}/\text{cm}^2$]	$\mathbf{P}_{s,\text{Bi}2}$ [$\mu\text{C}/\text{cm}^2$]	$\mathbf{P}_{s,\text{Fe}}$ [$\mu\text{C}/\text{cm}^2$]	$\mathbf{P}_{s,\text{Cr}}$ [$\mu\text{C}/\text{cm}^2$]	$\mathbf{P}_{s,\text{O}1\text{-O}6}$ [$\mu\text{C}/\text{cm}^2$]
FiMHS BFCO R3	(-4.7; -4.7; -4.8)	(6.9; 7.0; 6.6)	(1.0; 1.2; 1.1)	(-4.5; -4.6; -4.6)	(45.3; 47.1; 48.9)

Consequently, the large displacements of the oxygen atoms in the case of BFCO provide the main contribution to the BFCO total spontaneous polarization, while in the case of BFO, Bi atoms are the most displaced, providing the main contribution to the BFO total spontaneous polarization (oxygen influence on polarization is very small).

CHAPTER 5

DFT STUDY OF $\text{Bi}_2\text{FeCrO}_6$: NONCOLLINEAR SPIN POLARIZED CALCULATIONS

The structural, magnetic and ferroelectric properties of BFCO have been investigated in the Chapter 4 by using magnetic collinear spin-polarized DFT calculations that do not impose any constraints on the direction of atomic magnetic moments. To understand the interplay of crystalline and magnetic symmetry breaking, the dependence of the total energy of the system on the orientation of the magnetic moment, i.e., magnetic anisotropy, is studied. Experimentally, magnetic anisotropy was already revealed for BFCO nanostructures (Nechache & Rosei, 2012; Nechache et al., 2011) where saturated magnetization was estimated to be $5.2 \mu_B$ per Fe-Cr pair, about 2.7 higher than the $1.91 \mu_B$ per Fe-Cr pair magnetization observed in epitaxial continuous BFCO films (Nechache et al., 2009), or 2.6 higher than the $2 \mu_B/\text{f.u.}$ predicted through theoretical calculations (Baettig & Spaldin, 2005a; Baettig et al., 2005b; Goffinet et al., 2012). Because the origin of the magnetic anisotropy is the coupling between the spin and orbital degrees of freedom, i.e., it is a fundamentally relativistic effect (Blonski et al., 2011), the present chapter analyzes the effect of the spin-orbit coupling (SOC) on the BFCO properties using noncollinear spin structures (Hobbs et al., 2000; Marsman & Hafner, 2002) wherein fully relativistic calculations are performed for the core electrons and valence electrons are treated in a scalar relativistic approximation. Even though noncollinear calculations are computationally expensive compared with the faster collinear one, the unexpectedly large saturated magnetization in the BFCO nanostructures, which is intermediate between ferromagnetic and an antiferromagnetic coupling, deserves further investigation. Moreover, studies presented in this thesis are referring to FM and FiM states where collinear calculations already proved possible magnetizations of $4 \mu_B/\text{f.u.}$ or $8 \mu_B/\text{f.u.}$ in addition to the well known $2 \mu_B/\text{f.u.}$

5.1. Computational details

Calculations were performed using the projector-augmented plane-wave (PAW) formalism (Blöchl 1994; Kresse & Joubert, 1999) of the density functional theory by including spin-orbit interactions in the noncollinear mode (Hobbs et al., 2000; Marsman & Hafner, 2002)

implemented in the *Vienna ab initio Simulation Package* (VASP 5.3; 5.4) (Kresse & Furthmüller 1996a; 1996b) as integrated in the MedeA® computational environment (MedeA 2017; 2015). VASP allows interatomic and intra-atomic noncollinearity of the magnetization density and uses spin interpolation of Vosko-Wilk-Nusair (Vosko et al., 1980) that is compatible with the considered exchange-correlation functional LSDA+U, and the gradient-corrected PBEsol+U & RevPBE+U functionals (see Chapter 4). The use of gradient-corrected exchange-correlation functionals in connection with noncollinear magnetism deserves few remarks (Marsman & Hafner, 2002): the PBE functionals depend on the electronic density, the magnetization density, and their respective gradients, but these functionals do not apply directly to the case of noncollinear magnetism because they do not incorporate any dependence on changes in the direction of magnetization. Thus, VASP projects the gradient of the magnetization in every point onto the direction of the magnetization at these points; the projected quantity is seen as a gradient with respect to a local spin quantization axis, denoted by S (called SAXIS in the VASP manual (Kresse & Lebacq, 2017)), and then it is used in the gradient-corrected functionals. Based on these considerations, the magnetization density tends to be almost collinear on the intra-atomic scale, and hence the gradient-corrected functionals may be used. Note that when SOC is included, noncollinear magnetic vectors are initially aligned to a spin quantization axis S, and then they are allowed to rotate during the optimization procedure until convergence to a minimum of energy (Kresse & Lebacq, 2017), without imposing any constraint on the symmetry (e.g., the \mathbf{k} -points mesh is not restricted anymore to a symmetry-irreducible set of the primitive cell and magnetic moments break the symmetry). If SOC is not included, the energy does not depend on the direction of the magnetic moment, i.e., rotating all magnetic moments by the same angle results in principle exactly in the same energy. Therefore the main effect of SOC is to couple the spin to the crystal structure.

For treating exchange and correlation, the same parameters $U=3$ eV for the Coulomb repulsion, and $J=0.8$ eV for the exchange interaction, respectively (Baettig & Spaldin, 2005a; Baettig et al., 2005b; Goffinet et al., 2012), were used, as in the case of the collinear spin polarized calculations. To obtain the BFCO cell shape relaxation within noncollinear magnetic calculations when spin-orbit coupling effects are taken into account, we started from the optimized structures of the FiMHS, FiMLS, FMHS and FMLS magnetic phases computed via collinear spin, without imposing any symmetry to the cell (i.e., the spinor wavefunctions is allowed to rotate until the ground state is found). For each phase, various spin quantization axes S were considered, starting from a S parallel to [111] direction and then rotated slowly until S became perpendicular to the [111] direction (this is because in the previous chapter, it was found that the

polarization vector is parallel to [111] direction, and it is expected that magnetic vector will be in a plane perpendicular to the polarization – an assumption widely used in literature that is not proven as far as we know). After full optimizations followed by single-point energy calculations were performed, ground state energies were found and then the easy axis of the magnetization was determined for all configurations. In addition, the effects of the broken symmetries and of the noncollinear spin and spin-orbit interactions on the crystals structure, and on the magnetic and ferroelectric properties were found.

To validate the noncollinear calculations procedure, a well explored material was considered, namely BiFeO_3 (BFO), whose weak ferromagnetism was investigated by using noncollinear spin-polarized calculations including spin-orbit coupling (Dixit et al., 2015; Ederer & Spaldin, 2005a, 2005b) within the LSDA+U functional. First, collinear spin-polarized calculations were performed for the BFO rhombohedral structure ($R\bar{3}c$ symmetry) with G-type antiferromagnetic ordering and with Fe^{3+} -high spin (HS) and Fe^{3+} -low spin (LS), as it can be seen in Fig. 5.1a-c.

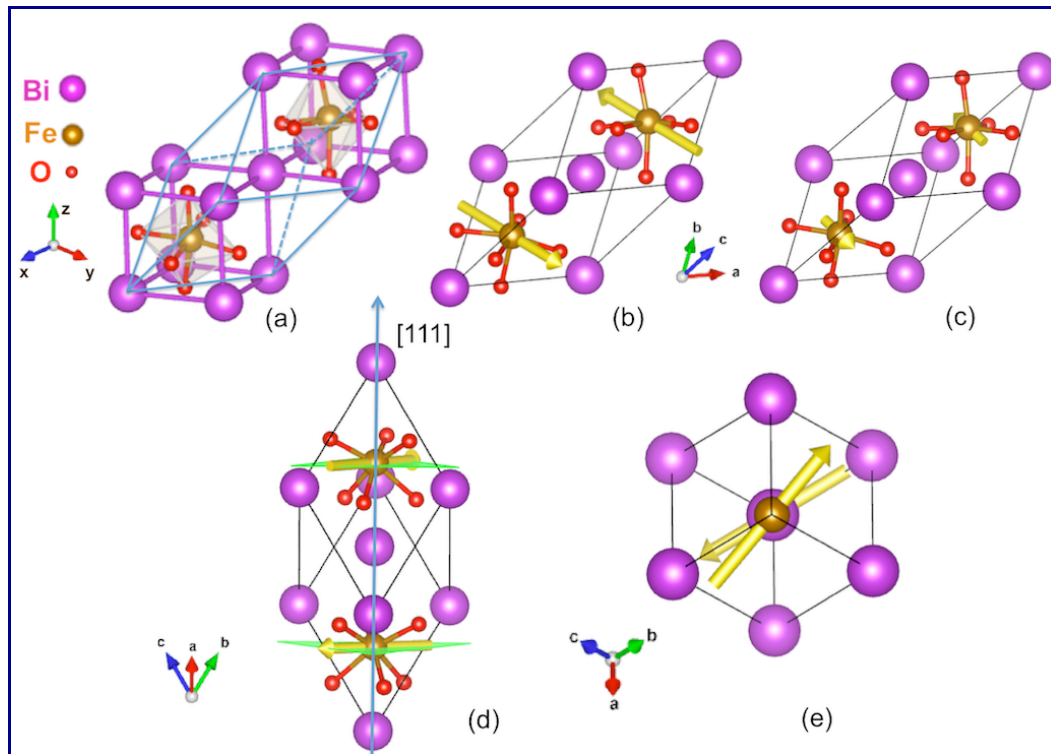


Figure 5.1 The rhombohedral $R\bar{3}c$ symmetry of BiFeO_3 versus the ideal cubic rock-salt structure of $(\text{BiFeO}_3)_2$ (a); The computed optimized $R\bar{3}c$ magnetic structure of BiFeO_3 within the LSDA+U functional (b-d). The ferromagnetic Fe^{3+} -high spin state (FiMHS), without spin-orbit coupling (b); The ferromagnetic Fe^{3+} -low spin state (FiMLS), without spin-orbit coupling (c); The ferrimagnetic Fe^{3+} -high spin state (FiMHS) including spin-orbit coupling (d); The (111) plane projection of the optimized magnetic structure (d) emphasizing Bi, Fe atoms and the canted noncollinear magnetic moments (e). Visualizations are performed using VESTA (Momma & Izumi, 2011).

It was found that antiferromagnetic high spin (FiMHS) is more stable, with a ground state energy of about ~4 eV lower than that of the antiferromagnetic LS state. The optimized structure parameters of FiMHS were the same as those reported in Ref. (Baettig & Spaldin, 2005b), with a null total magnetic moment per unit cell, as the magnetic moments of the two Fe atoms are +3.84 and -3.84 μ_B (in collinear calculations, magnetic vectors could be parallel or antiparallel). A null magnetic moment is not in agreement with experimental data, which revealed a weak ferromagnetism between 0.03 - 1 μ_B /f.u., depending on the film thickness, which is attributed to a slight canting of the antiferromagnetic moments (Wang et al., 2003). To obtain canted magnetic moments, and hence weak antiferromagnetism, noncollinear spin-polarized calculations including SOC were performed for BFO.

For a better comparison with previous theoretical data reported in literature, two types of noncollinear SOC calculations were performed for BFO: (i) starting from the optimized collinear FiMHS structure, noncollinear single point calculations were performed, taking into account SOC, without cell relaxation, i.e., following the idea presented in Refs. (Ederer & Spaldin, 2005a, 2005b) ; (ii) starting from the same optimized collinear FiMHS structure, but performing full noncollinear optimization with SOC, together with additional static calculations for refining the magnetic and orbital moments, i.e., following the idea presented in Ref. (Dixit et al., 2015), which is the technique that will be further used for BFCO calculations.

The results faithfully reproduced the findings reported by previous theoretical research groups (Dixit et al., 2015; Ederer & Spaldin, 2005a, 2005b), as the computed saturated total magnetic moment per unit cell was 0.146 μ_B and noncollinear magnetic vectors showed canting (see Figure 5.1e). The initial noncollinear magnetic vectors were aligned with different spin quantization axes S=[111], [001], [100], [010], [1-21], [11-2] and then let to rotate until the ground state was found. All ground state energies for SOC calculations were about 1 eV lower than the energy obtained in the case of collinear spin polarized calculations for FiMHS.

The first type of noncollinear calculations were faster; the easy axis was found to be S=[1-21] and the saturated total magnetization of 0.146 μ_B /f.u. was shown along the easy axis, i.e., perpendicular to the [111] direction, while the other considered spin quantization axes gave total magnetizations smaller than 0.146 μ_B /f.u. Regarding the direction of the magnetic vectors per Fe atom: the noncollinear magnetic vectors were perfectly antiparallel and along the [111] direction when initial spin quantization axis S=[111] was considered, while for S=[1-21] the noncollinear magnetic vectors were included in a plane perpendicular to the [111] direction (see the green planes in Figure 5.1d), antiparallel and with a canting angle of about 1.29° (sketch

depicted in the Figure 5.1e). These findings agree with the results of Ederer and Spaldin (Ederer & Spaldin, 2005a, 2005b). In addition, Born effective charges were computed to see the effect of the SOC on the spontaneous polarization, and it was found the same polarization as those obtained in the collinear case (see Chapter 4). Actually, this behaviour was expected as full cell optimization was not performed in this case, and SOC was just added to the static calculations.

For the second type of noncollinear calculations, i.e. including SOC with full cell optimization, the total magnetizations per unit cell were slightly higher, but the saturated magnetization of $0.146 \mu_B/\text{formula unit}$ shown along the same easy axis, $S=[1-21]$, did not change. We found an additional contribution between $(0.1 ; 0.1 ; 0.1)$ and $(0.12 ; 0.12 ; 0.12) \mu\text{C}/\text{cm}^2$ to the spontaneous polarization due to SOC (depending on the considered spin quantization axis S), to the polarization computed for the collinear magnetic BFO structure, which has never been reported so far. Since the spontaneous polarization of BFO is about $84-87 \mu\text{C}/\text{cm}^2$ (Neaton et al., 2005), the contribution due to SOC however represents only about 0.2%. In the following, this second type (ii) of noncollinear calculations including SOC, together with simultaneous full cell optimization will be considered for investigating BFCO.

5.2. Ground-state structures and magnetic orderings

In order to understand how spin-orbit interactions affect the multiferroic properties of the rhombohedral BFCO, noncollinear spin polarized calculations taking into account SOC were performed within the LSDA+U, PBEsol+U and RevPBE+U functionals. The optimized magnetic FiMHS, FiMLS, FMHS and FMLS phases from the previous collinear spin polarized calculations (see Chapter 4) were used as input structures for each functional. Then, noncollinear spin structures were introduced together with spin-orbit interactions without imposing any constraint on the symmetry. The initial noncollinear magnetic vectors were aligned with different spin quantization axes S_i ($i=1$ to 6), such that the angle between S_i and the polarization direction [111] increases from 0° to 90° as follows: 0° , 9.4° , 14° , 22° , 45° , 90° . Thus, the spin quantization axes $S_1=[111]$, $S_2=[0.98 0.90 1.06]$, $S_3=[0.97 0.84 1.09]$, $S_4=[0.5, 1.0, 1.5]$, $S_5=[0.70, 0.35, 1.06]$ and $S_6=[-0.5, 0.5, 0]$ were considered based on the preliminary calculations performed for BFO FiMHS phase that showed an easy axis (corresponding to the saturated total magnetization) perpendicular to the polarization direction. However, BFCO is more complex than BFO, and

hence more detailed studies are necessary for all four magnetic states FiMHS, FiMLS, FMHS and FMLS.

Tables 5.1-5.3 summarize the structural and electronic properties of the noncollinear magnetic phases computed within LSDA+U, PBEsol+U and RevPBE+U functionals, corresponding to the collinear FiMHS, FiMLS, FMHS and FMLS structures by using the two spin quantization axes $S_1=[111]$ and $S_6=[-0.5\ 0.5\ 0]\perp[111]$.

Table 5.1 Summary of the structural and electronic properties of the noncollinear SOC magnetic phases corresponding to the collinear FiMHS, FiMLS, FMHS, and FMLS phases of BFCO as computed using the LSDA+U functional starting from initial magnetic vectors parallel to spin quantizations $S=[111]$ and $S=[-0.5\ 0.5\ 0]\perp[111]$. The rhombohedral unit cell lattice parameters are: lattice length a_r and angle α_r for collinear structure with R3 rhombohedral symmetry, and respectively lengths a_r , b_r , c_r and angles α_r , β_r , γ_r for pseudo-rhombohedral symmetry; V_r is the unit cell volume; x_i , y_i , and z_i represent the Wyckoff positions of the space group 146 ($R\bar{3}$ symmetry) in the rhombohedral setting, i.e. $Bi_{1,2}(x, x, x)$, $Fe(x, x, x)$, $Cr(x, x, x)$ and $O_1(x_{01}, y_{01}, z_{01})$, $O_2(z_{01}, x_{01}, y_{01})$, $O_3(y_{01}, z_{01}, x_{01})$, $O_4(x_{02}, y_{02}, z_{02})$, $O_5(z_{02}, x_{02}, y_{02})$, $O_6(y_{02}, z_{02}, x_{02})$; μM_{Fe} and μM_{Cr} are the magnitudes of the local magnetic moments of Fe and Cr; μL_{Fe} and μL_{Cr} are the magnitudes of the orbital moments of Fe and Cr; μM_{BFCO} is the magnitude of the total magnetic moment per cell; ΔE is the energy relative to the collinear FiMHS ground state.

	LSDA+U collinear spin polarized calculations				LSDA+U noncollinear spin polarized calculations with SOC, $S=[111]$				LSDA+U noncollinear spin polarized calculations with SOC, $S=[-0.5\ 0.5\ 0]$			
	FiMHS	FiMLS	FMHS	FMLS	FiMHS	FiMLS	FMHS	FMLS	FiMHS	FiMLS	FMHS	FMLS
a_r in Å	5.48	5.36	5.49	5.37	5.47	5.35	5.48	5.36	5.47	5.35	5.48	5.35
b_r in Å	5.48	5.36	5.49	5.37	5.47	5.35	5.48	5.36	5.47	5.35	5.48	5.35
c_r in Å	5.48	5.36	5.49	5.37	5.47	5.35	5.48	5.36	5.47	5.36	5.48	5.35
α_r in °	60.04	60.80	60.04	60.76	60.10	60.96	60.05	60.89	60.09	60.93	60.05	60.92
β_r in °	60.04	60.80	60.04	60.76	60.10	60.96	60.05	60.89	60.08	60.91	60.05	60.91
γ_r in °	60.04	60.80	60.04	60.76	60.10	60.96	60.05	60.89	60.08	60.94	60.05	60.97
V_r , Å³	116.3	111.1	116.9	111.5	116.4	111.0	116.5	111.0	116.5	111.0	116.5	110.8
x_{Bi}	0.000	0.000	0.000	0.000	0.000	0.000	0.000	0.000	0.000	0.000	0.000	0.000
x_{Bi}	0.503	0.495	0.504	0.496	0.504	0.494	0.504	0.495	0.503	0.505	0.503	0.494
x_{Fe}	0.732	0.726	0.731	0.727	0.732	0.726	0.732	0.726	0.732	0.726	0.732	0.726
x_{Cr}	0.226	0.227	0.226	0.228	0.226	0.228	0.225	0.228	0.225	0.225	0.225	0.228
x_{O1}	0.544	0.545	0.545	0.546	0.542	0.546	0.543	0.545	0.543	0.546	0.542	0.545
y_{O1}	0.950	0.952	0.949	0.950	0.950	0.951	0.949	0.951	0.949	0.948	0.949	0.950
z_{O1}	0.398	0.410	0.400	0.410	0.399	0.411	0.399	0.411	0.399	0.402	0.399	0.413
x_{O2}	0.046	0.041	0.044	0.041	0.045	0.041	0.045	0.040	0.045	0.044	0.045	0.039
y_{O2}	0.905	0.904	0.905	0.905	0.907	0.904	0.907	0.905	0.907	0.900	0.907	0.906
z_{O2}	0.447	0.457	0.449	0.454	0.447	0.456	0.447	0.455	0.447	0.450	0.447	0.455
μM_{Fe} in μ_B	-3.98	-0.86	+4.03	+1.02	3.936	0.827	3.974	0.957	3.936	0.884	3.977	0.956
μM_{Cr} in μ_B	+2.54	+2.74	+2.86	+2.72	2.465	2.634	2.716	2.725	2.465	2.610	2.716	2.606
μL_{Fe} in μ_B	-	-	-	-	0.029	0.016	0.022	0.496	0.027	0.414	0.022	0.447
μL_{Cr} in μ_B	-	-	-	-	0.056	0.038	0.048	0.029	0.052	0.039	0.049	0.043
μM_{BFCO} in μ_B	-1.98	+1.90	+7.66	+3.82	1.992	2.027	7.955	3.749	1.999	2.048	7.957	3.748
ΔE in meV	0 I	372.6 III	164 II	749.9 IV	-1234.1 I	-754.1 III	-1082.1 II	-639.5 IV	-1234.7 I	-715.7 III	-1081.2 II	-706.3 IV

For an easier comparison of the SOC results with collinear calculations, all the energies are expressed relatively to the energy of the collinear FiMHS magnetic phase (because energies are lower for SOC, the corresponding ΔE will be mainly negative). Spin up/down are marked by signs + or -, assigned to the magnetic moments from collinear calculations, although in the case of noncollinear calculations we cannot speak about spin up/down, and hence signs are not assigned to the magnetic and orbital moments (their directions will be discussed later in details, together with magnetocrystalline anisotropy energy).

The computed first-principles structural parameters from the noncollinear spin polarized calculations are consistent with those reported in the collinear case, and the order of the magnetic states FiMHS (I), FMHS (II), FiMLS (III), and FMLS (IV) on the energy scale is preserved for all three considered functionals LSDA+U, PBEsol+U and RevPBE+U, even though different spin quantization axes are considered. The energy differences ΔE show that the states obtained in the noncollinear cases are more stable than those from the collinear case.

Table 5.2 As in Table 5.1 but for the PBEsol+U functional.

Phase	PBEsol+U collinear spin polarized calculations				PBEsol+U noncollinear spin polarized calculations with SOC, S=[111]				PBEsol+U noncollinear spin polarized calculations with SOC, S=[-0.5 0.5 0]			
	FiMHS	FiMLS	FMHS	FMLS	FiMHS	FiMLS	FMHS	FMLS	FiMHS	FiMLS	FMHS	FMLS
a, in Å	5.42	5.35	5.43	5.33	5.56	5.43	5.56	5.43	5.55	5.41	5.57	5.45
b, in Å	5.42	5.35	5.43	5.33	5.56	5.43	5.56	5.43	5.55	5.41	5.57	5.46
c, in Å	5.42	5.35	5.43	5.33	5.56	5.43	5.56	5.43	5.55	5.41	5.57	5.43
α , in °	60.74	61.02	60.74	61.08	59.76	60.52	59.76	60.55	59.82	61.04	59.73	60.48
β , in °	60.74	61.02	60.74	61.08	59.76	60.52	59.76	60.55	59.82	61.04	59.73	60.61
γ , in °	60.74	61.02	60.74	61.08	59.76	60.52	59.76	60.55	59.82	61.05	59.73	60.25
V _r , Å ³	114.7	111.2	115.1	110.2	120.6	114.7	121.1	114.8	120.5	114.5	121.2	115.3
X _{Bi}	0.000	0.000	0.000	0.000	0.000	0.000	0.000	0.000	0.000	0.000	0.000	0.000
X _{Bi}	0.504	0.496	0.505	0.497	0.506	0.497	0.506	0.497	0.505	0.493	0.506	0.497
X _{Fe}	0.732	0.726	0.731	0.726	0.731	0.726	0.731	0.726	0.731	0.726	0.731	0.726
X _{Cr}	0.226	0.228	0.225	0.228	0.225	0.228	0.225	0.228	0.225	0.227	0.225	0.228
X _{O1}	0.545	0.546	0.546	0.547	0.543	0.545	0.544	0.545	0.543	0.547	0.543	0.545
y _{O1}	0.950	0.948	0.948	0.947	0.949	0.948	0.948	0.948	0.949	0.952	0.948	0.949
Z _{O1}	0.397	0.411	0.399	0.410	0.398	0.411	0.401	0.410	0.398	0.408	0.400	0.410
X _{O2}	0.047	0.038	0.044	0.039	0.044	0.038	0.042	0.039	0.044	0.042	0.041	0.041
y _{O2}	0.905	0.904	0.905	0.905	0.906	0.906	0.907	0.905	0.906	0.903	0.906	0.904
Z _{O2}	0.447	0.456	0.449	0.455	0.446	0.454	0.448	0.454	0.446	0.457	0.448	0.450
μM_{Fe} in μ_B	-4.06	-0.75	+4.09	+0.91	4.000	0.956	4.029	0.978	3.999	0.905	4.026	0.901
μM_{Cr} in μ_B	+2.63	+2.75	+2.91	+2.76	2.524	2.642	2.765	2.647	2.524	2.657	2.746	2.680
μL_{Fe} in μ_B	-	-	-	-	0.025	0.819	0.018	0.899	0.026	0.905	0.018	0.240
μL_{Cr} in μ_B	-	-	-	-	0.054	0.038	0.047	0.022	0.051	0.038	0.045	0.041
μM_{BFCO} in μ_B	-1.99	+1.88	+7.69	+3.84	1.997	1.910	7.974	4.010	1.997	2.319	7.968	3.984
ΔE in meV	0 I	713.9 III	112.8 II	1204.8 IV	-1117.8 I	-201.0 III	-1014.2 II	-94.9 IV	-1117.8 I	-321.3 III	-880.5 II	502.1 IV

The computed volumes of the optimized cells show the effect of the noncollinear spin structures and SOC on the unit cell (where change in symmetry was allowed). Volumes are generally higher in the noncollinear case than those obtained in collinear calculations: volumes are about 5% higher for HS states within both PBE+U functionals, and about 3%-6% within the PBEsol+U & 8.4% within the RevPBE+U, respectively, in the case of LS states. LSDA+U functional yield very small cell volumes variations between -0.6% to 0.2 %.

Table 5.3 As in Table 5.1 but for the RevPBE+U functional.

	RevPBE+U collinear spin polarized calculations				RevPBE+U noncollinear spin polarized calculations with SOC, S=[111]				RevPBE+U noncollinear spin polarized calculations with SOC, S=[-0.5 0.5 0]			
	FiMHS	FiMLS	FMHS	FMLS	FiMHS	FiMLS	FMHS	FMLS	FiMHS	FiMLS	FMHS	FMLS
a_r in Å	5.61	5.55	5.61	5.62	5.75	5.71	5.77	5.76	5.76	5.71	5.76	5.76
b_r in Å	5.61	5.55	5.61	5.62	5.75	5.77	5.77	5.76	5.75	5.76	5.76	5.75
c_r in Å	5.61	5.55	5.61	5.62	5.75	5.20	5.77	5.76	5.75	5.19	5.76	5.75
α_r in °	59.72	59.98	59.75	59.73	58.92	62.19	58.82	58.99	58.91	62.21	58.99	59.90
β_r in °	59.72	59.98	59.75	59.73	58.92	63.26	58.82	58.99	58.91	63.34	58.99	59.90
γ_r in °	59.72	59.98	59.75	59.73	58.92	58.28	58.82	58.99	58.91	58.38	58.99	59.90
V_r , Å ³	124.4	121.3	124.7	125.3	131.5	124.2	132.3	132.2	131.5	124.1	132.3	131.7
x_{Bi}	0.000	0.000	0.000	0.000	0.000	0.000	0.000	0.000	0.000	0.000	0.000	0.000
x_{Bi}	0.511	0.505	0.512	0.505	0.512	0.527	0.513	0.505	0.512	0.526	0.512	0.513
x_{Fe}	0.732	0.726	0.731	0.725	0.732	0.727	0.731	0.725	0.733	0.728	0.731	0.731
x_{Cr}	0.224	0.225	0.224	0.227	0.225	0.225	0.224	0.227	0.224	0.225	0.224	0.223
x_{O1}	0.544	0.546	0.545	0.547	0.540	0.543	0.541	0.547	0.541	0.543	0.546	0.544
y_{O1}	0.947	0.948	0.947	0.946	0.946	0.953	0.946	0.946	0.947	0.953	0.945	0.946
z_{O1}	0.393	0.402	0.396	0.403	0.396	0.411	0.399	0.403	0.396	0.405	0.394	0.396
x_{O2}	0.044	0.044	0.042	0.043	0.041	0.041	0.037	0.043	0.041	0.042	0.043	0.039
y_{O2}	0.903	0.900	0.903	0.900	0.905	0.899	0.907	0.900	0.906	0.899	0.902	0.905
z_{O2}	0.445	0.450	0.446	0.450	0.444	0.453	0.446	0.450	0.444	0.455	0.446	0.425
μM_{Fe} in μ_B	-4.10	-0.93	+4.12	+0.87	4.046	0.896	4.065	1.115	4.046	0.898	4.063	0.862
μM_{Cr} in μ_B	+2.71	+2.89	+2.96	+2.82	2.611	2.749	2.814	2.693	2.611	2.748	2.817	2.697
μL_{Fe} in μ_B	-	-	-	-	0.025	0.097	0.019	1.328	0.023	0.037	0.019	0.166
μL_{Cr} in μ_B	-	-	-	-	0.055	0.055	0.047	0.026	0.053	0.044	0.049	0.042
μM_{BFCO} in μ_B	-1.98	+1.91	+7.71	+3.84	1.999	1.812	7.983	4.026	2.000	1.876	7.981	3.991
ΔE in meV	0 I	1020.5 III	68.7 II	1199.4 IV	-1118.2 I	-359.2 III	-1057.5 II	293.8 IV	-1118.6 I	-351.1 III	-1050.2 II	594.5 IV

In addition, when breaking symmetry was allowed, small variations appeared in the lattice lengths and angles. In many cases, cell shape and size variations appeared on the 3rd or 4th digits, which is the reason why they cannot be seen in the above tables, where data are presented with only two digits. Generally, in the LS cases, variations were stronger so that they can be seen on the 1st or 2nd digits, e.g., FMLS for LSDA+U and S=[-0.5 0.5 0] in Table 5.1, and PBEsol+U for S=[-0.5 0.5 0] in Table 5.2, or FiMLS within the RevPBE+U in Table 5.3.

Symmetry breaking also affects the orbital angular momentum as it can be seen in Tables 5.1-5.3. More precisely, the orbital magnetic moments for Cr³⁺ and Fe³⁺ HS are strongly quenched at the amount of 0.049-0.056 μ_B per Cr atom, and 0.018-0.029 μ_B per Fe HS atom (i.e., orbital moments are very small, and hence the total magnetic moment is due to the spin). In addition, calculations within the functionals LSDA+U, PBEsol+U and RevPBE+U show that in the case of FiMHS and FMHS states, both orbital moments of Fe and Cr participate in a small percent, about 1%-4% to the total magnetic moment, while the spin moments of Fe and Cr contribute for about 74%-86%. The trend is opposite in the case of Fe³⁺ LS, where largely unquenched magnetic orbital moments are observed. Because SOC brings small changes in the R3 structures computed using the LSDA+U functional, the degree of (un)quenching of the magnetic orbital moments depends on the chosen spin quantization axis for FiMLS (see S=[111] versus S \perp [111], and Table 5.4). For PBE+U functionals, Fe³⁺ LS shows very large unquenched magnetic orbital moments for both FiMLS and FMLS states, and spin quantization axes S=[111] & S \perp [111] (see Tables 5.2 & 5.3). Experimentally, both strongly quenched and large unquenched orbital moments were proven for bulk Fe-clusters (Niemeyer et al., 2012). How quenching versus unquenching of the orbital moments influences oxygen octahedra distortions for FiMHS, FMHS, FiMLS and FMLS states in the case of BFCO will be seen in the Section 5.4.

Regarding the magnetocrystalline anisotropy energy (MAE) and easy axis for the FiMHS state, computational results show that the saturated magnetic moment of 1.999 μ_B /f.u. is achieved along the easy axis S₆=[-0.5 0.5 0] \perp [111] (i.e., this is the most energetically favorable direction). The computed MAEs relatively to the easy axis (i.e. MAE=0 at easy axis), are presented in the Table 5.4 for LSDA+U functional. The magnitudes of the magnetic and orbital moments are given for Fe and Cr, as well as their corresponding vectors. Note that the vectors were normalized for easier comparison with the spin quantization axes S_i and analysis of the degree of canting.

Table 5.4 The computed magneto-crystalline anisotropy energies for FiMHS state within the LSDA+U functional, corresponding to the spin quantization axes $S_1=[111]$, $S_2=[0.98 0.90 1.06]$, $S_3=[0.97 0.84 1.09]$, $S_4=[0.5, 1.0, 1.5]$, $S_5=[0.70, 0.35, 1.06]$ and $S_6=[-0.5, 0.5, 0]$, which make angles 0° , 9.4° , 14° , 22° , 45° , 90° with the polarization axis [111]; as well as the computed magnitudes of the magnetic (μM) and orbital (μL) moments together with their corresponding vectors for Fe and Cr.

FiMHS LSDA+U	$S_1=[111]$ $\angle(S_1,[111])=0^\circ$	$S_2=[0.98 0.90 1.06]$ $\angle(S_2,[111])=9.4^\circ$	$S_3=[0.97 0.84 1.09]$ $\angle(S_3,[111])=14^\circ$	$S_4=[0.5, 1.0, 1.5]$ $\angle(S_4,[111])=22^\circ$	$S_5=[0.70, 0.35, 1.06]$ $\angle(S_5,[111])=45^\circ$	$S_6=[-0.5, 0.5, 0]$ $\angle(S_6,[111])=90^\circ$
MAE in meV	0.659	0.238	0.136	0.005	0.003	0
μM_{BFCO} in μ_B	1.992	1.992	1.992	1.992	1.992	1.999
M_{BFCO} vector	(0.99; 1.00; 1.00)	(0.99; 0.89; 1.06)	(0.97; 0.84; 1.09)	(0.58; 1.10; 1.74)	(0.70; 0.35; 1.06)	(-0.49; 0.45; 0.04)
μM_{Fe} in μ_B	3.936	3.936	3.936	3.936	3.937	3.936
M_{Fe} vector	(-1.00; -1.00; -1.00)	(-0.98; -0.90; -1.06)	(-0.97; -0.85; -1.09)	(-0.56; -1.14; -1.72)	(-0.70; -0.35; -1.06)	(0.49; -0.50; 0.00)
μL_{Fe} in μ_B	0.029	0.029	0.029	0.028	0.028	0.023
L_{Fe} vector	(-1.00; -1.00; -1.00)	(-0.98; -0.90; -1.07)	(-0.97; -0.84; -1.09)	(-0.64; -1.26; -1.76)	(-0.74; -0.40; -1.07)	(0.49; -0.51; 0.01)
μM_{Cr} in μ_B	2.465	2.465	2.465	2.465	2.465	2.465
M_{Cr} vector	(1.00; 0.99; 0.99)	(0.99; 0.89; 1.06)	(0.97; 0.84; 1.09)	(0.58; 1.12; 1.74)	(0.70; 0.35; 1.06)	(-0.49; 0.48; 0.01)
μL_{Cr} in μ_B	0.056	0.056	0.056	0.054	0.054	0.053
L_{Cr} vector	(-1.00; -1.00; -1.00)	(-0.98; -0.92; -1.06)	(-0.96; -0.89; -1.08)	(-0.60; -1.22; -1.72)	(-0.69; -0.43; -1.07)	(0.49; -0.53; 0.03)
Comments	$M_{BFCO} \parallel S_1=[111]$ canting $M_{Fe} \parallel S_1=[111]$ $M_{Cr} \parallel S_1=[111]$ canting $M_{Fe} \parallel M_{Cr}$ canting $L_{Fe} \parallel S_1=[111]$ $L_{Cr} \parallel S_1=[111]$	$M_{BFCO} \parallel S_2$ canting $M_{Fe} \parallel S_2$ $M_{Cr} \parallel S_2$ canting $M_{Fe} \parallel M_{Cr}$ canting $L_{Fe} \parallel S_2$ canting $L_{Cr} \parallel S_2$ canting	$M_{BFCO} \parallel S_3$ $M_{Fe} \parallel S_3$ canting $M_{Cr} \parallel S_3$ $M_{Fe} \parallel M_{Cr}$ canting $L_{Fe} \parallel S_3$ $L_{Cr} \parallel S_3$ canting	Canting became stronger such that vectors are not parallel anymore to S_4 , but $M_{BFCO} \parallel M_{Cr}$ and $M_{BFCO} \parallel M_{Fe}$ and they are canted	$M_{BFCO} \parallel S_5$ $M_{Fe} \parallel S_5$ $M_{Cr} \parallel S_5$ L_{Fe} and L_{Cr} became strongly canted with S_5 and antiparallel tendency	$M_{BFCO} \parallel S_6$ canting $M_{Fe} \parallel S_6$ canting $M_{Cr} \parallel S_6$ canting $M_{Fe} \parallel M_{Cr}$ canting $L_{Fe} \parallel S_2$ canting $L_{Cr} \parallel S_2$ canting

Calculations show that saturated magnetization is achieved along the easy axis $S_6=[-0.5 0.5 0]$. MAE evolves monotonically from the easy axis $S_6=[-0.5 0.5 0]$, to the hard axis $S_1=[111]$ of the magnetization ([111] represents the polarization direction, see Chapter 4). However, MAEs are lower than 1 meV, meaning low anisotropy, and we were able to emphasize these differences because the electronic self-consistent calculations were done with the high convergence precision of 10^{-8} eV. Magnetic and orbital momentum vectors are parallel or antiparallel with the spin quantization axes with a degree of canting that increases from the hard magnetization axis to the easy magnetization axis (i.e., when the angle between S_i and the polarization direction [111] increases), achieving a peak at around 22° , for S_4 , and after that they stabilize again closer to the easy axis. Also, it was found that the magnitude of the orbital moments decreases slightly from the hard axis to the easy axis, while the magnetic moments increases. This behavior is similar with that seen in the case of BFO for R3c rhombohedral symmetry with Fe^{3+} HS following an antiferromagnetic arrangement.

Similar studies performed for the other states FiMLS, FMHS and FMLS show that the physics becomes more complex. For example, looking at the FiMLS case, it can be seen easily from Tables 5.1-5.3 that the easy axis is not the same for all functionals: LSDA+U and RevPBE+U indicate the easy axis $S_1=[111]$, while the PBEsol+U functional indicates $S_6=[-0.5 0.5 0]$ as the easy axis (see Tables 5.5-5.6). Despite this contradiction, it is worth taking a more careful look

at the magnetic and orbital moments along with their corresponding vectors as shown in Table 5.5.

Table 5.5 As in Table 5.4 but for the FiMLS state.

FiMLS LSDA+U	$S_1=[111]$ $\angle(S_1,[111])=0^\circ$	$S_2=[0.98\ 0.90\ 1.06]$ $\angle(S_2,[111])=9.4^\circ$	$S_3=[0.97\ 0.84\ 1.09]$ $\angle(S_3,[111])=14^\circ$	$S_4=[0.5,\ 1.0,\ 1.5]$ $\angle(S_4,[111])=22^\circ$	$S_5=[0.70,\ 0.35,\ 1.06]$ $\angle(S_5,[111])=45^\circ$	$S_6=[-0.5,\ 0.5,\ 0]$ $\angle(S_6,[111])=90^\circ$
MAE in meV	0	0.067	0.224	21.596	30.934	38.422
μM_{BFCO} in μ_B	2.027	2.029	2.024	2.584	2.143	2.048
M_{BFCO} vector	(0.99; 0.99; 1.00)	(0.96; 0.82; 1.09)	(0.95; 0.74; 1.11)	(0.97; 1.00; 0.91)	(0.70; 0.31; 0.80)	(-0.54; 0.40; 0.00)
μM_{Fe} in μ_B	0.827	0.828	0.830	0.913	0.837	0.884
M_{Fe} vector	(-1.00; -1.00; -1.00)	(-1.00; -0.99; -0.99)	(-1.00; -0.96; -1.02)	(-1.00; -0.89; -0.51)	(-0.68; -0.11; -0.86)	(0.23; -0.32; 0.00)
μL_{Fe} in μ_B	0.016	0.013	0.010	0.212	0.228	0.414
L_{Fe} vector	(1.00; 1.00; 1.00)	(0.93; 0.90; 0.90)	(-0.58; 0.49; -0.49)	(0.53; -0.28; -0.10)	(-0.57; -0.14; -0.61)	(0.43; -0.51; 0.03)
μM_{Cr} in μ_B	2.634	2.634	2.634	2.629	2.465	2.465
M_{Cr} vector	(0.99; 0.99; 1.00)	(1.00; 0.97; 1.01)	(0.98; 0.94; 1.04)	(0.97; 1.00; 0.83)	(0.19; 0.35; 0.58)	(-0.50; 0.57; 0.01)
μL_{Cr} in μ_B	0.038	0.038	0.038	0.034	0.054	0.039
L_{Cr} vector	(-1.00; -1.00; -1.00)	(-0.99; -0.98; -1.02)	(-0.97; -0.97; -1.04)	(0.41; -0.45; -0.18)	(0.58; -0.53; -0.67)	(0.40; -0.62; 0.04)
Comments Vectors are: Parallel // Antiparallel \\ Canted	$M_{BFCO} // S_1$ canting $M_{Fe} \setminus S_1 = [111]$ $M_{Cr} // S_1$ canting $M_{Fe} \setminus M_{Cr}$ canting $L_{Fe} // S_1 = [111]$ $L_{Cr} \setminus S_1 = [111]$	M_{BFCO} canting between S_2 and S_1 $M_{Fe} \setminus S_1$ canting $M_{Cr} // S_1$ canting $M_{Fe} \setminus M_{Cr}$ canting $L_{Fe} // S_1$ canting $L_{Cr} \setminus S_1$ canting	M_{BFCO} strong canted with S_3 $M_{Fe} \setminus S_1$ canting $M_{Cr} // S_1$ $M_{Fe} \setminus M_{Cr}$ canting L_{Fe} not parallel $L_{Cr} \setminus S_1$ canting	Canting became stronger such that vectors are not parallel anymore with any axis	Vectors are too far by the S_5 or S_1	Vectors are too far by the S_6 or S_1

The computed MAEs increase from the easy axis $S_1=[111]$ to the hard axis $S_6=[-0.5\ 0.5\ 0]$, indicating strong anisotropy. Magnetic and orbital momentum vectors are parallel or antiparallel with the spin quantization axis $S_1=[111]$, i.e., the direction of the polarization, when the angle between S_i and [111] is small. If this angle increases then the magnetic and orbital vectors do not align with [111] anymore, and do not align with S_i either. This case is highly interesting as the easy axis is not perpendicular to the direction of the polarization [111], in contradiction with the unproven assumption mentioned above (i.e., magnetic vector likes to be perpendicular on the polarization axis [111]).

This contradiction is also observed for the ferromagnetic state FMHS, where the easy axis $S_1=[111]$ is confirmed by all functionals LSDA+U, PBEsol+U, and RevPBE+U (see Table 5.6).

Table 5.6 The computed easy and hard magnetization axes of R3 BFCO corresponding to the FiMHS, FiMLS, FMHS and FMLS states within LSDA+U, PBEsol+U and RevPBE+U functional approximations (SOC effect is included).

Funct.	LSDA+U noncollinear spin polarized				PBEsol+U noncollinear spin polarized				RevPBE+U noncollinear spin polarized			
	FiMHS	FiMLS	FMHS	FMLS	FiMHS	FiMLS	FMHS	FMLS	FiMHS	FiMLS	FMHS	FMLS
Easy axis	$\perp [111]$	[111]	[111]	$\perp [111]$	$\perp [111]$	$\perp [111]$	[111]	[111]	$\perp [111]$	[111]	[111]	[111]
Hard axis	[111]	$\perp [111]$	$\perp [111]$	[111]	[111]	[111]	$\perp [111]$	$\perp [111]$	[111]	$\perp [111]$	$\perp [111]$	$\perp [111]$

For FMLS, according to the Tables 5.1-5.3, 5.6, the two PBE+U functionals indicate an easy axis $S_1=[111]$, while LSDA+U shows an easy axis $S_6=[-0.5\ 0.5\ 0] \perp[111]$.

Note that in the case of HS, calculations show low magnetic anisotropy energies and hence the magnetization axis is easy to change, behaviour also confirmed by the canting of spin and orbital moments around the chosen spin quantization axis as input. All functional approximations LSDA+U, PBEsol+U and RevPBE+U show the easy axis $S_6=[-0.5\ 0.5\ 0] \perp[111]$ for FiMHS, and $S_1=[111]$ for FMHS, respectively.

In the LS states, calculations show higher magneto-crystalline anisotropy energies and easy axis [111] is confirmed by two functionals out of three.

Experimentally, for BFCO grown epitaxially by PLD through a nanostencil (a shadow mask with nanometer-scale features (Nechache et al., 2011)), a saturated magnetization of $5.2\ \mu_B$ per Fe-Cr pair along the two directions perpendicular to [111] was found. Considering the possible magnetizations found theoretically (see Tables 5.1-5.3), our results suggest that the BFCO epitaxial nanostructures synthesized in the laboratory are intermediate between FMHS and FMLS. If we take into account that HS states showed a lower anisotropy theoretically, then FMLS is the most likely. On the other hand, chances to get FMLS as ground state are low, as this is the last state in the energetic order; there are better chances for FMHS to be obtained as this has the second lowest ground state energy. Definitively, these investigations deserve to be continued for more spin quantization axes and eventually to use a new approximation, namely Heyd–Scuseria–Ernzerhof (HSE06) screened Coulomb hybrid density functional that contains a Hartree–Fock (HF) mixing constant (25%) and can improve PBE results (Heyd et al., 2004).

5.3. Electronic properties

To gain more insights into the electronic structure and the effect of the noncollinear magnetism with SOC on BFCO, partial and total density of states (DOS), and the corresponding band structures were calculated for the crystal structures discussed in the Section 5.2. Comparisons between DOSs and band structures obtained from collinear calculations and those from noncollinear calculations with SOC were made. Note that, in the case of collinear spin-polarized calculations, the spin of the Cr ion defines the *spin-up states* on the positive axis of the DOS plots, and hence the *spin-down states* are represented on the negative axis. For noncollinear calculations where notions of *spin-up*, *-down* do not have sense, as the electron spin can rotate in any 3D direction, all DOSs are plotted on the positive axis (see Figs. 5.2-5.4).

Figure 5.2 compares the partial and total DOSs of the rhombohedral *R*3 distorted FiMHS phase obtained from collinear calculations within LSDA+U functional, with those obtained from noncollinear spin-polarized calculations where SOC is taken into account within the LSDA+U, PBEsol+U and RevPBE+U functionals. As there are no major differences between DOSs computed for different spin quantization axes (except very small band-gap variations that can be seen in Table 5.7, and the case of two spin channels for FMLS that will be depicted in Fig. 5.4), DOSs are here represented for the spin quantization axis S=[111].

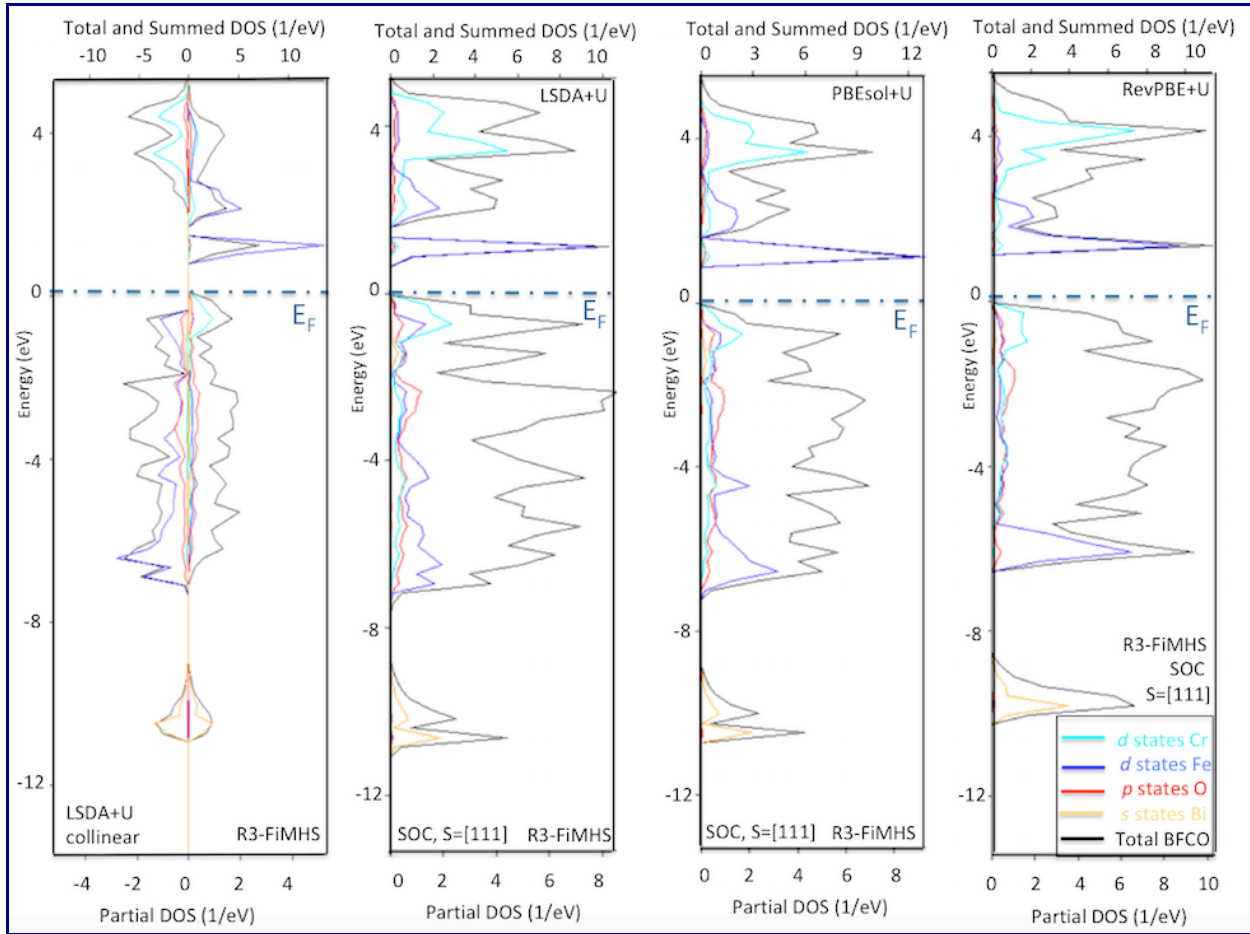


Figure 5.2 The computed partial and total DOS for the rhombohedral *R*3 FiMHS magnetic state of BFCO. Comparison between DOSs obtained from collinear calculations within LSDA+U functional with those obtained from noncollinear calculations taking into account SOC effect within LSDA+U, PBEsol+U and RevPBE+U functionals, where the spin quantization axis is S=[111]. Note that the bottom axis indicating partial DOS and the top axis indicating total DOS have different scales.

DOSs show that spin-orbit coupling mixes the spin-up and spin-down components of the Bloch states, and a moderate increasing of band gap takes place in the case of FiMHS state where SOC is included. Investigating the detailed electronic structure near the Fermi level E_F , a broad

orbital excitation is seen in vicinity of E_F , as it is expected to have orbital excitations between occupied and unoccupied bands in the presence of SOC.

Similar DOSs, with those plotted in Fig. 5.2, are plotted for FMHS states in the Fig. 5.3.

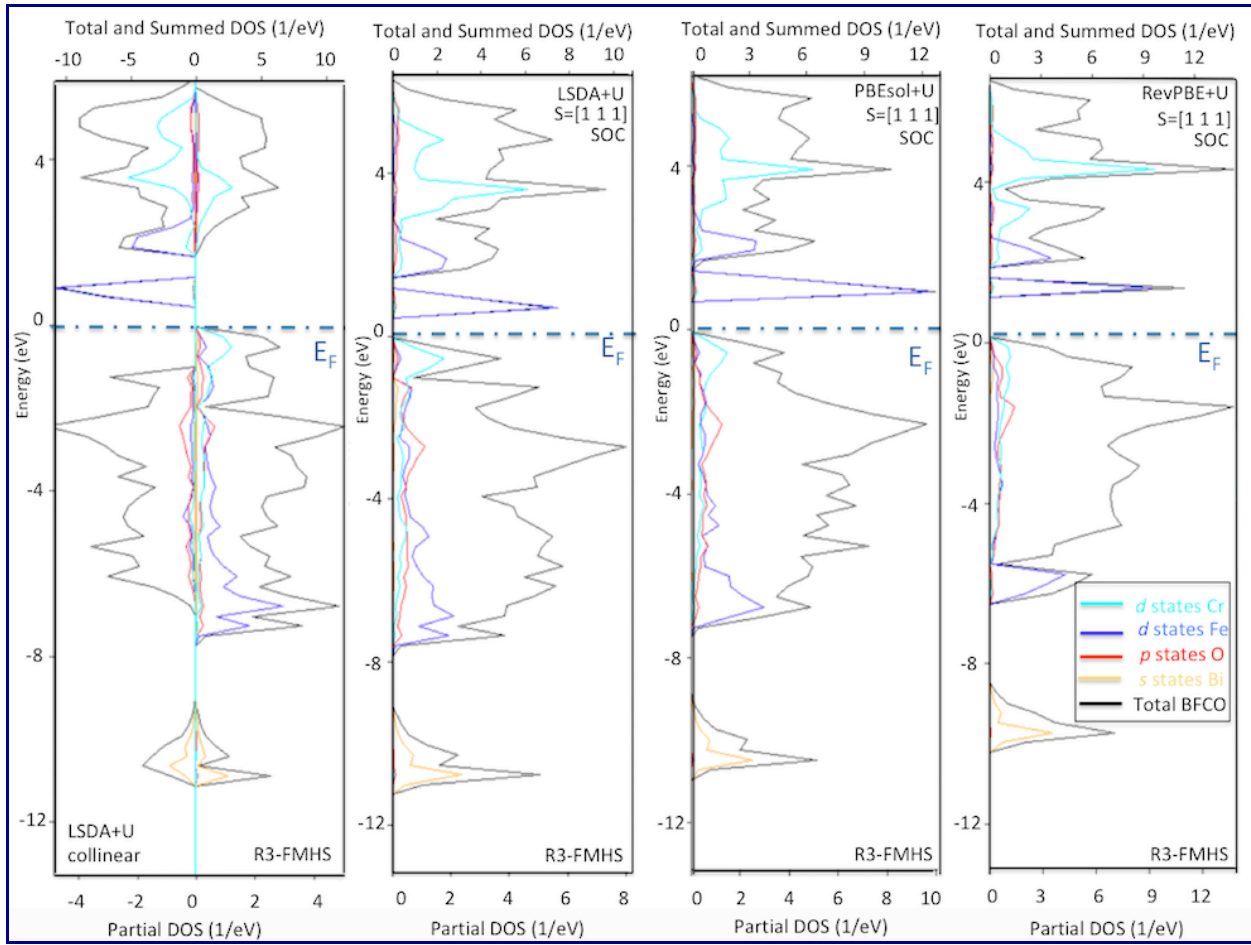


Figure 5.3 As in Figure 5.2 but for the FMHS state.

DOSs show that mixing between spin-up and spin-down components does not always lead to an increase in the band gaps: for LSDA+U, SOC lowers the band-gap, while calculations within PBEsol+U and RevPBE+U show a larger band gap due to SOC. Actually, the fact that orbital excitations are larger for PBE functionals will help opening the band gap.

The calculated band gap values obtained with and without SOC are presented in the Table 5.7 for all magnetic states and functionals discussed in this thesis.

Table 5.7 The computed band gaps of the R3 FiMHS, FiMLS, FMHS and FMLS magnetic phases of BFCO within the LSDA+U, PBESol+U and RevPBE+U functional.

Functional	Band gap [eV] FiMHS	Band gap [eV] FiMLS	Band gap [eV] FMHS	Band gap [eV] FMLS
LSDA+U Collinear calculations	0.921	1.073	0.735	0.592 & 1.246 two spin channels
LSDA+U noncollinear SOC, S=[111]	0.968	0.974	0.610	0.976
LSDA+U noncollinear SOC, S=[-0.5 0.5 0]	0.952	0.970	0.607	0.938
PBESol+U Collinear calculations	1.058	1.210	0.873	0.686 & 1.299 two spin channels
PBESol+U noncollinear SOC, S=[111]	1.220	0.993	0.969	1.025
PBESol+U noncollinear SOC, S=[-0.5 0.5 0]	1.113	1.165	0.842	0.550
RevPBE+U Collinear calculations	1.249	1.541	1.172	0.418 & 1.424 two spin channels
RevPBE+U noncollinear SOC, S=[111]	1.303	1.642	1.265	0.937
RevPBE+U noncollinear SOC, S=[-0.5 0.5 0]	1.290	1.597	1.229	0.660

Calculations show clearly the effect of SOC on the band gaps: for HS states, the band gaps are generally larger within SOC (few exceptions for FMHS), while in the case of the FiMLS states, band gap values are smaller within the LSDA+U and RevPBE+U functionals.

The case of FMLS is analyzed in more details as SOC does not preserves the half-metallicity (two spin channels) observed in the collinear calculations. Pickett and Eschrig reported a study on the effect of SOC on half-metallicity (Pickett & Eschrig, 2007). As the fully relativistic theory (including SOC) in principle destroys half-metallicity, the question is: “does this make half-metals a half truth?”. Authors showed that the relativistic effect of SOC on half-metallicity, it is a minor effect for the smaller magnetic atoms (atomic number $Z \sim 30$ or less). In our case, the atomic numbers for Fe and Cr ($Z_{\text{Cr}}=24$, and $Z_{\text{Fe}}=26$) are at the limit of the range reported by Ref. Pickett & Eschrig, 2007), and the calculations clearly show the effect of SOC on the semi-metallic BFCO. If we analyze DOSs for different quantization axes, we can see that spin channels can be found along different quantization axes S. For example Fig.5.4 represents DOSs obtained within the PBESol+U functional for the spin quantization axis S=[111] (band gap is 1.025 eV), and S=[-0.5 0.5 0] (band gap is 0.55 eV), respectively.

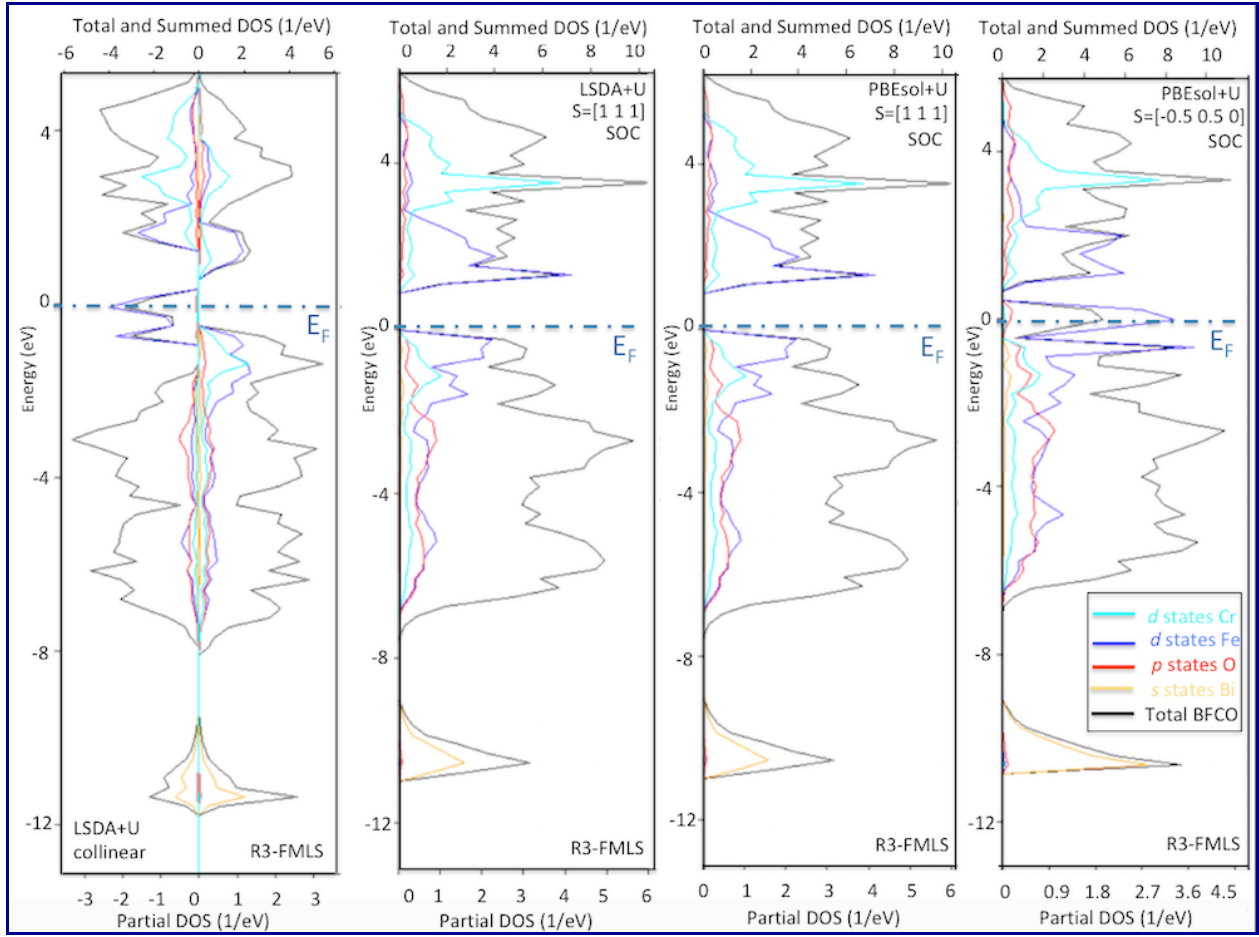


Figure 5.4 As in Figure 5.2 but for the FMLS state.

The band structures were not plotted here, as they do not bring additional insights. They are similar with those presented in the previous chapter referring to the collinear spin-polarized calculations, with small differences in the vicinity of the Fermi energy as it was already seen in DOSs.

5.4. Spin-orbit coupling effects on magnetic structure distortions

It was shown previously (Section 4.5 from Chapter 4) that self-consistent collinear spin-polarized calculations performed for the magnetic phases FiMHS, FiMLS, FMHS and FMLS undergo Jahn-Teller distortions, i.e., off-centering of Fe^{3+} and Cr^{3+} ions within their oxygen octahedra, and off-center distortion induced by the lone pair on the Bi^{3+} ion. These distortions of the *R*3 BFCO rhombohedra include trigonal distortion of the octahedra, i.e., the Fe-O and Cr-O bonds corresponding to the first group of oxygen atoms with Wyckoff positions (x_{01}, y_{01}, z_{01}) ,

(z_{O1}, x_{O1}, y_{O1}) , (y_{O1}, z_{O1}, x_{O1}) were equally elongated along the [111] direction, on one side of the Fe^{3+} or Cr^{3+} cations, and the other three bonds corresponding to the oxygen atoms with Wyckoff positions (x_{O2}, y_{O2}, z_{O2}) , (z_{O2}, x_{O2}, y_{O2}) , (y_{O2}, z_{O2}, x_{O2}) , were also equally elongated on the other side of the Fe^{3+} or Cr^{3+} cations.

When SOC effects are taken into account within noncollinear calculations, and hence the symmetry breaking is allowed, the above triplets of the Fe-O and Cr-O bonds may have additional variations (elongations, contractions). As discussed earlier in Section 5.2, variations in the lattice lengths and angles were stronger in the states containing Fe^{3+} LS states, i.e., FMLS and FiMLS structures. In addition, it was observed that Fe^{3+} LS had largely unquenched magnetic orbital moments which we believe to be connected with additional distortions appearing when SOC effect is considered.

For a better understanding of how the magnitude of the magnetic orbital moments influences the octahedra distortions for the FiMHS, FMHS, FiMLS and FMLS states in the case of BFCO, the calculated bond lengths between Bi_1 , Cr, Bi_2 and Fe (see top-left panel of Fig. 4.4, section 4.3) along the diagonal [111] of BFCO, as well as the computed Cr-O, Fe-O bond lengths corresponding to the Wyckoff oxygen positions (x_{O1}, y_{O1}, z_{O1}) and (x_{O2}, y_{O2}, z_{O2}) are presented in the Tables 5.8a,b to 5.11a,b. The results obtained through noncollinear calculations with SOC performed within the LSDA+U, PBEsol+U and RevPBE+U functionals using the two spin quantization axes $S=[111]$ and $S \perp [111]$, were compared with those from Section 4.5 corresponding to the collinear calculations (no spin-orbit interactions and breaking symmetry).

Table 5.8a The calculated bond lengths between Bi_1 , Cr, Bi_2 and Fe (see top-left panel of Fig. 4.4, section 4.3) along the diagonal [111] of BFCO for FiMHS state. Comparison between values obtained using collinear calculations within the LSDA+U, PBEsol+U and RevPBE+U functionals, and noncollinear calculations with SOC and spin quantization axes $S=[111]$ and $S \perp [111]$.

BFCO Magnetic state	Bi ₁ -Cr [Å]	Cr-Bi ₂ [Å]	Bi ₂ -Fe [Å]	Fe-Bi ₁ [Å]	Diagonal Bi ₁ -Cr-Bi ₂ -Fe-Bi ₁	Cell Volume [Å ³]
FiMHS LSDA+U Collinear calculations	3.02	3.72	3.06	3.60	13.40	116.3
FiMHS LSDA+U SOC, S=[111]	3.02	3.72	3.06	3.59	13.39	116.4
FiMHS LSDA+U SOC, S \perp [111]	3.02	3.72	3.06	3.59	13.39	116.5
FiMHS PBEsol+U Collinear calculations	3.03	3.60	3.06	3.50	13.19	114.7
FiMHS PBEsol+U SOC, S=[111]	3.04	3.82	3.07	3.68	13.61	120.6
FiMHS PBEsol+U SOC, S \perp [111]	3.04	3.81	3.07	3.68	13.60	120.5
FiMHS RevPBE+U Collinear calculations	3.07	3.86	3.11	3.73	13.77	124.4
FiMHS RevPBE+U SOC, S=[111]	3.07	4.09	3.12	3.91	14.19	131.5
FiMHS RevPBE+U SOC, S \perp [111]	3.07	4.09	3.12	3.91	14.19	131.5

Table 5.8b The calculated Cr-O, Fe-O bond lengths corresponding to the oxygen positions (x_{01} , y_{01} , z_{01}) and (x_{02} , y_{02} , z_{02}) in the R3 BFCO for FiMHS state. Comparison between values obtained using collinear calculations within the LSDA+U, PBEsol+U and RevPBE+U functionals, and noncollinear calculations with SOC and spin quantization axes S=[111] and S \perp [111].

BFCO Magnetic state	Cr-O [\AA] for (x_{02} , y_{02} , z_{02})	Cr-O [\AA] for (x_{01} , y_{01} , z_{01})	Fe-O [\AA] for (x_{01} , y_{01} , z_{01})	Fe-O [\AA] for (x_{02} , y_{02} , z_{02})
FiMHS LSDA+U Collinear calculations	1.979	1.949	2.072	1.943
FiMHS LSDA+U SOC, S=[111]	1.978 1.978 1.978	1.949 1.949 1.949	2.073 2.073 2.073	1.942 1.942 1.942
FiMHS LSDA+U SOC, S \perp [111]	1.978 1.978 1.978	1.950 1.950 1.950	2.072 2.072 2.072	1.942 1.942 1.942
FiMHS PBEsol+U Collinear calculations	1.972	1.948	2.046	1.946
FiMHS PBEsol+U SOC, S=[111]	2.004 2.004 2.004	1.972 1.972 1.972	2.101 2.101 2.101	1.960 1.960 1.960
FiMHS PBEsol+U SOC, S \perp [111]	2.003 2.003 2.003	1.972 1.972 1.972	2.100 2.100 2.100	1.961 1.961 1.961
FiMHS RevPBE+U Collinear calculations	2.037	1.966	2.125	1.982
FiMHS RevPBE+U SOC, S=[111]	2.077 2.077 2.077	2.017 2.017 2.017	2.194 2.194 2.194	1.992 1.992 1.992
FiMHS RevPBE+U SOC, S \perp [111]	2.077 2.077 2.077	2.017 2.017 2.017	2.195 2.195 2.195	1.991 1.991 1.991

Calculations show that in the case of FiMHS (Table 5.8b) the trigonal distortions of the octahedral are preserved even in presence of symmetry breaking and SOC (Fe-O and Cr-O triplets bonds can be seen in the table).

Regarding the magnitude of the bond lengths with SOC, their change in length is of order 10^{-3} \AA for the different quantization axes. Comparing collinear versus noncollinear calculations, it can be seen that the Bi₁-Cr and Bi₂-Fe bonds do not change significantly, while Cr-Bi₂ and Fe-Bi₁ bonds are elongated about 5-6% when the PBE+U functionals are used with SOC, as it can be seen in the Table 5.8a, because the length of cell diagonal increased. We believe that his “one side” elongation is attributed to the lone pair of the Bi³⁺ which acts stronger due to symmetry reduction, and not to the SOC as Fe³⁺ HS and Cr have quenched magnetic orbital moments. Also, triplets bond lengths are elongated about 1-4 % within SOC and PBE+U functionals, having larger percentages for the bonds corresponding to the (x_{01} , y_{01} , z_{01}) Wyckoff oxygen positions.

Further, similar data corresponding to the FiMLS are presented in the Tables 5.9a,b.

Table 5.9a The calculated bond lengths between Bi₁, Cr, Bi₂ and Fe (see top-left panel of Fig. 4.4, section 4.3) along the diagonal [111] of BFCO for FiMLS state. Comparison between values obtained using collinear calculations within the LSDA+U, PBEsol+U and RevPBE+U functionals, and noncollinear calculations with SOC effects and spin quantization axes S=[111] and S ⊥ [111].

BFCO Magnetic state	Bi ₁ -Cr [Å]	Cr-Bi ₂ [Å]	Bi ₂ -Fe [Å]	Fe-Bi ₁ [Å]	Diagonal Bi ₁ -Cr-Bi ₂ -Fe-Bi ₁	Cell Volume [Å ³]
FiMLS LSDA+U Collinear calculations	2.97	3.49	3.01	3.57	13.04	111.1
FiMLS LSDA+U SOC, S=[111]	3.03	3.47	3.02	3.49	13.01	111.0
FiMLS LSDA+U SOC, S ⊥ [111]	3.03	3.47	3.02	3.49	13.01	111.0
FiMLS PBEsol+U Collinear calculations	3.04	3.46	3.03	3.47	13.00	111.2
FiMLS PBEsol+U SOC, S=[111]	3.05	3.57	3.03	3.59	13.24	114.7
FiMLS PBEsol+U SOC, S ⊥ [111]	3.07	3.49	3.06	3.51	13.13	114.5
FiMLS RevPBE+U Collinear calculations	3.06	3.74	3.06	3.74	13.60	121.3
FiMLS RevPBE+U SOC, S=[111]	3.24	3.72	3.07	3.47	13.50	124.2
FiMLS RevPBE+U SOC, S ⊥ [111]	3.24	3.72	3.07	3.46	13.49	124.1

Table 5.9b The calculated Cr-O, Fe-O bond lengths corresponding to the oxygen positions (x_{O1} , y_{O1} , z_{O1}) and (x_{O2} , y_{O2} , z_{O2}) in the R3 BFCO for FiMLS state. Comparison between values obtained using collinear calculations within the LSDA+U, PBEsol+U and RevPBE+U functionals, and noncollinear calculations with SOC effects and spin quantization axes S=[111] and S ⊥ [111].

BFCO Magnetic state	Cr-O [Å] for (x_{O2} , y_{O2} , z_{O2})	Cr-O [Å] for (x_{O1} , y_{O1} , z_{O1})	Fe-O [Å] for (x_{O1} , y_{O1} , z_{O1})	Fe-O [Å] for (x_{O2} , y_{O2} , z_{O2})
FiMLS LSDA+U Collinear calculations	1.982	1.953	1.931	1.922
FiMLS LSDA+U SOC, S=[111]	1.982 1.982 1.982	1.956 1.956 1.956	1.927 1.927 1.927	1.923 1.923 1.923
FiMLS LSDA+U SOC, S ⊥ [111]	1.980 1.980 1.980	1.954 1.954 1.954	1.928 1.928 1.928	1.924 1.924 1.924
FiMLS PBEsol+U Collinear calculations	1.978	1.955	1.937	1.926
FiMLS PBEsol+U SOC, S=[111]	2.011 2.011 2.011	1.973 1.973 1.973	1.953 1.953 1.953	1.935 1.935 1.935
FiMLS PBEsol+U SOC, S ⊥ [111]	1.999 1.999 1.999	1.974 1.974 1.974	1.956 1.956 1.956	1.943 1.943 1.943
FiMLS RevPBE+U Collinear calculations	2.039	2.001	2.018	1.982
FiMLS RevPBE+U SOC, S=[111]	2.021 2.132 2.042	1.994 2.086 2.004	2.236 1.944 2.008	2.128 1.872 2.003
FiMLS RevPBE+U SOC, S ⊥ [111]	2.022 2.043 2.129	1.996 2.000 2.086	2.237 2.127 2.014	1.870 1.944 2.002

Calculations show that in the case of FiMLS (Table 5.9b) the trigonal distortions of the octahedra are preserved when the functionals LSDA+U and PBEsol+U are used with symmetry

breaking and SOC, but that they change when spin quantization axis changes. When the RevPBE+U functional is used, the effects of symmetry breaking are highly visible on the bond lengths, as they are not triplets anymore (Fe-O and Cr-O triplets bonds can be seen in the table). Comparing collinear versus SOC data, it can be seen that Bi₁-Cr, Bi₂-Fe, Cr-Bi₂ and Fe-Bi₁ bonds change significantly for all considered functionals (Table 5.9a) as follow: Bi₁-Cr and Bi₂-Fe are elongated about 2% to 6%, and 0.5% to 3%, respectively; while Cr-Bi₂ and Fe-Bi₁ bonds are elongated or contracted about -0.5% to 3%, and -7% to 2%, respectively. Also, variations can be seen in Fe-O and Cr-O bond lengths (Table 5.9b) when SOC is considered: about -0.2% to 1% for LSDA+U and PBEsol+U, and stronger variations about -5% to 9% for RevPBE+U. In addition, Table 5.5 shows that for quantization axes making angles larger than around 22° with the [111] direction, magnetic and orbital vectors do not align with [111] or to the chosen quantization axis. Definitively, this is due to the unquenched magnetic orbital moments for Fe³⁺ LS which is not visible in the octahedra bonds for LSDA+U. The effect is better seen for both PBE+U functionals. Actually, distortions seen in FiMLS state are consequences of the unquenched magnetic orbital moments for Fe³⁺ LS, central Bi³⁺ lone pair, and other unstudied physics coming together with symmetry breaking and SOC.

Similar behaviours as those presented in FiMHS and FiMLS states can be seen for FMHS and FMLS presented in the Tables 5.10a,b-5.11a,b.

Table 5.10a The calculated bond lengths between Bi₁, Cr, Bi₂ and Fe (see top-left panel of Fig. 4.4, section 4.3) along the diagonal [111] of BFCO for FMHS state. Comparison between values obtained using collinear calculations within the LSDA+U, PBEsol+U and RevPBE+U functionals, and noncollinear calculations with SOC effects and spin quantization axes S=[111] and S ⊥ [111].

BFCO Magnetic state	Bi ₁ -Cr [Å]	Cr-Bi ₂ [Å]	Bi ₂ -Fe [Å]	Fe-Bi ₁ [Å]	Diagonal Bi ₁ -Cr-Bi ₂ -Fe-Bi ₁	Cell Volume [Å ³]
FMHS LSDA+U Collinear calculations	3.03	3.73	3.05	3.61	13.42	116.9
FMHS LSDA+U SOC, S=[111]	3.02	3.73	3.06	3.59	13.40	116.5
FMHS LSDA+U SOC, S ⊥ [111]	3.02	3.72	3.09	3.59	13.39	116.5
FMHS PBEsol+U Collinear calculations	3.04	3.60	3.06	3.51	13.21	115.1
FMHS PBEsol+U SOC, S=[111]	3.04	3.84	3.06	3.70	13.64	121.1
FMHS PBEsol+U SOC, S ⊥ [111]	3.04	3.84	3.06	3.70	13.64	121.2
FMHS RevPBE+U Collinear calculations	3.07	3.87	3.10	3.73	13.77	124.7
FMHS RevPBE+U SOC, S=[111]	3.06	4.14	3.10	3.95	14.25	132.3
FMHS RevPBE+U OC, S ⊥ [111]	3.06	4.10	3.11	3.93	14.20	132.3

Table 5.10b The calculated Cr-O, Fe-O bond lengths corresponding to the oxygen positions (x_{O1}, y_{O1}, z_{O1}) and (x_{O2}, y_{O2}, z_{O2}) in the R3 BFCO for FMHS state. Comparison between values obtained using collinear calculations within the LSDA+U, PBEsol+U and RevPBE+U functionals, and noncollinear calculations with SOC effects and spin quantization axes S=[111] and S \perp [111].

BFCO Magnetic state	Cr-O [\AA] for (x_{O2}, y_{O2}, z_{O2})	Cr-O [\AA] for (x_{O1}, y_{O1}, z_{O1})	Fe-O [\AA] for (x_{O1}, y_{O1}, z_{O1})	Fe-O [\AA] for (x_{O2}, y_{O2}, z_{O2})
FMHS LSDA+U Collinear calculations	1.988	1.966	2.055	1.940
FMHS LSDA+U SOC, S=[111]	1.978 1.978 1.978	1.951 1.951 1.951	2.072 2.072 2.072	1.942 1.942 1.942
FMHS LSDA+U SOC, S \perp [111]	1.978 1.978 1.978	1.950 1.950 1.950	2.072 2.072 2.072	1.942 1.942 1.942
FMHS PBEsol+U Collinear calculations	1.979	1.961	2.032	1.934
FMHS PBEsol+U SOC, S=[111]	2.010 2.010 2.010	1.988 1.988 1.988	2.083 2.083 2.083	1.958 1.958 1.958
FMHS PBEsol+U SOC, S \perp [111]	2.011 2.011 2.011	1.988 1.988 1.988	2.083 2.084 2.084	1.957 1.957 1.957
FMHS RevPBE+U Collinear calculations	2.040	2.011	2.109	1.980
FMHS RevPBE+U SOC, S=[111]	2.080 2.080 2.080	2.034 2.034 2.034	2.179 2.179 2.179	1.991 1.991 1.991
FMHS RevPBE+U SOC, S \perp [111]	2.082 2.082 2.082	2.045 2.045 2.045	2.177 2.177 2.177	2.001 2.001 2.001

Table 5.11a The calculated bond lengths between Bi₁, Cr, Bi₂ and Fe (see top-left panel of Fig. 4.4, section 4.3) along the diagonal [111] of BFCO for FMLS state. Comparison between values obtained using collinear calculations within the LSDA+U, PBEsol+U and RevPBE+U functionals, and noncollinear calculations with SOC effects and spin quantization axes S=[111] and S \perp [111].

BFCO Magnetic state	Bi ₁ -Cr [\AA]	Cr-Bi ₂ [\AA]	Bi ₂ -Fe [\AA]	Fe-Bi ₁ [\AA]	Diagonal Bi ₁ -Cr-Bi ₂ -Fe-Bi ₁	Cell Volume [\AA^3]
FMLS LSDA+U Collinear calculations	3.02	3.50	3.03	3.50	13.05	111.5
FMLS LSDA+U SOC, S=[111]	3.03	3.47	3.02	3.50	13.02	111.0
FMLS LSDA+U SOC, S \perp [111]	3.03	3.45	3.01	3.48	12.97	110.8
FMLS PBEsol+U Collinear calculations	3.05	3.44	3.02	3.45	12.96	110.2
FMLS PBEsol+U SOC, S=[111]	3.05	3.57	3.03	3.59	13.24	114.8
FMLS PBEsol+U SOC, S \perp [111]	3.04	3.59	3.03	3.61	13.27	115.3
FMLS RevPBE+U Collinear calculations	3.07	3.84	3.05	3.85	13.81	125.3
FMLS RevPBE+U SOC, S=[111]	3.06	4.10	3.11	3.93	14.20	132.2
FMLS RevPBE+U SOC, S \perp [111]	3.06	4.11	3.10	3.92	14.19	131.7

Table 5.11b The calculated Cr-O, Fe-O bond lengths corresponding to the oxygen positions (x_{O1} , y_{O1} , z_{O1}) and (x_{O2} , y_{O2} , z_{O2}) in the R3 BFCO for FMLS state. Comparison between values obtained using collinear calculations within the LSDA+U, PBEsol+U and RevPBE+U functionals, and noncollinear calculations with SOC effects and spin quantization axes S=[111] and S \perp [111].

BFCO Magnetic state	Cr-O [\AA] for (x_{O2} , y_{O2} , z_{O2})	Cr-O [\AA] for (x_{O1} , y_{O1} , z_{O1})	Fe-O [\AA] for (x_{O1} , y_{O1} , z_{O1})	Fe-O [\AA] for (x_{O2} , y_{O2} , z_{O2})
FMLS LSDA+U Collinear calculations	1.989	1.950	1.944	1.920
FMLS LSDA+U SOC, S=[111]	1.982 1.982 1.982	1.954 1.954 1.954	1.927 1.927 1.927	1.922 1.922 1.922
FMLS LSDA+U SOC, S \perp [111]	1.985 1.985 1.985	1.953 1.953 1.953	1.911 1.911 1.911	1.908 1.908 1.908
FMLS PBEsol+U Collinear calculations	1.986	1.954	1.920	1.912
FMLS PBEsol+U SOC, S=[111]	2.010 2.010 2.010	1.973 1.973 1.973	1.953 1.953 1.953	1.939 1.939 1.939
FMLS PBEsol+U SOC, S \perp [111]	2.014 2.012 2.011	1.975 1.968 1.969	1.945 1.980 1.961	1.927 1.961 1.943
FMLS RevPBE+U Collinear calculations	2.072	2.024	2.037	2.003
FMLS RevPBE+U SOC, S=[111]	2.082 2.082 2.082	2.046 2.045 2.046	2.177 2.177 2.177	2.001 2.001 2.001
FMLS RevPBE+U SOC, S \perp [111]	2.075 2.075 2.075	2.036 2.037 2.037	2.177 2.177 2.177	1.993 1.993 1.993

What is new in the case of the ferromagnetic states, is the fact that off-centering of Fe^{3+} and Cr^{3+} ions within their oxygen octahedra preserve trigonal distortions in all states computed within the three LSDA+U, PBEsol+U and RevPBE+U functionals. The effect of breaking symmetry for FM states is not highly visible as it is for FiM states, and we believe that this is due to the ferromagnetic in the FM case instead of the anti-ferromagnetism coupling (present in ferrimagnetism) for FiM states since Fe-O-Cr bond angles are different in FM and FiM cases.

For a better understanding of the SOC on the distortion-generated effects, their contributions to the spontaneous polarization are investigated in the following section.

For a better understanding of the SOC on the distortion-generated effects, their contributions to the spontaneous polarization are investigated in the following section.

5.5. Spin-orbit coupling effects on the spontaneous polarization

As it was described in the Chapter 4, to predict spontaneous polarization in ferroelectrics, i.e., to compute the difference $\Delta\mathbf{P}$ in the polarization between two different states of the same solid (centrosymmetric paraelectric reference structure versus ferroelectric structure), the first step

consists in identifying the structures and then to compute Born charges for each atom. Because we are interested to find out the effects of the SOC on the spontaneous polarization, two scenarios are possible:

- (i) *Use a reference structure which is the same centrosymmetric paraelectric structure as in the case of collinear case without SOC, and use ferroelectric structures from SOC noncollinear calculations for finding spontaneous polarization in the case of SOC. Then, comparing the polarizations of FiMHS, FiMLS, FMHS and FMLS for SOC with the corresponding polarizations from the collinear case (no SOC, Chapter 4), the effect of SOC on the spontaneous polarizations can be seen.*
- (ii) *Use as a reference structure the optimized FiMHS, FiMLS, FMHS and FMLS from the collinear case (without SOC) and then the contribution of the SOC over polarizations obtained from collinear calculations can be obtained directly.*

Note that the Tables 5.8a,b-5.11a,b from the Section 5.4, showed mainly bond elongations when SOC is considered, and hence it is expected to see larger polarizations as the atom displacements $\Delta u_{k,\alpha}$ are contained in the spontaneous polarization formula (3.27),

$$P_{s,\beta} = (\Delta P)_\beta = \frac{e}{V} \sum_{k,\alpha} Z_{k,\alpha\beta}^* (\Delta u_{k,\alpha})$$

On the other hand, the unit cell volume V increases with SOC, and V is inversely proportional to the spontaneous polarization, so a lower spontaneous polarization should no be surprising either.

Because spontaneous polarizations from the collinear case (Chapter 4) showed consistency between LSDA+U and PBEsol+U, these functionals will be considered in the following to analyze SOC effect on the polarization values. Table 5.12 presents spontaneous polarizations for the collinear case, together with the contributions of SOC, by using the Scenario (ii), which shows the direct effect of SOC.

Table 5.12 Spontaneous polarization vectors P_s in the ferroelectric FiMHS, FiMLS, FMHS, and FMLS phases of BFCO calculated using Born effective charges within the LSDA+U and PBEsol+U functionals, and the corresponding vectors due to SOC effect with spin quantization axis S=[111].

	$P_s [\mu\text{C}/\text{cm}^2]$ LSDA+U collinear	$P_{\text{SOC}} [\mu\text{C}/\text{cm}^2]$ LSDA+U+SOC	$P_s [\mu\text{C}/\text{cm}^2]$ PBEsol+U collinear	$P_{\text{SOC}} [\mu\text{C}/\text{cm}^2]$ PBEsol+U+SOC
FiMHS	$\ (40.0; 46.0; 47.2)\ =79.24$	$\ (0.6 ; 0.6 ; 0.6)\ =1.0$	$\ (44.4; 46.3; 47.7)\ =79.92$	$\ (0.3 ; 0.3 ; 0.3)\ =0.5$
FiMLS	$\ (46.3; 48.4; 49.8)\ =83.46$	$\ (0.3 ; 0.3 ; 0.3)\ =0.5$	$\ (46.0; 47.5; 49.3)\ =82.24$	$\ (2.7 ; 2.7 ; 2.7)\ =4.6$
FMHS	$\ (43.3; 45.3; 46.4)\ =77.97$	$\ (0.4 ; 0.4 ; 0.4)\ =0.7$	$\ (43.9; 45.9; 47.3)\ =79.27$	$\ (0.8 ; 0.8 ; 0.8)\ =1.4$
FMLS	$\ (47.5; 51.1; 51.2)\ =86.53$	$\ (0.2 ; 0.2 ; 0.2)\ =0.3$	$\ (46.1; 48.1; 51.1)\ =83.97$	$\ (2.8 ; 2.8 ; 2.8)\ =4.8$

Calculations show that effect of SOC on the spontaneous polarizations is small, the changes in the bond lengths being counterbalanced by the changes in volumes. Hence to avoid lengthy calculations, polarization values from collinear calculations can generally be used as a good approximation.

CHAPTER 6

CONCLUSIONS AND FUTURE PERSPECTIVES

BFCO has been shown experimentally to exhibit strong multiferroic properties and, as such, appears as a promising material for many potential applications. The recent developments in the growth and characterization of BFCO epitaxial thin films by PLD technique at INRS-EMT, have shown that BFCO has many intriguing properties, including for instance a film thickness variation of the multiferroic properties and of the $\text{Fe}^{2+}/\text{Cr}^{4+}$ cationic order.

In order to provide more insight into the properties of this fascinating material, we performed theoretical studies via density functional theory calculations within the *Vienna ab initio Simulation Package* (VASP) as integrated in the MedeA® computational environment, for collinear and noncollinear spin structures with Fe^{3+} high-spin (HS) and low-spin (LS) arrangements. For a better description of the Fe and Cr 3d electrons, local-spin-density approximation with a *Hubbard-U* correction (LSDA+U), as well as the modern Perdew-Burke-Ernzerhof (PBE) generalized gradient approximations PBEsol+U and RevPBE+U functionals were used in our investigations.

Calculations performed for collinear spin structures (without SOC), confirmed the existence of four stable states on the energy scale, arranged as follows, from the ground state to the higher energy state: FiMHS (I), FMHS (II), FiMLS (III), and FMLS (IV), within all the functionals used, namely the LSDA+U, PBEsol+U and RevPBE+U functionals. FiMHS represents the ground state with a net magnetic ordering of $2 \mu_B/\text{f.u.}$, followed by FMHS with a net magnetic moment $8 \mu_B/\text{f.u.}$. The small energy difference between FiMHS and FMHS phases (in the range 68.7 to 164 meV, depending on the chosen functional) allows to envision the possibility of using appropriate perturbations (such as strains, defects, etc.) in order to obtain FMHS phase of BFCO as material for applications requiring higher magnetization. The Fe^{3+} low-spin states FiMLS with a net magnetic moment of $2 \mu_B/\text{f.u.}$, also presents an interest because it corresponds to the experimental value measured, and it can possibly be obtained in strained films. In addition, two spin channels were found for FMLS magnetic phase, where metallic and semiconducting properties are combined in a single system at the microscopic level within the unit cell (half-metallic), which was never reported before.

Our investigations also revealed that Jahn-Teller distortions and oxygen-octahedra rotations/tiltings are strongly coupled with spin arrangements, due to the lone electron pair of the Bi³⁺ ions, and to a lesser extent by the first-order Jahn-Teller effect in the Fe³⁺ low-spin states. These distortions contribute to the BFCO ferroelectricity, as confirmed by the spontaneous polarizations, reported for the first time for all four magnetic phases. The computed magnitudes of their spontaneous polarization are about 64.0 to 86.5 [$\mu\text{C}/\text{cm}^2$] for all considered functionals (i.e., in the range of the measured values for BFCO), and they appear to be along the [111] direction for all phases. In addition, the Born effective charges of the ions appear to be significantly larger than the nominal charges, indicating substantial electron exchanges between neighbouring ions. A novel and significant result is that, for all phases, the main contribution to polarization comes from the oxygen atoms and not from the Bi atoms with the lone electron pair as in the case of BiFeO₃ (BFO), which is due to the asymmetry of the Fe-O and Cr-O bonds leading to larger displacements of the oxygen atoms in the case of BFCO.

SOC was introduced via noncollinear spin structures. The noncollinear magnetic vectors were aligned initially with the different spin quantization axes, and then they rotated during the optimization procedure until convergence to a minimum of energy, without imposing any constraint on the symmetry (e.g., the \mathbf{k} -points mesh is not restricted anymore to a symmetry-irreducible set of the primitive cell and magnetic moments break the symmetry). Calculations showed that symmetry breaking affects the orbital magnetic moments for Cr³⁺ and Fe³⁺- high spin (HS) which are strongly quenched to the amount of 0.049-0.056 μ_B per Cr atom, and 0.018-0.029 μ_B per Fe HS atom (i.e., orbital moments are very small, and hence the total magnetic moment is mostly due to the spins). Our results obtained within the LSDA+U, PBEsol+U and RevPBE+U functionals show that in the case of FiMHS and FMHS states, both orbital moments of Fe and Cr participate to a small extent (about 1%-4%) to the total magnetic moment, while the spin moments contribute about 74%-86%. The effect is opposite in the case of Fe³⁺-low spin where largely unquenched magnetic orbital moments are observed. Further, magneto-crystalline anisotropy energy (MAE) showed that saturation of magnetization, with a magnetic moment of about 2 μ_B /f.u. for FiMHS, is achieved along the easy axis, which is perpendicular on the polarization direction [111]. Spin and orbital magnetic vectors are canted parallel or antiparallel with the spin quantization axes. Our studies on MAE for the other states FiMLS, FMHS and FMLS shows that the physics is more complex, e.g., the easy axis for LS states is parallel to the polarization direction [111] within LSDA+U and RevPBE+U functionals, while the PBEsol+U functional shows an easy axis perpendicular on [111]. The latter results are more in

line with the generally admitted principle that the magnetization and polarization vectors are perpendicular.

Investigations also revealed the effects of SOC on octahedral distortions: FiMHS shows that trigonal distortions are preserved even though symmetry is broken, but the Fe-O and Cr-O bond lengths change. Comparing collinear versus noncollinear calculations, it is found that, for the FiMHS phase, triplets bond lengths are elongated about 1-4 % with SOC using the PBE+U functionals, the percentages being larger for the bonds corresponding to the (x_{01}, y_{01}, z_{01}) Wyckoff oxygen positions. In the case of FiMLS, variations on the Fe-O and Cr-O bond lengths are of -0.2% to 1% for LSDA+U and PBEsol+U, and stronger variations of -5% to 9% are observed for RevPBE+U, so that triplets bond lengths are not anymore preserved. Distortions revealed in the FiMLS state are consequences of the unquenched magnetic orbital moments for Fe^{3+} LS, central Bi^{3+} lone pair, and other unstudied physics coming together with symmetry breaking and SOC. However, for FMLS states, the trigonal distortions are kept. Finally, the effect of SOC on the spontaneous polarizations is small, about 0.3 to 4.6 $\mu\text{C}/\text{cm}^2$, and the changes in the bond lengths are counterbalanced by the changes in volumes.

These investigations provide new insights for controlling lattice distortions and tuning multiferroic properties. However, in order to achieve such a challenging goal, future developments are necessary, and here are few perspectives:

- (i) In addition to the study of Jahn-Teller distortions from this thesis, a new approach called JT vibronic coupling effects could be used, giving the possibility for a better understanding of physics present in a whole range of spectroscopy techniques (UV, X-ray, photoelectron), structural phase transitions, ferroelectricity, colossal magneto-resistance, etc.
- (ii) Noncollinear calculations are computational expensive but a continuation of this work by considering more quantization axes would be useful.
- (iii) Detailed investigations about how the BFCO properties are affected by epitaxial strain would also be very useful to understand the experimental observations about epitaxial BFCO grown on different substrates.
- (iv) As our investigations show that FMHS has the highest magnetic moment and hence is very interesting for applications requiring higher magnetization, ways to obtain switchability between ferri- and ferromagnetism could be found and investigated, based on the fact that FMHS state is the second on the energy scale after FiMHS.

- (v) Another popular functional, namely Heyd–Scuseria–Ernzerhof (HSE06) screened Coulomb hybrid density functional that contains a Hartree–Fock (HF) mixing constant (25%), can be used to improve the PBE results and provide more insights regarding the multiferroic properties.
- (vi) Recent experiments proved that Fe/Cr cation ordering is facilitated by oxygen vacancies, and hence theoretical investigations could be done to examine the dependence of the vacancy/defect states on the cell size and on the position of the excited states, and to analyze their nature together with their expected location in real systems along with the resulting charges of these vacancies/defects.
- (vii) Experimentally, it was found that single phase BFCO can be obtained only in a very narrow pressure-temperature range. To understand better the competition between the different magnetic states as a function of both pressure and temperature, a combination between DFT and molecular dynamics (MD) calculations could bring important insights for experimentalists, e.g., by providing a pressure-temperature phase-diagram which would assure that a single phase BFCO with the highest magnetization (FMHS) can be achieved experimentally.
- (viii) Studies on the optimization of supercells in different spin arrangements and various Fe/Cr cation ordering would allow to further expand the possible application of BFCO.

CHAPTER 7

REFERENCES

- [1] Ahn CH, Rabe KM & Triscone JM (2004) Ferroelectricity at the nanoscale : local polarization in oxide thin films and heterostructures. *Science* 303 : 488 -491.
- [2] Amadon B, Jollet F & Torrent M (2008) γ and β cerium: LDA+U calculations of ground-state parameters. *Physical Review B* 77 : 155104-1-10.
- [3] Anisimov VI & Izyumov Y (2010) *Electronic structure of strongly correlated materials*, Springer seried in Solid-State Sciences, Springer-Verlag Berlin Heidelberg, 288 p.
- [4] Anisimov VI, Aryasetiawan F & and Liechtenstein AI (1997) First-principles calculations of the electronic structure and spectra of strongly correlated systems: the LSDA+U. *J. Phys.: Condens. Matter* 9 : 767-808.
- [5] Autschbach J & Ziegler T (2002) Relativistic computation of NMR shieldings and spin-spin coupling constants. *Encyclopedia of Nuclear Magnetic Resonance, Vol.9 Advances in NMR* (John Wiley and Sons, Chichester) p. 306-323.
- [6] Axe JD (1967) Apparent ionic charges and vibrational eigenmodes of BaTiO₃ and other perovskites. *Physical Review* 157(2) : 429-435.
- [7] Baettig P & Spaldin NA (2005) Ab initio prediction of a multiferroic with large polarization and magnetization. *Appl. Phys. Lett.* 86 : 012505-1-3.
- [8] Baettig P, Ederer C & Spaldin NA (2005) First principle study of the multiferroic BiFeO₃, Bi₂FeCrO₆, and BiCrO₃: Structure, polarization, and magnetic ordering temperature. *Physical Review B* 72 : 214105-1-8.
- [9] Baroni S, Giannozzi P & Testa A (1987) Green's function approach to linear response in solids. *Phys. Rev. Lett.* 58 : 1861-1864.
- [10] Barth U & Hedin L (1972) A local exchange-correlation potential for the spin polarized case : I. *J. Phys. C : Solid State Phys.* 5 : 1629-1642.
- [11] Bea H, Gajek M, Bibes M & Barthelemy A (2008) Spintronics with multiferroics. *J. Phys.: Condens. Matter* 20 : 434221-1-11.

- [12] Becke AD & Edgecombe KE (1990) A simple measure of electron localization in atomic and molecular systems. *J. Chem. Phys.* 92(9) : 5397-5403.
- [13] Bersuker IB (2006) *The Jahn-Teller effect*, Cambridge University Press, 616 p.
- [14] Bersuker IB (2001) Modern aspects of the Jahn-Teller effect theory and applications to molecular problems. *Chem. Rev.* 101 : 1067-1114.
- [15] Bibes M & Barthélémy A (2008) Towards a magnetoelectric memory. *Nature Materials* 7 : 425-426.
- [16] Bilc DI, Orlando R, Shaltaf R, Rignanese GM, Iniguez J & Ghosez P (2008) Hybrid exchange-correlation functional for accurate prediction of the electronic and structural properties of ferroelectric oxides. *Physical Review B* 77 : 165107-1-13.
- [17] Blöchl PE (1994) Projector augmented-wave method. *Physical Review B* 50 :17953-17979.
- [18] Blonski P, Dennler S & Hafner J (2011) Strong spin-orbit effects in small Pt clusters : geometric structure, magnetic isomers and anisotropy. *The Journal of Chemical Physics* 133 : 034107-1-12.
- [19] Bousquet E & Spaldin N (2010) J dependence in the LSDA+U treatment of the noncollinear magnets. *Physical Review B* 82: 220402(R)-1-4.
- [20] Brink J & Khomskii DI (2008) Multiferroicity due to charge ordering. *J. Phys. : Condens. Matter* 20 :434217-1-12.
- [21] Carpenter MA and Howard CJ (2009) Symmetry rules and strain/order-parameter relationships for coupling between octahedral tilting and cooperative Jahn-Teller transitions in ABX_3 perovskites. I. Theory. *Acta Cryst. B* 65 : 134-146.
- [22] Cheong SW & Mostovoy M (2007) Multiferroics : a magnetic twist for ferroelectricity. *Nature Materials* 6 : 13-20.
- [23] M. Côté (2013) Personal communications. Département de Physique, Université de Montréal, Québec http://physique.umontreal.ca/~michel_cote/Physique/Accueil.html
- [24] Curie P (1894) Sur la symétrie dans les phénomènes physiques, symétrie d'un champ électrique et d'un champ magnétique. *J. Physique*, 3^{ième} série III, 393 p. (Reprinted in (1908) *Oeuvres de Pierre Curie* Gauthier-Villars, Paris, 118–141).

- [25] Dixit H, Lee JH, Krogel J, Okamoto S & Cooper VR (2015) Stabilization of weak ferromagnetism by strong magnetic response to epitaxial strain in multiferroic BiFeO₃. *Scientific Reports* 5 : 12969-1-9.
- [26] Dudarev SL, Botton GA, Savrasov SY, Humphreys CJ & Sutton AP (1998) Electron-energy-loss spectra and the structural stability of nickel oxide : An LSDA+U study. *Physical Review B* 57(3) : 1505-1509.
- [27] Ederer C & Spaldin NA (2005) Weak ferromagnetism and magnetoelectric coupling in bismuth ferrite. *Physical Review B* 71 : 060401-1-4.
- [28] Ederer C & Spaldin NA (2005) Recent progress in first-principles studies of magnetoelectric multiferroics. *Current Opinion in Solid State and Materials Science* 9 : 128-139.
- [29] Eerenstein W, Mathur ND & Scott JF (2006) Multiferroic and magnetoelectric materials. *Nature* 442 : 759-765.
- [30] Fiebig M (2005) Revival of the magnetoelectric effect. *J. Phys. D: Appl. Phys.* 38: R123-R152.
- [31] Garg A (2001) *Growth and characterization of epitaxial oxide thin films*. PhD dissertation in Materials Science and Metallurgy (University of Cambridge, Cambridge). 191 p.
- [32] Ghosez Ph, Gonze X & Michenaud JP (1998) Dynamical charges : The case of ABO₃ compounds. *Physical Review B* 58 : 6224-6240.
- [33] Ghosez Ph, Gonze X & Michenaud JP (1996) Coulomb interaction and ferroelectric instability of BaTiO₃. *Europhys. Lett.* 33 : 713-718.
- [34] Ghosez Ph, Gonze X & Michenaud JP (1995) A microscopic study of barium titanate. *Ferroelectrics* 164 : 113-121.
- [35] Gibb TC (1984) Magnetic exchange interactions in perovskite solid solutions. Part 4 : The Fe³⁺-O-Cr³⁺ superexchange interaction. *J. Chem. Soc. Dalton Trans.* 4 : 667-671.
- [36] Glazer AM (2011) A brief history of tilts. *Phase Transitions: A Multinational Journal* 84: 405-420.
- [37] Glazer AM (1972) The classification of tilted octahedra in perovskites. *Acta Crystallogr. B* 28: 3384-3392.

- [38] Goffinet M, Iniguez J & Ghosez P (2012) First-principles study of a pressure-induced spin transition in multiferroic $\text{Bi}_2\text{FeCrO}_6$. *Physical Review B* 86: 024415-1-6.
- [39] Goldschmidt VM (1926) Laws of crystal chemistry. *Die Naturwissenschaften* 14(21): 477-485.
- [40] Gonze X, Allan DC & Teter MP (1992) Dielectric tensor, effective charges, and phonons in α -quartz by variational density-functional perturbation theory. *Phys. Rev. Lett.* 68 : 3603-3606.
- [41] Goodenough JB (1955) Theory of the role of covalence in the perovskite-typo manganites $[\text{La},\text{M}(\text{II})]\text{MnO}_3$. *Physical Review* 100(2) : 564-573.
- [42] Guterman DC & Fong YK (2001) *Multi-state memory*. Patent 6,222,762 B1 (USA) Issued Apr.24, 2001.
- [43] Hammer B, Hansen LB & Nørskov JK (1999) Improved adsorbtion energetics within desndity-functional theory using revised Perdew-Burke-Ernzerhof functionals. *Physical Review B* 59(11) : 7413-7421.
- [44] Henkelman G, Arnaldsson A & Jonsson H (2006) A fast and robust algorithm for Bader decomposition of charge density. *Computational Materials Science* 36 : 354-360.
- [45] Heyd J & Scuseria GE (2004) Efficient hybrid density functional calculations in solids : Assessment of the Heyd-Scuseria_Ernzerhof screened Coulomb hybrid functionl. *Journal of Chemical Physics* 121 (3) : 1187-1192.
- [46] Hill NA, Bäettig P & Daul C (2002) First principles search for multiferroism in BiCrO_3 . *J. Phys. Chem. B* 106 : 3383-3388.
- [47] Hobbs D, Kresse G & Hafner J (2000) Fully unconstrained noncollinear magnetism within the projectstor augmented-wave metod. *Physical Review B* 62 : 11556 -11570.
- [48] Hoffmann R (1987) How chemistry and physics meet in the solid state. *Angew. Chem. Int. Ed. Engl.* 26 : 846-878.
- [49] Hohenberg P & Kohn W (1964) Inhomogeneous electron gas. *Physical Review* 136 (3B): B864-871.
- [50] Hubbard J (1964) Electron correlation in narrow energy bands II. The degenerate band case. *Proc. R. Soc., London A* 277: 237; Electron correlation in narrow energy bands III. An improved solution. *Proc. R. Soc., London A* 281: 401.

- [51] Iliev MN, Padhan P & Gupta A (2008) Temperature-dependent Raman study of multiferroic $\text{Bi}_2\text{NiMnO}_6$ thin films. *Physical Review B* 77 : 172303-1-3.
- [52] Imada M, Fujimori A & Tokura Y (1998) Metal-insulator transitions. *Rev. of Modern Physics* 70(4) : 1039-1263.
- [53] Johnsson M & Lemmens P (2008) Perovskites and thin films-crystallography and chemistry. *J. Phys.: Condens. Matter* 20 : 264001-1-6.
- [54] Ju S & Guo GY (2008) Colossal nonlinear optical magnetoelectric effects in multiferroic $\text{Bi}_2\text{FeCrO}_6$. *Appl. Phys. Lett.* 92 : 202504-1-3.
- [55] Kanamori J (1960) Crystal distortion in magnetic compounds. *J. Appl. Phys.* 31: S14-23.
- [56] Kanamori J (1959) Superexchange interaction and symmetry properties of electron orbitals. *J. Phys. Chem. Solids* 10 : 87-98.
- [57] King G & Woodward PM (2010) Cation ordering in perovskites. *J. Mater. Chem.* 20 : 5785-5796.
- [58] Khomskii D (2009) Classifying multiferroics : Mechanisms and effects. *Physics* 2 :20-1-8.
- [59] Kohn W & Sham L (1965) Self-consistent equations including exchange and correlation effects. *Physical Review* 140(4A) : A1133 -1138.
- [60] Kresse G & Lebacq O (2017) VASP Manual
<http://cms.mpi.univie.ac.at/vasp/vasp/vasp.html> (Accessed September 1, 2017).
- [61] Kresse G & Joubert D (1999) From ultrasoft pseudopotentials to the projector augmented-wave method. *Physical Review B* 59: 1758-1775.
- [62] Kresse G & Furthmüller J (1996) Efficiency of ab-initio total energy calculations for metals and semiconductors using a plane-wave basis set. *Computational Materials Science* 6 : 15-50.
- [63] Kresse G & Furthmüller J (1996) Efficient iterative schemes for ab initio total-energy calculations using a plane-wave basis set. *Physical Review B* 54(16) : 11169-11186.
- [64] Kübler J, Höck KH, Sticht J & Williams AR (1988) Local spin-density functional theory of noncollinear magnetism. *J. Appl. Phys.* 63(8) : 3482-3486.

- [65] Landau LD & Lifshitz EM (1960), *Electrodynamics of Continuous Media*, Addison-Wesley Publishing Co., Inc., Reading, Mass., 119 p. English translation of a 1958 Russian edition.
- [66] Liechtenstein AI, Anisimov VI & Zaanen J (1995) Density-functional theory and strong interactions: Orbital ordering in Mott-Hubbard insulators. *Physical Review B* 52(8) : R5467-5470.
- [67] Lou J, Reed D, Pettiford C, Liu M, Han P, Dong S & Sun NX (2008) Giant microwave tunability in FeGaB/lead magnesium niobate-lead titanate multiferroic composites. *Appl. Phys. Lett.* 92 : 262502-1-3.
- [68] Lufaso MW & Woodward PM (2004) Jahn-Teller distortions, cation ordering and octahedral tilting in perovskites. *Acta Crystallographica B* 60 : 10-20.
- [69] Marsman M & Hafner J (2002) Broken symmetries in the crystalline and magnetic structures of γ -iron. *Physical Review B* 66 : 224409-1-13.
- [70] Martin LW & Ramesh R (2012) Multiferroic and magnetoelectric heterostructures. *Acta Materialia* 60(151) : 2449-2470.
- [71] Martin LW, Chu YH & Ramesh R (2010) Advances in the growth and characterization of magnetic, ferroelectric, and multiferroic oxide thin films. *Materials Science and Engineering R* 68 : 89-133.
- [72] Martin RM (2004) *Electronic Structure: Basic Theory and Practical Methods*, Cambridge University Press, 624 p.
- [73] MedeA (2017) MedeA©-2.21, Materials Design, Inc., San Diego, CA, USA, 2017. <http://www.materialsdesign.com> (Accessed December 12, 2017).
- [74] MedeA (2015) MedeA©-2.17, Materials Design, Inc., San Diego, CA, USA, 2015. <http://www.materialsdesign.com> (Accessed December 12, 2017).
- [75] Miao J, Zhang X, Zhan Q, Jiang Y & Chew KH (2011) Bi-relaxation behaviors in epitaxial multiferroic double-perovskite $\text{BiFe}_{0.5}\text{Mn}_{0.5}\text{O}_3/\text{CaRuO}_3$ heterostructures. *Appl. Phys. Lett.* 99 : 062905-1-3 (2011).
- [76] Momma K & Izumi F (2011) VESTA 3 for three-dimensional visualization of crystal, volumetric and morphology data. *J. Appl. Cryst.* 44 : 1272-1276.

- [77] Monkhorst HJ & Pack JD (1976) Special points for Brillouin-zone integrations. *Physical Review B* 13(12) : 5188-5192.
- [78] Moskvin AS, Ovanesyan NS & Trukhtanov VA (1975) Angular dependence of the superexchange interaction $\text{Fe}^{3+}\text{-O}^{2-}\text{-Cr}^{3+}$. *Hyperfine Interactions* 1 : 265-281.
- [79] Mott NF (1956) On the transition to metallic conduction in semiconductors. *Canadian Journal of Physics* 34 : 1356-1382.
- [80] Nan CW, Bichurin MI, Dong S , Viehland D & Srinivasan G (2008) Multiferroic magnetoelectric composites : Historical perspective, status, and future directions. *J. Appl. Phys.* 103 : 031101-1-35.
- [81] Neaton JB, Ederer C, Waghmare UV, Spaldin NA & Rabe KM (2005) First-principles study of spontaneous polarization in multiferroic BiFeO_3 . *Physical Review B* 71 : 014113-1-8.
- [82] Néchache R, Harnagea C, Li S, Cardenas L, Huang W, Chakrabarty & Rosei F (2015) Bandgap tuning of multiferroic oxide solar cells. *Nature Photonics* 9 : 61-67.
- [83] Néchache R, Harnagea C & Pignolet A (2012) Multiferroic properties-structure relationships in epitaxial $\text{Bi}_2\text{FeCrO}_6$ thin films : recent developements. *J. Phys.: Condensed Matter* 24: 096001-1-13.
- [84] Néchache R & Rosei F (2012) Recent progress in nanostructures multiferroic $\text{Bi}_2\text{FeCrO}_6$ thin films. *Journal of Solid State Chemistry* 189: 12-20.
- [85] Néchache R, Cojocaru CV, Harnagea C, Nauenheim C, Nicklaus M, Ruediger A, Rosei F & Pignolet A (2011) Epitaxial patterning of $\text{Bi}_2\text{FeCrO}_6$ double perovskite nanostructures: multiferroic at room temperature. *Advanced Materials* 23: 1724-1729.
- [86] Néchache R, Harnagea C, Carignan LP, Gautreau O, Pintilie L, Singh MP, Menard D, Fournier P, Alexe M & Pignolet A (2009) Epitaxial thin films of the multiferroic double perovskite $\text{Bi}_2\text{FeCrO}_6$ grown on (100)-oriented SrTiO_3 substrates : Growth, characterization and optimization. *J. Appl. Phys.* 105 : 061621-1-9.
- [87] Néchache R, Harnagea C, Pignolet A, Normandin F, Veres T, Carignan LP & Menard D (2006) Growth, structure, and properties of epitaxial thin films of first-principles predicted multiferroic $\text{Bi}_2\text{FeCrO}_6$. *Appl. Phys. Lett.* 89 : 102902-1-3.
- [88] Néel L (1954) L'approche à la saturation de la magnétostricction. *J. Phys. Radium* 15(5): 376-378.

- [89] Niemeyer M, Hirsch K, Zamudio-Bayer V, Langenberg A, Vogel M, Kossick M, Ebrecht C, Egashira K, Terasaki A, Moller T, Issendorff BV & Lau JT (2015) Spin coupling and orbital angular momentum quenching in free iron clusters. *Physical Review Letters* 108 : 057201-1-5.
- [90] Ohtomo A, Chakraverty S, Mashiko H & Oshima T (2013) Spontaneous atomic ordering and magnetism in epitaxially stabilized double perovskites. *J. Mater. Res.* 28(5) : 689-695.
- [91] Palkar VR, John J & Pinto R (2002) Observation of saturated polarization and dielectric anomaly in magnetoelectric BiFeO₃ thin films. *Appl. Phys. Lett.* 80:1628-1630.
- [92] Perdew JP, Burke K & Ernzerhof M (1996) Generalized gradient approximation made simple. *Physical Review Letters* 77(18): 3865-3868.
- [93] Perdew JP, Ruzsinszky A, Csonka GI, Vydrov OA, Scuseria GE, Constantin LA, Zhou X & Burke K (2008) Restoring the density-gradient expansion for exchange in solid and surfaces. *Physical Review Letters* 100: 136406-1-4.
- [94] Perdew JP & Kurth S (2003) *Density Functionals for Non-relativistic Coulomb Systems in the New Century in: A Primer in Density Functional Theory*, Fiolhais C, Nogueira F & Marques M (Eds.), Springer. p. 1-55.
- [95] Pick RM, Cohen MH & Martin RM (1970) Microscopic theory of force constants in the adiabatic approximation. *Physical Review B* 1(2): 910-920.
- [96] Pickett W & Eschrig E (2007) Half metals : from formal theory to real material issues. *J. Phys. : Condens. Matter* 19 : 315203-1-10.
- [97] Popkov AF, Davydova MD, Zvezdin KA, Solov'yov SV & Zvezdin AK (2016) Origin of the giant linear magnetoelectric effect in perovskite like multiferroic BiFeO₃. *Physical Review B* 93 : 094435-1-5.
- [98] Posternak M, RestaR & Baldereschi A (1994) Role of covalent bonding in the polarization of perovskite oxides : The case of KNbO₃. *Physical Review B* 50(12) : 8911-8914.
- [99] Ramesh R & Spaldin NA (2007) Multiferroics : progress and prospects in thin films. *Nature Materials* 6 : 21-29.
- [100] Ravindran P, Vidya R, Kjekshus A & Fjellvåg H (2006) Theoretical investigation of magnetoelectric behavior in BiFeO₃. *Physical Review B* 74 : 224412-1-18.

- [101] Resta R & Vanderbilt D (2007) Theory of polarization : A modern approach. *Physics of Ferroelectrics : a Modern Perspective*. Ahn CH, Rabe KM & Tricome JM Eds., Springer-Verlag & Business Media.
- [102] Resta R (1994) Macroscopic polarization in crystalline dielectrics : the geometric phase approach. *Reviews of Modern Physics* 66(3) : 899-915.
- [103] Resta R, Posternak M & Baldereschi A (1993) Towards a quantum theory of polarization in ferroelectrics : The case of KNbO₃. *Phys. Rev. Lett.* 70 :1010-1013.
- [104] Richinschi D, Yun KY & Okuyama M (2006) First-principles study of BiFeO₃ films with giant polarization and its dependence on structural parameters. *Ferroelectrics* 335 : 181-190.
- [105] Rivero P, Meunier V & Shelton W (2016) Structural, and magnetic properties of LaMnO₃ phase transition at high temperature. *Physical Review B* 93:024111-1-10.
- [106] Rondinelli JM, May SJ & Freeland JW (2012) Control of octahedral connectivity in perovskite oxide heterostructures: An emerging route to multifunctional materials discovery. *MRS Bulettin* 37: 261-270.
- [107] Rondinelli JM & Spaldin NA (2011) Structure and properties of functional oxide thin films : Insights from electronic-structure calculations. *Adv. Mater.* 23 : 3363-3381.
- [108] Roy A, Prasad R, Auluck S & Garg A (2010) First-principles calculations of Born effective charges and spontaneous polarization of ferroelectric bismuth titanate. *J. Phys. : Condens. Matter* 22 : 165902-1-10.
- [109] Sanville E, Kenny SD, Smith R & Henkelman G (2007) Improved grid-based algorithm for Bader charge allocation. *J. Comput. Chem.* 28 : 899-908.
- [110] Savin A, Nesper R, Wengert S & Fässler T (1997) ELF : The electron localization function. *Angew. Chem. Int. Ed. Engl.* 36 : 1808-1832.
- [111] Schmid H (1973) On a magnetoelectric classification of materials. *Int. J. Magn.* 4: 337-361.
- [112] Schmid H (2008) Some symmetry aspects of ferroics and single phase multiferroics. *J. Phys.: Condens. Matter* 20 : 434201-1-24.
- [113] Scott JF (2007) Applications of Modern Ferroelectrics. *Science* 315 : 954-959.

- [114] Seshadri R & Hill NA (2001) Visualizing the role of Bi 6s « lone pairs » in the off-center distortion in ferromagnetic BiMnO_3 . *Chem. Mater.* 13 : 2892-2899.
- [115] Shick AB, Liechtenstein AI & Pickett WE (1999) Implementation pf the LDA+U method using the full-potential linearized augmented plane-wave basis. *Physical Review B* 60 : 10763-10769.
- [116] Souza ECC & Muccillo R (2010) Properties and applications of perovskite proton conductors. *Materials Research* 13(3): 385-394.
- [117] Spaldin NA (2012) A beginner's guide to the modern theory of polarization. *J. Solid State Chem.* 195: 2-10.
- [118] Spaldin NA, Fiebig M & Mostovoy M (2008). The toroidal moment in condensed-matter physics and its relation to the magnetoelectric effect. *J. Phys.: Condens. Matter* 20 : 434203-1-15.
- [119] Spaldin NA & Fiebig M (2005) The renaissance of magnetoelectric multiferroics. *Science* 309 : 391-392.
- [120] Szabo A & Ostlund NS (1996) *Modern Quantum Chemistry*, Dover Publications Inc., New York, 480 p.
- [121] Tang W, Sanville E & Henkelman G (2009) A grid-based Bader analysis algorithm without lattice bias. *J. Phys. : Condens. Matter* 21 : 084204-1-7.
- [122] Teague JR, Gerson R & James WJ (1970) Dielectric hysteresis in single crystal BiFeO_3 . *Solid State Commun.* 8 : 1073-1074.
- [123] Ueda K, Tabata H & Kawai T (1998) Ferromagnetism in $\text{LaFeO}_3\text{-LaCrO}_3$ superlattices. *Science* 280 : 1064-1066.
- [124] Vanderbilt D & King-Smith RD (1993) Electric polarization as a bulk quantity and its relation to surface charge. *Physical Review B* 48(7): 4442-4455.
- [125] Virtual NanoLab version 2016.4, QuantumWise A/S www.quantumwise.com (Accessed November 23, 2017).
- [126] Vosko SH, Milk L & Nusair M (1980) Accurate spin-dependent electron liquid correlation energies for local spin density calculations : a critical analysis. *Canadian Science Publishing, Can. J. Phys.* 58 : 1200-1211.

- [127] Wang J, Neaton JB, Zheng H, Nagarajan V, Ogale SB, Liu B, Viehland D, Vaithyanathan V, Schlom DG, Waghmare UV, Spaldin NA, Rabe KM, Wuttig M & Ramesh R (2003) Epitaxial BiFeO₃ multiferroic thin film heterostructures. *Science* 299 :1719-1722.
- [128] Web of Science (2017) apps.webofknowledge.com/WOS_GeneralSearch_input.do (Accessed September 1, 2017).
- [129] Windiks R (2000) *Paramagnetic Na₄³⁺ guest clusters embeded in sodalite hosts: density functional calculations oft he hyperfine interactions and magnetic coupling*. PhD dissertation in Chemsitry (Humboldt-Universität zu Berlin, Berlin) 146 p.
- [130] Woodward PM (1997) Octahedral tilting in perovskites. I. Geometrical considerations. *Acta Crystallogr. B* 53 : 32-43.
- [131] Zaanen J, Sawatzky GA & Allen JW (1985) Band gaps and electronic structure of transition-metal compunds. *Phys. Rev. Lett.* 55(4) : 418-421.

APPENDIX I

The DOSs and band structures corresponding to the Bi, Fe, Cr and O atoms of the rhombohedral *R*3 BFCO, in the case of collinear spin polarized calculations within LSDA+U and PBEsol+U functionals

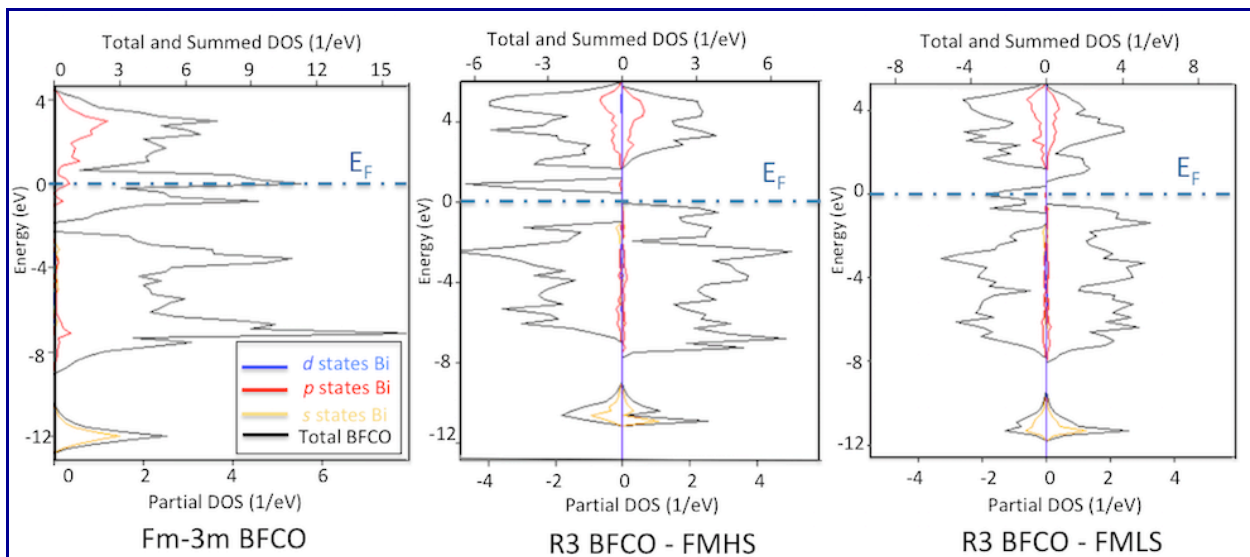
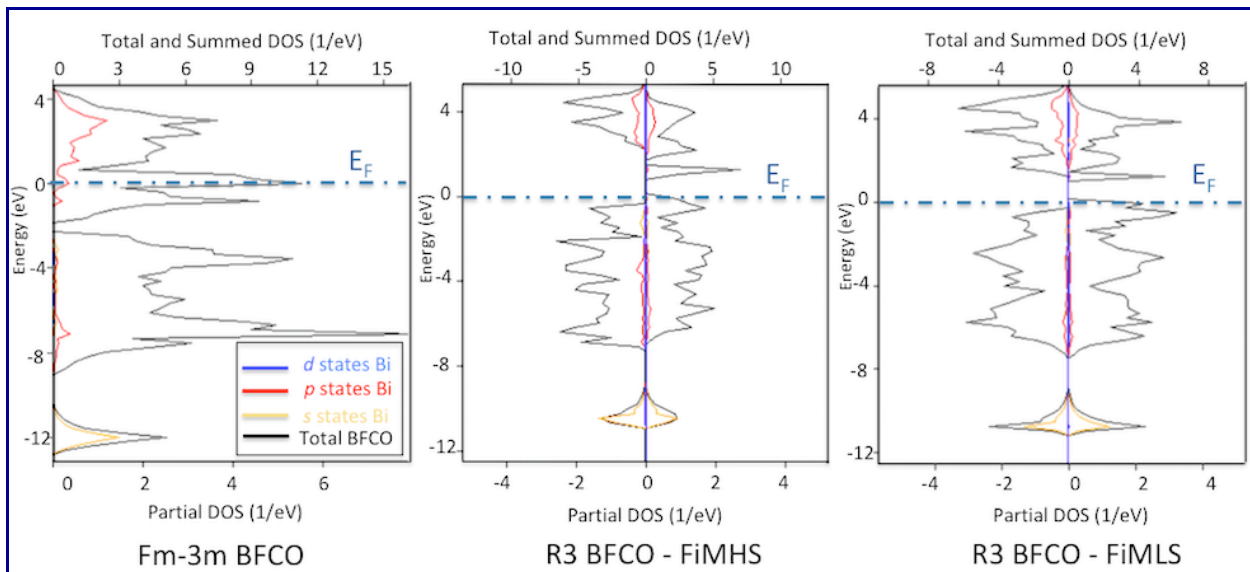


Figure AI.1 The computed Bi density of states within the LSDA+U functional for the BFCO highly symmetric structure (Fm-3m) compared with the corresponding Bi states of the rhombohedral BFCO (R3) for the FiMHS, FiMLS, FMHS and FMLS magnetic states.

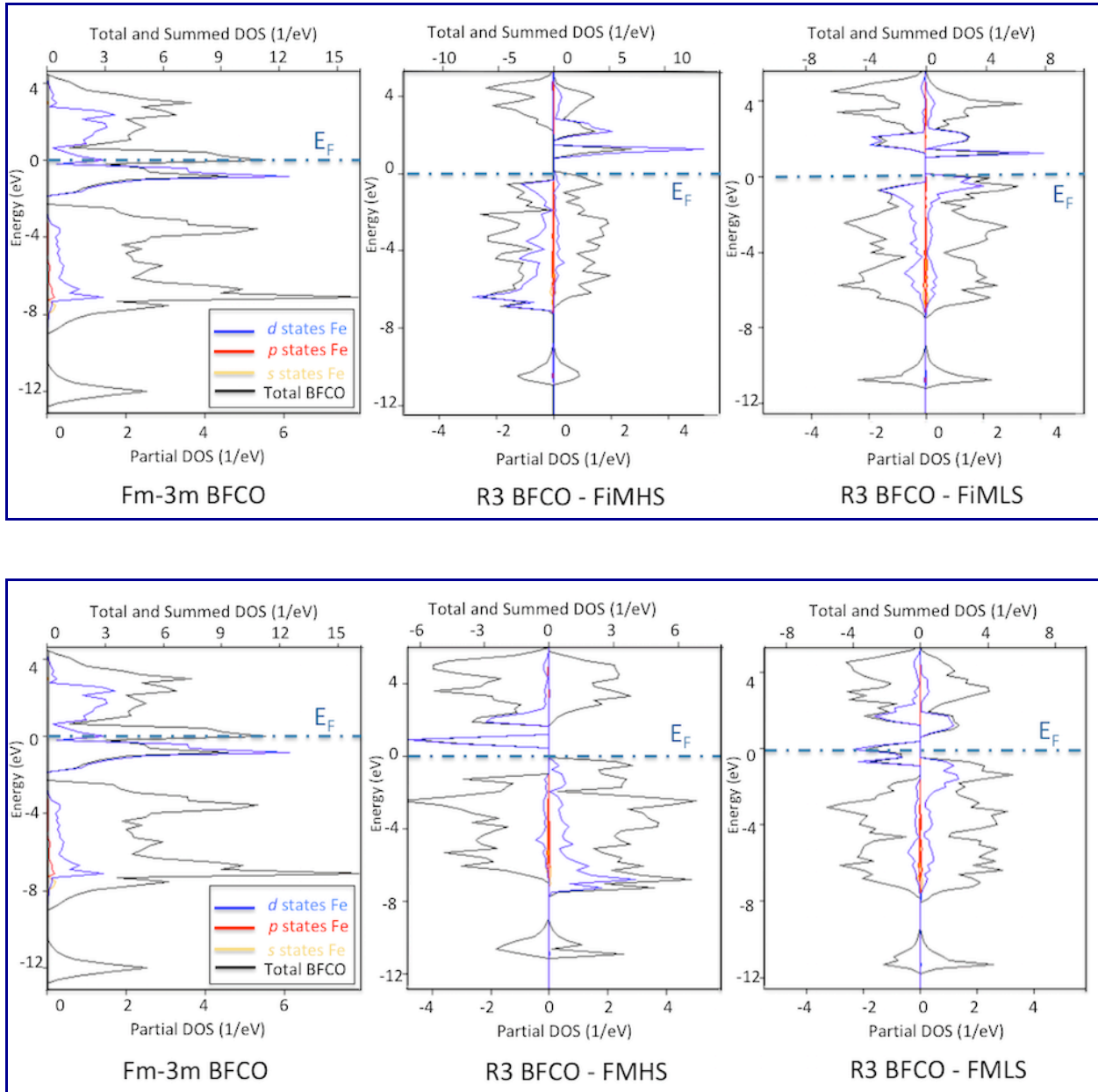


Figure A1.2 The computed Fe density of states within the LSDA+U functional for the BFCO highly symmetric structure (Fm-3m) compared with the corresponding Fe states of the rhombohedral BFCO (R3) for the FiMHS, FiMLS, FMHS and FMLS magnetic states.

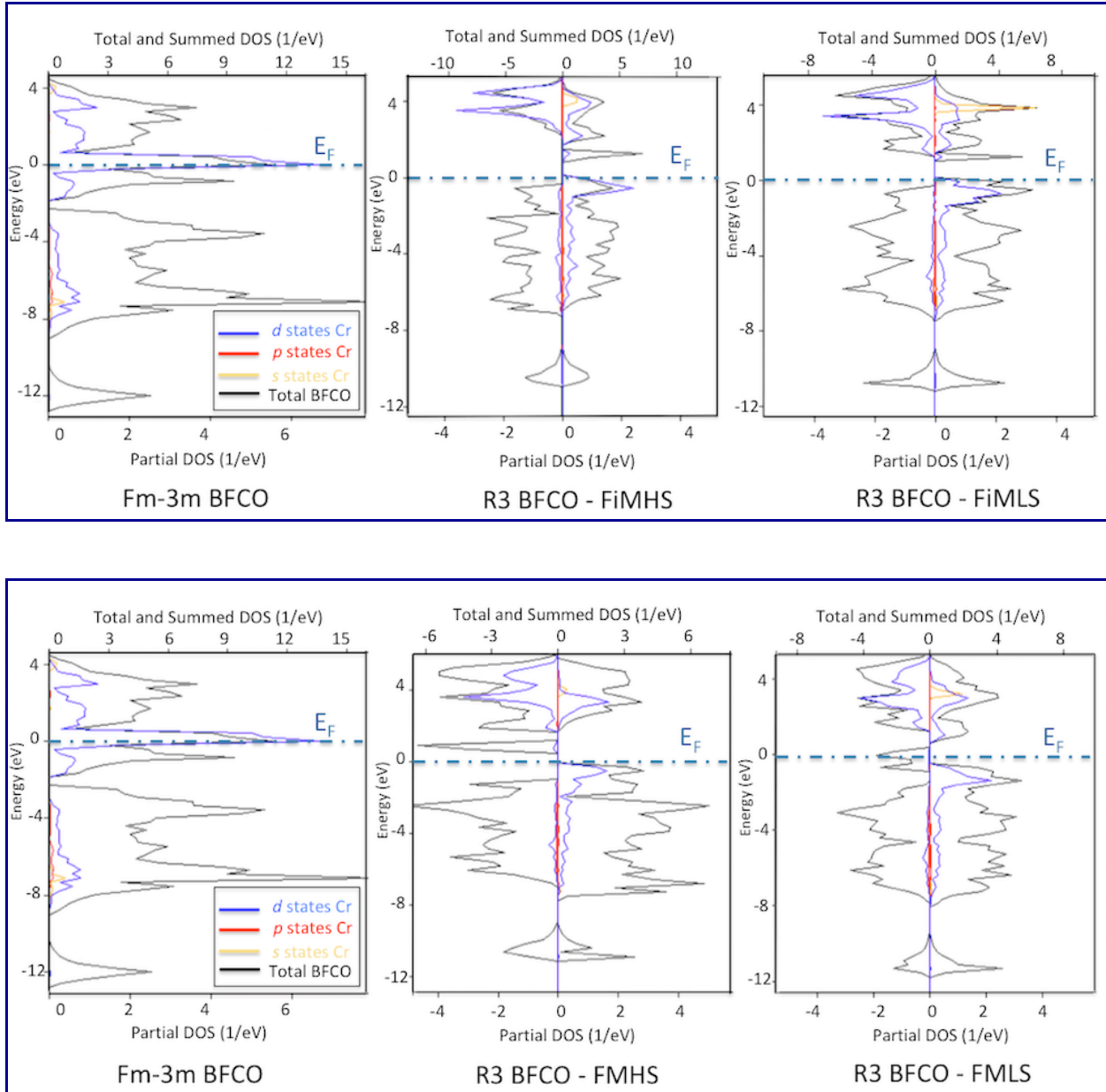


Figure AI.3 The computed Cr density of states within the LSDA+U functional for the BFCO highly symmetric structure (Fm-3m) compared with the corresponding Cr states of the rhombohedral BFCO (R3) for the FiMHS, FiMLS, FMHS and FMLS magnetic states.

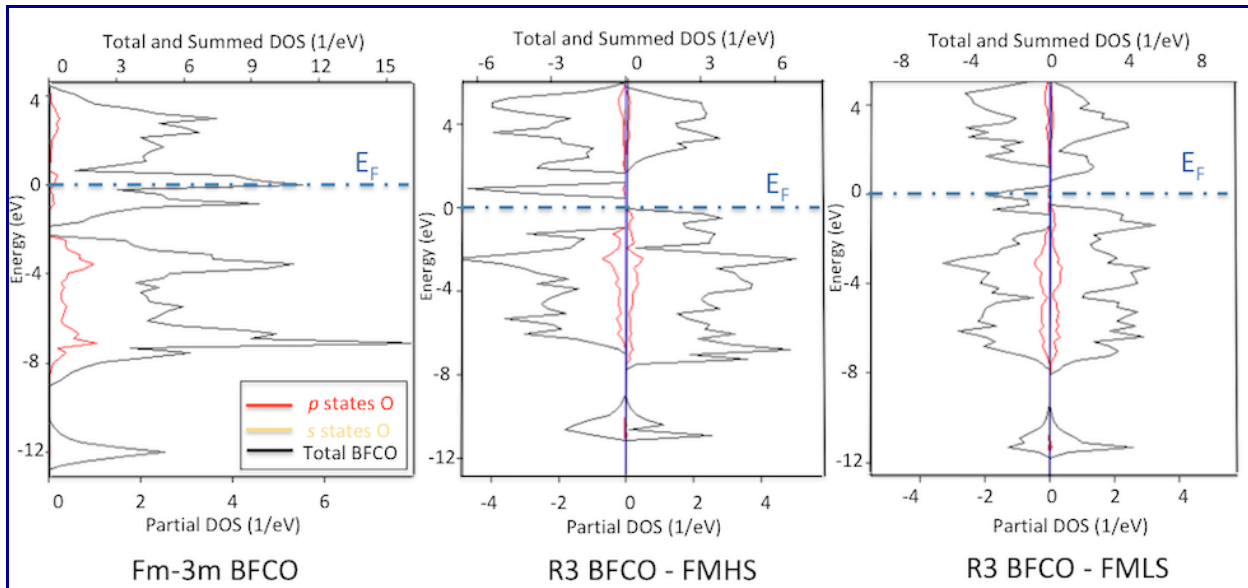
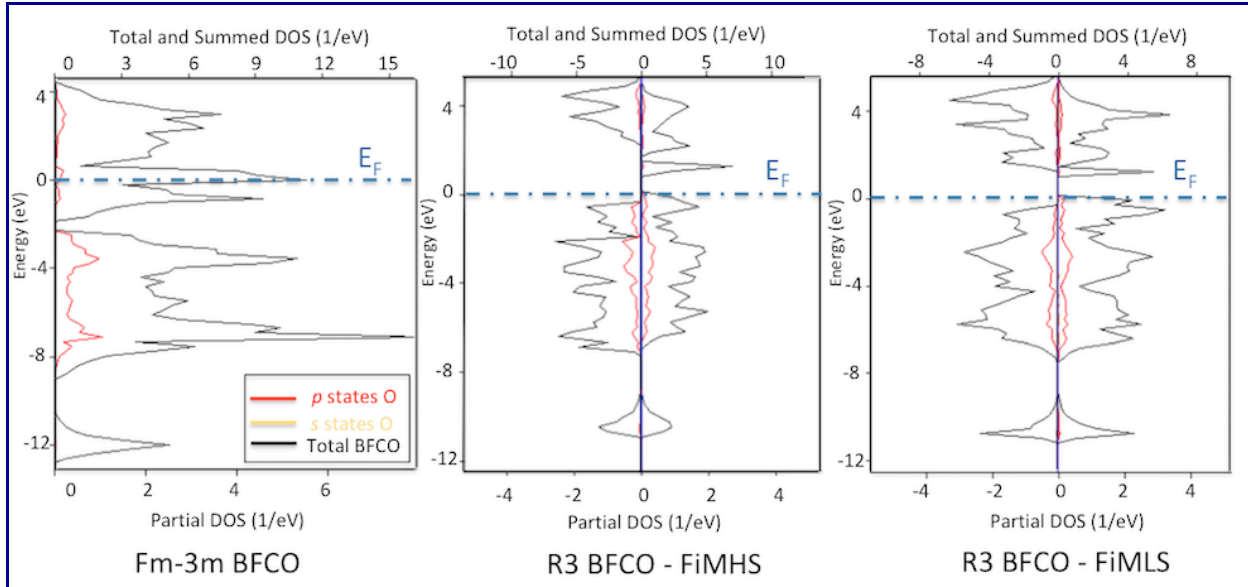


Figure AI.4 The computed O density of states within the LSDA+U functional for the BFCO highly symmetric structure (Fm-3m) compared with the corresponding O states of the rhombobedral BFCO (R3) for the FiMHS, FiMLS, FMHS and FMLS magnetic states.

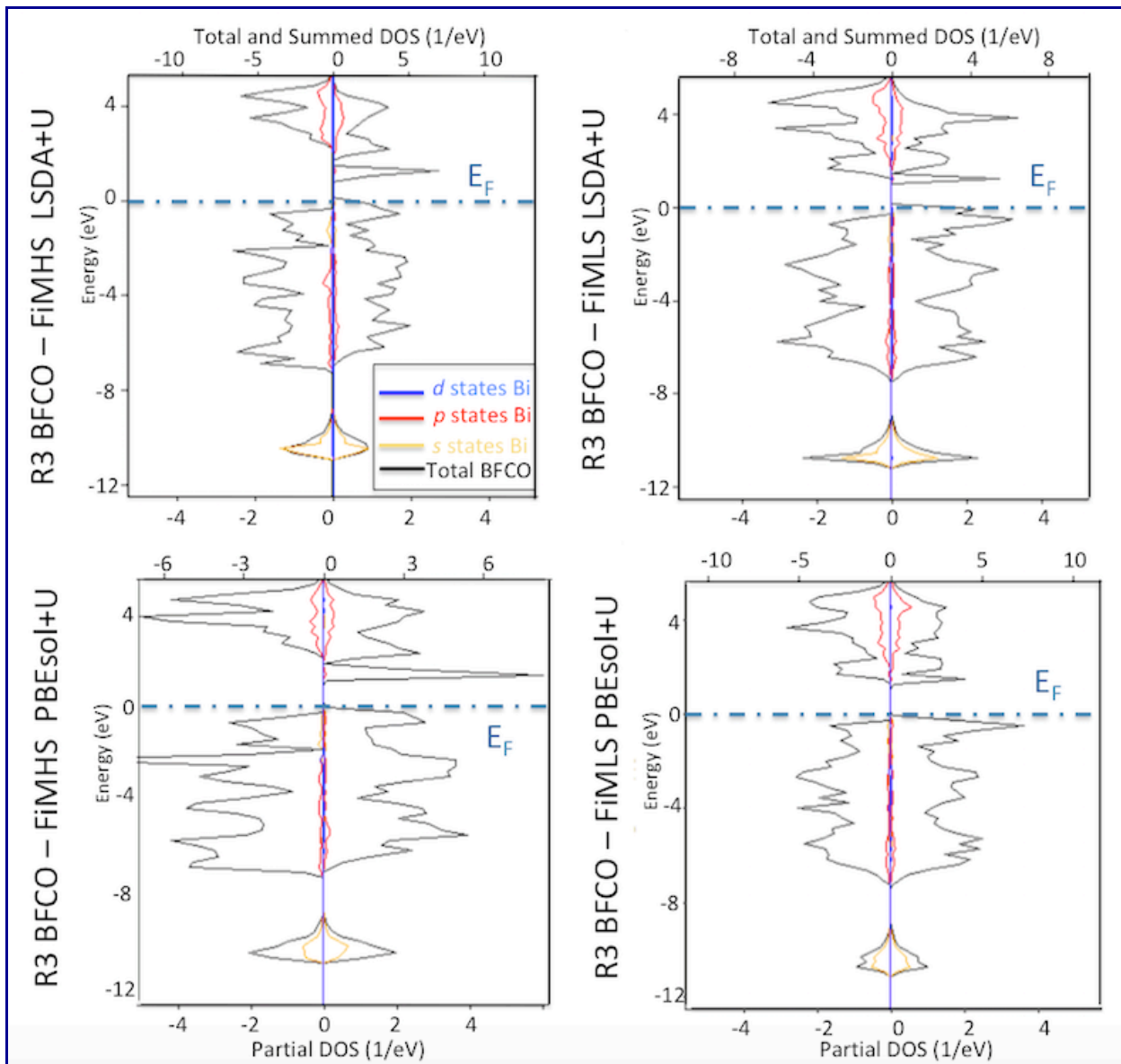


Figure Al.5a DOSs of Bi for FiMHS, FiMLS from LSDA+U compared with PBEsol+U.

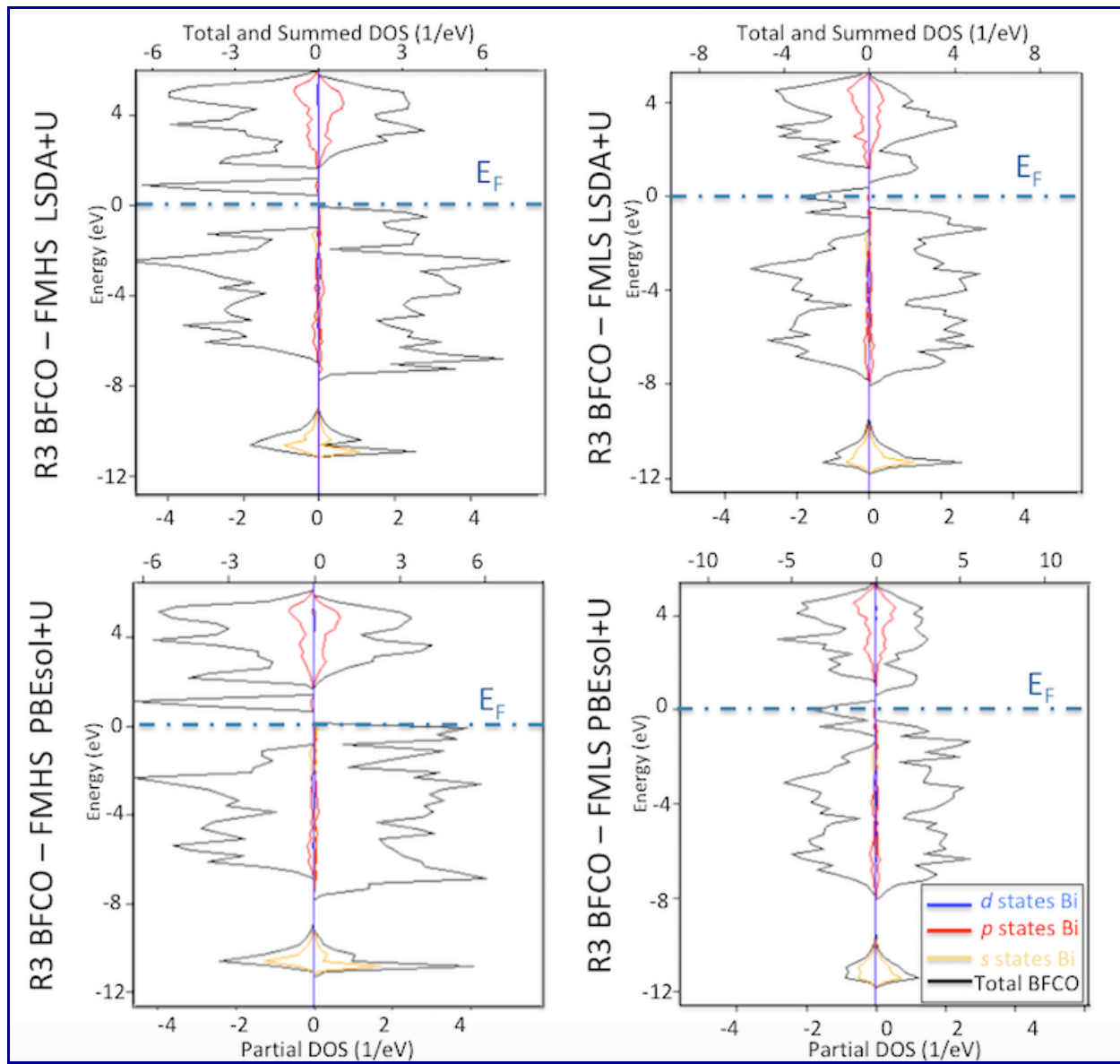


Figure A1.5b DOSs of Bi for FMHS, FMLS from LSDA+U compared with PBEsol+U.

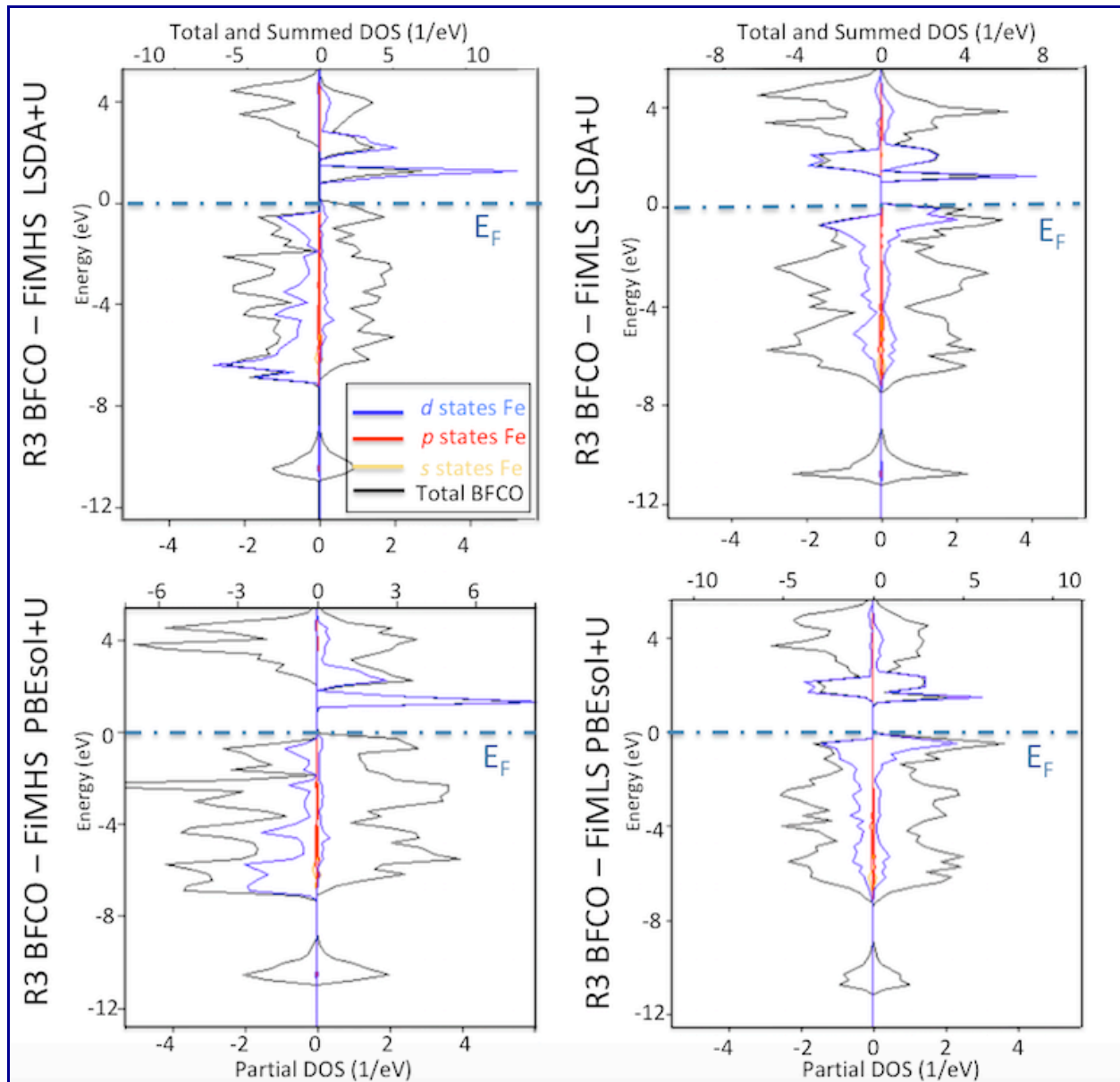


Figure AI.6a DOSs of Fe for FiMHS, FiMLS from LSDA+U compared with PBEsol+U.

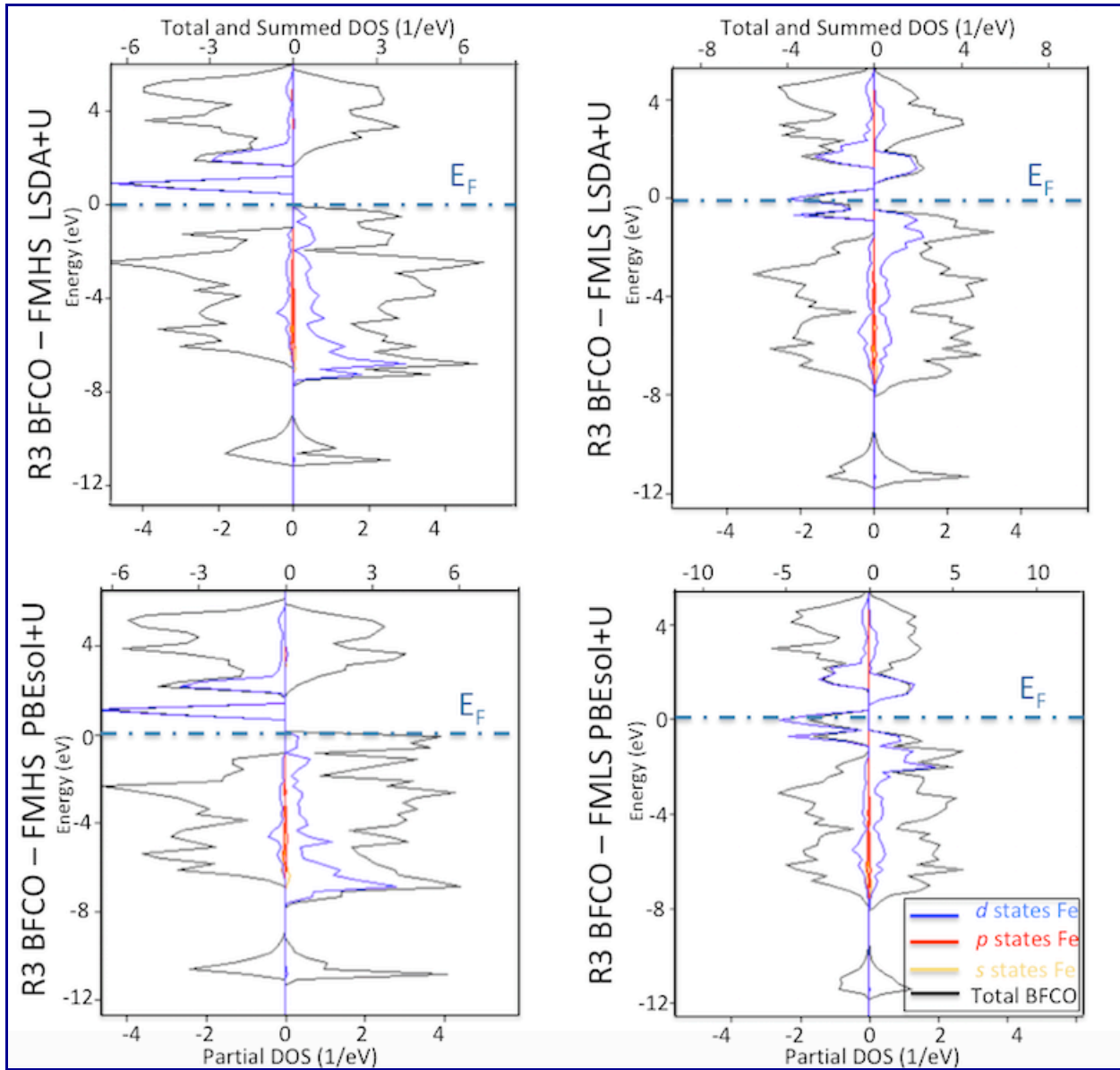


Figure AI.6b DOSs of Fe for FMHS, FMLS from LSDA+U compared with PBEsol+U.

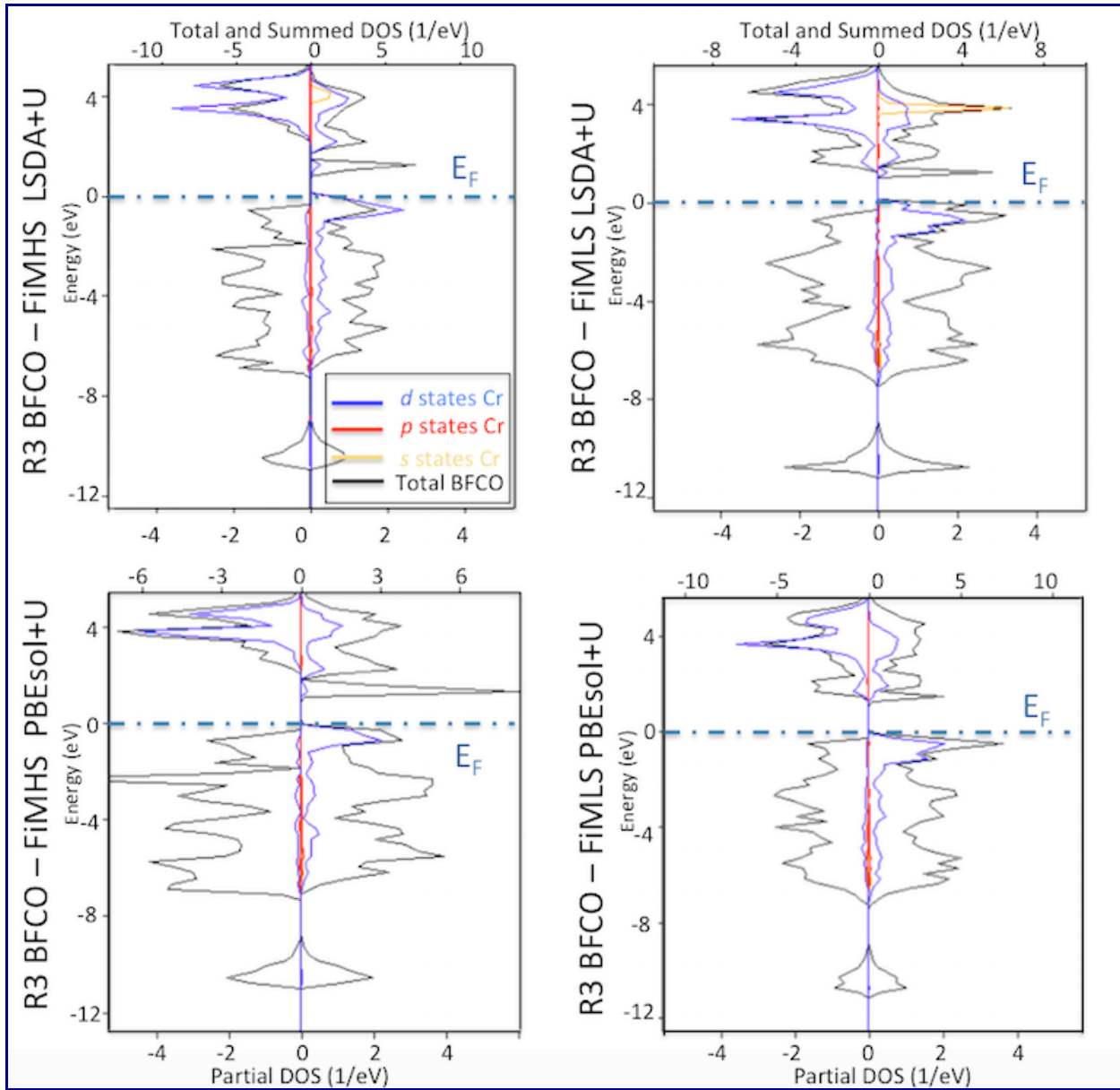


Figure Al.7a DOSs of Cr for FiMHS, FiMLS from LSDA+U compared with PBEsol+U.

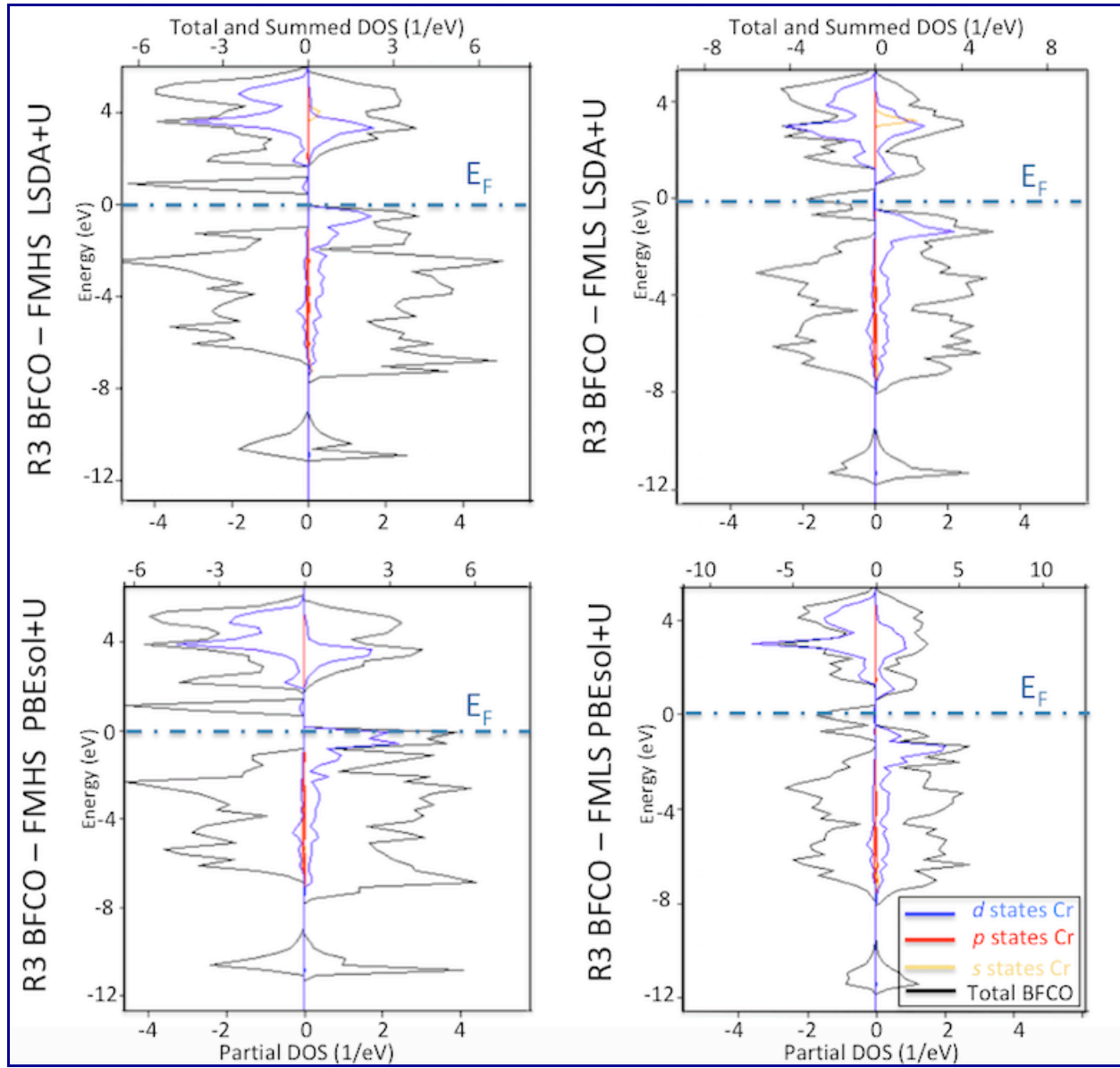


Figure AI.7b DOSs of Cr for FMHS, FMLS from LSDA+U compared with PBEsol+U.

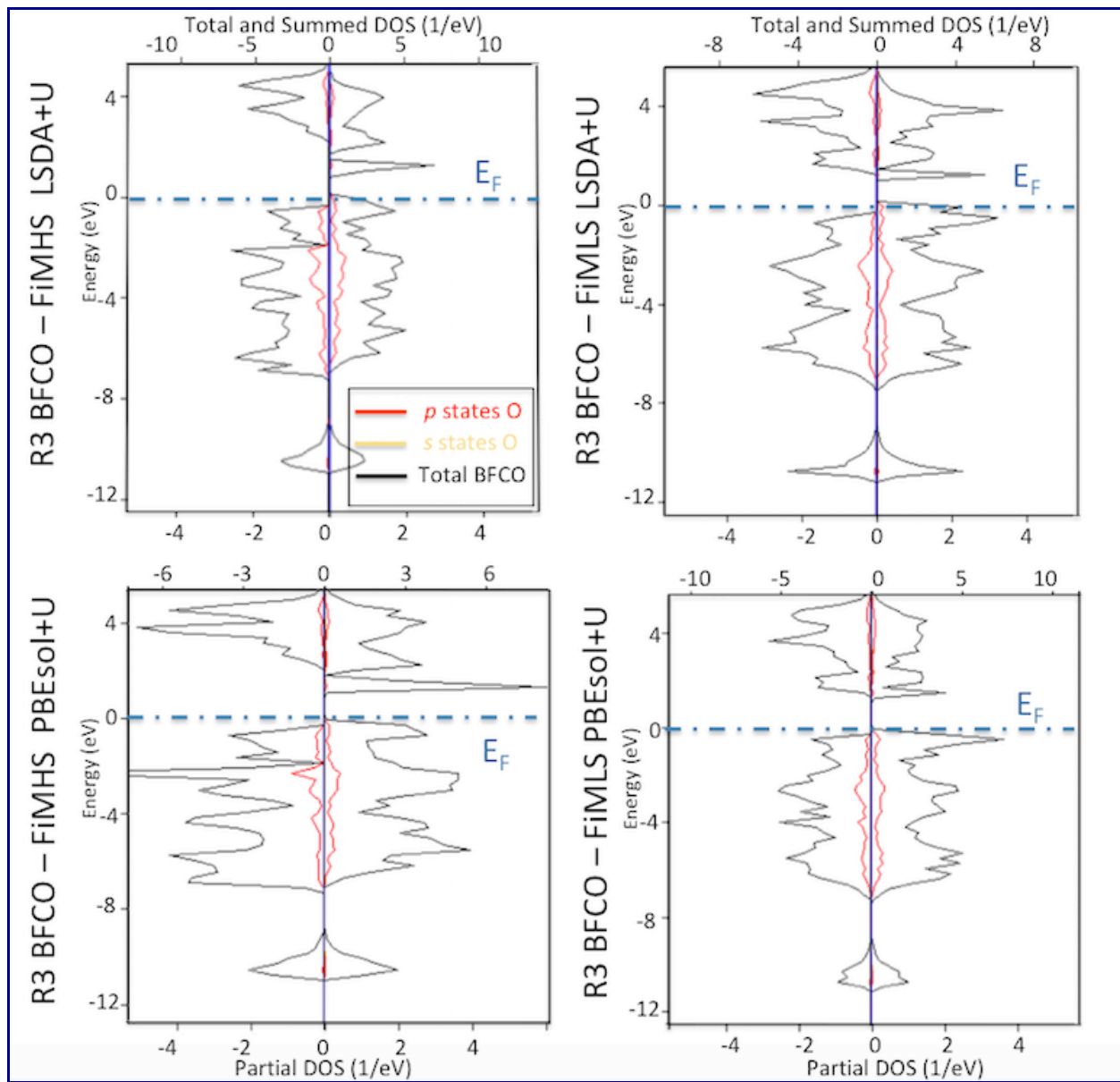


Figure A1.8a DOSs of O for FiMHS, FiMLS from LSDA+U compared with PBEsol+U.

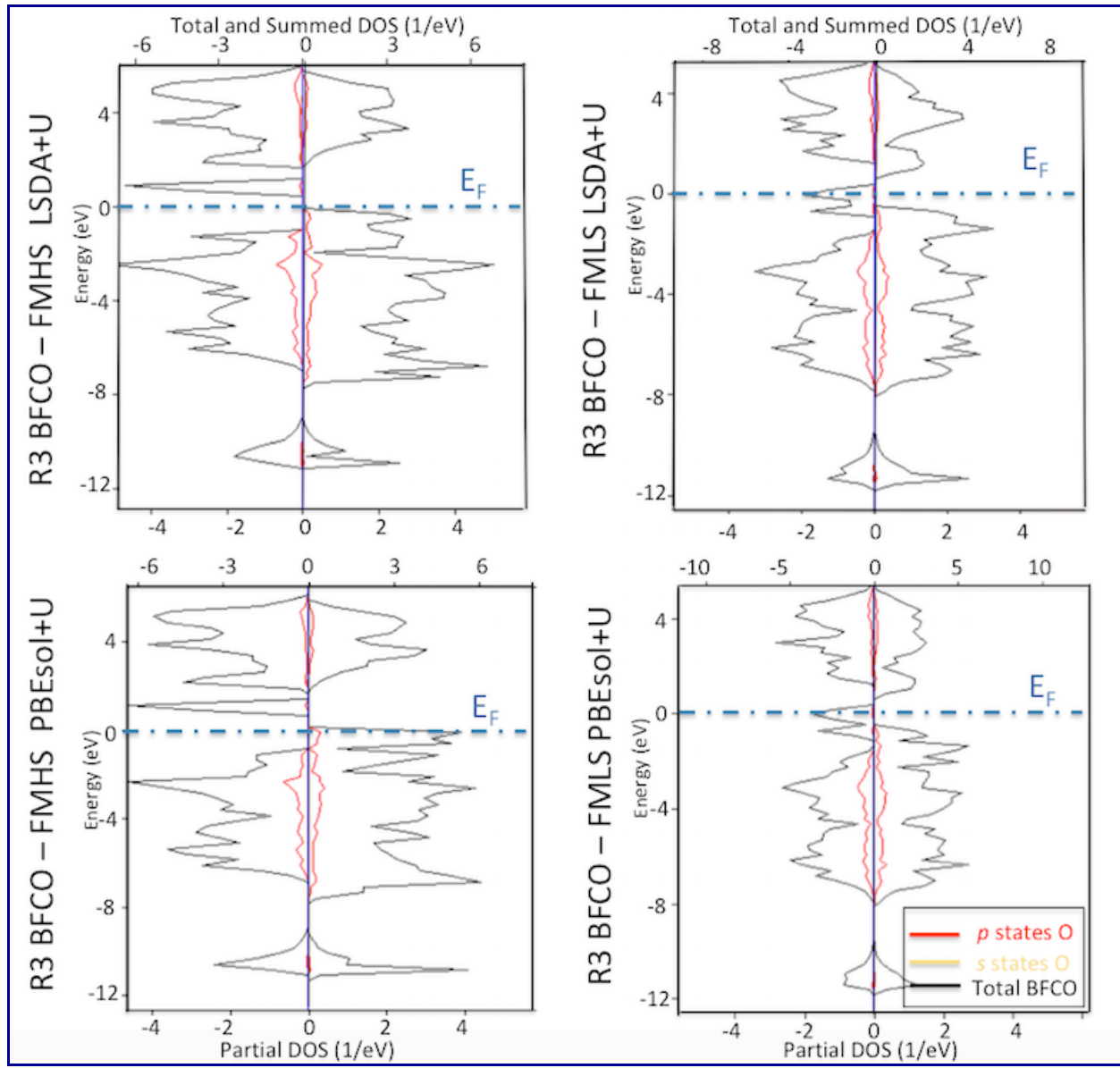


Figure AI.8b DOSs of O for FMHS, FMLS from LSDA+U compared with PBESol+U.